Object Based Wetland Mapping in Newfoundland and Labrador Using Synthetic Aperture RADAR (SAR) and Optical Data

by

© Sahel Mahdavi

A thesis submitted to the

School of Graduate Studies

in partial fulfilment of the

requirements for the degree of

Doctor of Philosophy

Department of Electrical and Computer Engineering

Memorial University of Newfoundland

September 2018

St. John's Newfoundland

"...They encompass not a thing of His knowledge except for what He wills..."

Holy Quran

Dedicated to

those who, with the sake of the sun,

illuminate a light in the dark.

Abstract

Wetlands are amongst the most valuable natural resources that provide many advantages to the ecosystem and humans. Therefore, their mapping and monitoring is crucial. In today's dynamic world, where vast areas require observation with increasing frequency, remote sensing is an accessible, cost effective way of environmental monitoring.

This thesis proposes novel remote sensing methods for mapping and monitoring wetlands and other complicated land covers and facilitates this by proposing alternative pre-processing or post-processing techniques. In Chapter 2, a comprehensive literature review was conducted that elaborates on different aspects of wetland studies. Various methods for wetland classification, along with the benefits and limitations of each, were provided, and areas which could be improved were highlighted. In Chapter 3, an innovative filter was proposed for reducing speckle in Synthetic Aperture RADAR (SAR) images, which is considered an important pre-processing step for land cover classification using SAR data. The proposed filter applies window sizes to each pixel based on the size of the object in which the pixel is placed. The filter was applied to two simulated and two real SAR images in both single-channel and full-polarimetric cases, and the filter results were comparable to several state-of-the-art filters. In Chapter 4, wetlands in four pilot sites within Newfoundland and Labrador were classified using multi-temporal RADARSAT-2 imagery by applying the proposed method for segmentation of SAR images. The covariance matrix was found to be a valuable feature, although textural and ratio features slightly increased the overall accuracy of wetland mapping. Furthermore, August was determined to be

the best month for wetland classification. In Chapter 5, an innovative dynamic classification scheme was proposed for mapping complicated land covers. In this method, objects are not assigned labels simultaneously, but different classes are mapped using a separate feature selection and classification. The proposed method was applied to wetlands in NL and increased the wetland accuracy by up to 25% compared to the classic mapping scheme. Finally, in Chapter 6, a change detection scheme was presented using full-polarimetric SAR data by considering neighbourhood information, which proved effective in detecting changes in land covers and, therefore, can be applied to various environments including wetlands.

Overall, the methods proposed herein offer novel and accurate techniques for the classification of complex land cover types, such as wetlands in NL, Canada that may be applied in other areas of the world in future studies.

Acknowledgements

First and foremost, I wish to express my sincere gratitude to God Almighty, who gave me the ability, knowledge, and opportunity to complete my PhD. Without God's blessings, I would never been able to achieve my goals.

I would like to thank my supervisory committee, Dr. Bahram Salehi, Dr. Weimin Huang, and Dr. Brian Brisco, for their continuous support and guidance during my PhD program. Without their encouragement and constructive criticisms, it would have been difficult for me to accomplish this level.

I also would like to extend my appreciation to Dr. Cecilia Moloney, who compassionately encouraged me throughout the course of my PhD and offered me sensible advices in difficult situations.

My PhD research would not be possible without the collaboration of several organizations who assisted us with financial support, providing satellite imagery, collecting field data, and giving valuable advice. These organizations include the Natural Sciences and Engineering Research Council of Canada, the Canada Center for Mapping and Earth Observation, Environment and Climate Change Canada, Ducks Unlimited Canada, the Government of Newfoundland and Labrador Department of Environment and Conservation, and Nature Conservancy Canada.

In addition, I wish to appreciate the kindness and support of my fellow graduate students at Memorial University who accompanied me throughout my PhD.

I would also like to deeply thank my dear parents. With their ever-lasting, sincere affection, they provided the opportunity for me to continue my studies in Canada and have been always supporting me from a million miles away.

Finally, I would like to thank my husband, Meisam Amani, who inspired me during the years I was away from home. Dear Meisam, the sweetest memory of my PhD is receiving your love from God!

Contents

List of Tables

List of Figures

Nomenclature

$\bar{Z}$	Average of the covariance matrices
$\bar{I}$	Average intensity in a local window
$\hat{f}$	Despeckled image
$\hat{R}$	Estimated intensity
$\hat{Z}$	Filtered covariance matrix
κ	Kappa Coefficient
Σ_i	Covariance matrix for the ith class
σ_I^2	Variance of the intensity in the local window
σ_u^2	Ratio of the standard deviation to mean in a homogeneous area
B_{ij}	Bhattacharyya distance between classes i and j
C_g	Coefficient of variation of the noisy image
C_u	Coefficient of variation of the speckle noise
f	Speckled image

f_p	Ground-truth image
FNs	False Negatives
FPs	False Positives
I	Observed intensity
J_{ij}	Jeffries-Matusita (JM) Distance between classes i and j
ln	Natural logarithm
m_i	Mean for the ith class
OE	Overall Error
PCC	Percentage Correct Classification
Q	Wishart Maximum Likelihood Ratio
TNs	True Negatives
TPs	True Positives
UA	User Accuracy
W	Weight parameter
Z	Covariance matrix
ASF	Alaska Satellite Facility
ASTER	Advanced Spaceborne Thermal Emission and Reflection Radiometer

AVIRIS	Airborne Visible/Infrared Imaging Spectrometer
CART	Classification and Regression Tree
CASI	Compact Airborne Spectrographic Imager
CCS	Cowardin Classification System
CDEM	Canadian Digital Elevation Model
CTI	Compound Topographic Index
CVA	Change Vector Analysis
CWCS	Canadian Wetland Classification System
CWI	Canadian Wetland Inventory
DEM	Digital Elevation Model
DT	Decision Tree
ENL	Equivalent Number of Looks
EO	Earth Observation
ESA	European Space Agency
FQ	Fine-Resolution Quad-Polarimetric
GA	Genetic Algorithm
GBFM	Global Boreal Forest Mapping

GIS	Geographical Information System
GLCM	Grey Level Co-occurrence Matrix
GLRT	Generalized Likelihood Ratio Test
GPS	Global Positioning System
IDAN	Intensity Driven Adaptive Neighbourhood
KCE	Curvelet Coefficient Energy
KNN	K Nearest Neighbours
LiDAR	Light Detection and Ranging
LST	Land Surface Temperature
MERIS	MEdium Resolution Imaging Spectrometer
MESMA	Multiple Endmember Spectral Mixture Analysis
MLR	Maximum Likelihood Ratio
ML	Maximum Likelihood
MNF	Minimum Noise Fraction
MSE	Mean Square Error
NDVI	Normalized Difference Vegetation Index
NL	Newfounaland and Labrador

NWI	National Wetland Inventory
OBIA	Object Based Image Analysis
PCA	Principal Components Analysis
PolSARpro	Polarimetric SAR Data Processing and Educational Toolbox
PolSAR	Polarimetric SAR
PPB	Probabilistic Patch-Based filter
PSO	Particle Swarm Optimization
PWF	Polarimetric Whitening Filter
RF	Random Forest
RS	Remote Sensing
SAR	Synthetic Aperture Radar
SLC	Single Look Complex
SLIC	Simple Linear Iterative Clustering
SMA	Spectral Mixture Analysis
SNR	Signal-to-Noise Ratio
SSIM	Structural Similarity Index Measurement
SVM	Support Vector Machine

TPI	Topographic Position Index
UAV	Unmanned Aerial Vehicle
USFWS	United States Fish and Wildlife Service
USR	Unsupervised Spectral Regression
VHR	Very High Resolution
WAM	WAter indication Mask

Chapter 1

Introduction

1.1 Background

"Wetland is a land transitional between terrestrial and aquatic systems, where the water table is usually at or near the surface or the land is covered by shallow water" [1]. Wetlands provide numerous advantages to the environment and humans, such as purification of water, protection from natural hazards, and conservation of soil and water [2–4]. Although wetlands cover about 7 million square kilometres of the earth, they are degrading quickly [5] as a result of extensive ground water extraction, irrigation, and drainage [6]. Therefore, mapping and monitoring wetlands is important for their conservation.

Many wetland inventories have been developed since the value of wetlands and the potential of Remote Sensing (RS) for wetland mapping have been realized. A prerequisite for producing wetland inventories is developing classification methods that can be widely applied to field-based and RS methods. RS, as a cost-effective and

timely option, has been popular among researchers considering the need for frequent maps with large coverages [7].

Although RS methods have advanced considerably, wetland classification using RS remains a challenging task [8,9]. There are several reasons for this, among which are the high spectral similarity of wetlands with each other and with non-wetland classes and the high spatial and temporal variability of wetlands [10–13]. However, RS techniques are still preferred and, therefore, the development of innovative and effective RS methods for the purpose of wetland mapping with minimal need of *in situ* measurements is necessary.

1.2 Research Motivations and Objectives

With the above introduction, there are several motivations behind this research. For example, although a number of review papers have been published on wetlands [7,11,14], there is a need for a comprehensive literature review which considers various aspects of wetland studies, including different classification methods along with benefits and limitations of each.

Moreover, considering that Newfoundland and Labrador (NL) is the only province in Atlantic Canada that lacks a provincial wetland map [15] and approximately 14% of Canada is covered by wetlands [16] many of which are located in remote locales, *in situ* monitoring of wetlands is almost impossible due to issues of time and coverage limitation, laboriousness, and cost. Therefore, RS is a valuable tool for practical and operational mapping and monitoring of wetlands. However, due to the high number of similarities among different wetland classes, wetland classification is a challenging

task from a RS perspective. Therefore, few robust RS methods have been proposed that specifically fit wetland characteristics. Moreover, freely available satellite images have not been adequately used for this purpose.

At the same time, monitoring land covers including wetlands demands appropriate change detection techniques. However, there are few SAR change detection techniques for land cover monitoring which yield noiseless, connected changed areas, which are necessary in order to make correct managerial decisions.

Based on the above discussion, the objectives of this research are to:

1. Conduct a comprehensive literature review of wetland classification using satellite imagery that considers various aspects of wetland studies.

2. Propose a speckle reduction method as a preprocessing step for wetland classification that filters each pixel based on the size of the object in which the pixel is located.

3. Evaluate the potential of multi-temporal Polarimetric SAR (PolSAR) data for wetland mapping and determine the optimal feature and time for wetland classification using SAR data.

4. Propose a novel dynamic classification scheme for mapping spectrally similar classes, including those of wetlands, using a combination of Synthetic Aperture Radar (SAR), optical, and other types of RS data. This method also evaluates the potential of freely available satellite data.

5. Detect changes in land covers by utilizing neighbourhood information using the ratio of total power (span) of the images before and after the event.

1.3 Research Methodology

In order to achieve the objectives described above, a number of studies with methodologies specific to each were conducted. First, a literature review was performed to gain a deeper understanding of wetland characteristics in terms of RS. Second, an innovative method was introduced for speckle reduction in SAR images as a preprocessing step for wetland classification using SAR imagery. Third, the potential of multi-temporal PolSAR data for wetland mapping was evaluated. This determined the most appropriate feature and month for conducting wetland studies. Fourth, a dynamic classification scheme was proposed for mapping spectrally similar classes, including those of wetlands. The proposed method is specially useful for wetland classification and also utilizes freely available satellite data. Finally, a change detection approach was suggested using neighbourhood information to monitor changes in various land covers including wetlands. A summary of each segment of the research is provided below.

1.3.1 Literature Review

1.3.1.1 Overview and Problem Statement

There are a number of literature review papers dealing with wetland classification. Nevertheless, there is a need for a comprehensive review including wetland importance, the requirement of wetland mapping and monitoring, and a complete description of the methods for wetland classification. The aim of this part of the research was to familiarize readers with different aspects of wetland studies. Initially, the importance, characteristics, and challenges of wetlands were introduced. Then,

a thorough discussion of various RS approaches for wetland classification along with the drawbacks and benefits of each were provided.

1.3.1.2 Contribution(s) to the Body of Knowledge

This review provides novel insights on wetland classification through the use of different techniques, such as optical, SAR, UAV, and hyperspectral imagery. The existing research on wetland classification is either outdated or considers only a single aspect of wetland classification.

1.3.1.3 Overall Progress

This task has been completed and a review paper, resulting from this work, has been published in the *GIScience & Remote Sensing* journal.

1.3.2 Speckle Filtering of SAR Images using Filters with Object-size Adapted Windows

1.3.2.1 Overview and Problem Statement

Speckle negatively affects the radiometric quality of a SAR image. Most previously proposed filters for reducing speckle in SAR image have used a fixed size window for filtering the entire image. This, however, might not be effective for land covers with different sizes, such as wetlands. Therefore, in this part of research, a novel filter was proposed by which the pixels within the image are filtered with a window size proportional to the size of the object within which the pixel is located.

1.3.2.2 Methodology

In the proposed method, the optimal window size was determined based on the minimum standard deviation associated with the in-phase and the quadrature components of the SAR images. Afterwards, the obtained window size for each pixel was applied to filter that pixel in the intensity image. The proposed method was presented for both single-channel and polarimetric SAR images, and the results of several common filters were modified and presented.

1.3.2.3 Contribution(s) to the Body of Knowledge

The majority of previously proposed speckle filters use a fixed window size (see Section 1.3.2.1 for details). Using the proposed method, however, all objects within the image are filtered with a window size proportional to their area.

1.3.2.4 Overall Progress

This task is completed, and the resulting paper has been published in the *International Journal of Digital Earth*.

1.3.3 Object-based Wetland Mapping in NL Using Multi-Temporal PolSAR Data

1.3.3.1 Overview and Problem Statement

A considerable part of NL is covered by wetlands, but this province lacks a provincial wetland inventory. In this study, multi-temporal SAR data were analyzed for wetland classification at four pilot sites across NL using an alternative segmentation

method, since the current segmentation methods of SAR images were not as effective as those proposed for optical images.

1.3.3.2 Methodology

In this study, object-based classification using the proposed segmentation method was compared to pixel-based classification. Next, the multi-temporal wetland classification was compared to the conventional single-date classification in each pilot site. Finally, an evaluation of the ratio and textural features was also performed.

1.3.3.3 Contribution(s) to the Body of Knowledge

As mentioned before, NL is the only province in Atlantic Canada which lacks a comprehensive wetland inventory. In this part of the work, four pilot sites within NL were classified, which is the initial step for classifying the entire province. Additionally, an alternative segmentation method of SAR images was proposed based on optical images. Moreover, the potential of ratio and textural features was evaluated in this work, which is not common in previous studies of wetland classification.

1.3.3.4 Overall Progress

This task is completed, and the resulting paper has been published in the *Canadian Journal of Remote Sensing*.

1.3.4 A Novel Dynamic Classification Scheme for Mapping Spectrally Similar Classes

1.3.4.1 Overview and Problem Statement

Feature selection is necessary for classification of complicated land covers when numerous features are available. Although high overall accuracies can be obtained when selected features are used for mapping spectrally similar classes, such as wetlands, some poor individual class accuracies may also exist. One reason might be that a single feature subset may not be useful for the discrimination of all pairs of classes. Moreover, overall accuracy can be influenced by the accuracy of a few classes that are spectrally distinct. In this part of the research, a novel method for classification of complicated land covers was proposed that maps each class individually using a separate feature selection and classification.

1.3.4.2 Methodology

In this study, the classes were not mapped simultaneously, but were classified individually with a different feature selection associated with each. For determining the order of the classes and the merging scheme introduced in the paper, spectral analysis was utilized. The proposed method was applied to wetland classification using data from five pilot sites throughout NL, Canada.

1.3.4.3 Contribution(s) to the Body of Knowledge

Determining a classification order, a merging scheme, and, in general, mapping various classes separately are unprecedented in the RS community, and proved very

useful for wetland classification.

1.3.4.4 Overall Progress

This task is completed, and the yielded paper has been submitted, and is currently *under review*.

1.3.5 A Synthetic Aperture Radar change detection method based on neighbourhood information

1.3.5.1 Overview and Problem Statement

Change detection using SAR images is valuable because of their all-weather, day and night acquisition capabilities. As a result of the presence of speckle, considering neighbourhood information in SAR images is recommended for more accurate change detection. Based on this fact, a polarimetric change detection index was proposed which uses the ratio of span (total power) values to detect changes between two full-polarimetric SAR images.

1.3.5.2 Methodology

In this study, a single-channel index based on neighbourhood information was extended to full polarimetric SAR data. In the proposed index, the ratio of span (total power) was considered for both the central pixel and its neighbourhood, and a weight parameter was used to adjust the effect of central versus surrounding pixels. Since a long-term dataset of SAR images from NL was not available at the time of conducting this research, the proposed index was applied to detect changes caused

by a flooding event in Dongting lake, Hunan, China.

1.3.5.3 Contribution(s) to the Body of Knowledge

While there are very few studies that consider neighbourhood information for SAR change detection, this study proposed a full polarimetric SAR change detection index based on neighbourhood information that produces less noisy and more connected changed areas compared to other measures.

1.3.5.4 Overall Progress

This task has been completed, and the resulting paper has been submitted, and is currently *under review*.

1.4 Achievements

The overall findings of this study have been presented in a number of formats including a book chapter, peer-reviewed journal papers, conference papers and presentations, a software package, and a website. The details can be found in the following sections.

1.4.1 Book Chapter

- Salehi, B., Mahdianpari, M., Amani, M., Mohammadimanesh, F., Granger, J., **Mahdavi, S.**, Brisco, B., 2018, "A collection of novel algorithms for wetland classification with SAR and optical data", *under review*, *InTech Open*.

1.4.2 Journal Papers

- **Mahdavi, S.**, Salehi, B., Granger, J., Amani, M., Brisco, B., Huang, W., "Remote sensing for wetland classification: a comprehensive review", 2017, *GIScience & Remote Sensing*,55, 5, 623-658.

- **Mahdavi, S.**, Salehi, B., Moloney, C., Huang, W., and Brisco, B. "Speckle filtering of Synthetic Aperture Radar images using filters with object-size-adapted windows", 2017, *International Journal of Digital Earth*, 11, 7, 703-729.

- **Mahdavi, S.**, Salehi, B., Amani, M., Granger, J., Brisco, B., Huang., W., Hanson, A., "Object-based classification of wetlands in Newfoundland and Labrador using multi-temporal PolSAR data", 2017, *Canadian Journal of Remote Sensing*, 43, 5, 432-450.

- **Mahdavi, S.**, Salehi, B., Amani, M., Granger, J., Brisco, B., Huang, W., "A novel dynamic classification scheme for mapping spectrally similar classes: application to wetland classification", 2018, *under review.*

- **Mahdavi, S.**, Salehi, B., Amani, M., Brisco, B., Huang, W., "A polarimetric Synthetic Aperture RADAR index based on neighbourhood information", 2018, *under review.*

- Amani, M., Salehi, B., **Mahdavi, S.**, Brisco, B., Shehata, M., "A Multiple Classifier System to improve mapping complex land covers: a case study of wetland classification using SAR data in Newfoundland, Canada", 2018, *International Journal of Remote Sensing*, *In press.*

- Mahdianpari, M., Salehi, B., Mohammadimanesh, F., Brisco, B., **Mahdavi, S.**, Amani, M., Granger, J. E., "A novel approach for object-based wetland classification of PolSAR data using Fisher-based Random Forest algorithm", 2018, *Remote Sensing of Environment*, 206, 300-317.

- Amani, M., Salehi, B., **Mahdavi, S.**, Granger, J., Brisco, B., "Wetland classification in Newfoundland and Labrador using multi-source SAR and optical data integration", 2017, *GIScience and Remote Sensing*, 54, 6, 779-796.

- Amani, M., Salehi, B., **Mahdavi, S.**, Granger, J., Brisco, B., "Wetland Classification Using Multi-Source and Multi-Temporal Optical Remote Sensing Data in Newfoundland and Labrador, Canada", 2017, *Canadian Journal of Remote Sensing*, 43, 4, 360-373.

- Amani, M., Salehi, B., **Mahdavi, S.**, Brisco, B., "Spectral analysis of wetlands using multi-source optical satellite imagery", 2018, *ISPRS Journal of Photogrammetry and Remote Sensing*, 144, 119-136.

- Amani, M., Salehi, B., Mahdavi, S., Brisco, B., Separability Analysis of Wetlands Using Multi-source SAR data, 2018, *under review*.

1.4.3 Conference Papers

- **Mahdavi, S.**, Salehi, B., Amani, M., Granger, J., Brisco, B., Huang., W., "A dynamic hierarchical feature selection method for object-based classification of wetlands", 2017, in *International Geoscience and Remote Sensing Symposium (IGARSS) 2017* proceedings, Fort Worth, Texas, USA.

- **Mahdavi, S.**, Salehi, B., Amani, M., Granger, J., Brisco, B., Huang, W., "A novel method for classification of complicated land covers using Remote Sensing techniques", 2017, in *Newfoundland Electrical and Computer Engineering Conference (NECEC)* proceedings, St. John's, Newfoundland and Labrador, Canada.

- **Mahdavi, S.**, Salehi, B., Amani, M., Granger, J., Brisco, B., Huang, W., "An investigation into the capability of various Synthetic Aperture RADAR (SAR) sensors for wetland classification in Newfoundland and Labrador", 2017, in *IGTF 2017, ASPRS Annual Conference* proceedings, Baltimore, Maryland, USA.

- **Mahdavi, S.**, Salehi, B., Moloney, C., Huang, W., and Brisco, B., "A new method for speckle reduction in Synthetic Aperture RADAR (SAR) images using optimal window size", 2017, in *9th Symposium of the International Society for Digital Earth (ISDE)* proceedings, 2015, Halifax, Nova Scotia, Canada.

- Amani, M., Salehi, B., **Mahdavi, S.**, Granger, J., "Spectral analysis of wetlands in Newfoundland using Sentinel 2A and Landsat 8 imagery", 2017, in *IGTF 2017, ASPRS Annual Conference* proceedings, Baltimore, Maryland, USA.

- Amani, M., Salehi, B., **Mahdavi, S.**, Granger, J., Brisco, B. "Evaluation of multi-temporal Landsat 8 data for wetland classification in Newfoundland, Canada", 2017, in *International Geoscience and Remote Sensing Symposium (IGARSS) 2017* proceedings, Fort Worth, Texas, USA.

- Amani, M., Salehi, B., **Mahdavi, S.**, Granger, J., "An Operational Wetland Classification Model in Newfoundland and Labrador using Advanced Remote Sensing Methods", 2017, in *Newfoundland Electrical and Computer Engineering Conference (NECEC)* proceedings, St. John's, Newfoundland and Labrador, Canada.

1.4.4 Conference Presentations

- **Mahdavi, S.**, Salehi, B., Amani, M., Brisco, B., Huang, W., "An operational method for wetland classification in Newfoundland and Labrador using publicly available satellite data", 2017, *Geomatics Atlantic Conference*, St. John's, Newfoundland and Labrador, Canada.

- **Mahdavi, S.**, Salehi, B., Amani, M., Granger, J., Brisco, B., Huang., W., 2016, "Object-based, multi-Temporal SAR analysis for wetland classification in Newfoundland and Labrador", *37th Canadian Symposium on Remote Sensing (CSRS)*, Winnipeg, Manitoba, Canada.

- **Mahdavi, S.**, Salehi, B., Brisco, B., Huang., W., 2015, "Object-Based classification of wetlands using optical and SAR data with a compound kernel in Support Vector Machine", *American Geophysical Union (AGU) Fall Meeting*, San Francisco, California, USA

- **Mahdavi, S.**, Maghsoudi, Y., Salehi, B., "A Speckle filtering approach of SAR data based on a coherent decomposition", 2015, *37th Canadian Symposium for Remote Sensing Conference (CSRS)*, St. John's, Newfoundland and Labrador, Canada.

1.4.5 A Software Package

The candidate contributed to developing a software package in C-CORE named Advanced Remote Sensing Lab (ARSeL) which includes various RS algorithms for wetland classification.

1.4.6 A Website

The candidate contributed to developing a website (http://nlwetlands.ca/) which includes the final maps of pilot sites as well as other information about wetlands in Newfoundland and Labrador. In fact, the maps illustrated on the website were obtained during this research by using the novel dynamic classification scheme introduced in Chapter 5.

1.5 Organization of the Thesis

This thesis is organized as follows. Chapter 2 provides a comprehensive literature review of wetland classification using various RS methods. In Chapter 3, the speckle reduction filter is elaborated upon. Wetland classification using multi-temporal Pol-SAR data and the novel dynamic classification scheme are explained in Chapters 4 and 5, respectively. Change detection for land cover monitoring using neighbourhood information is discussed in Chapter 6, before the concluding remarks are presented in Chapter 7.

1.6 Co-authorship Statement

Ms. Sahel Mahdavi was the primary author of the research papers provided in chapters 2 to 6. The other co-authors are listed as follows:

- **Dr. Bahram Salehi (thesis supervisor)**: Reseatch Scientist at C-CORE, and cross-appointed Professor at Memorial University of Newfoundland.
- **Dr. Weimin Huang (thesis co-supervisor)**: Associate Professor, Faculty of Engineering and Applied Science, Memorial University of Newfoundland.
- **Dr. Brian Brisco (thesis co-supervisor)**: Research Scientist at the Canada Center for Mapping and Earth Observation, Natural Resources Canada.
- **Dr. Cecilia Moloney (course instructor)**: Full Professor, Faculty of Engineering and Applied Science, Memorial University of Newfoundland.
- **Dr. Alan Hanson**: Head, Migratory Bird Conservation Unit, Canadian Wildlife Service, Sackville, New Brunswick.
- **Meisam Amani**: PhD Candidate, Faculty of Engineering and Applied Science, Memorial University of Newfoundland.
- **Jean Granger**: M.Sc Candidate, department of geography, Memorial University of Newfoundland.

The PhD candidate was responsible for developing and coding each algorithm, processing primary data, and preparing the manuscript. The co-authors provided revisions to the paper or collaborated with processing adjunct data.

Bibliography

[1] WJ Mitsch and James G Gosselink. Wetlands, 2nd, 1993.

[2] Marcelle Grenier, Anne-Marie Demers, Sandra Labrecque, Martine Benoit, Richard A Fournier, and Bruno Drolet. An object-based method to map wetland using radarsat-1 and landsat etm images: test case on two sites in quebec, canada. *Canadian Journal of Remote Sensing*, 33(S1):S28–S45, 2007.

[3] Ryan P Powers, Geoffrey J Hay, and Gang Chen. How wetland type and area differ through scale: A geobia case study in alberta's boreal plains. *Remote Sensing of Environment*, 117:135–145, 2012.

[4] Wei Ji, Xiaofan Xu, and Dzingirai Murambadoro. Understanding urban wetland dynamics: cross-scale detection and analysis of remote sensing. *International Journal of Remote Sensing*, 36(7):1763–1788, 2015.

[5] Millennium Ecosystem Assessment. Ecosystems and human well-being: wetlands and water. *World resources institute, Washington, DC*, 5, 2005.

[6] Evaluating full polarimetric c-and l-band data for mapping wetland conditions in a semi-arid environment in central spain.

[7] Stacy L Ozesmi and Marvin E Bauer. Satellite remote sensing of wetlands. *Wetlands ecology and management*, 10(5):381–402, 2002.

[8] Tobias Landmann, Matthias Schramm, Rene R Colditz, Andreas Dietz, and Stefan Dech. Wide area wetland mapping in semi-arid africa using 250-meter modis metrics and topographic variables. *Remote Sensing*, 2(7):1751–1766, 2010.

[9] Jennifer Corcoran, Joseph Knight, Brian Brisco, Shannon Kaya, Andrew Cull, and Kevin Murnaghan. The integration of optical, topographic, and radar data for wetland mapping in northern Minnesota. *Canadian Journal of Remote Sensing*, 37(5):564–582, 2012.

[10] SE Bunn, PI Boon, MA Brock, and NJ Schofield. National wetlands R& D program: Scoping review. *Land and Water Resources Research and Development Corporation, Canberra*, 1997.

[11] Floyd M Henderson and Anthony J Lewis. Radar detection of wetland ecosystems: a review. *International Journal of Remote Sensing*, 29(20):5809–5835, 2008.

[12] Alisa L Gallant. The challenges of remote monitoring of wetlands, 2015.

[13] Linda Moser, Andreas Schmitt, Anna Wendleder, and Achim Roth. Monitoring of the lac bam wetland extent using dual-polarized X-Band SAR data. *Remote Sensing*, 8(4):302, 2016.

[14] Elhadi Adam, Onisimo Mutanga, and Denis Rugege. Multispectral and hyperspectral remote sensing for identification and mapping of wetland vegetation: a review. *Wetlands Ecology and Management*, 18(3):281–296, 2010.

[15] AR Hanson and L Calkins. *Wetlands of the Maritime Provinces: revised documentation for the wetlands inventory*. Environment Canada, Canadian Wildlife Service, Atlantic Region, 1996.

[16] Government of Canada. Water sources: wetlands, 2016.

Chapter 2

Literature Review

2.1 Preface

In this chapter, a complete literature review was conducted on various aspects of wetland studies, and different algorithms for wetland classification using satellite imagery. The paper resulted from this chapter has been published in the *GIScience & Remote Sensing* Journal.

2.2 Abstract

Wetlands are valuable natural resources which provide many benefits to the environment. Therefore, mapping wetlands is crucially important. Several review papers on Remote Sensing (RS) of wetlands have been published thus far. However, there is no recent review paper that contains an inclusive description of the importance of wetlands, the urgent need for wetland classification, along with a thorough explanation of the existing methods for wetland mapping using RS methods. This article attempts

to provide readers with an exhaustive review regarding different aspects of wetland studies. First, the readers are acquainted with the characteristics, importance, and challenges of wetlands. Then, various RS approaches for wetland classification are discussed along with their advantages and disadvantages. These approaches include wetland classification using aerial, multispectral, Synthetic Aperture Radar (SAR), and several other datasets. Different pixel-based and object-based algorithms for wetland classification are also explored in this study. The most important conclusions drawn from the literature are that the red edge and near infrared bands are the best optical bands for wetland delineation. In terms of SAR imagery, large incidence angles, short wavelengths, and HV (horizontal transmission and vertical reception) polarization are best for detecting herbaceous wetlands, while small incidence angles, long wavelengths, and HH (horizontal transmission and reception) polarization are appropriate for mapping forested wetlands.

2.3 Introduction

"Wetland is a land transitional between terrestrial and aquatic systems, where the water table is usually at or near the surface or the land is covered by shallow water" [1], and provide vital habitats for several unique species of flora and fauna. Some of the benefits associated with wetlands are water purification, protection from natural hazards, conservation of soil and water, as well as recreational values [2–4]. According to [5], wetlands cover at least 7 million square kilometers of the earth. Unfortunately, however, wetlands are prone to an accelerated degradation [6] due to extensive irrigation practices, extraction of ground water, and drainage [7]. Further-

more, many wetlands have been changed to urban or agricultural lands. In fact, thus far up to 57% of the world's wetlands have been converted or lost [8]. Therefore, mapping and monitoring wetlands is of crucial importance.

Many stakeholders have realized the value of wetlands as well as the high potential of Remote Sensing (RS) for mapping these valuable natural resources, and consequently have developed different wetland inventories for this purpose. Wetland inventories can be defined as maps illustrating the area and the distribution of wetlands over geographical regions, and are useful tools for evaluating the effectiveness of wetland polices. Producing wetland inventories, however, demands developing classification schemes to describe the type of wetland classes to be mapped. Consequently, for implementation of classification schemes numerous classification methods were generated, which can be widely divided to field-based and RS methods. Unlike field-based methods, RS is a cost-effective tool which is capable of acquiring frequent measurements from inaccessible places and providing timely information. Given the current need for up-to-date information, as well as the wide spread coverage of wetland maps, satellite RS has been demonstrated to be the most efficient and cost-effective method for this purpose [9].

Despite many advances in RS technology, wetland classification is still a challenging task from the RS perspective [10, 11]. A major reason for this difficulty is that although each of the wetland classes have several distinctive characteristics, they share some ecological similarities with each other [12], and with other non-wetland classes [13]. For example, the vegetation within bog and fen are very similar to each other. However, bog's only source of water is precipitation, while fen has other water sources as well. This fact sometimes make their shape different. Therefore, different

wetlands exhibit similar spectral and/or backscattering information in RS imagery. In addition, wetlands vary significantly in space and time [14, 15]. Despite these difficulties, RS approaches are preferential, especially since field work is the potential alternative, which is a laborious, comparatively costly, and time-consuming task. Therefore, many studies have attempted to develop innovative and effective RS methods for the purpose of wetland mapping with minimal need of in situ measurements.

There are several review papers published on wetland classification and various challenges associated with this task. For instance, [9] conducted an inclusive review on various sensors used for wetland mapping and monitoring, in which SAR sensors were covered in a small section. Different methods for the classification of wetlands, including aerial photo interpretation, and unsupervised and supervised classification methods, were also investigated in this review paper. [13] also presented a comprehensive review on wetland detection using Synthetic Aperture Radar (SAR) sensors. This review provides the readers with considerable insights on the benefits and limitations of SAR sensors for wetland detection. Besides, it advises the users on choosing the appropriate sensor configuration. In another paper, [16] reviewed wetland classification using multispectral and hyperspectral RS sensors, and explored spectral characteristics of various vegetation within wetlands. Similarly, [17] did a thorough and useful literature review on object-based wetland classification and explored object-oriented mapping of wetlands in terms of its pros and cons, and the elements which affect its accuracy. Additionally, [14] explained RS methods briefly for wetland classification and investigated the challenges of mapping wetlands. Finally, [18] investigated the SAR RS methods for mapping and monitoring surface water and wetlands.

Each of the mentioned reviews has explored wetland classification from a specific

point of view. Therefore, there is a need for a more inclusive literature review, which contains an introduction to wetland importance and the reason for the need on wetland mapping and monitoring, as well as a diverse description of the various methods for classifying and monitoring wetlands using RS. In this review, the aim is not to simply report the method and results of each study, but rather, to recapitulate the research on a variety of subjects and present the benefits and limitations associated with each. This review is especially useful for the users who intend to become familiar with characteristics and importance of wetlands, and also need a general knowledge on the classification of wetlands to decide what approach conforms to their requirements in the best way.

This paper is organized as follows. First, various definitions of wetlands are provided. Then, the benefits and extent of wetlands, and the threatening rate of wetland loss are reviewed. Wetland inventories and classification schemes are discussed in the next section.

Wetland classification methods and their features are then presented on an individual basis. Readers are also referred to several studies, which have utilized each method of wetland classification. In addition, the benefits of object-based compared to pixel-based classification are presented in this section. Further, various classifiers for wetland mapping are explored and reviewed. Finally, the summary and conclusions, along with some recommendations for the future, are provided.

2.4 Wetland Definition

Although wetlands share many similar characteristics, they are highly variable in terms of size, location and hydrology [19], they often constitute transitional zones on the edge of explicit terrestrial and aquatic regions [19]. This fact creates difficulty in defining these natural resources, and is the reason for the existence of various definitions of wetland in the literature [19, 20].

One of the most commonly used definitions of wetland is provided by the Ramsar Convention [21]: "areas of marsh, fen, peatland or water, whether natural or artificial, permanent or temporary, with water that is static or flowing, fresh, brackish or salt, including areas of marine water the depth of which at low tide does not exceed 6m".

Although this definition suffices for the majority of international purposes, most nations have their own definition of wetland developed for various scientific, managerial, and governmental purposes. The United States Fish and Wildlife Service (USFWS), for example, defines wetland as follows [1]: "Wetland is a land transitional between terrestrial and aquatic systems, where the water table is usually at or near the surface or the land is covered by shallow water. For the purposes of this classification, wetlands must have one or more of the following three attributes: (i) at least periodically, the land supports predominantly hydrophytes; (ii) the substrate is predominantly undrained hydric soil; and (iii) the substrate is non-soil and is saturated with water or covered by shallow water at some times during the growing season of each year". Another well-known definition applied in Canada is defined by the National Wetland Working Group [22]. The group describes a wetland as: "an area that is saturated with water long enough to promote wetland or aquatic processes as

indicated by poorly drained soils, hydrophytic vegetation and various kinds of biological activities that are adapted to a wet environment". To summarize, wetlands can be described as occupying zones where terrestrial and aquatic regions meet [23], and share some characteristics of both ecosystems. Notably, wetlands contain water for some parts of a year [23]. [20] provided a simple definition of wetlands by introducing three main features by which wetlands can be described: the presence of (i) water; (ii) hydric soil; and (iii) specific vegetation adapted to a wet environment. It is worth noting that artificial water bodies are not usually considered as wetlands by many classification systems [24].

2.5 Wetland Importance

Since the realization of the potential of RS for various applications, many researchers have exploited RS for wetland classification/monitoring. Wetland classification has attracted much attention amongst RS experts for several reasons, including the numerous advantages associated with wetlands, the considerable global coverage of wetlands which can be estimated using RS tools, and vulnerability of wetlands to loss and degradation which can be similarly estimated by application of RS methods. Therefore, in this section, each of those reasons are described so that the readers are acquainted with the significance of wetland classification at the current time.

2.5.1 Wetland Advantages

Wetlands are one of the most important natural resources which provide many advantages to the environment and humans. Purification of water, reduction of flood

risk, protection of shorelines, conservation of soil and water, filtration of sediment, removal of pollution, as well as aesthetic and recreational values are only some of the benefits associated with wetlands [2–4]. Wetlands are also a great habitat for hundreds of plants and animals, including one-third of all species at risk [9,25,26]. Due to their vital biological services, wetlands have been called the kidneys of nature [27], and are important indicators of environmental health [28]. Other than the countless natural benefits of wetlands, the local economy is dependent on wetlands for fisheries and grazing [29]. Therefore, monitoring wetlands is of vital significance, and the first step in monitoring is mapping.

2.5.2 Wetland Geographical Extent

Currently, there are only a few studies which have estimated the global coverage of wetlands. Referenced global estimates are often compiled from numerous localized wetland inventories or are predicted using models that apply various types of data inputs. Table 2.1 introduces these studies and illustrates a summary of their obtained results. There are, however, disagreements in total estimates of global wetland extent among various studies. These disagreements are due, at least in part, to the difficulties in obtaining accurate and cohesive wetland distribution estimations from around the world [30]. Most of the predicted global wetland extents may be considered as minimum estimates, as several countries have not yet completed or even initiated the collection of wetland inventories [31]. More accurate and improved global wetland estimates could be theoretically obtained through the creation and implementation of a global standardization for conducting wetland inventories [30]. This is an ideal

case, however, and the creation of such standardization is a substantial challenge that requires the availability of data sets, methods, and funding in all countries on the earth.

Table 2.1: Various estimates of the global wetland extent

Estimated Wetland Extent (million km^2)	Main Wetland Locations	Study
7-9	N/A	[1]
6.8	Asia and North America	[32]
8-10	Asia and North America	[33]
7.1-26.9	N/A	[5]

2.5.3 Wetland Loss

Despite the numerous services provided by wetlands, they were frequently drained to be replaced with other types of human land use, such as urban space and agriculture, since they had excellent soil for farming [4, 6, 27, 34–37]. Other than land use, climate change also affects the integrity of wetlands [4, 12, 38]. Furthermore, wetlands have been and continue to be seriously affected by exhaustive land irrigation, groundwater extraction, and draining [7]. Drought, salinization, eutrophication, and pollution also negatively affect wetlands [39–41].

While the statistics regarding destruction of wetlands worldwide are concerning,

they are challenging to estimate. This is, in part, due to the lack of historical documentation, in addition to the multitude of wetland definitions and the temporal variability of these ecosystems [35]. However, there are some old documents used by the USFWS to report on wetland loss between the 1780s to the 1980s, stating that approximately 53% of wetlands were lost in the lower 48 states within 200 years [42]. Documentation of wetland destruction in Canada dates back as early as the 1600s, during which time at least 85% of salt marsh habitats in the Bay of Fundy (between Nova Scotia and New Brunswick) were drained and dyked by settler Acadians [43].

Other than the few described studies, most research estimated wetland loss during the last century, when aerial photographs, satellite imagery, and detailed documentation were extensively available [44–47]. In an assessment of 189 published scientific studies and reports covering various time periods and geographies, [8] reported that as much as 54 to 57% of the world's wetlands have been converted or lost and was most accelerated during the 20th and early 21st centuries. Other studies have occasionally reported various amounts of wetland loss. For example, more than half of the total mangrove area in the world was destroyed in recent decades [6]. By the same token, more than 60% of the wetlands in Europe and North America have been drained and transformed for agricultural use [6].

2.5.4 Wetland Inventories

Since the value of wetlands along with the great potential of RS for wetland mapping/monitoring have been well realized, the concept of wetland inventory was developed. Assessing the effectiveness of wetland policies requires an understanding

of the extent of current wetland resources as well as a basis for trend analysis of wetland distribution and extent change. A way that this can be done is through the creation and maintenance of wetland inventories [48, 49]. A wetland inventory is a map that displays the extent and distribution of wetlands over a geographical area. Inventories around the world have been carried out, all with varied purposes, methods, and geographical coverages ranging from local to nation-wide [49–51].

One example of a nation-wide inventory is the National Wetland Inventory (NWI). The NWI was established in 1975 by the USFWS and was mainly conducted via the manual interpretation of aerial images [52] along with the inclusion of other data types, such as soil data and topographic maps [53, 54]. Since its implementation, the NWI has mapped wetlands throughout the United States. Another example is the Canadian Wetland Inventory (CWI). Although Canada had several prior attempts for provincial-based inventories, the lack of a national inventory was not addressed by Canada until 2002 upon the establishment of the CWI partnership between Ducks Unlimited Canada, the Canadian Space Agency, the North American Wetlands Conservation Council, as well as various other institutions [50].

The initiation of wetland inventories was followed by the development of wetland classification systems. Examples of classification systems range from the early peatland classifications of Europe and North America [27, 55] to the globally applied and conservation-based Ramsar Wetland Classification System [56]. Several classification systems address only a specific wetland type, and are designed for application in specific situations, and localized geographic contexts, while others are developed for country-wide use [22, 57, 58]. A major purpose behind the development of these country-wide classification systems is the creation of national inventories of

wetlands. For example, country-wide classification systems applied in the context of North American wetland inventories include the Cowardin Classification System (CCS, Figure 2.1) and Canadian Wetland Classification System (CWCS, Figure 2.2). CCS and CWCS are applicable to the United States NWI and the CWI, respectively.

Table 2.2: Classification system of wetlands and deep water habitats of the United States (see [57] for more details).

System	Description
Marine	Open ocean and associated coastline which are: exposed to waves and currents, influenced by tides and winds, and have high salinities.
Estuarine	Tidal deep water and wetland habitats open partially to the ocean and influenced by some freshwater runoff. Salinity levels can vary depending on the circumstances.
Riverine	Wetlands and deep water habitats contained within a channel, a channel being an open conduit which contains periodically or continually moving water.
Lacustrine	Wetlands and deep water habitats found in topographic depressions or dammed river channels which occur in sizes greater than 8 hectare.
Palustrine	Non-tidal wetlands dominated by trees, shrubs, and persistent emergent vegetation.

The classification of wetlands and deep water habitats of the United States (CCS) was developed in 1979 for use in a nationwide inventory, and was designed for resource managers. Like many other national classification systems, the CCS is structured

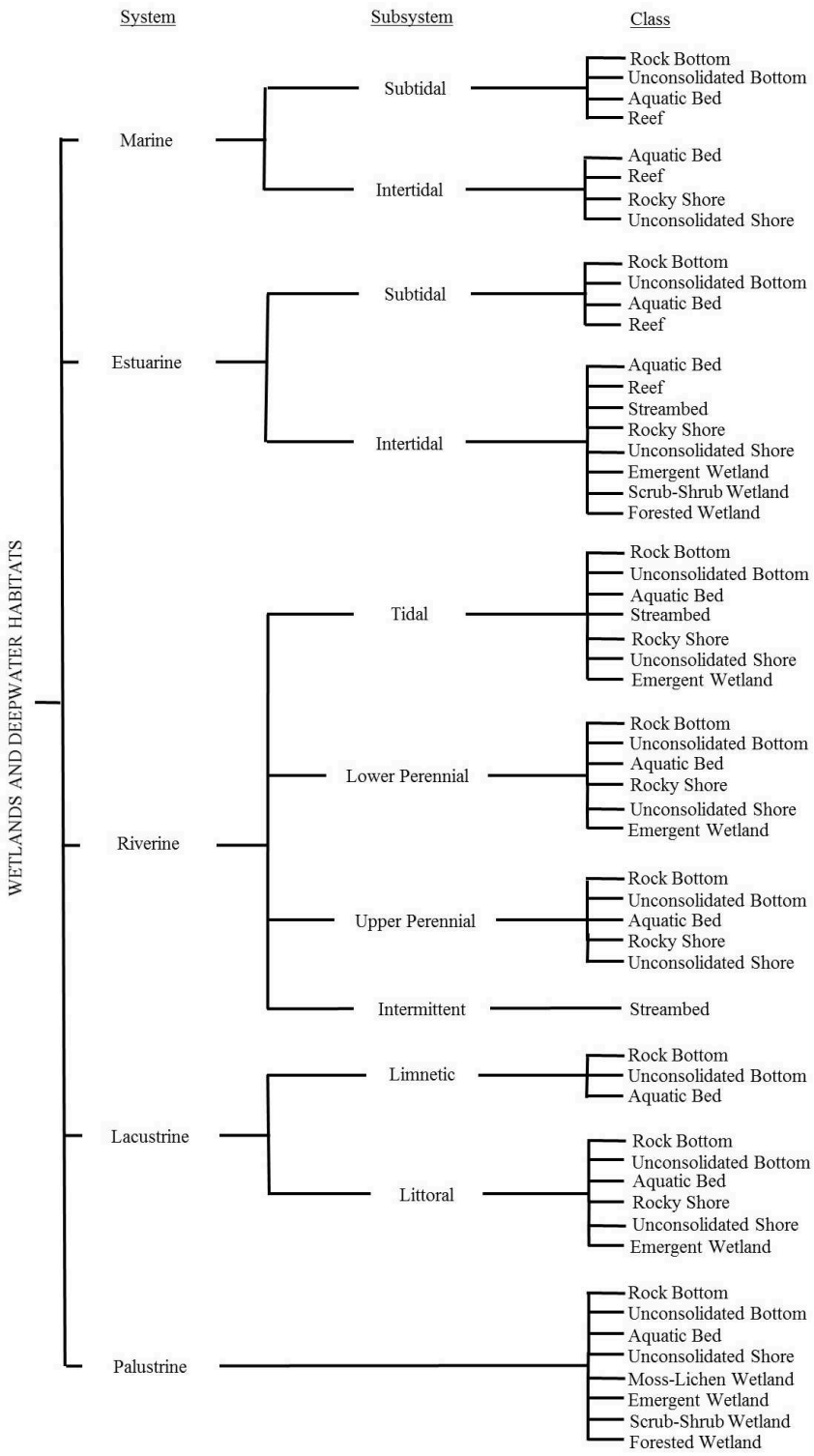

Figure 2.1: Cowardin Classification System (CCS, [57])

hierarchically, beginning with a broadly defined system level, and moving towards more specificity at the subsystem and class levels. The classes can be further divided into subclasses and dominance types. Brief descriptions of each system level in the CCS are provided in Table 2.2.

Table 2.3: Wetland classes defined by the Canadian Wetland Classification System (see [22] for more details).

Class	Description
Bog	Ombrotrophic peatland dominated by sphagnum moss species.
Fen	Minerotrophic peatland dominated by graminoid species and brown mosses.
Swamp	Peatland or mineral wetland dominated by woody vegetation.
Marsh	Minerotrophic wetland with periodic standing water or slow-moving water, dominated by graminoids, shrubs, forbs, and emergent plants.
Shallow Water	Minerotrophic wetland where water is up to 2m deep for most of the year and, where there is less than 25% of emergent plants or woody plants.

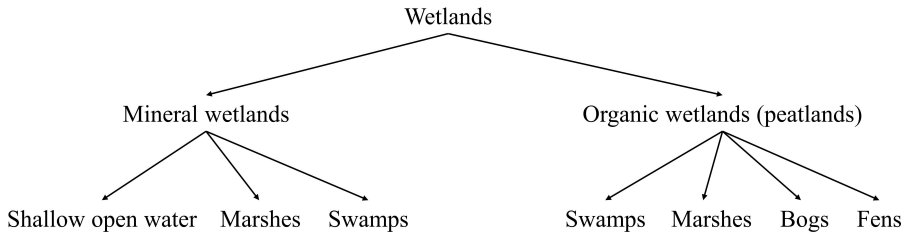

Figure 2.2: Canadian Wetland Classification System (CWCS, [59])

In a similar vein, though developed some time later, the CWCS was published in 1987 by Environment Canada and was last updated in 1997. This system was specifically designed for practical use by both specialists and non-specialists, as well as for use in both local and regional contexts [22]. Due to its overarching geographical application, CWCS was selected as the official classification system of the CWI [60]. The CWCS defines a 3 level hierarchy of class, form, and type. Categories within the class level are defined on the basis of broad descriptions of soil, vegetation, hydrology, and chemistry. Variations in these characteristics designate a wetland as being bog, fen, swamp, marsh, and shallow water wetland classes (Figure 2.3), the specifics of which are summarized in Table 2.3.

2.6 Wetland Classification Methods

Wetland classification grew out of a managerial need [27] to describe these highly diverse ecosystems in a systematic manner, as well as to create baseline references for the exchange of wetland information across space, time and disciplines [61]. The process of wetland classification is carried out by grouping wetland ecosystems into categories on the basis of sharing several common ecological characteristics [62] which are usually described by a classification system, as explained in the previous section. During the past few decades, diverse approaches have been applied for mapping and monitoring wetlands, in which they can be generally divided into traditional (i.e. in situ) and RS methods.

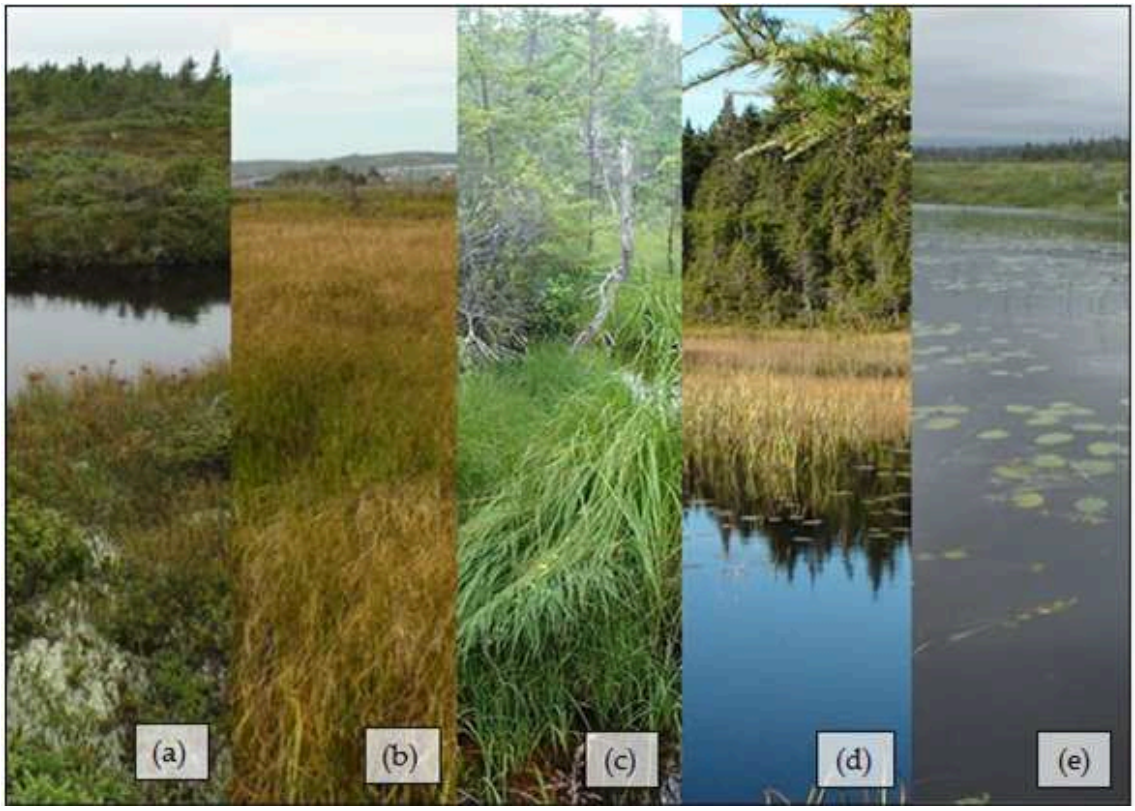

Figure 2.3: Wetlands located in Newfoundland, Canada classified following the Canadian Wetlands Classification System (a) Bog (b) Fen (c) Swamp (d) Marsh (e) Shallow Water.

2.6.1 Traditional Wetland Classification

Wetland identification and classification in the field may variably involve the application of previously established wetland classification systems [22,57], wetland field guides [63, 64], delineation manuals, and the use of tools and sampling methodologies [52]. In situ methodologies have long been used to delineate and monitor ecosystem structure, function, and condition [65, 66]. Many wetlands can be identified by their characteristic vegetation. This serves as a major basis for in-field wetland identification and classification [52]. Both the CWCS and CCS apply vegetation-based descriptions of wetlands. However, vegetation alone cannot always identify and classify a wetland, and assessments of hydrology and hydric soils is also necessary for this purpose [52].

Although in situ methodologies are important and necessary for effective wetland management, at large managerial scales [60], the techniques have many disadvantages for wetland mapping. In situ methods are infeasible given the cost and time requirements, as well as the difficulties of accessing many wetlands. A large number of wetlands are located in remote areas, where topography, vegetation cover, and hydrology make field visitation challenging and costly [17, 67–70]. Therefore, reliance on field methodologies alone would mean disregarding many large and diverse wetland areas [17]. Moreover, given the temporal variability of wetlands over time, repeated in-field visitation is necessary [13, 14]. Additionally, classification using in situ information often requires cover percentage to be estimated visually, or needs other sources of data [14, 16]. Consequently, in situ method can be feasibly practiced only in a small geographical context [14–16], despite the current needs of wetland

information at wider ranges, such as at watershed, continental or global scales [14]. On the other hand, RS methods resolve these issues of cost, time, accessibility, and repeatability effectively.

2.6.2 RS-based Wetland Classification

In the context of this paper, RS includes using any Earth Observation (EO) data such as aerial photos, satellite imagery, and so on. RS provides numerous advantages over the previously described traditional approach. RS is a comparatively cost-effective and timely method for the collection of data over a wide area at the same time. It also allows for repeated measurements in short time intervals [9, 17, 71]. Likewise, RS is capable of acquiring images from inaccessible places, where many wetlands are located. Additionally, RS can provide information on the landscapes surrounding wetlands and their variation over time and, therefore, can give the users information about wetland loss [9]. Another benefit of RS for monitoring wetlands is that RS products can be conveniently imported into Geographical Information System (GIS) to be combined with other types of information [9]. Additionally, many researchers have mentioned that since wetlands appear in various sizes, their mapping should also be performed at several spatial scales, which can be easily carried out using RS tools [3, 4, 17]. As a result of these advantages, many researchers have reported that RS is effective in terms of the operational classification and monitoring of wetlands [72–75].

However, although RS methods reduce the need for detailed on-site based methods considerably compared to the ground-based methods, they do not completely elimi-

nate this requirement. In terms of wetland classification and inventory, in situ data are needed to train and validate the RS methods. For instance, there is a need for a sufficient number of field-validated measurements to conduct accuracy assessments on classified RS images [76]. Thus, most wetlands classification schemes require the application of both RS and in situ data [77].

2.6.2.1 Limitations in RS-based Wetland Classification Methods

Though RS provides efficient tools for wetland mapping and monitoring, there are various technical limitations in wetland classification using RS data. These limitations are briefly outlined and discussed below.

- Wetland morphology is a considerable difficulty of wetland mapping using RS data [14, 20]. Wetlands of one type, which lay in one class according to most classification systems, can be forested, shrubby, or herbaceous [20,71]. This fact causes a single wetland class to demonstrate different spectral and/or backscattering signature in RS data [14, 78]. On the other hand, some specific wetland types, which should be classified separately according to the mapping systems, share some ecological characteristics. For example, swamp and forest are similar to each other from RS perspective, but swamp's substrate includes water. This fact causes these classes to have similar spectral and/or backscattering behavior in optical and SAR data. Consequently, high confusions are observed when classifying these wetland types [13]. In summary, wetlands have high intra-class, and low inter-class variability, which makes their mapping challenging.

- Although the presence of water is a common feature of all wetland types and

is expected to alleviate distinguishing them, it does not make the detection of wetlands easier. The reason is that the water in wetlands can often be under the earth's surface, where the plant roots are located [14]. To further complicate matters, the water level in wetlands can change seasonally, sometimes rapidly resulting from snowmelt or precipitation, or gradually as a result of anthropogenic activities [1, 14, 15, 57, 79].

- Wetlands normally lack a defined boundary and their border is almost always fuzzy, since they gradually transit from wetland to other land cover classes, such as upland or open water, or even other types of wetlands [17]. In addition, the ecotones in and around wetland areas are sometimes very narrow, which makes their detection difficult [14]. The ecotones might also have some characteristics of each biological community between which the ecotone exist, which makes their identification even more difficult. Therefore, the quality of image interpretation and feature extraction methodologies in wetland mapping, and generally in all types of land cover classification, should also be considered [17].

- Wetlands, in both boreal and arctic regions, are located in areas which are less accessible for collecting field samples. Furthermore, even with having Global Positioning System (GPS) points determining a few points on wetland areas, delineating exact wetland boundaries surrounding the point using fine spatial resolution imagery is challenging, and there are always chances of overlapping with other wetland types. This fact sometimes results in having insufficient training samples for a specific wetland type.

- RS images are also restricted to a specific spatial resolution, which might limit

detection of small wetlands [4, 9]. For example, if we consider a cluster of three-by-three pixels as the minimum detectable size of wetlands in an image, Landsat TM would only be able to delineate wetlands which are larger than approximately 0.01 km^2.

To recapitulate, it is quite challenging to reach a high overall accuracy for wetland mapping using only RS techniques (Dronova 2015), and the ecological characteristics of wetlands cause many difficulties in wetland classification using RS methods (Cordeiro and Rossetti 2015; Gallant 2015).

2.6.2.2 Wetland Classification Using Aerial Imagery

One common method for the delineation of wetlands is the interpretation of aerial images, which was the first RS method for mapping wetlands [52, 80–82]. Aerial images usually have a higher spatial resolution compared to that of satellite imagery and, consequently, allow for the recognition of small or narrow wetlands [9]. Furthermore, aerial images can be useful when detailed mapping of wetlands is required [9, 14].

However, applying aerial images for wetland monitoring can be expensive and more time-consuming when compared to the application of space-borne imagery. Satellite RS is more appropriate when the budget is limited and the area is rather unknown in terms of wetland and non-wetland areas [9]. In addition, most aerial images have limitations in spectral and temporal resolutions [16, 83], which hinders differentiation between the spectrally similar wetland classes, as well as the ability to frequently update the maps.

Despite the above-mentioned difficulties, several researchers still prefer to interpret aerial images rather than applying optical or SAR satellite images [84–87]. Moreover,

there are a number of aerial sensors which are rich in terms of spectral bands, including Airborne Visible/Infrared Imaging Spectrometer (AVIRIS), and Compact Airborne Spectrographic Imager (CASI). Several programs, such as the United States Natural Agriculture Imagery Program, also support more frequent flights over some areas in the recent years [14]. Nevertheless, using satellite images along with aerial photos will probably provide more useful information than either image type alone [9], for example in a sampling strategy such as regression estimators.

2.6.2.3 Wetland Classification Using Multispectral Optical Imagery

Generally, multispectral sensors are especially useful in analyzing the spectral characteristics of wetlands, since they acquire information in various spectral bands, including the visible and near infrared, shortwave infrared, and thermal infrared parts of the electromagnetic spectrum (Figure 2.4) [14, 39, 83, 88, 89]. Although optical imagery sometimes need atmospheric correction, most optical data have already been geometrically and radiometrically corrected, and is ready to be used in the classification. Therefore, pre-processing optical satellite data is easier than most other RS data, including SAR, Light Detection and Ranging (LiDAR), and Unmanned Aerial Vehicle (UAV). Several prepared products of optical data are also freely downloadable for users (e.g. various products of MODIS and Landsat 8).

However, optical sensors provide poor information regarding the vegetation's physical characteristics, such as morphology and height [14], and are hindered by the inability to penetrate through clouds [91–93]. As a result, some of the information that would otherwise be obtainable using satellite optical imagery is lost when the weather is cloudy. This is a common problem when monitoring wetlands, and is a

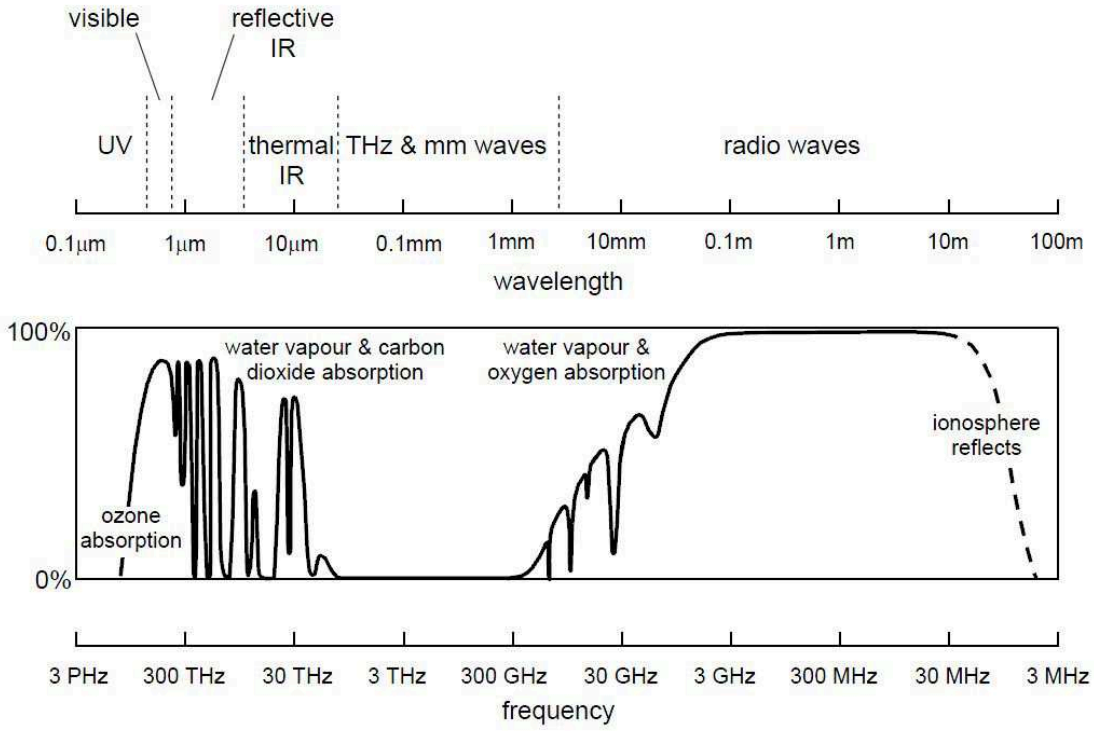

Figure 2.4: The electromagnetic spectrum [90]

drawback in the applicability of optical imagery given the operational need for continuous monitoring [94]. This problem can be partially addressed through the use of optical imagery with higher temporal resolution providing the users with the ability to select cloud-free images [14]. It should also be noted that the penetration depth of optical sensors is so low that detection of the water beneath trees/dense vegetation is not possible [14, 72]. As a result of the mentioned disadvantages of optical data, several studies have reported that the sole use of optical sensors is not sufficient for accurate classification of wetlands [9, 20].

Nevertheless, there are many studies that have attempted to map wetlands with the sole use of optical images. [34] evaluated both supervised and unsupervised classification methods (i.e Linear Discriminant Analysis and ISODATA, respectively) for wetland classification using multi-temporal IKONOS-2 imagery. The Normalized Difference Vegetation Index (NDVI) and several texture features were used to identify 22 different vegetation classes, as well as shallow water, deep water, and road in the study. Comparing the obtained accuracies in different seasons, the highest accuracy (Overall Accuracy=96%) was obtained using the fused IKONOS imagery captured in May and July, plus the texture information. Moreover, [95] used multi-temporal satellite images obtained by different Landsat satellites (Landsat 2, 3, 4, 5, and 7) for long-term change detection of wetlands in Ontario, Canada. Two different methods, including post classification comparison and multi-temporal data clustering were evaluated to detect the changes in the Long Point wetlands over a 23 year period. [96] also used SPOT-4 images for wetland classification in the context of greenhouse gases emissions. In their study, the multiscale object-based method based on the CWCS was used to estimate a regional carbon budget. They also reported that SPOT-4 images

with finer spatial resolution compared to those of Landsat and RADARSAT-1 data were more suitable for identifying various wetland classes. As another example, [3] used SPOT images in a decision tree algorithm to classify wetlands based on two different classification schemes (i.e. CWI and DU) in five different scales. Incorporating texture information into the classification also improved the results. Finally, [4] investigated wetlands in different scales using SPOT imagery. First a general maximum likelihood classification was applied on the images to detect large wetland areas, and then, a knowledge-based classification was used to fine-tune the identified regions. The authors reported that the knowledge-based classification method improved the results.

Currently, there are many operating optical sensors which could be applied for wetland classification. The most important difference between these sensors is the spectral resolution (the range and number of spectral bands) which the sensors employ. As mentioned before, the optical bands include: red, green, blue, red edge, near infrared, shortwave infrared, and thermal infrared. The role of visible bands in classification is not central, which is not surprising, because wetlands are difficult to distinguish visually. The red edge band is located between the red and near infrared bands, where the reflectance value of green vegetation significantly rises from the red band to the near infrared band. The red edge band, although not available in all sensors, provides additional information for the studies that investigate vegetation and quality of inland water bodies with relatively high phytoplankton content [97,98]. The reflectance value in this band is related to vegetation biochemical parameters (e.g. chlorophyll content), biophysical parameters (e.g. leaf area index), and water deficit in vegetation biomass [99–101]. Consequently, the red edge band is a useful spectral

band for wetland classification [16, 101–103]. Many studies have reported that vegetation in different wetland classes show the greatest variation in the red edge and near infrared bands. Therefore, these two bands are the most useful optical bands for the detection of wetlands [16,78,102,104–107]. The shortwave infrared bands are sensitive to soil moisture and vegetation moisture. Thus, they are important bands for obtaining moisture characteristics of both soil and vegetation in wetlands [108–111].

Thermal infrared bands collect the energy emitted by land surfaces and, therefore, are useful for obtaining Land Surface Temperature (LST) information. Several studies have illustrated that there is a correlation between the water temperature acquired by thermal sensors and different types of vegetation within water [71, 112]. Thermal bands are useful in discriminating water areas from dense vegetation, as well as inundated regions of wetlands [113]. A problem associated with thermal bands, however, is the coarse spatial resolution of these bands. Both visible, and infrared (near, shortwave) bands usually have finer spatial resolution than thermal bands and, therefore provide more detailed information about wetlands.

2.6.2.4 Wetland Classification Using SAR Imagery

SAR images are capable of penetrating through the clouds and can therefore provide imagery in any weather conditions [103,114]. SAR data with various sensor configurations and all-weather capability are useful in operational monitoring when the information about the extent, location, and conditions of wetlands is necessary [13]. At the same time, SAR sensors are able to acquire valuable information regarding the ground conditions under vegetation canopies [72, 103]. Several studies have reported significant improvements in accuracy of wetland classification, especially for swamps,

when utilizing SAR imagery [13].

Water bodies, if calm, can also be easily detected by SAR sensors. This is due to the fact that backscattering energy from the calm water is mostly specular as the water surface is flat and, consequently, the backscattered energy is very small [74]. Many studies have also reported that SAR images are successful in the delineation of flooded areas, as a result of the double-bounce scattering between the flooded surface and tree trunks and tall vegetation [13, 15, 103, 115, 116]. Likewise, the coefficient of variation has been reported useful for distinguishing between swamp and upland [117]. An important feature to be used for discriminating between various wetland types is the dominant scattering type phase φ_{as}, which has been introduced by [118] and [28]. This parameter is especially useful for distinguishing between bog and fen at C-band. The reason is that this parameter is able to detect water beneath the vegetation at various depths, as explained in [117]. By the same token, the dominant scattering type phase is able to differentiate conifer-dominated treed bog from deciduous forest in leafy conditions [117]. As reported by [117], none of the other polarimetric features, including entropy or phase difference have such a capability. However, it should be considered that both the dominant scattering type phase and magnitude are needed for the unambiguous characterization of wetlands [28].

Despite the advantages of SAR data for wetland classification, it should be noted that pre-processing of SAR data is more time-consuming than optical images, and sometimes requires knowledge in this field. Equally important, during pre-processing performed by an operator, various uncertainties might be involved in the generation of the final image. For instance, one of the most obvious problems associated with SAR data is the presence of speckle. Speckle degrades the radiometric quality of the

image and, therefore, hinders image segmentation and classification [119]. Another issue that results from the presence of speckle on a SAR image is that the training samples must be several times larger than that required for the optical data [13].

The first attempt to classify wetlands using SAR images began in the late 1960s and early 1970s [13]. Subsequently, a host of studies have utilized SAR data for wetland mapping and monitoring. In [120], JERS L-band SAR imagery was applied for the generation of a wetlands thematic map. [28] investigated the potential of full-polarimetric C-band images for wetland mapping using Convair-580 data. Several polarimetric parameters extracted from the Touzi decomposition [118], illustrated a high potential for distinguishing bog and fen. Similarly, [121] evaluated several polarimetric decompositions, including Freeman-Durden [122] and Cloude-Pottier [123] decompositions, for wetland mapping using Convai-580 data. After separability analyses, the authors concluded that full-polarimetric data are more informative than the other data sources for wetland mapping using a maximum likelihood classifier. Additionally, a study that was conducted by [124], applied RADARSAT-2 image time series to investigate the sensitivity of different polarimetric parameters to the change in water level in saturated wetlands. They found that the Shannon Entropy is the most useful parameter for the detection of saturated wetland areas. Likewise, a comprehensive study was carried out by [89], who investigated the potential of several polarimetric features, such as the Touzi decomposition, for wetland mapping using a decision tree classifier. Finally, [125] investigated the capability of RADARSAT-2 full polarimetric images for wetland classification in the Canadian province of NL.

The SAR system configuration plays a pivotal role in the capability of a SAR system for wetland classification [73,88,89,121,126,127]. An appropriate SAR config-

uration should be adopted such that there is maximum distinction between wetlands and uplands, as well as between different types of wetlands [20]. Therefore, the effects of each sensor specification are reviewed in the following subsections.

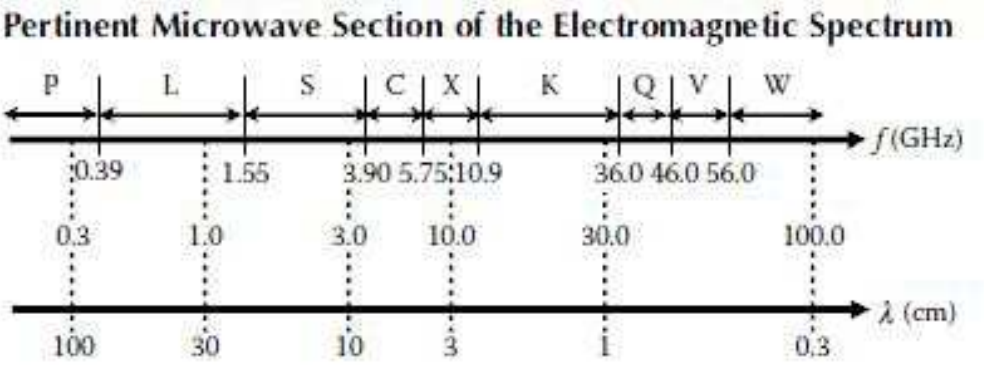

Figure 2.5: Radar bands [128].

Wavelength SAR sensors operate in various bands. These bands, among other SAR bands, include P-, L-, S-, C-, and X-bands with wavelengths of approximately 100cm, 25cm, 11cm, 6cm, and 3cm, respectively (Figure 2.5). L-band was the most used band in early studies for wetland mapping, and was frequently cited as the best wavelength for wetland mapping [13, 15]. Several studies have also reported that longer wavelengths are more appropriate for the separation of forested or densely vegetated wetlands (e.g. swamp) from non-flooded ones [13, 72, 103, 120, 129, 130]. The reason is that the penetration depth of P- and L-band signals is high [72]. Consequently, these signals can pass through the woody vegetation canopy and detect the water beneath the flooded trees and/or dense vegetation. On the other hand, several studies have mentioned the potential of short-wavelength SAR images for characterizing herbaceous wetlands (e.g. bog, fen, and marsh), as well as detecting water

beneath the short vegetation [13, 17, 72, 103]. Short wavelengths are also able to distinguish between emergent wetlands and agricultural fields/herbaceous uplands [20]. However, it is worth mentioning that there is still a considerable confusion between different short vegetated wetlands, such as bogs and fens in wetland classification using SAR imagery [72, 131].

Polarization SAR sensors can be single-, dual-, or quad (full)- polarized. Each polarization channel is represented in the form of PQ, where P is the transmitting, and Q is the receiving polarization. Both P and Q can either be horizontal (H) or vertical (V) (Figure 2.6).

Single-polarization SAR data are not very effective for wetland classification, because the received energy in a SAR image consists of several different backscattering types, which cannot be distinguished using a single channel [15, 28, 121]. Single-polarized data, however, have been reported to be effective for the detection of calm open water bodies [15].

Generally, HH polarization is the most useful for wetland delineation [20]. Moreover, L-HH and C-HH are especially effective in the detection of flooded forest, and are more sensitive to inundation than vertical polarization [13, 15, 132, 133]. In addition, the correlation between C-band backscatter and inundation is stronger in leaf-off season [133]. For vertically oriented vegetation, the HH-polarized wave has more penetration into the canopy relative to the VV-polarized wave and, thus, is more sensitive to soil conditions [94]. HV polarization is also effective in the discrimination between woody and herbaceous wetlands as a result of its sensitivity to biomass [20]. Although less than the HH-polarized wave, VV polarization is also sensitive to soil moisture

and flood conditions [20, 134]. When interacting with vertically oriented vegetation, the VV-polarized wave has the most response, and therefore the penetration into the vegetation is reduced [94].

Co-polarized waves (HH and VV) are more effective in the detection flooded from non-flooded wetlands and generate higher contrast between dry forest and flooded swamp compared to cross-polarized waves. The reason for this is that the signal response from like-polarized waves is enhanced in flood conditions [13]. Cross-polarized waves, however, are more appropriate for distinguishing swamp from marsh [13]. Dual co-polarized data are also successful in the characterization of flooded vegetation mapping.

Polarization ratios, which include HH backscatter, are also useful for distinguishing flooded versus non flooded vegetation [121]. In addition, the ratio of L-HV and L-HH bands have proved promising for the discrimination of non-forested wetland types [20].

Phase difference between HH and VV channels also helps in the discrimination of swamp and upland, or flooded from non-flooded vegetation [13, 115, 117]. Furthermore, this phase difference was recognized as the most useful parameter for natural target characterization [117].

Incidence Angle To detect water bodies under vegetation, steep incidence angles (smaller than 35 degree) are the most appropriate [20, 136], as low incidence angles have more penetration depth. Several studies have reported that short wavelengths with low incidence angles can be applied for the delineation of forested wetlands in leaf-off conditions [13]. However, some studies have shown no specific correlation

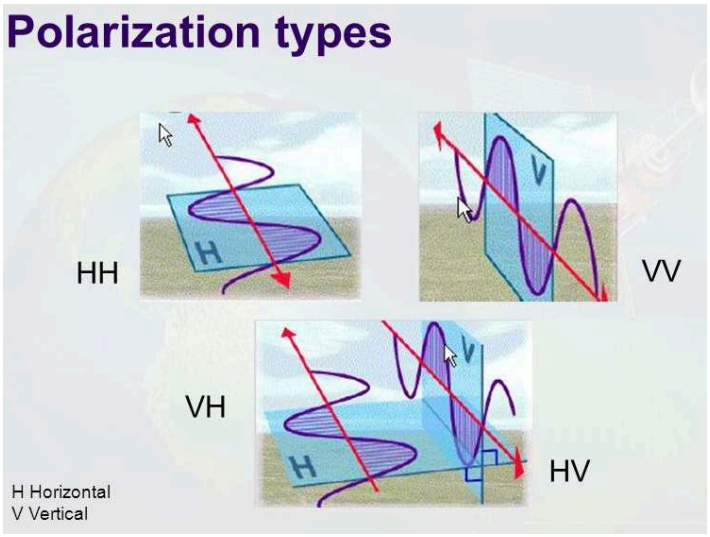

Figure 2.6: Polarization types [135].

between incidence angle and the vegetation type/structure [13, 115, 137]. According to [13], moderate incidence angles do not seem to provide much useful information for wetland detection, especially if the image has fine resolution. Further, fine beam modes of RADARSAT-2, because of having a high incidence angle, are not suggested for the discrimination and classification of wetlands, but are appropriate in terms of spatial details [136] also investigated various RADARSAT-2 beam modes (incidence angles) for the discrimination of different wetland types. The main difference was the dynamic range of backscatter for wetland sites, which was the largest in S5 mode and the smallest in F1 mode (refer to [138] for more information about RADARSAT-2 beam modes). However, it should be considered that the range in incidence angle is small in the Fine mode of RADARSAT-2. Another result of [131] was that a significant difference was not observed between the backscatter of bog and fen in any of the incidence angles. Finally, [131] reported that low incidence angles can penetrate into both shrubby and herbaceous wetlands, while high incidence angles are only able

to pass through low-density vegetation.

Orbit SAR sensors are capable of acquiring images in both ascending and descending modes. The ascending mode for SAR imagery is recommended for wetland mapping, since at the time when the descending image is acquired, dew on vegetation can decrease the contrast between wetlands and non-wetlands [2].

According to the studies described above, the effects of SAR configuration are summarized in Table 2.4.

2.6.2.5 Wetland Classification Using Other Resources

Digital Elevation Model (DEM) Data The Digital Elevation Model (DEM) has proved useful for distinguishing wetland classes. At the same time, many studies have reported that the topographic features extracted from DEM, were also effective for finding the distribution and location of wetlands [17, 51, 51, 72, 121, 139–142]. For example, the Topographic Position Index (TPI, [143]), Compound Topographic Index (CTI, [144]), slope, and orientation of the DEM have been used in several studies for wetland classification [51,68,139,145,146]. DEMs can also be included in the wetland mapping procedure to correct the areas of misclassification as a result of layover and shadowing [120, 141]. However, it should be noted that the applied DEM should have a resolution high enough for deriving precise topographic information. DEMs obtained from EO images and LiDAR data can yield spatial resolutions up to 1 m and 15 to 30 cm, respectively.

Table 2.4: Description of various SAR configurations for wetland mapping.

Wavelength	Short	Best for characterizing herbaceous wetlands
	Long	Most appropriate for detection of frosted or densely vegetated wetlands
Polarization	Co-polarization	HH: useful for detection of flooded forest and inundation - more effective for wetland classification than VV
	Cross-polarization	HV: useful for discrimination between herbaceous and woody vegetation- e.g. discrimination of swamp from marsh
Incidence Angle	Small	useful for detection of water body under vegetation
	Large	useful for detection of shrubby and herbaceous wetlands
Orbit	Ascending	recommended for wetland mapping
	Descending	not recommended for wetland classification because of presence of dew at the time of image acquisition

LiDAR Data LiDAR can be effectively used for the extraction of topographic information and structural indices [17]. Since topographic information is capable of predicting the location and distribution of wetlands, LiDAR has also been applied in wetland mapping in many studies [142,147–151]. In general, information derived from LiDAR are applied as ancillary information in addition to the spectral and textural data [17]. For instance, [147] applied DEMs derived from LiDAR instead of the typical DEMs, and observed 8% improvement in the accuracy of wetland mapping. [148] combined IKONOS imagery with LIDAR data to classify wetlands in Wisconsin, and achieved an accuracy of 75%, which was superior to the accuracy of the existing map for that region. Furthermore, [149] observed a considerable improvement in wetland detection when using LiDAR for mapping streams.

Hyperspectral Data Hyperspectral data have high spectral resolution, which is particularly useful for the detection of detailed variations between various wetland vegetation species [16]. The data, containing hundreds of bands, have many advantages in assessing the biochemical and biophysical properties of wetlands (e.g. leaf water content, Leaf Area Index, as well as chlorophyll and biomass concentrations). However, it should be noted that the number of bands should be reduced using statistical methods, such as Principal Components Analysis (PCA) or Minimum Noise Fraction (MNF), to omit the redundant information. Furthermore, hyperspectral images are rather expensive, and tedious to process, which hinders their application in wetland studies [16]. Nevertheless, there are several studies that have used hyperspectral imagery for wetland monitoring and classification [67, 102, 152–154]. For example, [152] mapped wetlands in the San Francisco Bay using both Spectral Mix-

ture Analysis (SMA) and Multiple Endmember Spectral Mixture Analysis (MESMA) and AVIRIS images, and concluded that both methods can be applied for investigating the structure of wetlands. Moreover, [153] did a laboratory-based study to see if mangrove species are distinguishable, using numerous spectral channels between 350 nm and 2500 nm. They introduced four bands of 720 nm, 1277 nm, 1415 nm, and 1644 nm as bands which guarantee 80% of overall accuracy.

UAV Data UAV has only recently been applied in natural landscapes, including wetlands [19]. Images acquired by UAVs contain great advantages over the typical aerial images given that UAV is capable of acquiring images below the cloud cover [155]. In addition, UAV images provide a great level of detail as a result of their fine spatial resolution [19, 155]. Consequently, there are several studies which have explored the possibility of using this technology for wetland mapping [19, 155–157]. For example, [156] processed UAV images using both automatic and manual methods to map wetlands in the Honghe National Nature Reserve, and found UAV images useful for this purpose. In a similar study, [157] combined UAV data with a new classification algorithm to map wetlands in Utah with an accuracy of 95%. However, it is worth noting that many UAVs are limited to acquiring images in the visible and near infrared domain, and only a few UAVs can provide rich spectral information [155]. Moreover, images taken by UAV are prone to many radiometric and geometric errors [155, 158]. Geometric errors, however, can be corrected using ground control points.

2.6.2.6 Multi-source Wetland Classification

Combining several types of RS data is very common in classification procedures, and has also proved useful in wetland classification [2, 7, 13, 103, 131]. By combining various types of imagery, it is possible to take advantages of each type of data and improve wetland classification. However, a problem with multi-source classification is the large volume of various datasets, many containing different spatial resolutions [140]. By the same token, there is an inconsistency regarding which combination of data sources yields the best results [13].

[159] combined GIS and RS data to map wetlands in Florida. [51] also used a combination of PALSAR data, aerial imagery, and DEM data in an attempt to update the NWI. The authors also applied other data, such as the soil water regime and the percentage of hydric soil for wetland classification. Similarly, [140] applied ASTER, ALOS, and DEM data for the object-based mapping of wetlands in North Brazilian Amazonia. Finally, [142] conducted a study in northern Canada using RADARSAT-2, Landsat-8, and geomorphometric information extracted from LiDAR data. In general, the accuracy which was obtained using multi-source data was superior to using SAR or optical data individually.

Fusion of optical and SAR data is one of the most common, yet most auspicious types of data combination for wetland mapping and monitoring [2,7,13,103,160–162]. For example, [2] used a combination of RADARSAT-1 and Landsat data for mapping wetlands at several scales. This was performed by applying various scale parameters in the segmentation process. The classification began at a coarse level using membership functions. Then, the identified areas were masked, and the remaining areas

were segmented and classified with a finer scale. This process continued until all the desired areas were detected. Additionally, [163] combined Global Boreal Forest Mapping (GBFM) JERS-1 SAR data with MEdium Resolution Imaging Spectrometer (MERIS) optical data for wetland mapping on a continental scale. In their study, an object-based classification was applied to the images. Furthermore, [20] combined SAR and optical data to map wetlands in several regions in Alberta, Canada. [103] also combined RapidEye images and various SAR decompositions extracted from TerraSAR-X images for classification of wetlands in Florida Finally, [162] mapped wetlands over five pilot sites across the Canadian province of Newfoundland and Labrador, using a combination of optical and SAR imagery, achieving the accuracy of up to 96%.

Another common type of multi-source combination for wetland classification is the use of multiple SAR sensor configurations (e.g. multiple wavelengths or multiple incidence angles). For instance, [13] reported that using multiple wavelengths is useful for the detection of both forested and herbaceous wetlands. According to their results, multi-frequency data are as good as or better than multi-temporal data for wetland detection. Multi-incidence angle data, however, are not expected to improve the classification accuracy considerably. [103] reported that using a combination of polarimetric SAR configurations holds great promise for distinguishing wetland vegetation types. Other studies that have used different configurations of SAR sensors for mapping wetlands are: [131], [136], and [164].

2.6.2.7 Multi-temporal Versus Single Date Wetland Classification

A characteristic feature of wetlands is their dynamicity, which is a result of interactions and feedback between climate, weather, geomorphology, biota, and hydrology and anthropomorphic effects [22,27]. The dynamic nature of these ecosystems causes wetland features, such as water, vegetation, and chemical characteristics to change over time. Consequently, a wetland may look different over years, months, or even days [22,165]. For example, seasonality influences the availability of water, affecting the growth and lushness of vegetation, resulting in wetland vegetation looking different from summer to winter [166,167]. In the short term, rain can cause flooding and briefly fill depressions, which can change the appearance of wetlands within days. On the other hand, in the long term, wetlands can change from one type to another, as demonstrated by the climate-driven fen-bog transitions of the Holocene [168].

As a result of the ever-changing nature of wetlands, the use of multi-temporal images has been found to improve wetland classification accuracy [9,15,20,34,72,89, 94,95,125,169,170]. It should be noted that the selection of the appropriate acquisition date for images applied for wetland mapping is crucially important, even more-so than the number of images. This is because wetland morphology and water level vary considerably throughout a year [13,20]. However, an optimum range of image acquisition has not been yet determined [13]. [13] reported that adding images from multiple dates can increase the accuracy only to a certain extent. This is because once a certain accuracy is reached, the accuracy does not change, or in some cases may even decrease. Typically, summer images are the best for wetland classification [125,171]. The images acquired in spring or fall can be also helpful, but the combination of the

high water level/leaf off an low water level/leaf on images hold the greatest promise.

2.6.2.8 General Algorithms for Image Classification

Object-based Versus Pixel-based Wetland Classification Pixel-based classification methods analyze the value of each pixel in an image without considering the spatial or contextual information of the surrounding pixels. Generally, classifying fine spatial resolution imagery using pixel-based methods results in a salt and pepper effect and, consequently, the accuracy of classification is reduced [172–174].

On the other hand, Object Based Image Analysis (OBIA) is the process of segmenting an image into spectrally and spatially homogeneous objects, and then incorporating the spectral, geometric, and other features of those objects into a classification process [3, 141, 175–177]. OBIA has several advantages some of which are reviewed below:

- By applying OBIA, it is possible to include many object-based features, such as textural, geometrical, and morphological features into classification in addition to the spectral features [17, 21, 159].
- The result of object-based classification has a more ecologically meaningful interpretation compared to that of pixel-based classification [142, 159].
- OBIA can facilitate the processing of a large volume of multi-source data [140], and can be efficiently combined with supplementary datasets without a complicated data fusion process [17].
- OBIA minimizes the effect of unusual pixels, such as shadows or isolated elements [17, 159].

- By applying OBIA it is possible to work with images on several scales, which can be nested in each other.

Because of the mentioned advantages, OBIA has been widely used for wetland classification compared to pixel-based methods [2, 3, 20, 96, 140, 142, 178].

However, choosing the optimum scale for segmentation in an object-based classification is difficult [17]. Besides, mismatching image layers and errors in their co-registration might influence OBIA [17]. Another difficulty associated with object-based classification is that there are many object-based features, and an expert needs to know what features result in the best accuracy [140]. It should be considered that spectral features in classification are much more important than other object-based features [17]. Geometric objects are also less commonly used in wetlands, as wetlands rarely exhibit a regular or consistent shapes and sizes [17]. The most commonly used contextual variables for the identification of wetland classes are also distance, proximity, adjacency, and relative border to specific classes, such as water bodies [17].

Different Algorithms for Wetland Classification

Supervised Classification There are many classification algorithms, most commonly used of which are K Nearest Neighbours (KNN, [179]), Maximum Likelihood (ML, [180]), Support Vector Machine (SVM, [181]) , Decision Tree (DT, [116]), and Random Forest (RF, [116]). In each of the classifiers there are factors which can greatly affect the classification accuracy. The image segmentation phase, selection of training samples, feature selection, and the setting of tuning parameters are amongst the most important factors [182]. It is important to bear in mind that classification

accuracy is not the only thing to be considered about the classifier, if the classifier can be used for operational monitoring purposes is also important [94]. In summary, there is no single classification method considered to be optimal for all applications and, thus, the desired algorithm should be selected based on the objectives and study area [16]. The most famous classification algorithms are explained below.

K Nearest Neighbours (KNN) The KNN classifier is based on the distance of unknown pixels/objects from training samples in a feature space. The K nearest training sample(s) determine the class of an unknown pixel with a majority vote [179]. Because of several limitations of the KNN algorithm, only a few studies have utilized this classifier for wetland mapping [103, 178].

Maximum Likelihood (ML) The ML algorithm is based on Bayesian statistics, and assumes that feature vectors of each class are normally distributed [178]. Based on the normal distribution, a discriminant function is defined for each class, and the unknown pixel is assigned to the class with the highest value of the discriminant function for that pixel [183]. An advantage of the ML algorithm is that it adopts a tangible and clear statistical approach for classification, and does not contain a black box as in RF or SVM [15]. The algorithm was the most widely used classifier selected for wetland classification in the early years of the 2000s [9]. As a result of the advantages of the ML algorithm, there are many studies that have used the classifier for wetland classification [83, 88, 89, 121].

Support Vector Machine (SVM) The SVM classification method is a non-parametric algorithm. The algorithm defines a hyperplane, which maximizes the

distance between the training samples of two classes, and then, classifies the other pixels/objects based on this hyperplane [178]. SVM is also less sensitive to the amount of training samples, and can result in a higher classification accuracy given a relatively small number of samples compared to other classification algorithms [178]. However, it should be noted that SVM needs a kernel function, defining which is time-consuming and subjective [178, 184]. Several studies, including [182], [178], and [185] have evaluated the accuracy of the SVM classifier for wetland classification.

Decision Tree (DT) The DT classifier, belonging to the category of classification and regression trees (CART), includes several nodes, by which the input data are divided into mutually exclusive groups based on their attributes, such that each group has the most homogeneous objects. The division recursively continues into increasingly homogeneous subsets until each node represents one of the desired classes [72, 140, 186]. DT is a fast, simple, and flexible classification method, which is more effective in the prediction of class labels when the boundary between classes is not linear. The DT algorithm does not need any assumption regarding the distribution of the classes [3, 16, 72, 140, 176]. A problem associated with DT, however, is that it cannot be adapted to regional or national scales, because the algorithm overfits the training samples [2]. There are several recent studies which have adopted the DT algorithm for wetland classification [3, 89, 178, 187].

Random Forest (RF) The RF algorithm, also belonging to in the category of classification and regression trees (CART), is actually an extension of DT. RF consists of an ensemble of decision trees, in which each tree is constructed using a

subset of training samples with replacements. Only a subset of features is used for finding the best split at each node, which is a constant number over all nodes and all trees. After training, the input feature vector is ingested into every single tree. and then, is assigned a class label to each pixel/object at the terminal node based on the majority of votes [116]. Like the SVM and DT algorithms, RF is also a non-parametric classifier. Non-parametric methods do not require any assumptions for the distribution of the data sets and, therefore, have several advantages compared to the parametric algorithms, such as the ML classifier. It is also worth mentioning that the RF algorithm has recently gained increasing attention in wetland monitoring [101, 120, 141, 142, 188].

2.7 Recommendations

In this section, several recommendations are provided which can contribute to the improvement of wetlands management:

- The creation of more specialized classification systems which are compatible with the nation-wide classification system [61] would be an asset. This would create a common baseline and facilitate the exchange of information across different wetland classifications. An example of such a system is the Ducks Unlimited Enhanced Wetland Classification System [189]. This classification system was developed for the purpose of inventorying and addressing the diversity of wetlands [189, 190].

- Applying advanced automatic or semi-automatic methods, specific to wetlands,

for the purpose of wetland mapping is valuable. For example, for the wetland classes which are very similar to each other, fuzzy classification can be applied. In the fuzzy method, the object/pixel is not strictly classified into one of the wetland classes, but a certain probability is assigned to the membership of the object/pixel to each wetland class.

- The method and the applied dataset for wetland mapping should be wisely selected according to the target classes and the required accuracy. Usually, multi-source, and multi-temporal data yield the best accuracy.

- The need for field data collection should be reduced with advanced RS techniques which give reasonable accuracy with a small amount of training samples.

- Instead of concentrating over a small area over a short period of time for wetland classification, the proposed methods should be operational over large geographical regions. Moreover, researchers should make the most of the freely available satellite images, because these images provide the possibility of producing maps over large regions with frequently updating it. In the case of wetland mapping, the operationality and the cost of the method is often as important as the accuracy of the final map.

- The potential of quad-polarimetric or compact-polarimetric images should be fully exploited in wetland mapping.

2.8 Summary and Conclusion

This review is an attempt to acquaint readers with wetland definition, benefits, extent, and loss. Wetland inventory and classification schemes are also defined and examples are provided. Furthermore, various RS methods for wetland classification along with their values and limitations were reviewed. There are also sections describing object-based classifications and the characteristics of various classifiers.

Although some studies have estimated the global wetland coverage, a more up-to-date and precise estimation is required, because for the most part, the current estimation for the global wetland coverage is not accurate. The reason for the inaccurate global wetland estimation might partly lay in the fact that several wetland inventories are usually incomplete, out-of-date, or imprecise. The Cowardin and CWCS classification systems are designed to be general enough so that the classifications are relevant across geographically large areas and, thus, ecologically, climatologically, and geologically diverse areas. As a result, these country-wide classification systems often do not contain enough information for addressing more specific wetland-related questions [61].

Considering the advantages of the satellite RS methods, including its cost-efficiency, timeliness, and potential to be applied with regular frequency at the global level, it is the best method for generating and updating wetland inventories. Based on the literature it can be concluded that the red edge and near infrared bands are the most useful bands in optical imagery for wetland classification. In terms of SAR imagery, generally steep incidence angles and long wavelengths are suitable for the detection of shrubby or forested wetlands, while large incidence angles and short wavelengths are

proper for the detection of herbaceous wetlands. Full polarimetric images are ideal for wetland mapping, but HH polarization is the best amongst other polarizations for this purpose. Additionally, multi-source and multi-temporal classifications are promising for the delineation of wetlands. At the same time, Random Forest (RF) classifier has proved most promising for wetland mapping, since various types of data with different sources can be utilized in RF and reasonable accuracies can be achieved without the problem of overfitting to the training samples. It is hoped that the current review helps researchers to adopt a method, which provides the opportunity for accurate mapping of wetlands, as well as continuously monitoring them.

Acknowledgements

This project was undertaken with the financial support of the Government of Canada through the federal Department of Environment and Climate Change, the Natural Sciences and Engineering Research Council of Canada (NSERC) under Grants to B. Salehi (NSERC RGPIN-2015- 05027) and W. Huang (NSERC RGPIN-2017-04508 and RGPAS-2017-507962). The authors thank these organizations for the financial support.

Bibliography

[1] WJ Mitsch and James G Gosselink. Wetlands, 2nd, 1993.

[2] Marcelle Grenier, Anne-Marie Demers, Sandra Labrecque, Martine Benoit, Richard A Fournier, and Bruno Drolet. An object-based method to map wetland using RADARSAT-1 and Landsat ETM images: test case on two sites in Quebec, Canada. *Canadian Journal of Remote Sensing*, 33(S1):S28–S45, 2007.

[3] Ryan P Powers, Geoffrey J Hay, and Gang Chen. How wetland type and area differ through scale: A GEOBIA case study in Alberta's Boreal Plains. *Remote Sensing of Environment*, 117:135–145, 2012.

[4] Wei Ji, Xiaofan Xu, and Dzingirai Murambadoro. Understanding urban wetland dynamics: cross-scale detection and analysis of remote sensing. *International Journal of Remote Sensing*, 36(7):1763–1788, 2015.

[5] JR Melton, R Wania, EL Hodson, B Poulter, B Ringeval, Renato Spahni, T Bohn, CA Avis, DJ Beerling, G Chen, et al. Present state of global wetland extent and wetland methane modelling: conclusions from a model intercomparison project (WETCHIMP). *Biogeosciences*, 10:753–788, 2013.

[6] Millennium Ecosystem Assessment. Ecosystems and human well-being: wetlands and water. *World resources institute, Washington, DC*, 5, 2005.

[7] Magaly Koch, Thomas Schmid, Melissa Reyes, and Jose Gumuzzio. Evaluating full polarimetric C-and L-band data for mapping wetland conditions in a semi-arid environment in Central Spain. *IEEE Journal of Selected Topics in Applied Earth Observations and Remote Sensing*, 5(3):1033–1044, 2012.

[8] Nick C Davidson. How much wetland has the world lost? long-term and recent trends in global wetland area. *Marine and Freshwater Research*, 65(10):934–941, 2014.

[9] Stacy L Ozesmi and Marvin E Bauer. Satellite remote sensing of wetlands. *Wetlands ecology and management*, 10(5):381–402, 2002.

[10] Tobias Landmann, Matthias Schramm, Rene R Colditz, Andreas Dietz, and Stefan Dech. Wide area wetland mapping in semi-arid Africa using 250-meter MODIS metrics and topographic variables. *Remote Sensing*, 2(7):1751–1766, 2010.

[11] Jennifer Corcoran, Joseph Knight, Brian Brisco, Shannon Kaya, Andrew Cull, and Kevin Murnaghan. The integration of optical, topographic, and radar data for wetland mapping in northern Minnesota. *Canadian Journal of Remote Sensing*, 37(5):564–582, 2012.

[12] SE Bunn, PI Boon, MA Brock, and NJ Schofield. National wetlands R&D program: Scoping review. *Land and Water Resources Research and Development Corporation, Canberra*, 1997.

[13] Floyd M Henderson and Anthony J Lewis. Radar detection of wetland ecosystems: a review. *International Journal of Remote Sensing*, 29(20):5809–5835, 2008.

[14] Alisa L Gallant. The challenges of remote monitoring of wetlands, 2015.

[15] Linda Moser, Andreas Schmitt, Anna Wendleder, and Achim Roth. Monitoring of the Lac Bam wetland extent using dual-polarized X-Band SAR data. *Remote Sensing*, 8(4):302, 2016.

[16] Elhadi Adam, Onisimo Mutanga, and Denis Rugege. Multispectral and hyperspectral remote sensing for identification and mapping of wetland vegetation: a review. *Wetlands Ecology and Management*, 18(3):281–296, 2010.

[17] Iryna Dronova. Object-based image analysis in wetland research: a review. *Remote Sensing*, 7(5):6380–6413, 2015.

[18] Brian Brisco. Mapping and monitoring surface water and wetlands with synthetic aperture radar. *Remote Sensing of Wetlands: Applications and Advances*, pages 119–136, 2015.

[19] MA Boon, R Greenfield, and S Tesfamichael. WETLAND ASSESSMENT USING UNMANNED AERIAL VEHICLE (UAV) PHOTOGRAMMETRY. *International Archives of the Photogrammetry, Remote Sensing & Spatial Information Sciences*, 41, 2016.

[20] Laura L Bourgeau-Chavez, Kevin Riordan, Richard B Powell, Nicole Miller, and Mitch Nowels. Improving wetland characterization with multi-sensor, multi-

temporal sar and optical/infrared data fusion. In *Advances in geoscience and remote sensing*. InTech, 2009.

[21] Aaron K Shackelford and Curt H Davis. A combined fuzzy pixel-based and object-based approach for classification of high-resolution multispectral data over urban areas. *IEEE Transactions on GeoScience and Remote sensing*, 41(10):2354–2363, 2003.

[22] Canada Committee on Ecological (Biophysical) Land Classification. National Wetlands Working Group. *The Canadian wetland classification system*. Lands Conservation Branch, Canadian Wildlife Service, Environment Canada, 1997.

[23] Srinivas Sura. *Effects of herbicide mixtures on microbial communities from a prairie wetland ecosystem*. PhD thesis, Citeseer, 2012.

[24] MM Barson and JE Williams. *Wetland inventory: towards a unified approach*. 1991.

[25] K Reimer. The need for a canadian wetland inventory. *Conservator*, 30:37–45, 2009.

[26] Richard T Kingsford, Alberto Basset, and Leland Jackson. Wetlands: conservation's poor cousins. *Aquatic Conservation: Marine and Freshwater Ecosystems*, 26(5):892–916, 2016.

[27] William J Mitsch and James G Gosselink. *Wetlands*.

[28] Ridha Touzi, A Deschamps, and G Rother. Wetland characterization using polarimetric RADARSAT-2 capability. *Canadian Journal of Remote Sensing*, 33(sup1):S56–S67, 2007.

[29] K Amanuel. Gis and remote sensing based analysis of population and environmental change: The case of jarmet wetland and its surruonding environments in Western Ethiopia.

[30] CM Finlayson, NC Davidson, AG Spiers, and NJ Stevenson. Global wetland inventory–current status and future priorities. *Marine and Freshwater Research*, 50(8):717–727, 1999.

[31] Edward Maltby and Tom Barker. *The Wetlands Handbook, 2 Volume Set*. John Wiley & Sons, 2009.

[32] Elaine Matthews and Inez Fung. Methane emission from natural wetlands: Global distribution, area, and environmental characteristics of sources. *Global biogeochemical cycles*, 1(1):61–86, 1987.

[33] Bernhard Lehner and Petra Döll. Development and validation of a global database of lakes, reservoirs and wetlands. *Journal of Hydrology*, 296(1-4):1–22, 2004.

[34] JA Dechka, SE Franklin, MD Watmough, RP Bennett, and DW Ingstrup. Classification of wetland habitat and vegetation communities using multi-temporal Ikonos imagery in southern Saskatchewan. *Canadian Journal of Remote Sensing*, 28(5):679–685, 2002.

[35] LH Fraser and PA Keddy. The future of large wetlands: a global perspective. *The World's Largest Wetlands: Ecology and Conservation Eds LH Fraser, PA Keddy (Cambridge University Press, Cambridge) pp*, pages 446–468, 2005.

[36] GA Baldassarre and EG Bolden. Waterfowl ecology and Management. Malabar.(Florida). 567 p. 2006.

[37] Alisa L Gallant, Robert W Klaver, Gary S Casper, and Michael J Lannoo. Global rates of habitat loss and implications for amphibian conservation. *Copeia*, 2007(4):967–979, 2007.

[38] Thomas R Karl, JM Melillo, TC Peterson, et al. Global climate change impacts in the united states. *Global Climate Change Impacts In The United States*, 2009.

[39] V Klemas, FC Daiber, D Bartlett, OW Crichton, and AO Fornes. Inventory of delaware's wetlands. *Photogrammetric Engineering*, 40(4), 1974.

[40] M Alvarez-Cobelas, S Sánchez-Carrillo, S Cirujano, and DG Angeler. Long-term changes in spatial patterns of emergent vegetation in a Mediterranean floodplain: natural versus anthropogenic constraints. *Plant Ecology*, 194(2):257–271, 2008.

[41] S Sánchez-Carrillo and M Alvarez-Cobelas. Nutrient dynamics and eutrophication patterns in a semi-arid wetland: the effects of fluctuating hydrology. *Water, air, and soil pollution*, 131(1-4):97–118, 2001.

[42] Thomas E Dahl. Wetlands losses in the united states, 1780's to 1980's. report to the congress. Technical report, National Wetlands Inventory, St. Petersburg, FL (USA), 1990.

[43] Donald F McAlpine and Ian M Smith. *Assessment of species diversity in the Atlantic maritime ecozone*. NRC Research Press, 2010.

[44] ES Papastergiadou, A Retalis, A Apostolakis, and Th Georgiadis. Environmental monitoring of spatio-temporal changes using remote sensing and GIS in a Mediterranean wetland of Northern Greece. *Water Resources Management*, 22(5):579–594, 2008.

[45] Eric D Stein, Shawna Dark, Travis Longcore, Robin Grossinger, Nicholas Hall, and Michael Beland. Historical ecology as a tool for assessing landscape change and informing wetland restoration priorities. *Wetlands*, 30(3):589–601, 2010.

[46] Kate Fickas et al. Landsat-based monitoring of annual wetland change in the main-stem Willamette River floodplain of Oregon, USA from 1972 to 2012. 2014.

[47] Francisco Cellone, Eleonora Carol, and Luigi Tosi. Coastal erosion and loss of wetlands in the middle Río de la Plata estuary (Argentina). *Applied Geography*, 76:37–48, 2016.

[48] CM Finlayson and AG Van der Valk. Wetland classification and inventory: a summary. *Vegetatio*, 118(1-2):185–192, 1995.

[49] Ramsar Secretariat. The ramsar handbooks for the wise use of wetlands, 2010.

[50] GR Milton and R Hélie. Wetland inventory and monitoring: partnering to provide a national coverage. In *Wetland Stewardship in Canada: Contributed Papers from the Conference on Canadian Wetlands Stewardship*, pages 3–5, 2003.

[51] Steven M Kloiber, Robb D Macleod, Aaron J Smith, Joseph F Knight, and Brian J Huberty. A semi-automated, multi-source data fusion update of a wetland inventory for east-central Minnesota, USA. *Wetlands*, 35(2):335–348, 2015.

[52] Ralph W Tiner Jr. Use of high-altitude aerial photography for inventorying forested wetlands in the United States. *Forest Ecology and Management*, 33:593–604, 1990.

[53] Patrick Dugan. *Wetlands in danger: a world conservation atlas*. New York New York Oxford University Press 1993., 1993.

[54] John G Lyon and Lynn Krise Lyon. *Practical handbook for wetland identification and delineation*. CRC Press, 2011.

[55] Tim J Davis et al. The ramsar convention manual: a guide to the convention on wetlands. Gland (Switzerland) Ramsar Convention Bureau, 1997.

[56] Ramsar Convention Secretariat. The Ramsar Convention Manual : A Guide to the Convention on Wetlands (Ramsar, Iran, 1971) 6th edition, 2013.

[57] LM Cowardin, V Carter, FC Golet, and ET Laroe. Classification of wetlands and deepwater habitats. US Fish and Wildlife Service, Office of Biological Services, Washington, DC, USA. Technical report, FWS/OBS-79/31, 1979.

[58] Peng Gong, ZhenGuo Niu, Xiao Cheng, KuiYi Zhao, DeMin Zhou, JianHong Guo, Lu Liang, XiaoFeng Wang, DanDan Li, HuaBing Huang, et al. Chinas wetland change (1990–2000) determined by remote sensing. *Science China Earth Sciences*, 53(7):1036–1042, 2010.

[59] Alberta Wetland Policy. Canadian wetland classification system, 2017.

[60] Richard A Fournier, Marcelle Grenier, André Lavoie, and Robert Hélie. Towards a strategy to implement the canadian wetland inventory using satellite remote sensing. *Canadian Journal of Remote Sensing*, 33(sup1):S1–S16, 2007.

[61] SC Zoltai and DH Vitt. Canadian wetlands: environmental gradients and classification. *Vegetatio*, 118(1-2):131–137, 1995.

[62] SC Zoltai and FC Pollett. *Wetlands in Canada, Their Classification, Distribution, and Use*. Elsevier Scientific, 1983.

[63] GD Racey, AG Harris, JK Jeglum, RF Foster, and GM Wickware. Terrestrial and wetland ecosites of northwestern Ontario. Ontario Ministry of Natural Resources. *Northwest Science and Technology Field Guide GG-02, Ont*, 1996.

[64] WH MacKenzie and JR Moran. Wetlands of British Columbia: a guide to identification. *Res. Br., BC Min. For., Victoria, BC Land Manage. Handb*, 52(5), 2004.

[65] National Research Council et al. *Wetlands: Characteristics and boundaries*. National Academies Press, 1995.

[66] V Lawley, M Lewis, K Clarke, and B Ostendorf. Site-based and remote sensing methods for monitoring indicators of vegetation condition: An australian review. *Ecological Indicators*, 60:1273–1283, 2016.

[67] Enrica Belluco, Monica Camuffo, Sergio Ferrari, Lorenza Modenese, Sonia Silvestri, Alessandro Marani, and Marco Marani. Mapping salt-marsh vegetation by multispectral and hyperspectral remote sensing. *Remote sensing of environment*, 105(1):54–67, 2006.

[68] Lian P Rampi, Joseph F Knight, and Keith C Pelletier. Wetland mapping in the upper midwest United States. *Photogrammetric Engineering & Remote Sensing*, 80(5):439–448, 2014.

[69] Kunihiko Yoshino, Sayuri Kawaguchi, Fusayuki Kanda, Keiji Kushida, and Fuan Tsai. Very high resolution plant community mapping at high moor, kushiro wetland. *Photogrammetric Engineering & Remote Sensing*, 80(9):895–905, 2014.

[70] Victor V Klemas. Coastal and environmental remote sensing from unmanned aerial vehicles: An overview. *Journal of Coastal Research*, 31(5):1260–1267, 2015.

[71] Donald C Rundquist, Sunil Narumalani, and Ram M Narayanan. A review of wetlands remote sensing and defining new considerations. 2001.

[72] Junhua Li and Wenjun Chen. A rule-based method for mapping Canada's wetlands using optical, radar and DEM data. *International Journal of Remote Sensing*, 26(22):5051–5069, 2005.

[73] Andreas Schmitt and Brian Brisco. Wetland monitoring using the curvelet-based change detection method on polarimetric sar imagery. *Water*, 5(3):1036–1051, 2013.

[74] D Nagesh Kumar and TV Reshmidevi. Remote sensing applications in water resources. *Journal of the Indian Institute of Science*, 93(2):163–188, 2013.

[75] Mohammed Dabboor, Lori White, Brian Brisco, and François Charbonneau. Change detection with compact polarimetric sar for monitoring wetlands. *Canadian Journal of Remote Sensing*, 41(5):408–417, 2015.

[76] M. Grenier, S. Labrecque, M. Benoit, and M. Allard. Accuracy asessment method for object-based classification.

[77] Don Faber-Langendoen, William Nichols, Joe Rocchio, Kathleen Walz, Joanna Lemly, Regan Smyth, and Kristin Snow. Rating the Condition of Reference Wetlands Across States: NatureServes Ecological Integrity Assessment Method. *National Wetlands Newsletter*, 38(3):12–16, 2016.

[78] M Amani, B Salehi, S Mahdavi, and J Granger. Spectral Analysis of wetlands in Newfoundland using Sentinel 2A and Landsat 8 imagery. *Proceedings of the IGTF*, 2017.

[79] Lewis M Cowardin and Francis C Golet. US Fish and Wildlife Service 1979 wetland classification: A review. In *Classification and inventory of the worlds wetlands*, pages 139–152. Springer, 1995.

[80] J Scott Seher and Paul T Tueller. Color aerial photos for marshland. *Photogrammetric Engineering*, 9(5), 1973.

[81] Lurie Jessie Shima, Richard R Anderson, and Virginia P Carter. The use of aerial color infrared photography in mapping the vegetation of a freshwater marsh. *Chesapeake Science*, 17(2):74–85, 1976.

[82] William G Howland et al. Multispectral aerial photography for wetland vegetation mapping. *Photogrammetric Engineering and Remote Sensing*, 46(1):87–99, 1980.

[83] Sepideh Arzandeh and Jinfei Wang. Texture evaluation of RADARSAT imagery for wetland mapping. *Canadian Journal of Remote Sensing*, 28(5):653–666, 2002.

[84] Maxim Neumann, Andreas Reigber, and Laurent Ferro-Famil. Data classification based on PolInSAR coherence shapes. In *Geoscience and Remote Sensing Symposium, IGARSS'05 proceedings*, volume 7, pages 4852–4855, 2005.

[85] John M Farrell, Brent A Murry, Donald J Leopold, Alison Halpern, Molly Beland Rippke, Kevin S Godwin, and Sasha D Hafner. Water-level regulation and coastal wetland vegetation in the upper St. Lawrence River: inferences from historical aerial imagery, seed banks, and Typha dynamics. *Hydrobiologia*, 647(1):127–144, 2010.

[86] Dániel Cserhalmi, János Nagy, Dániel Kristóf, and Dóra Neidert. Changes in a wetland ecosystem: a vegetation reconstruction study based on historical panchromatic aerial photographs and succession patterns. *Folia Geobotanica*, 46(4):351–371, 2011.

[87] Jacob F Berkowitz, Jason Pietroski, and Daniel Krenz. Identifying areas of potential wetland hydrology in irrigated croplands using aerial image interpretation and analysis of rainfall normality. Technical report, US Army Engineer Research and Development Center Vicksburg United States, 2016.

[88] J Wang, J Shang, B Brisco, and RJ Brown. Evaluation of multidate ERS-1 and multispectral Landsat imagery for wetland detection in southern Ontario. *Canadian journal of remote sensing*, 24(1):60–68, 1998.

[89] Gabriel Gosselin, Ridha Touzi, and François Cavayas. Polarimetric Radarsat-2 wetland classification using the Touzi decomposition: case of the Lac Saint-Pierre Ramsar wetland. *Canadian Journal of Remote Sensing*, 39(6):491–506, 2014.

[90] John Alan Richards et al. *Remote sensing with imaging radar*, volume 1. Springer, 2009.

[91] Zhe Zhu, Curtis E Woodcock, John Rogan, and Josef Kellndorfer. Assessment of spectral, polarimetric, temporal, and spatial dimensions for urban and peri-urban land cover classification using Landsat and SAR data. *Remote Sensing of Environment*, 117:72–82, 2012.

[92] Ruhul Amin, Richard Gould, Weilin Hou, Robert Arnone, and Zhongping Lee. Optical algorithm for cloud shadow detection over water. *IEEE Transactions on Geoscience and Remote Sensing*, 51(2):732–741, 2013.

[93] Meisam Amani and Mohammad Reza Mobasheri. A parametric method for estimation of leaf area index using landsat ETM+ data. *GIScience & Remote Sensing*, 52(4):478–497, 2015.

[94] Heather McNairn, Catherine Champagne, Jiali Shang, Delmar Holmstrom, and Gordon Reichert. Integration of optical and Synthetic Aperture Radar (SAR) imagery for delivering operational annual crop inventories. *ISPRS Journal of Photogrammetry and Remote Sensing*, 64(5):434–449, 2009.

[95] Michael G Leahy, Marilyne Y Jollineau, Philip J Howarth, and Adina R Gillespie. The use of landsat data for investigating the long-term trends in wetland change at long point, ontario. *Canadian Journal of Remote Sensing*, 31(3):240–254, 2005.

[96] Marcelle Grenier, Sandra Labrecque, Michelle Garneau, and Alain Tremblay. Object-based classification of a SPOT-4 image for mapping wetlands in the context of greenhouse gases emissions: the case of the Eastmain region, Québec, Canada. *Canadian Journal of Remote Sensing*, 34(S2):S398–S413, 2008.

[97] Weichelt H, Rosso P, Marx A, Reigber S, Douglass K, and Heynen M. The rapideye red edge band, 2011.

[98] X Wen, Z Zhou, B Chen, Z Li, and X Tang. Research on the features of chlorophyll-a derived from rapideye and eos/modis data in chaohu lake. IOP Conference Series: Earth and Environmental Science, 2014.

[99] I Filella and J1 Penuelas. The red edge position and shape as indicators of plant chlorophyll content, biomass and hydric status. *International Journal of Remote Sensing*, 15(7):1459–1470, 1994.

[100] JGPW Clevers, SM De Jong, GF Epema, FD Van Der Meer, WH Bakker, AK Skidmore, and KH Scholte. Derivation of the red edge index using the meris standard band setting. *International Journal of Remote Sensing*, 23(16):3169–3184, 2002.

[101] Onisimo Mutanga, Elhadi Adam, and Moses Azong Cho. High density biomass estimation for wetland vegetation using WorldView-2 imagery and random forest regression algorithm. *International Journal of Applied Earth Observation and Geoinformation*, 18:399–406, 2012.

[102] KS Schmidt and AK Skidmore. Spectral discrimination of vegetation types in a coastal wetland. *Remote sensing of Environment*, 85(1):92–108, 2003.

[103] Sang-Hoon Hong, Hyun-Ok Kim, Shimon Wdowinski, and Emanuelle Feliciano. Evaluation of polarimetric sar decomposition for classifying wetland vegetation types. *Remote Sensing*, 7(7):8563–8585, 2015.

[104] Gregory P Asner. Biophysical and biochemical sources of variability in canopy reflectance. *Remote sensing of Environment*, 64(3):234–253, 1998.

[105] MA Cochrane. Using vegetation reflectance variability for species level classification of hyperspectral data. *International Journal of Remote Sensing*, 21(10):2075–2087, 2000.

[106] Prasad S Thenkabail, Eden A Enclona, Mark S Ashton, and Bauke Van Der Meer. Accuracy assessments of hyperspectral waveband performance for vegetation analysis applications. *Remote sensing of environment*, 91(3-4):354–376, 2004.

[107] J Kamaruzaman and I Kasawani. Imaging spectrometry on mangrove species identification and mapping in Malaysia. *WSEAS Trans Biol Biomed*, 8:118–126, 2007.

[108] Eric P Crist and Richard C Cicone. A physically-based transformation of Thematic Mapper data—The TM Tasseled Cap. *IEEE Transactions on Geoscience and Remote sensing*, (3):256–263, 1984.

[109] Meisam Amani, Saeid Parsian, S Mohammad MirMazloumi, and Omid Aieneh. Two new soil moisture indices based on the NIR-red triangle space of Landsat-8 data. *International Journal of Applied Earth Observation and Geoinformation*, 50:176–186, 2016.

[110] Mohammad Reza Mobasheri and Meisam Amani. Soil moisture content assessment based on landsat 8 red, near-infrared, and thermal channels. *Journal of Applied Remote Sensing*, 10(2):026011, 2016.

[111] Meisam Amani, Bahram Salehi, Sahel Mahdavi, Ali Masjedi, and Sahar Dehnavi. Temperature-Vegetation-soil Moisture Dryness Index (TVMDI). *Remote Sensing of Environment*, 197:1–14, 2017.

[112] John R Jensen, M Hodgson, EJ Christensen, HE Mackey, and RR Sharitz. Multispectral remote sensing of inland wetlands in South Carolina: selecting the appropriate sensor. Technical report, South Carolina Univ., 1984.

[113] M Leblanc, Jacques Lemoalle, J-C Bader, S Tweed, and L Mofor. Thermal remote sensing of water under flooded vegetation: New observations of inundation patterns for the smalllake chad. *Journal of Hydrology*, 404(1-2):87–98, 2011.

[114] Nguyen Thanh Hoan and Ryutaro Tateishi. Cloud removal of optical image using SAR data for ALOS applications. Experimenting on simulated ALOS data. *Journal of The Remote Sensing Society of Japan*, 29(2):410–417, 2009.

[115] Laura L Hess, John M Melack, Solange Filoso, and Yong Wang. Delineation of inundated area and vegetation along the Amazon floodplain with the SIR-C synthetic aperture radar. *IEEE Transactions on Geoscience and Remote Sensing*, 33(4):896–904, 1995.

[116] Leo Breiman. Random forests. *Machine learning*, 45(1):5–32, 2001.

[117] Ridha Touzi, Alice Deschamps, and Gershon Rother. Phase of target scattering for wetland characterization using polarimetric C-band SAR. *IEEE Transactions on Geoscience and Remote Sensing*, 47(9):3241–3261, 2009.

[118] Ridha Touzi. Target scattering decomposition in terms of roll-invariant target parameters. *IEEE Transactions on Geoscience and Remote Sensing*, 45(1):73–84, 2007.

[119] Sahel Mahdavi, Bahram Salehi, Cecilia Moloney, Weimin Huang, and Brian Brisco. Speckle filtering of synthetic aperture radar images using filters with object-size-adapted windows. *International Journal of Digital Earth*, pages 1–27, 2017.

[120] Jane Whitcomb, Mahta Moghaddam, Kyle McDonald, Erika Podest, and Josef Kellndorfer. Wetlands map of Alaska using L-Band radar satellite imagery. In *Geoscience and Remote Sensing Symposium, 2007. IGARSS 2007. IEEE International*, pages 2487–2490. IEEE, 2007.

[121] B Brisco, M Kapfer, T Hirose, B Tedford, and J Liu. Evaluation of C-band polarization diversity and polarimetry for wetland mapping. *Canadian Journal of Remote Sensing*, 37(1):82–92, 2011.

[122] Anthony Freeman and Stephen L Durden. A three-component scattering model for polarimetric SAR data. *IEEE Transactions on Geoscience and Remote Sensing*, 36(3):963–973, 1998.

[123] Shane R Cloude and Eric Pottier. An entropy based classification scheme for land applications of polarimetric SAR. *IEEE Transactions on Geoscience and Remote Sensing*, 35(1):68–78, 1997.

[124] Cécile Marechal, Eric Pottier, Laurence Hubert-Moy, and Sebastien Rapinel. One year wetland survey investigations from quad-pol RADARSAT-2 time-series SAR images. *Canadian Journal of Remote Sensing*, 38(3):240–252, 2012.

[125] Sahel Mahdavi, Bahram Salehi, Meisam Amani, Jean Elizabeth Granger, Brian Brisco, Weimin Huang, and Alan Hanson. Object-Based Classification of Wetlands in Newfoundland and Labrador Using Multi-Temporal PolSAR Data. *Canadian Journal of Remote Sensing*, 43(5):432–450, 2017.

[126] Brian Brisco, Kun Li, Bill Tedford, Francois Charbonneau, Shao Yun, and Kevin Murnaghan. Compact polarimetry assessment for rice and wetland mapping. *International journal of remote sensing*, 34(6):1949–1964, 2013.

[127] Lori White, Brian Brisco, Mohammed Dabboor, Andreas Schmitt, and Andrew Pratt. A collection of sar methodologies for monitoring wetlands. *Remote sensing*, 7(6):7615–7645, 2015.

[128] Jong-Sen Lee and Eric Pottier. *Polarimetric radar imaging: from basics to applications*. CRC press, 2009.

[129] Eric S Kasischke, Kevin B Smith, Laura L Bourgeau-Chavez, Edwin A Romanowicz, Suzy Brunzell, and Curtis J Richardson. Effects of seasonal hydrologic patterns in south Florida wetlands on radar backscatter measured from ERS-2 SAR imagery. *Remote sensing of environment*, 88(4):423–441, 2003.

[130] Sahel Mahdavi, Yasser Maghsoudi, and Meisam Amani. Effects of changing environmental conditions on synthetic aperture radar backscattering coefficient,

scattering mechanisms, and class separability in a forest area. *Journal of Applied Remote Sensing*, 11(3):036015, 2017.

[131] Jennifer Sokol, TERRY J Pultz, and Victor Bulzgis. Monitoring wetland hydrology in Atlantic Canada using multi-temporal and multi-beam Radarsat data. *IAHS PUBLICATION*, pages 526–530, 2001.

[132] Megan W Lang and Eric S Kasischke. Using C-band synthetic aperture radar data to monitor forested wetland hydrology in Maryland's coastal plain, USA. *IEEE Transactions on Geoscience and Remote Sensing*, 46(2):535–546, 2008.

[133] Eric S Kasischke, Laura L Bourgeau-Chavez, Allison R Rober, Kevin H Wyatt, James M Waddington, and Merritt R Turetsky. Effects of soil moisture and water depth on ERS SAR backscatter measurements from an Alaskan wetland complex. *Remote Sensing of Environment*, 113(9):1868–1873, 2009.

[134] Sahel Mahdavi, Yasser Maghsoudi, and Sahar Dehnavi. A Method for Soil Moisture Retrieval in Vegetated Areas Using Multi-Frequency Data Considering Different kinds of Interaction in Different Frequencies. In *EUSAR 2014; 10th European Conference on Synthetic Aperture Radar; Proceedings of*, pages 1–4. VDE, 2014.

[135] Emilio Chuvieco. *Fundamentals of satellite remote sensing*. CRC press, 2009.

[136] Junhua Li, Wenjun Chen, and Ridha Touzi. Optimum RADARSAT-1 configurations for wetlands discrimination: a case study of the Mer Bleue peat bog. *Canadian Journal of Remote Sensing*, 33(sup1):S46–S55, 2007.

[137] SL Durden, ZS Haddad, LA Morrissey, and GP Livingston. Classification of radar imagery over boreal regions for methane exchange studies. *International Journal of Remote Sensing*, 17(6):1267–1273, 1996.

[138] Bob Slade. RADARSAT-2 product description. *RN-SP-52-1238*, (1/6), 2009.

[139] Aaron Smith, Robb Macleod, and Steve Kloiber. Updating the national wetland inventory in minnesota by integrating air photo-interpretation, object-oriented image analysis and multi-source data fusion. *Ann Arbor*, 1001:49233, 2011.

[140] Carlos Leandro de Oliveira Cordeiro and Dilce de Fátima Rossetti. Mapping vegetation in a late Quaternary landform of the Amazonian wetlands using object-based image analysis and decision tree classification. *International Journal of Remote Sensing*, 36(13):3397–3422, 2015.

[141] Timothy G Whiteside and Renée E Bartolo. Mapping aquatic vegetation in a tropical wetland using high spatial resolution multispectral satellite imagery. *Remote Sensing*, 7(9):11664–11694, 2015.

[142] Steven E Franklin and Oumer S Ahmed. Object-based Wetland Characterization Using Radarsat-2 Quad-Polarimetric SAR Data, Landsat-8 OLI Imagery, and Airborne Lidar-Derived Geomorphometric Variables. *Photogrammetric Engineering & Remote Sensing*, 83(1):27–36, 2017.

[143] Andrew Weiss. Topographic position and landforms analysis. In *Poster presentation, ESRI user conference, San Diego, CA*, volume 200, 2001.

[144] Ian Donald Moore, RB Grayson, and AR Ladson. Digital terrain modelling: a review of hydrological, geomorphological, and biological applications. *Hydrological processes*, 5(1):3–30, 1991.

[145] AR Hogg and KW Todd. Automated discrimination of upland and wetland using terrain derivatives. *Canadian Journal of Remote Sensing*, 33(sup1):S68–S83, 2007.

[146] Paul NC Murphy, Jae Ogilvie, Kevin Connor, and Paul A Arp. Mapping wetlands: a comparison of two different approaches for New Brunswick, Canada. *Wetlands*, 27(4):846–854, 2007.

[147] AR Hogg and J Holland. An evaluation of DEMs derived from LiDAR and photogrammetry for wetland mapping. *The Forestry Chronicle*, 84(6):840–849, 2008.

[148] Melissa Maxa and Paul Bolstad. Mapping northern wetlands with high resolution satellite images and LiDAR. *Wetlands*, 29(1):248–260, 2009.

[149] Megan Lang, Owen McDonough, Greg McCarty, Robert Oesterling, and Bill Wilen. Enhanced detection of wetland-stream connectivity using LiDAR. *Wetlands*, 32(3):461–473, 2012.

[150] Koreen Millard and Murray Richardson. Wetland mapping with LiDAR derivatives, SAR polarimetric decompositions, and LiDAR–SAR fusion using a random forest classifier. *Canadian Journal of Remote Sensing*, 39(4):290–307, 2013.

[151] Chengquan Huang, Yi Peng, Megan Lang, In-Young Yeo, and Greg McCarty. Wetland inundation mapping and change monitoring using Landsat and airborne LiDAR data. *Remote Sensing of Environment*, 141:231–242, 2014.

[152] PH Rosso, SL Ustin, and A Hastings. Mapping marshland vegetation of San Francisco Bay, California, using hyperspectral data. *International Journal of Remote Sensing*, 26(23):5169–5191, 2005.

[153] Chaichoke Vaiphasa, Suwit Ongsomwang, Tanasak Vaiphasa, and Andrew K Skidmore. Tropical mangrove species discrimination using hyperspectral data: A laboratory study. *Estuarine, Coastal and Shelf Science*, 65(1-2):371–379, 2005.

[154] Bruce W Pengra, Carol A Johnston, and Thomas R Loveland. Mapping an invasive plant, Phragmites australis, in coastal wetlands using the EO-1 Hyperion hyperspectral sensor. *Remote Sensing of Environment*, 108(1):74–81, 2007.

[155] Mozhdeh Shahbazi, Jérôme Théau, and Patrick Ménard. Recent applications of unmanned aerial imagery in natural resource management. *GIScience & Remote Sensing*, 51(4):339–365, 2014.

[156] Na Li, Demin Zhou, Fuzhou Duan, Shumin Wang, and Yingying Cui. Application of unmanned airship image system and processing techniques for identifying of fresh water wetlands at a community scale. In *Geoinformatics, 2010 18th International Conference on*, pages 1–5. IEEE, 2010.

[157] Bushra Zaman, Austin M Jensen, and Mac McKee. Use of high-resolution multispectral imagery acquired with an autonomous unmanned aerial vehicle

to quantify the spread of an invasive wetlands species. In *Geoscience and Remote Sensing Symposium (IGARSS), 2011 IEEE International*, pages 803–806. IEEE, 2011.

[158] Perry J Hardin and Ryan R Jensen. Small-scale unmanned aerial vehicles in environmental remote sensing: Challenges and opportunities. *GIScience & Remote Sensing*, 48(1):99–111, 2011.

[159] Molly Reif, Robert C Frohn, Charles R Lane, and Brad Autrey. Mapping isolated wetlands in a karst landscape: GIS and remote sensing methods. *GIScience & Remote Sensing*, 46(2):187–211, 2009.

[160] Jinfei Wang, Jiali Shang, Brian Brisco, and Ron J Brown. Comparison of multidate RADAR and multispectral optical satellite data for wetland detection in the Great Lakes region. *Proceedings of Geomatics in the era of RADARSAT*, 1997.

[161] Yanmei Lin and Chen Yue. China's new national rules on wetland protection. 2014.

[162] Meisam Amani, Bahram Salehi, Sahel Mahdavi, Jean Granger, and Brian Brisco. Wetland classification in Newfoundland and Labrador using multi-source SAR and optical data integration. *GIScience & Remote Sensing*, 54(6):779–796, 2017.

[163] L Durieux, J Kropáček, GD De Grandi, and F Achard. Object-oriented and textural image classification of the Siberia GBFM radar mosaic combined with

MERIS imagery for continental scale land cover mapping. *International Journal of Remote Sensing*, 28(18):4175–4182, 2007.

[164] Filipe Aires, Fabrice Papa, and Catherine Prigent. A long-term, high-resolution wetland dataset over the amazon basin, downscaled from a multiwavelength retrieval using SAR data. *Journal of Hydrometeorology*, 14(2):594–607, 2013.

[165] Winfrid Kluge, Frank Bartels, et al. FEUWAnet: a multi-box water level and lateral exchange model for riparian wetlands. *Journal of Hydrology*, 250(1-4):40–62, 2001.

[166] M Todd Merendino, Loren M Smith, Henry R Murkin, and Roger L Pederson. The response of prairie wetland vegetation to seasonality of drawdown. *Wildlife Society Bulletin (1973-2006)*, 18(3):245–251, 1990.

[167] Gunter Menz, Helida Oyieke, Miguel Alvarez, David N Kuria, Salome B Misana, M Becker, Neema Mogha, Hans P Thamm, and Emiliana Mwita. Seasonal vegetation changes in the Malinda Wetland using bi-temporal, multi-sensor, very high resolution remote sensing data sets. 2014.

[168] Minna Väliranta, Niina Salojärvi, Annina Vuorsalo, Sari Juutinen, Atte Korhola, Miska Luoto, and Eeva-Stiina Tuittila. Holocene fen–bog transitions, current status in finland and future perspectives. *The Holocene*, 27(5):752–764, 2017.

[169] Marie-Josée Racine, Monique Bernier, and Taha Ouarda. Evaluation of RADARSAT-1 images acquired in fine mode for the study of boreal peatlands:

a case study in James Bay, Canada. *Canadian Journal of Remote Sensing*, 31(6):450–467, 2005.

[170] Meisam Amani, Bahram Salehi, Sahel Mahdavi, Jean Elizabeth Granger, Brian Brisco, and Alan Hanson. Wetland Classification Using Multi-Source and Multi-Temporal Optical Remote Sensing Data in Newfoundland and Labrador, Canada. *Canadian Journal of Remote Sensing*, 43(4):360–373, 2017.

[171] C Munyati. Wetland change detection on the Kafue Flats, Zambia, by classification of a multitemporal remote sensing image dataset. *International Journal of Remote Sensing*, 21(9):1787–1806, 2000.

[172] Steven M de Jong, Tom Hornstra, and Hans-Gerd Maas. An integrated spatial and spectral approach to the classification of Mediterranean land cover types: the SSC method. *International Journal of Applied Earth Observation and Geoinformation*, 3(2):176–183, 2001.

[173] Manuel Lameiras Campagnolo and J Orestes Cerdeira. Contextual classification of remotely sensed images with integer linear programming. In *CompIMAGE*, pages 123–128, 2006.

[174] Yan Gao and Jean Francois Mas. A comparison of the performance of pixel-based and object-based classifications over images with various spatial resolutions. *Online journal of earth sciences*, 2(1):27–35, 2008.

[175] Ursula C Benz, Peter Hofmann, Gregor Willhauck, Iris Lingenfelder, and Markus Heynen. Multi-resolution, object-oriented fuzzy analysis of remote

sensing data for GIS-ready information. *ISPRS Journal of photogrammetry and remote sensing*, 58(3):239–258, 2004.

[176] CHR De Sousa, CG Souza, L Zanella, and LMT De Carvalho. Analysis of Rapideyes Red edge band for image segmentation and classification. *Proceedings of the 4th GEOBIA, Rio de Janeiro, Brazil*, 79:518, 2012.

[177] Bahram Salehi, Yun Zhang, Ming Zhong, and Vivek Dey. Object-based classification of urban areas using VHR imagery and height points ancillary data. *Remote Sensing*, 4(8):2256–2276, 2012.

[178] Yuguo Qian, Weiqi Zhou, Jingli Yan, Weifeng Li, and Lijian Han. Comparing machine learning classifiers for object-based land cover classification using very high resolution imagery. *Remote Sensing*, 7(1):153–168, 2014.

[179] Evelyn Fix and Joseph L Hodges Jr. Discriminatory analysis-nonparametric discrimination: consistency properties. Technical report, California Univ Berkeley, 1951.

[180] John Aldrich. RA Fisher and the making of maximum likelihood 1912-1922. *Statistical science*, pages 162–176, 1997.

[181] Corinna Cortes and Vladimir Vapnik. Support-vector networks. *Machine learning*, 20(3):273–297, 1995.

[182] Dennis C Duro, Steven E Franklin, and Monique G Dubé. A comparison of pixel-based and object-based image analysis with selected machine learning

algorithms for the classification of agricultural landscapes using SPOT-5 HRG imagery. *Remote Sensing of Environment*, 118:259–272, 2012.

[183] Richard O Duda, Peter E Hart, and David G Stork. Pattern recognition. 2001.

[184] Taskin Kavzoglu and Ismail Colkesen. A kernel functions analysis for support vector machines for land cover classification. *International Journal of Applied Earth Observation and Geoinformation*, 11(5):352–359, 2009.

[185] Elhadi Adam, Onisimo Mutanga, John Odindi, and Elfatih M Abdel-Rahman. Land-use/cover classification in a heterogeneous coastal landscape using rapideye imagery: evaluating the performance of random forest and support vector machines classifiers. *International Journal of Remote Sensing*, 35(10):3440–3458, 2014.

[186] Leo Breiman, Jerome Friedman, Charles J Stone, and Richard A Olshen. *Classification and regression trees*. CRC press, 1984.

[187] Julia Reschke, Annett Bartsch, Stefan Schlaffer, and Dmitry Schepaschenko. Capability of C-band SAR for operational wetland monitoring at high latitudes. *Remote Sensing*, 4(10):2923–2943, 2012.

[188] Mahesh Pal. Random forest classifier for remote sensing classification. *International Journal of Remote Sensing*, 26(1):217–222, 2005.

[189] KB Smith, CE Smith, SF Forest, and AJ Richard. A field guide to the wetlands of the boreal plains ecozone of Canada. *Ducks Unlimited Canada, Western Boreal Office: Edmonton, Alberta*, 2007.

[190] Ducks Unlimited Canada. Enhanced wetland classification inferred products user guide, 2011.

Chapter 3

Speckle Filtering of Synthetic Aperture Radar Images using Filters with Object-size Adapted Windows

3.1 Preface

In this chapter, a pre-processing method which is important for land cover classification using SAR imagery, namely a speckle reduction approach, was presented. The paper resulted from this chapter has been published in the *International Journal of Digital Earth*.

3.2 Abstract

Speckle degrades the radiometric quality of a Synthetic Aperture Radar (SAR) image. Previous methods for speckle reduction have used a fixed size window for filtering the entire image. This, however, may not be effective for the entire image, as land covers of different sizes require different filtering windows. In this paper, a novel method is proposed by which each pixel in the image is filtered with a window appropriate for the size of object within it. The real in-phase and the imaginary quadrature components of the SAR images determine the best window size and the pixels in the intensity image are filtered using their own optimal windows. The proposed method is presented for both single- and multi-polarized SAR images, and the results of several common filters that were modified are presented. This approach is applied to two RADARSAT-2 images: one over San Francisco, California, USA and the other over St. John's, Newfoundland and Labrador, Canada, producing results that were similar to, or outperformed, comparable filters while retaining details and suppressing speckle effectively. While the method was successful for single-look intensity data, it offers great potential for multi-look and amplitude data as well.

3.3 Introduction

Synthetic Aperture Radar (SAR) images are valuable assets for various applications because of their all-weather and day and night acquisition capability. However, these valuable resources are blemished with the presence of speckle. An intrinsic feature of SAR images, speckle originates from the coherently recorded pulses return-

ing from the earth surface. Speckle degrades the radiometric quality of the image, thus hindering image interpretation and reducing the accuracy of image segmentation and classification [1]. Consequently, since the advent of SAR images, there has been a host of studies addressing the issue of speckle reduction. Early on, starting from a study by Lee [2], it was understood that the typical techniques applied for image noise suppression are not effective for SAR images. Lee's research proposed filters that exploit local statistics of the image, namely adaptive filters. He suggested that speckle acts as multiplicative noise and, based on that, he proposed a filter by minimizing the Mean Square Error. the filter was known as the MMSE filter [2, 3] and became the basis of many other algorithms. The MMSE filter, however, fails to suppress speckle effectively close to edges [2], and hence Lee refined it by using edge-aligned, non-square windows [3]. He also proposed the sigma filter [4, 5] based on the sigma probability of a Gaussian distribution. As sigma filter was insufficient in maintaining strong targets and produced biased estimation, an improved version of that was proposed in [6]. Besides Lee's filters, other similar techniques were proposed for speckle reduction in single-band SAR images while preserving image sharpness. Frost et al. [7,8] calculated the impulse response of the filter by solving the MMSE problem using a different error measure. [9] also dealt with the MMSE problem and reached the same general form as [2], but with a different weight function for balancing the role of pixel reflectance and that of the local statistics.

In subsequent years, single-band SAR filters were further improved. [10] noted that there are different regions in a SAR image, namely homogeneous, heterogeneous and point targets. He stated that speckle should not be reduced by the same amount in the three different regions, and suggested measures for distinguishing between the

three different areas. He modified the commonly used filters based on his idea. A few years later, in 1993, [11] also proposed a filter which was known as the Gamma filter, in which homogeneous regions, edges, lines, and point targets are detected using more robust measures. There have also been a few other innovative studies. In [12], for example, a method was proposed for filtering which exploited local statistics to change the filtering window in a range. A growing regional method based on a statistical measure was applied for selection of window sizes in an approach suggested in [13]. Other filtering algorithms that have been proposed include [14], [15], and [16]. A more comprehensive review can be found in [17], [18], and [19].

With the advancement of SAR sensors, Polarimetric SAR (PolSAR) images became available, and this development was followed by the need for filters for PolSAR images. [20] pioneered in this field by developing the Polarimetric Whitening Filter (PWF). In the PWF all elements of the scattering matrix are combined optimally to form a single, speckle-reduced image. In [21], the MMSE filter was extended to the diagonal elements of the covariance matrix, but the off-diagonal elements were ignored. While speckle for the diagonal terms can be modelled as multiplicative noise, a multiplicative noise model is not effective for off-diagonal terms. Consequently, off-diagonal terms should be modelled by a combination of multiplicative and additive noise [1]. [22] continued Lee's work by MMSE filtering of all terms in the covariance matrix. [22] developed another filter for PolSAR data focusing on image texture. [23] suggested a filter useful for interferometric applications in forested areas. [24] also extended the improved single-band sigma filter to PolSAR data. In the proposed filter, the authors attempted to maintain the strong point targets and to preserve the scattering mechanisms. However, preliminary attempts for speckle filtering in PolSAR

images fail to preserve polarimetric features i.e. they introduce cross-talk between channels and/or alter the cross-correlation between bands, although they can be useful in some applications such as target detection [1]. Therefore, polarimetric filters such as those used in [25] and [26] were proposed to maintain polarimertric information. In polarimetric filters, all elements of the covariance matrix are filtered by the same amount and in the same way, and the filtering is performed independently on each term to avoid cross-talk, i.e. altering correlation between channels.

In recent years, some other valuable works have been also proposed on speckle reduction. For example, in [27], a three-step filter was proposed for speckle reduction in SAR images. First, the authors developed a line and edge detector, based on which they defined a homogeneity measure. Subsequently, they exploited the homogeneity measure to adjust the shape and size of filtering, and obtained promising results. Moreover, in [28], a speckle filtering approach was proposed that exploits the nonlocal means and stochastic distances to reduce speckle. [29], [30], and [31] also proposed non-local approaches for speckle reduction. Non-local filters define the weights based on the distance between the reference patch and similar neighbouring patches [32].

Although the speckle reduction methods described in the publications reviewed above perform reasonably well both in single-band and multi-polarized cases, selection of window size is almost always a challenging task. In fact, choosing a fixed window size for filtering the entire image has a proper outcome only if all the targets in the image are of the same size, which is not a valid assumption for most real world images. Thus as the weights of the filtering window for each pixel are adaptive, the window size should also be adaptive. The main objective of this paper is to introduce a method for automatically selecting the filtering window size for each pixel. This

approach is presented in both single-band and multi-polarized versions. Common filtering methods such as the box-car and MMSE filters have been adjusted using our proposed adaptive window size approach and the results are presented.

3.4 Method

When working with SAR images, it is the real value of the backscatter coefficient that is of interest. For distributed targets, this value is altered by the effect of interference [33]. The aim of speckle filtering is therefore to average the returned values from all the scatterers which contribute to the same distributed target in order to achieve a more accurate estimation of the backscattering coefficient. For this task, a fixed-sized rectangular window is not effective, for several reasons. First, the actual shape of a target might not be rectangular. Thus a rectangular window includes either fewer or more scatterers than the correct number which causes the estimated backscattering coefficient to be inaccurate. The defect can be observed by noting the smeared boundaries of the target near its edges. Second, not all the distributed targets in an image are of the same size. Hence a window size which can be appropriate for one part of the image might not be applicable for the targets in another part.

The first problem has been addressed extensively in the literature and much of it was mentioned in Section 1. Different adaptive filters have been introduced to exploit the local statistics in an attempt to include only the scatterers from the same target in the filtering process over that target. The second issue, however, has not been investigated as much as the first one. The main objective of this paper is to address this issue.

3.4.1 Average Filtering of Single-band SAR Data with Adaptive Window Size

Speckle can be regarded as the fluctuation of pixel values around a mean which is the desired backscattering coefficient of the target [33]. Naturally, the best possible estimation of the true mean is achieved when all the scatterers from the target are involved in the averaging process, and no scatterer from another neighbouring object is included in filtering. This is the definition which can specify the best filtering window for each pixel within the target as will be presented below.

Although in practice there is correlation between the neighbouring pixels of a SAR image [1], in principle each sample (resolution cell) in a target, here referred to as A, can be considered as an independent observation for estimating the true backscattering coefficient of target A. Thus, a rectangular window which lies entirely within the target includes n independent observations:

$$\Theta_n = \Theta(M_1, M_2, ..., M_n) \tag{3.1}$$

In Equation 3.1, Θ is an arbitrary parameter, which can be considered the real backscattering coefficient of the target in this context. Θ_n is the parameter to be estimated from n observations, which is the backscattering coefficient estimated from n resolution cells. M_i is the i_{th} observation made for estimating Θ which is assumed to be the pixel value of a SAR image. SAR images are provided in different formats: real and imaginary (in-phase and quadrature, respectively), amplitude and phase, and intensity images [33]. We assume that n observations are in real and imaginary format indicating that the pixel value consists of in-phase and quadrature components, i.e.:

$$M_i = X_i + jY_i \tag{3.2}$$

where $j = \sqrt{-1}$. It has been shown that the real and imaginary components in SAR images, when considered individually, tend to have a normal distribution [33]. For normally distributed data, the mean is an efficient estimator [34]. This means that if Θ_n is the average of the real or imaginary part of the observations, i.e.:

$$\begin{aligned} \Theta_{n,real} &= \frac{1}{n}\sum_{i=1}^{n} X_i \\ \Theta_{n,imaginary} &= \frac{1}{n}\sum_{i=1}^{n} Y_i \end{aligned} \tag{3.3}$$

Then, considering Θ_n as a random variable, n pixels result in a smaller standard deviation than $n-1$ pixels, and a greater standard deviation than $n+1$ pixels [35]. This means that if the window containing the observations to be averaged grows larger, the standard deviation will tend to decrease until the window also begins to contain outliers, i.e. observations from other targets. Therefore, the window which yields the minimum value for standard deviation will include a maximum number of observations from target A, but a minimum of observations from neighbouring objects. It should be noted, however, that while Θ_n is used to assign the optimal window size for each pixel, it cannot be applied for speckle reduction, since averaging real or imaginary data individually does not convey any useful information for SAR data analysis. In fact, averaging them is a coherent vector summation and has no effect on speckle reduction [1] while for speckle reduction an incoherent summation is needed. Consequently, while the real and imaginary data are exploited for the determination of the best window size for each pixel, it is the intensity image that is

to be used for averaging the samples using that optimal window size.

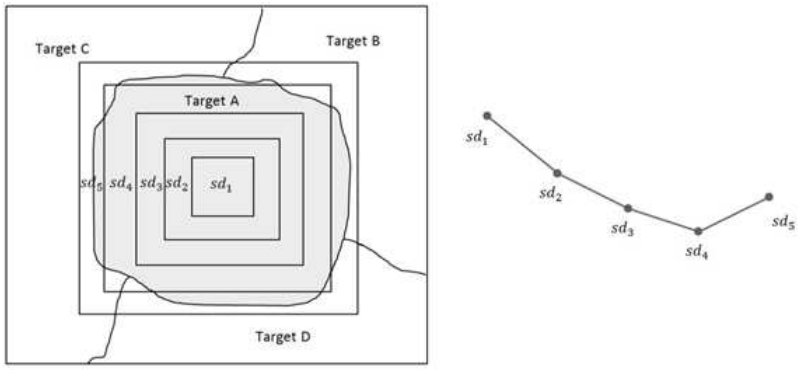

Figure 3.1: The variation of the standard deviation with the change in the window size

Figure 3.1 schematically shows the standard deviation of pixels (either from the real or the imaginary part of the image) with different window sizes. The smallest window contains limited pixels from target A which have standard deviation sd_1. With the explanation above, it is expected that as the number of samples for computation of the average increases, the value of standard deviation will decrease. This reduction continues until the window begins to overlap pixels of adjacent objects. Once the window contains pixels from two different objects, the standard deviation will tend to increase. Thus, the optimum window size is the one which corresponds to the minimum standard deviation, computed using the real or imaginary components of the samples in the window. Then, this window size is used in the intensity image to reduce speckle of the pixel at the center of the window. Based upon the above discussion, the filtering process can be outlined as follows:

1. A range of window sizes is selected by investigating the SAR image. This range

must contain appropriate filtering sizes for all the objects of the image, from the smallest target to the largest. An appropriate range of window sizes can be 3 to 21.

2. Both the real and imaginary parts of the image are averaged separately using the windows covering the entire range of sizes, thus computing the standard deviation corresponding to each window in the size range for all pixels.

3. The appropriate filter size for each pixel is selected as the one which corresponds to the minimum standard deviation for that pixel over the whole range of standard deviations (i.e. window sizes). If the optimal size obtained from the real and imaginary parts is different for any pixel, their average is considered as the optimal window size. When the standard deviation monotonically increases, this means that there is likely a point target in the image with a high amount of backscatter, and likely the best window size for filtering is the smallest. A monotonic decrease in standard deviation indicates that the area is likely completely homogeneous, and the largest window size is the best. In the events of two minimums, it is probable that the first minimum has occurred when all the samples from the first target have been taken into account and the second minimum has likely occurred when all the samples from the first targets and the other neighbouring (and similar) target(s) have been considered. Therefore, the first minimum standard deviation is the best choice.

4. Using a common method, a speckle-reduced intensity image is acquired by filtering each pixel with its corresponding optimal window. The simplest method is obviously averaging, which is the topic of this section. Other common methods,

however, can also be used and will be elaborated.

These steps are schematically illustrated in Figure 3.2.

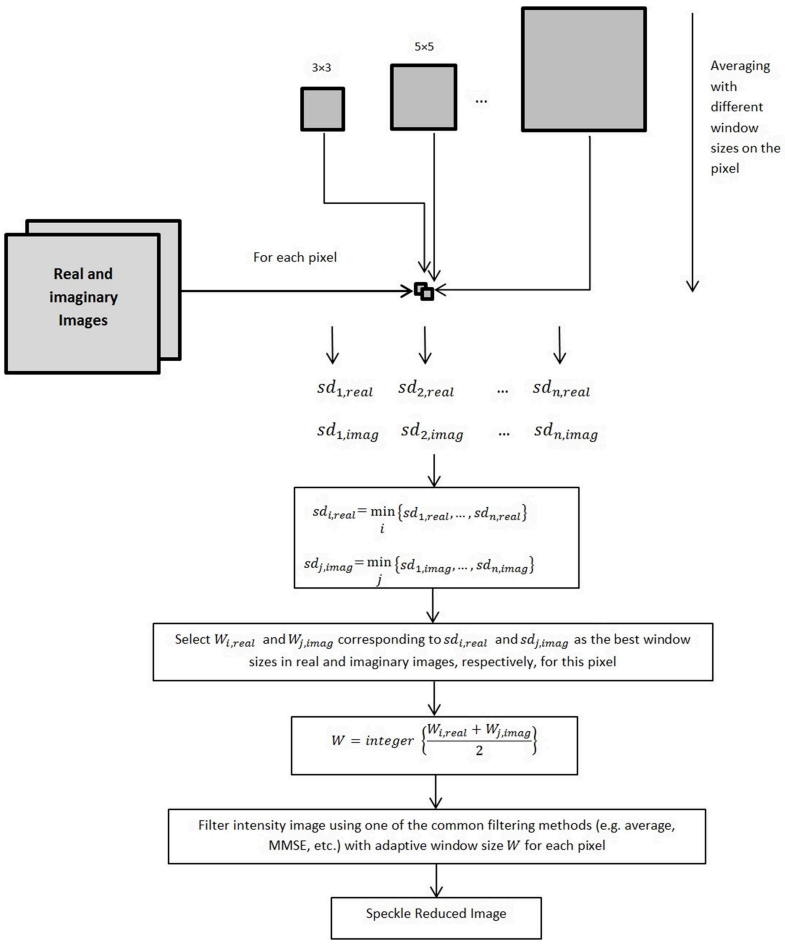

Figure 3.2: Flowchart of the proposed algorithm

3.4.2 MMSE Filtering of Single-band SAR Data with Adaptive Window Size

Figure 3.1 shows the ideal case, i.e. when the pixel to be filtered is almost in the center of the target. Apart from that, especially for the pixels near the edge of the target (see Figure 3.3), Average Filter with Adaptive Window Size might not perform best, a common problem of a simple averaging filter. The proposed method, therefore, can be combined with the MMSE filter [2] in order to solve this problem.

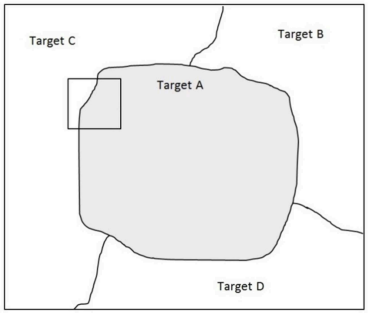

Figure 3.3: The issue near the edges of a target.

The MMSE filter, proposed by [2], has the following form:

$$\hat{R} = W(x,y) * I(x,y) + (1 - W(x,y)) * \bar{I}(x,y) \tag{3.4}$$

In Equation 3.4, $R(x,y)$ is the estimated intensity of the pixel (x,y), $I(x,y)$ is the observed intensity for the pixel (x,y) and $\bar{I}(x,y)$ is the average intensity in a local window. $W(x,y)$ is a weight parameter which is computed by the following formula (obtained by the concept of MMSE):

$$W(x,y) = \frac{\sigma_R^2(x,y)}{\sigma_I^2(x,y)} \tag{3.5}$$

where σ_I^2 is the variance of the intensity in the local window and

$$\sigma_R^2 = \frac{\sigma_I^2 - \bar{I}^2\sigma_u^2}{(1+\sigma_u^2)} \tag{3.6}$$

σ_u^2 is a characteristic of speckle which is the ratio of the standard deviation to the mean in a homogeneous area; its value for single-look SAR data is 1 [36].

The weight parameter $W(x,y)$ in Equation 3.5 will tend to be small in homogeneous regions and large in heterogeneous regions. Therefore, according to Equation 3.4, when using square-shaped windows the role of the local mean is minor when filtering the pixels near edges, while it is significant when the central pixel is located around the middle of the target. The local statistics in the Lee filter of Equation 3.4 are traditionally computed in a window of fixed size. However, $\bar{I}(x,y)$ in Equation 3.4 can be replaced with the optimal mean value computed over the optimal window for each pixel as described in the previous section. Moreover, $\sigma_I^2(x,y)$ in 3.5 can be replaced by the variance of the values included in the optimal window. By making these two changes, the MMSE filter with Adaptive Window Size is obtained.

3.4.3 Average Filtering of Polarimetric SAR Data with Adaptive Window Size

A full-polarimetric radar sensor records a scattering matrix of each target which is defined as below:

$$S = \begin{bmatrix} S_{hh} & S_{hv} \\ S_{vh} & S_{vv} \end{bmatrix} \tag{3.7}$$

where for each term S_{hh}, p and q represent transmitted and received polarizations, respectively. Using a well-known result in [37], for monostatic SAR $S_{hv} = S_{vh}$ and hence the target can be characterized entirely by the 3-D Lexicographic feature vector:

$$k = \begin{bmatrix} S_{hh} & \sqrt{2}S_{hv} & S_{vv} \end{bmatrix}^T \tag{3.8}$$

where superscript T denotes matrix transpose. Then the polarimetric covariance matrix and its span (total power) can be obtained using the target vector with Equations (9) and (10), respectively; i.e.

$$C = kk^{*T} = \begin{bmatrix} |S_{hh}|^2 & \sqrt{2}S_{hh}S_{hv}^* & S_{hh}S_{vv}^* \\ \sqrt{2}S_{hv}S_{hh}^* & 2|S_{hv}|^2 & \sqrt{2}S_{hv}S_{vv}^* \\ S_{vv}S_{hh}^* & \sqrt{2}S_{vv}S_{hv}^* & |S_{vv}|^2 \end{bmatrix} \tag{3.9}$$

$$span = k^{*T}k = |S_{hh}|^2 + 2|S_{hv}|^2 + |S_{vv}|^2 \tag{3.10}$$

where the superscript * represents the complex conjugate. A filter must have the following characteristics to preserve polarimetric features and be known as a polarimetric filter [25]:

1. All terms of the covariance matrix must be filtered in the same way and by the same amount;

2. Each term of the covariance matrix must be filtered independently to avoid cross-talk between polarization channels;

3. The filtering should be adaptive so that scattering characteristics are maintained.

The simplest way for filtering polarimetric images is to average the neighbouring covariance matrices in a window of specific size. Although this filter is not adaptive, it preserves polarimetric features and the correlation between channels, and can be adequate for some applications [1].

The idea proposed for using adaptive window sizes is extendable to the average filtering of covariance matrices. The feature vector in Equation 3.8 contains three real and three imaginary components from the three polarimetric channels. For the polarimetric case, all six components can be used to select the optimum window size for each pixel following the same procedure as described in Section 3.4.1, since the definition of target is the same in all bands, even if they might appear visually different in each band. If the optimal window sizes obtained from six images differ from each other, their average is used as the best window size. Then, the covariance matrices in the window selected for each pixel are averaged to form the speckle-reduced matrix for that pixel.

3.4.4 Polarimetric Filtering of SAR Data with Adaptive Window Size

[25] extended his refined filter [38] to PolSAR data. Let Z be the covariance matrix of the pixel to be filtered. Then, the filtered covariance matrix, $\hat{Z}$ can be estimated by the following expression [25]:

$$\hat{Z} = W * Z + (1 - W) * \bar{Z} \tag{3.11}$$

In Equation 3.11, $\bar{Z}$ is the average of the covariance matrices in a non-square, edge-aligned window chosen using the span image (see [25] for more details), and W is the same weight parameter in Equation 3.4.

In this paper, six real and imaginary images for all three channels are used for computing the optimal window as described in Section 3.4.1, and the obtained size per pixel from each image is averaged to achieve the final optimal size. Then, W is computed from the span image in the optimal window. After that, Equation 3.11 is applied to estimate the speckle-reduced polarimetric covariance matrix for each pixel.

3.5 Dataset and Study Areas

For testing the performance of our algorithm, two separate datasets were selected. The first one is a RADARSAT-2 full-polarimetric image over San Francisco, California, USA located at approximately $37°45'N$ and $122°26'W$. This image was acquired in FQ9 beam mode and Single Look Complex (SLC) format in 2008. This area contains divergent land covers such as vegetation, ocean and built-up areas, and has long been used for testing the performance of different SAR speckle reducing filters. The selected subset in the entire image is illustrated in Figure 3.4, a.

For the purpose of illustrating the robustness of the algorithm, the proposed filters were also applied to another image. This RADARSAT-2 full-polarimetric image was acquired in 2015 over the Avalon Peninsula near St. John's, Newfoundland and Labrador, Canada, at approximately $47°33'N$ and $52°32'W$, in FQ4 beam mode and

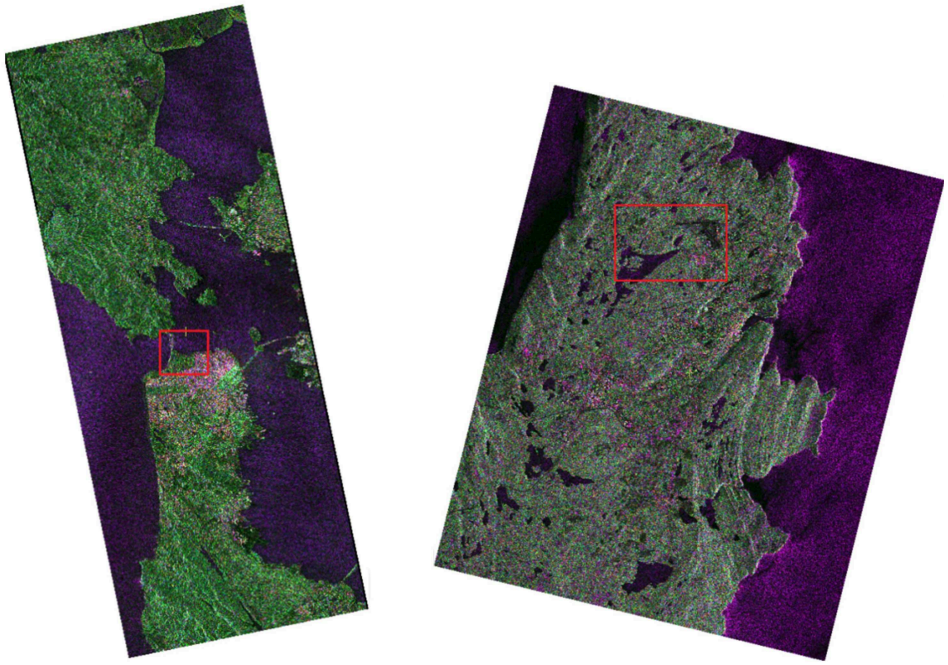

(a) San Francisco (b) St. John's

Figure 3.4: The selected subsets for applying the suggested filters.

SLC format. This image also covers natural, urban (including an international airport), and ocean areas. The study area specified in the whole image is displayed in Figure 3.4, b.

For a more precise visual inspection, a Google Earth^{TM} image from San Francisco, and a 2008 Very High Resolution (VHR) image from Avalon Peninsula have also been used. For the purpose of emphasizing the details, in this paper the results of the filters have been shown on selected sub-images. All odd numbers between and including 3 and 21 were considered as the range of window sizes to be applied on the images. This range was selected by visual inspection of both images.

3.6 Results

3.6.1 Single-band Case

For single-band case, the proposed method was applied on both simulated and real SAR images. The obtained results along with their validation are presented in the following sections.

3.6.1.1 Simulated SAR Image

In order to evaluate the performance of the proposed method, simulated images with and without speckle were applied. Here, the simulated, without speckle images are referred to as the ground-truth images. The simulation procedure of the speckled images is illustrated in Figure 3.5. As mentioned before, the real and imaginary parts of a SAR image have normal distribution with mean of zero and variance of $\frac{\sigma^2}{2}$.

Then, the intensity images were generated by combining the components to simulate a one-look SAR image (Figure 3.5).

Figure 3.6 shows the result of simulation. The left simulated SAR image shows a region containing two different classes, and the right simulated SAR image illustrates two objects within a clutter [33]. Different filters, including the proposed ones, were applied to these two images and the performance of those filters was evaluated using with-reference metrics. The details are presented below.

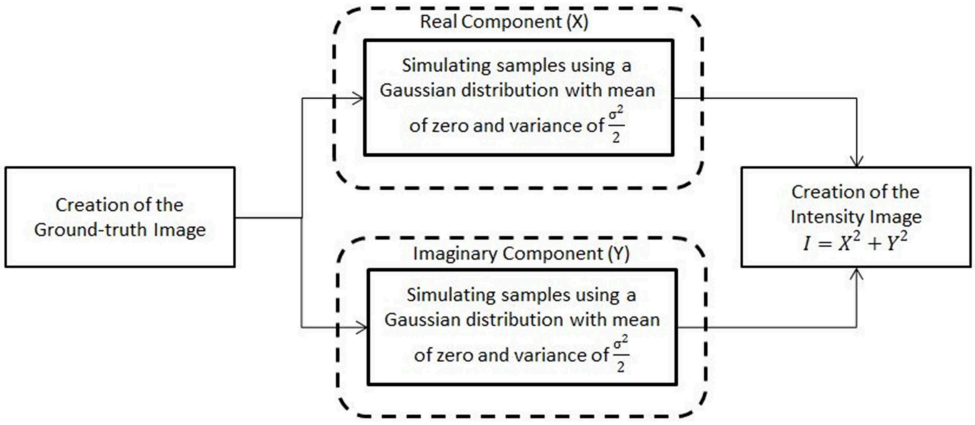

Figure 3.5: The block diagram of the simulation method.

Evaluation of the performance of different filters can also be done using with-reference metrics. One of the most well-known ones is Mean Square Error (MSE), which is defined as below:

$$MSE = E\left[(\hat{f} - f)^2\right] \tag{3.12}$$

where $\hat{f}$ and f are despeckled and ground-truth images, respectively. The ideal value for this metric is zero. Another useful measure is peak signal-to-noise ratio

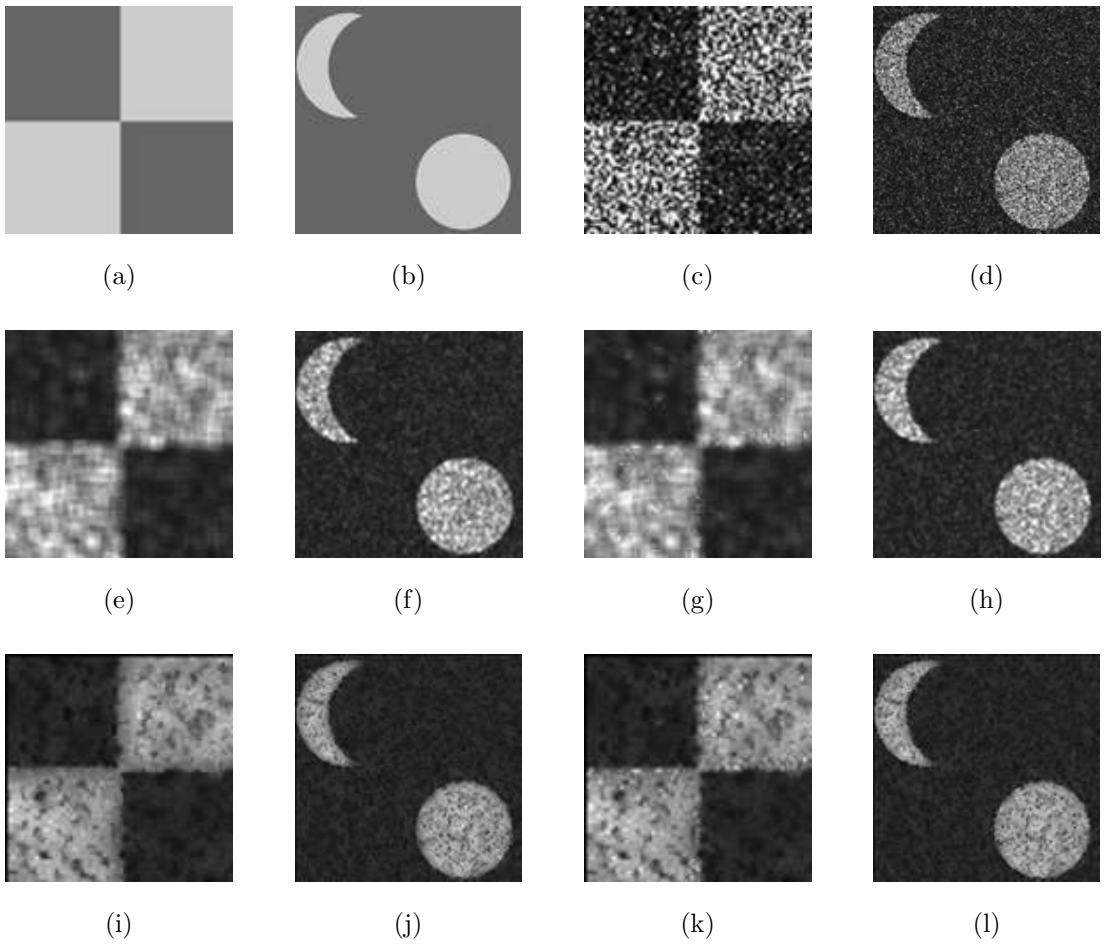

Figure 3.6: Simulated SAR images: (a-b) The ground-truth images, (c-d) The original intensity images, (e-f) The 5-by-5 average filtered images, (g-h) The 5-by-5 MMSE filtered images, (i-j) Average filtered images with Adaptive Window Size, (k-l) MMSE filtered images with Adaptive Window Size.

(PPSNR) which is shown in Equation 3.13:

$$PSNR = 10.log\Big[\frac{Var[f]}{MSE}\Big] \tag{3.13}$$

where f is the ground-truth image. the ideal value for PSNR is 1.

As MSE and PSNR are for evaluation of the general performance of a filter [32], Structural Similarity Index Measurement (SSIM) [39] can be used for estimating the amount of feature preservation in the image. This metric is defined as:

$$SSIM = 10.log\Big[\frac{2.E[f_p].E[\hat{f}_p] + C_1}{E[f_p^2] + E[\hat{f}_p^2] + C_1}\,\frac{2.Cov[f_p, \hat{f}_p] + C_2}{Var[f_p] + E[\hat{f}_p^2] + C_2}\Big] \tag{3.14}$$

where C_1 and C_2 are suitable constants which were chosen as 0.01 and 0.03 in this work. Moreover, f_p and $\hat{f}_p$ are the ground-truth and despeckled images, respectively.

The three above-mentioned metrics were computed for images filtered by the 5-by-5 average and MMSE [2] filters (for the sake of comparison) and their adaptive window size counterparts and the results are shown in Table 3.1. MSE is smaller for the fixed-size Average and MMSE filters than their adaptive-size counterparts which in turn causes PSNR to be larger for them. This means that the fixed-size filters introduced less bias to the image compared to the proposed ones. SSIM is also relatively larger for the fixed size filters, which means that they are more suitable in retaining the structures.

It should be noted that the result of filtering on the synthetically speckled SAR images is not enough for drawing conclusions about performance of filters on real SAR images [32], because the selected ground-truth image and the real ground-truth reflectivity can differ significantly [32]. Moreover, a simulated SAR image cannot

Table 3.1: Various metrics for evaluation of the proposed speckle filters on the simulated SAR images

Filter	MSE		PSNR		SSIM	
	1^{st} Image	2^{nd} Image	1^{st} Image	2^{nd} Image	1^{st} Image	2^{nd} Image
Average Filter	0.0537	0.0556	-1.2773	-3.3865	0.7086	0.6503
MMSE Filter	0.0565	0.0567	-1.5007	-3.4727	0.6905	0.6408
Average Filter with Adaptive Window Size	0.0815	0.0686	-3.0921	-4.2946	0.6519	0.6208
MMSE Filter with Adaptive Window Size	0.0813	0.0685	-3.0775	-4.2894	0.6429	0.6151

be consistent with a real SAR image in terms of image formation and acquisition process [32]. Therefore, the experiment should be done on real SAR images as well.

3.6.1.2 Real SAR Image

For the implementation of the single-band version of the method, the HH channel was selected from both full-polarimetric images introduced in Section 3. For comparison, the average, MMSE [2], enhanced Lee filter [10], and Gamma filter [11] with a fixed window size (5×5 window), and a non-local filter, the Probabilistic Patch-Based filter (PPB, [40]), were also applied to the image. The PPB filter has various user-defined parameters, namely half sizes of the search window width, half sizes of the window width, and number of iterations, and the value of each is described in the figure caption corresponding to both study areas. Figure 3.7 illustrates the results for a sub-image of the San Francisco area. The original one-look HH intensity image is blemished with the effect of speckle. Although the 5×5 average filter has improved the images visually in homogeneous regions, boundaries and subtle objects are smeared. The MMSE filter outperformed the average filter in retaining the edges and details; a fair amount of speckle, however, is still present in the image and occasional isolated pixels with higher intensity can be viewed in homogeneous regions. The enhanced Lee filter preserved even more details. However, in some parts, for example the urban area in the bottom right of the image, the objects seem rather noisy and have not been evenly filtered. Moreover, isolated points, i.e. the points brighter than their surrounding parts, are still present in the image. The Gamma filter had almost the same performance as the enhanced Lee filter, with isolated points being present sporadically. In addition, the objects in urban areas are also not completely clear in

the filtered image. It should be noted that in practice, usually larger window sizes are used for filtering, which causes more blurring. The PPB filter effectively reduced speckle although the urban area was slightly blurred. The proposed Average Filter with Adaptive Window Size shows a significant improvement, both by suppressing speckle in homogeneous areas and maintaining the object boundaries. Some details, however, are blurred as a result of overfiltering. This downside is not observed in the proposed MMSE filter with Adaptive Window Size. The result using adaptive window size shows that details were well preserved as seen in Figure 3.7, E and F, while speckle was successfully suppressed in homogenous regions.

Similar results were obtained for the St. John's image as depicted in Figure 3.8. The effect of speckle can be discerned in the original image and as expected, the average filter indiscriminately filtered all parts of the image by the same amount. The MMSE filter maintained the details but isolated points can be clearly noted. A similar outcome can be observed in the enhanced Lee filtered image, but some features were better preserved, such as the urban part near the bottom right of the image. The Gamma filter has also retained the details, but still there are many isolated bright points throughout the image and some parts not being filtered completely. The PPB filter effectively reduced speckle, but some subtle structures remain obscured. The proposed Average Filter with Adaptive Window Size, on the other hand, filtered the homogeneous areas reasonably well, while it has maintained the details. Isolated points cannot be observed anymore. Even better results have been achieved using the MMSE filter with Adaptive Window Size, where the smaller objects are preserved better.

Figure 3.9 demonstrates the variation of standard deviation with the change of

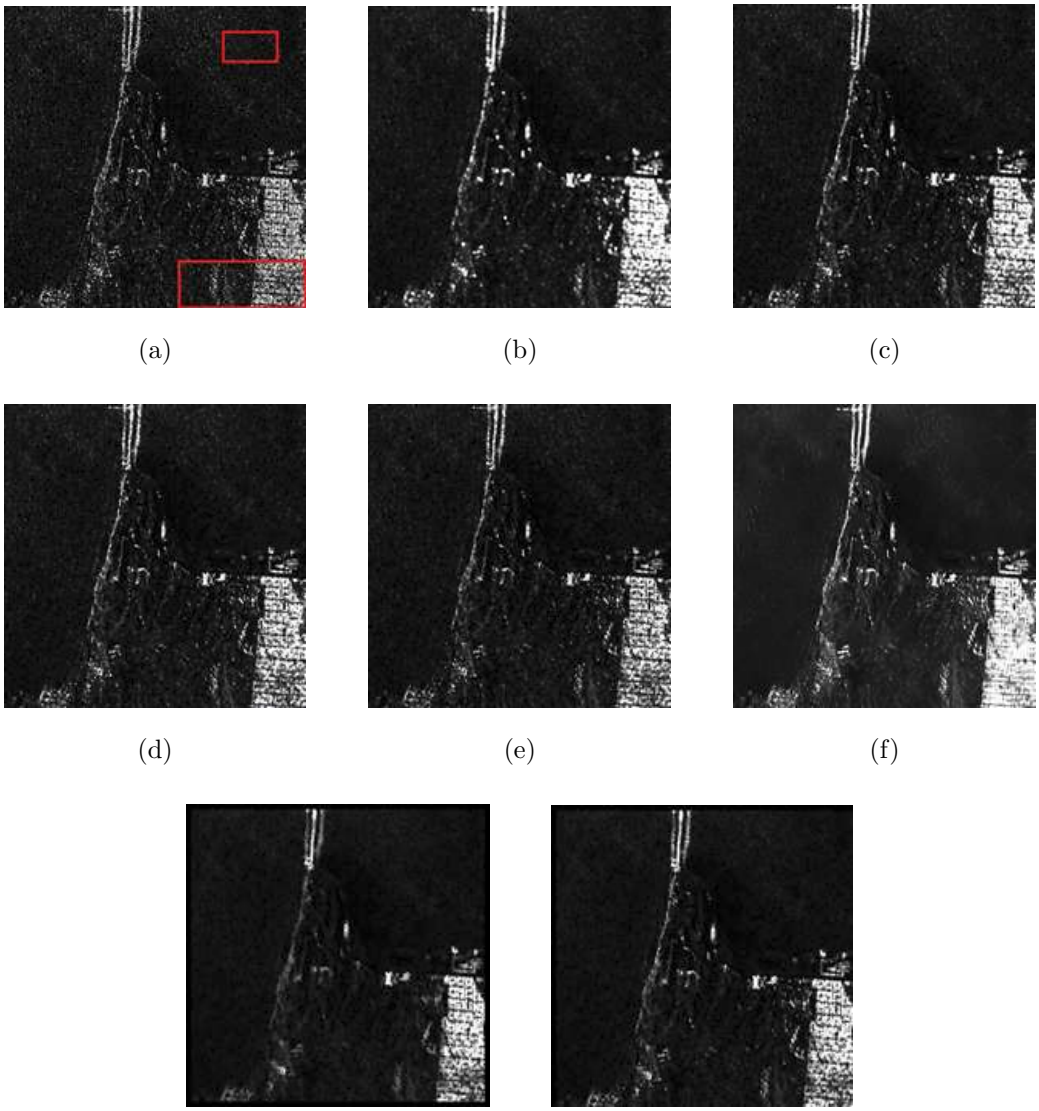

Figure 3.7: San Francisco: a) Original one-look HH intensity image. The rectangle on the top and the bottom of the image show the regions used for computation of ENL and Coefficient of Variation, respectively, b) The 5×5 average filtered image, c) The 5×5 MMSE filtered image, d) The 5×5 enhanced Lee filtered image, e) The 5×5 Gamma filtered image, f) PPB filtered image with hw=20, hd=5, and 1 iteration, g) Average filtered image with Adaptive Window Size, h) MMSE filtered image with Adaptive Window Size.

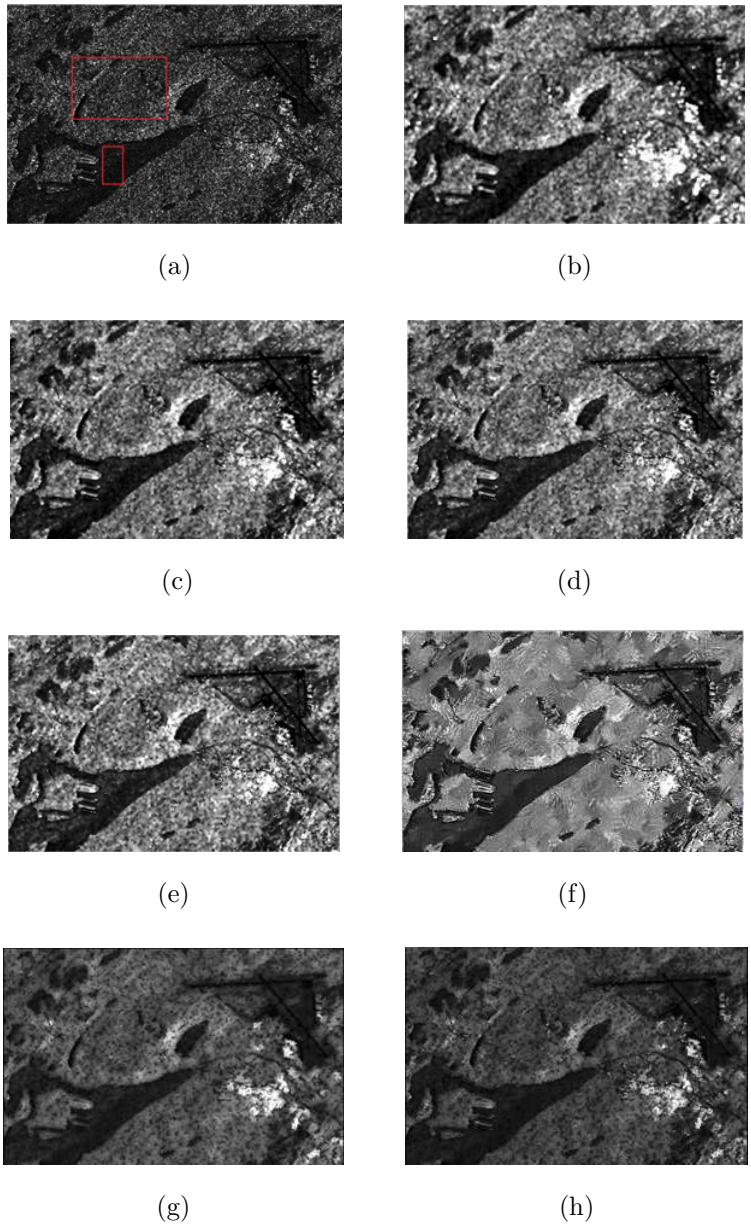

Figure 3.8: St. John's: a) Original one-look HH intensity image. The rectangle on the top and the bottom of the image show the regions used for computation of Coefficient of Variation and ENL, respectively, b) The 5×5 average filtered image, c) The 5×5 MMSE filtered image, d) The 5×5 enhanced Lee filtered image, e) The 5×5 Gamma filtered image, f) PPB filtered image with hw=10, hd=3, and 4 iterations, g) Average filtered image with Adaptive Window Size, h) MMSE filtered image with Adaptive Window Size.

filtering window size for a pixel located in a homogeneous and a heterogeneous area from the San Francisco image, respectively. The homogeneous region was selected from the ocean on the top right of Figure 3.7 and the heterogeneous area was chosen from the urban area on the bottom right of Figure 3.7. Theoretically, as proven in Section 3.4.1, a large window size is needed in a large, homogeneous area. This is the case in the represented homogeneous region in which the minimum standard deviation corresponds to the largest possible window size. On the other hand, in a heterogeneous area a small window size suffices. This fact was realized in the representative heterogeneous area in which the minimum standard deviation corresponds to the smallest possible window size. It should be noted that these examples are just two extreme instances amongst many other possible cases.

Assessment of the Results An ideal speckle filter should reduce the amount of speckle in homogeneous regions while it preserving the details of the image in heterogeneous areas. Moreover, it should not introduce any bias into the image after filtering. To evaluate the performance of the image from the various mentioned aspects, therefore, computation of some metrics is necessary.

For the assessment of the performance of the filter in homogeneous regions, the common measure for estimation of speckle level in the image, namely Equivalent Number of Looks (ENL) was selected. Number of looks is an appropriate measure for estimating the amount of speckle in the image, which is proportional to the speckle standard deviation to mean ratio [1]. For an intensity image, the ENL is defined as below [1]:

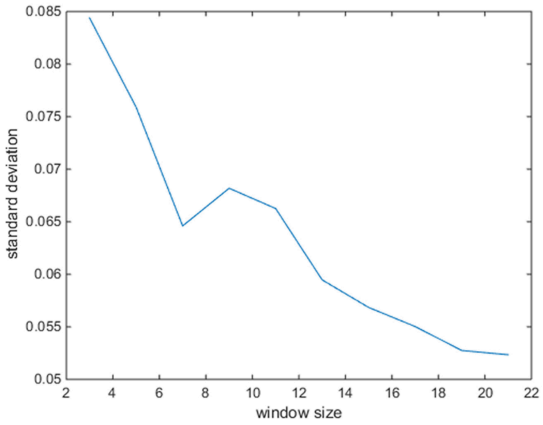

(a)

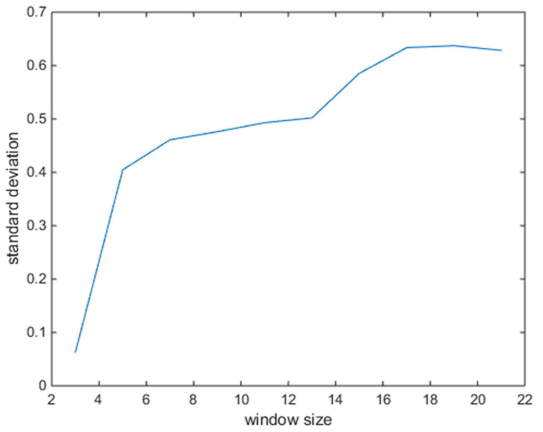

(b)

Figure 3.9: The variation of standard deviation with the change of the filtering window size. a) A homogeneous pixel, and b) A heterogeneous pixel.

Table 3.2: Various metrics for evaluation and comparison of the performance of the proposed speckle filters on real SAR images. $E\{r\}$ and $\sigma\{r\}$ show the mean and standard deviation of the ratio image, respectively.

Image	San Francisco				St. John's			
	ENL	$C_f(C_{\hat{f}})$	$E\{r\}$	$\sigma\{r\}$	ENL	$C_f(C_{\hat{f}})$	$E\{r\}$	$\sigma\{r\}$
Original Image	0.9233	2.6284	1	1	0.8919	0.8908	1	1
Average Filter	11.2384	1.7112	0.9663	0.9564	10.4493	0.7713	0.9653	0.9563
MMSE Filter	7.2548	2.8251	0.9100	0.7612	7.0836	0.9611	0.9086	0.7637
Enhanced Lee Filter	6.0499	3.7046	0.9360	0.7528	5.7243	1.0963	0.9317	0.7572
Gamma filter	6.8299	4.0011	1.0051	0.8108	5.7897	1.1009	1.0062	0.8079
PPB filter	6.9235	2.4647	0.6149	0.5231	5.7930	0.7014	0.7760	1.5383
Average Filter with Adaptive Window Size	10.4822	1.003	1.1394	1.5280	10.2089	0.7065	1.1356	1.4085
MMSE Filter with Adaptive Window Size	9.3041	2.7543	1.0037	0.9078	9.3788	0.8479	1.0152	0.8793

$$ENL = \frac{(mean)^2}{variance} \tag{3.15}$$

calculated over a large, homogenous area. A high value for ENL shows that speckle was suppressed effectively. It should be noted that the value of ENL, estimated by Equation 3.15 is usually less than the actual number of looks as a result of spatial correlation [1].

For the images available for this paper, ENL was calculated over the ocean in the top right of the San Francisco image (Figure 3.7) and over the large lake in the St. John's image (Figure 3.8). The results are shown in Table 3.2. As can be viewed in Table 3.2, the value of estimated ENL for both original images is less than but close to 1, as expected. The average filtered images have the highest value of ENL over all filtered images which shows the relatively effective suppression of speckle. The MMSE, enhanced Lee, Gamma, and PPB filters have a lower ENL which indicates the presence of speckle remaining in homogeneous parts of the images. By comparison, the Average Filter with Adaptive Window Size reduced speckle almost as much as the average filter; and the MMSE filter with Adaptive Window Size has a slightly smaller ENL, while this value is still higher than the corresponding values for the MMSE, enhanced Lee and Gamma filters.

For estimating the level of texture preservation in heterogeneous areas, a comparison can be made between the coefficient of variation computed over the despeckled image, namely $C_{\hat{f}}$, with its corresponding theoretical value, C_f, as mentioned in [19]. It can be concluded that loss of radiometric information leads to $C_f < C_{\hat{f}}$ while injection of impairments can yield $C_f > C_{\hat{f}}$ [32]. C_f and $C_{\hat{f}}$ are defined as:

$$C_f = \sqrt{\frac{C_g^2 - C_u^2}{1 + C_u^2}} \tag{3.16}$$

$$C_{\hat{f}} = \frac{Var[\hat{f}]}{E[\hat{f}]} \tag{3.17}$$

where C_g and C_u are the coefficient of variation of the noisy image and speckle noise, respectively, and $\hat{f}$ is the de-speckled image [19]. C_f for the original image and $C_{\hat{f}}$ for all filtered images have been computed over a heterogeneous area in both San Francisco (Figure 3.7) and St. John's (Figure 3.8) images and the results are depicted in Table 3.2. As can be observed, average filter poorly preserved the textural information in the images from both areas. MMSE, Enhanced Lee and Gamma filters have larger coefficients of variation in comparison with the original image which suggests that these filters introduced some impairment to the original image. The PPB filter yielded a slightly lower coefficient of variation with respect to the original image, which signifies a slight blurring in texture. Average Filter with Adaptive Window Size resulted in a significantly lower coefficient of variation, which implies that this filter performs poorly in maintaining textural patterns. MMSE filter with Adaptive Window Size, however, has the closest coefficient of variation to the original image in both areas, which shows that this filter had the best performance in texture preservation amongst all examined speckle filters.

Another useful measure for evaluating the overall performance of a speckle filter is the ratio image which is defined as:

$$r(n) = \frac{g(n)}{\hat{f}(n)} \tag{3.18}$$

where $g(n)$ is the noisy and $\hat{f}(n)$ is the despeckled image [33]. An ideal speckle filter yields a purely random ratio image while a poor speckle filter causes some patterns to be visible in the image [32]. The mean and standard deviation of the ratio image should be as close as possible to the theoretical values of speckle statistics [32]. Both of these values are 1 for a single-look image [41].

Ratio images resulting from all filtered images for both the San Francisco and St. John's areas are illustrated in Figure 3.10 and 3.11, respectively. Over both areas, some structures are visible in the enhanced Lee, Gamma and PPB filters, while the ratio images resulting from the Average filter with Adaptive Window Size and the MMSE filter with Adaptive Window Size have an almost random pattern. For a more accurate comparison, however, some numerical metrics are necessary.

The statistics were computed for the ratio image of all filtered images over both areas and the results are illustrated in Table 3.2. The mean and standard deviation of the ratio image resulted from the average filter is close to 1 which illustrates an unbiased performance. The value of the ratio image's mean for MMSE, Enhanced Lee and Gamma filters is close to 1. However, standard deviation of the ratio image of these filters differs significantly from the expected theoretical value. This is also true for the mean and standard deviation of the ratio image resulting from the PPB filter. The mean and standard deviation of the ratio image resulted from the Average Filter with Adaptive window size have a considerable difference with 1 which suggests that the filtering process introduces some bias into the image. The statistics computed from the ratio image of MMSE filter with Adaptive Window Size, however, have almost the closest values to 1, which shows that this filter introduces a small amount of bias to the image after filtering.

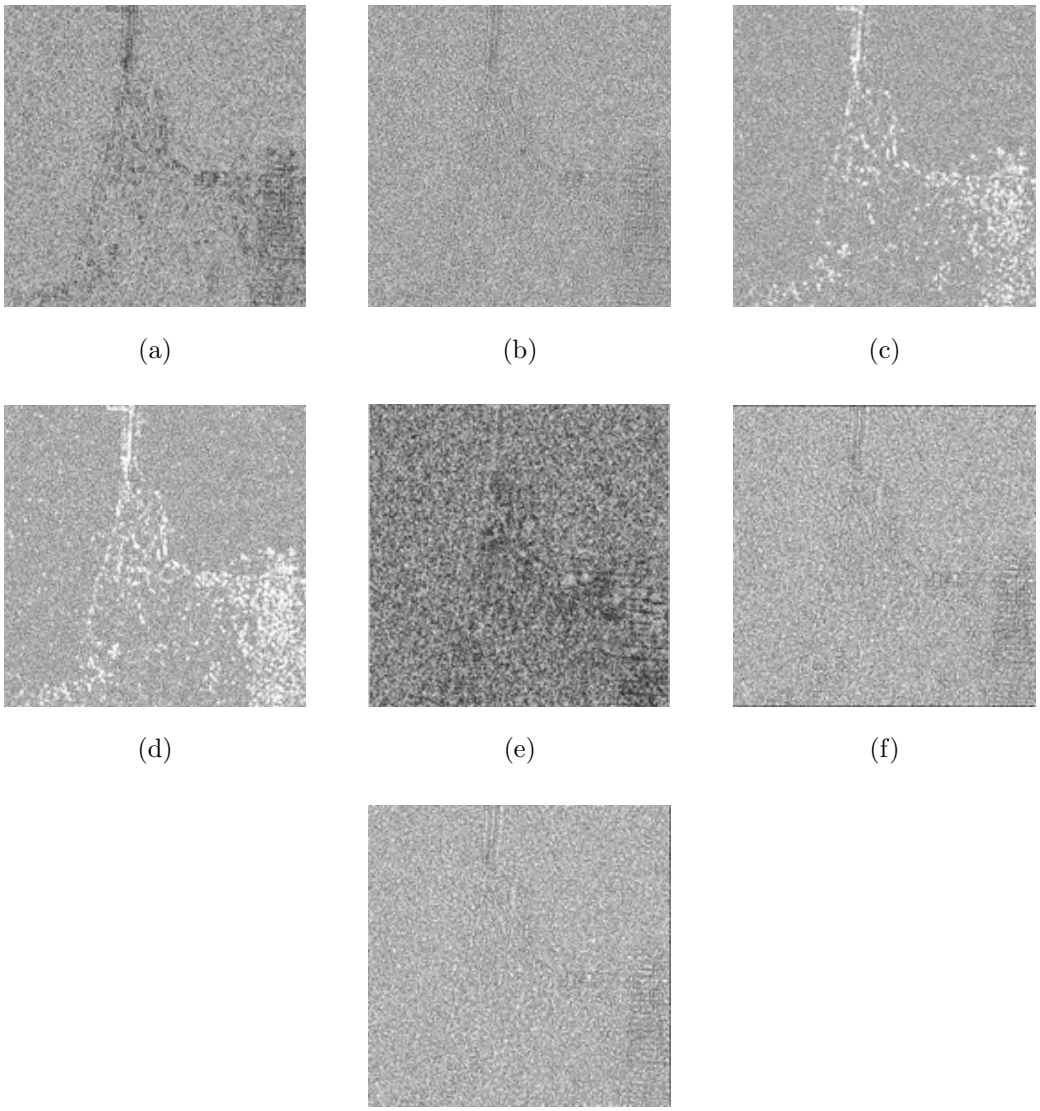

Figure 3.10: San Francisco: Ratio images resulted from: a) The 5×5 average filtered image, b) The 5×5 MMSE filtered image, c) The 5×5 enhanced Lee filtered image, d) The 5×5 Gamma filtered image, e) PPB filtered image with hw=20, hd=5, and 1 iteration, f) Average filtered image with Adaptive Window Size, g) MMSE filtered image with Adaptive Window Size from the San Francisco image

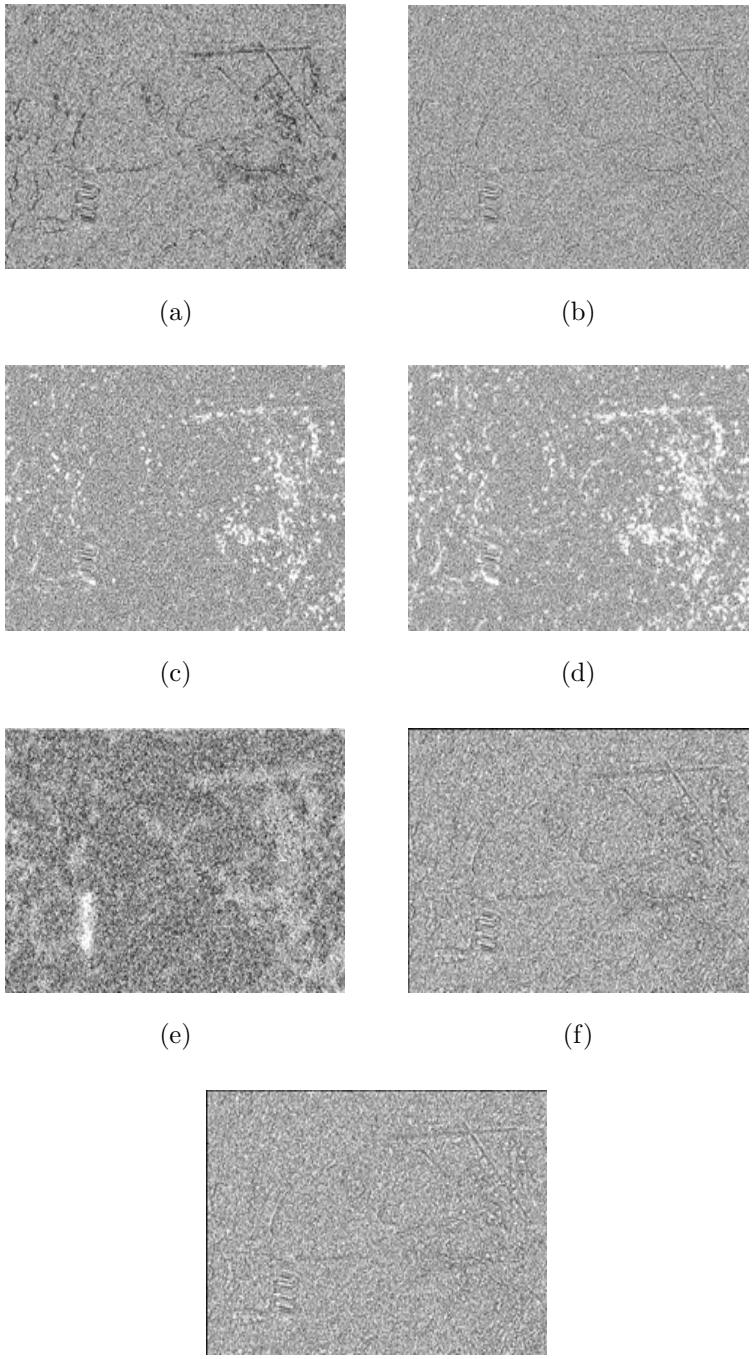

(a) (b) (c) (d) (e) (f) (g)

Figure 3.11: St. John's: Ratio images resulted from: a) The 5×5 average filtered image, b) The 5×5 MMSE filtered image, c) The 5×5 enhanced Lee filtered image, d) The 5×5 Gamma filtered image, e) PPB filtered image with hw=20, hd=5, and 1 iteration, f) Average filtered image with Adaptive Window Size, g) MMSE filtered image with Adaptive Window Size from the San Francisco image

Also, for estimating the degree of details preserved visually, a small subset from the urban area of both images is selected to be investigated more closely. These subsets are represented in Figure 3.12 and Figure 3.13.

The original San Francisco small sub-image illustrated in Figure 3.12 is affected by speckle and the buildings in the urban area seem disconnected. The average filter almost reduced speckle but the small objects are severely blurred. The MMSE filter balanced reducing speckle and retaining the details. However, the boundaries in the built-up area are smeared. If a window size larger than 5×5 was used, this effect would be more serious. The Enhanced Lee filter blurred the building boundaries in some parts, and disconnected them in other parts. The Gamma filter has filtered the image unevenly and the different parts of the urban area are either blurred or speckled. The PPB filter reduced speckle with slight overfiltering in urban areas. The Average Filter with Adaptive Window Size successfully maintained the shape of the buildings and reduced speckle, except for some objects which have been overly filtered. Finally, the MMSE filter with Adaptive Window Size has the best performance, preserving the shapes in Figure 12 as well and reducing speckle effectively.

The small sub-image from St. John's shows similar results. The urban area is severely affected by speckle in the original image in such a way that this part can hardly be discerned visually; the average filter destroyed the details. The urban area can be better distinguished from other parts in the images filtered by MMSE, enhanced Lee and Gamma filters, but speckle and isolated points are still present. The PPB filter successfully preserved the details, but a few subtle features are lost. Although the Average Filter with Adaptive Window Size caused slight blurring, it yielded a clear image for the urban area and reduced speckle evenly throughout this

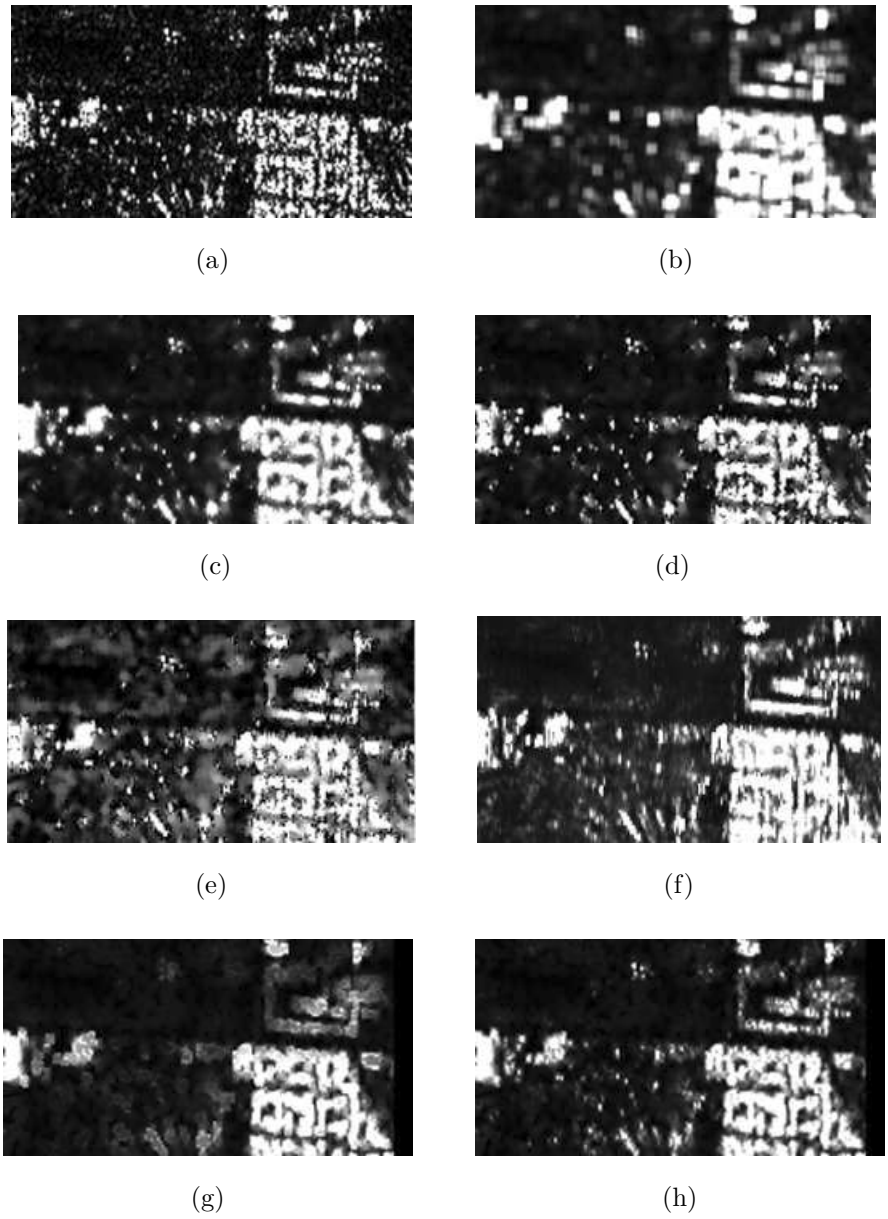

Figure 3.12: A small subset of the San Francisco image: a) Original one-look HH intensity image, b) The 5×5 average filtered image, c) The 5×5 MMSE filtered image, d) The 5×5 enhanced Lee filtered image, e) The 5×5 Gamma filtered image, f) PPB filtered image with hw=20, hd=5, and 1 iteration, g) Average filtered image with Adaptive Window Size, and h) MMSE filtered image with Adaptive Window Size highlighting urban areas from the San Francisco image.

region. Finally, the MMSE filter with adaptive window size compensated for the overly filtered parts in the Average filtered image with Adaptive Window Size, offering an efficiently speckle reduced image.

3.6.2 Polarimetric Case

3.6.2.1 Simulated PolSAR image

In order to test the performance of the proposed method for polarimetric SAR data, two PolSAR images without and with speckle (Figure 3.14, a and b) were simulated using the Monte Carlo simulation explained in [1]. First, for a covariance matrix, $C^{\frac{1}{2}}$ was generated such that:

$$C^{\frac{1}{2}}(C^{\frac{1}{2}})^{*T} = C \tag{3.19}$$

where $*T$ denotes the conjugate transpose. Then, a complex vector, $\underline{v}$, is simulated which has a normal distribution with zero mean and an identity covariance matrix. Then, the single-look vector $\underline{u}$ can be obtained using the following equation:

$$\underline{u} = C^{\frac{1}{2}}\underline{v} \tag{3.20}$$

Figure 3.14 illustrates the result of applying the proposed polarimetric filters to two simulated PolSAR images. For the sake of comparison, the results of applying the average polarimetric filter and the Lee PolSAR filter [25] on both images are also shown in Figure 3.14 , c and d, respectively. As can be observed, the average polarimetric filter blurred the boundaries. Moreover, the Lee PolSAR filter failed to completely remove speckle, and left some bright point in the image. The two

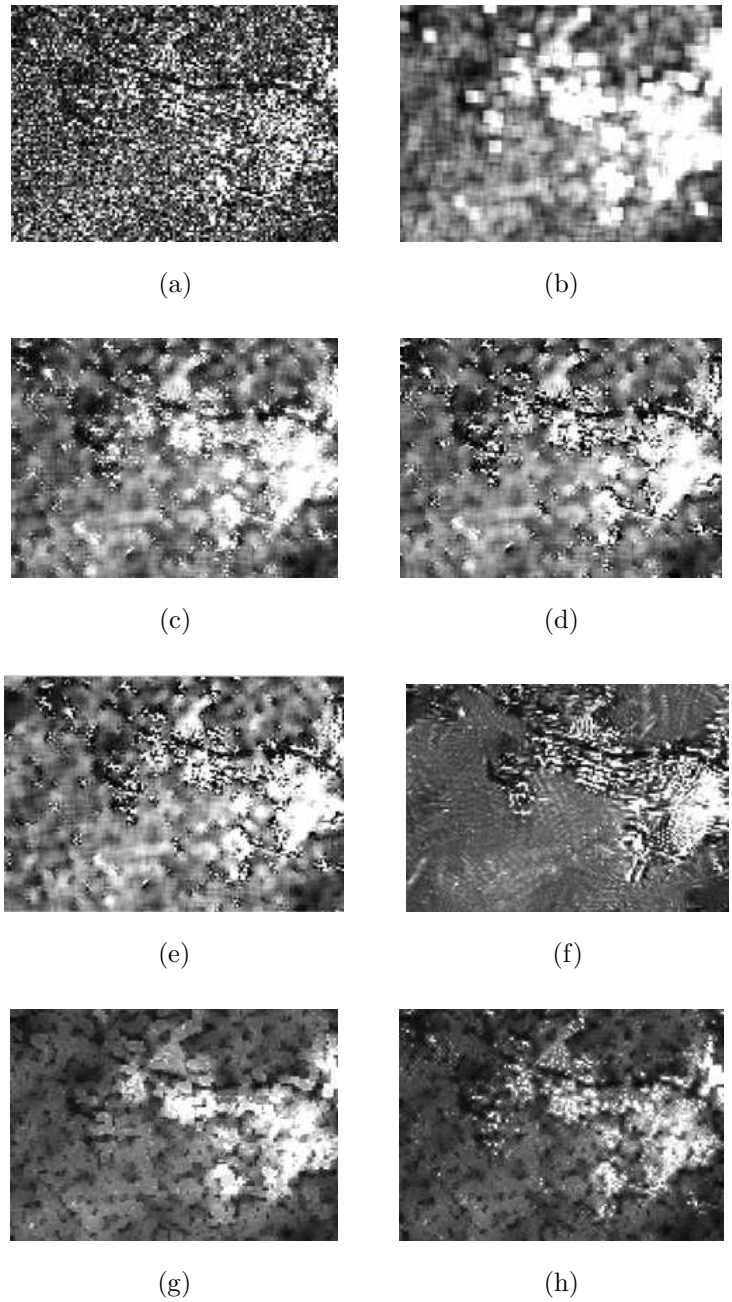

Figure 3.13: A small subset of the St. John's image: a) Original one-look HH intensity image, b) The 5×5 average filtered image, c) The 5×5 MMSE filtered image, d) The 5×5 enhanced Lee filtered image, e) The 5×5 Gamma filtered image, f) PPB filtered image with hw=20, hd=5, and 1 iteration, g) Average filtered image with Adaptive Window Size, h) MMSE filtered image with Adaptive Window Size highlighting urban areas from the San Francisco image.

proposed methods, however, suppressed speckle more effectively, and maintained the boundaries successfully.

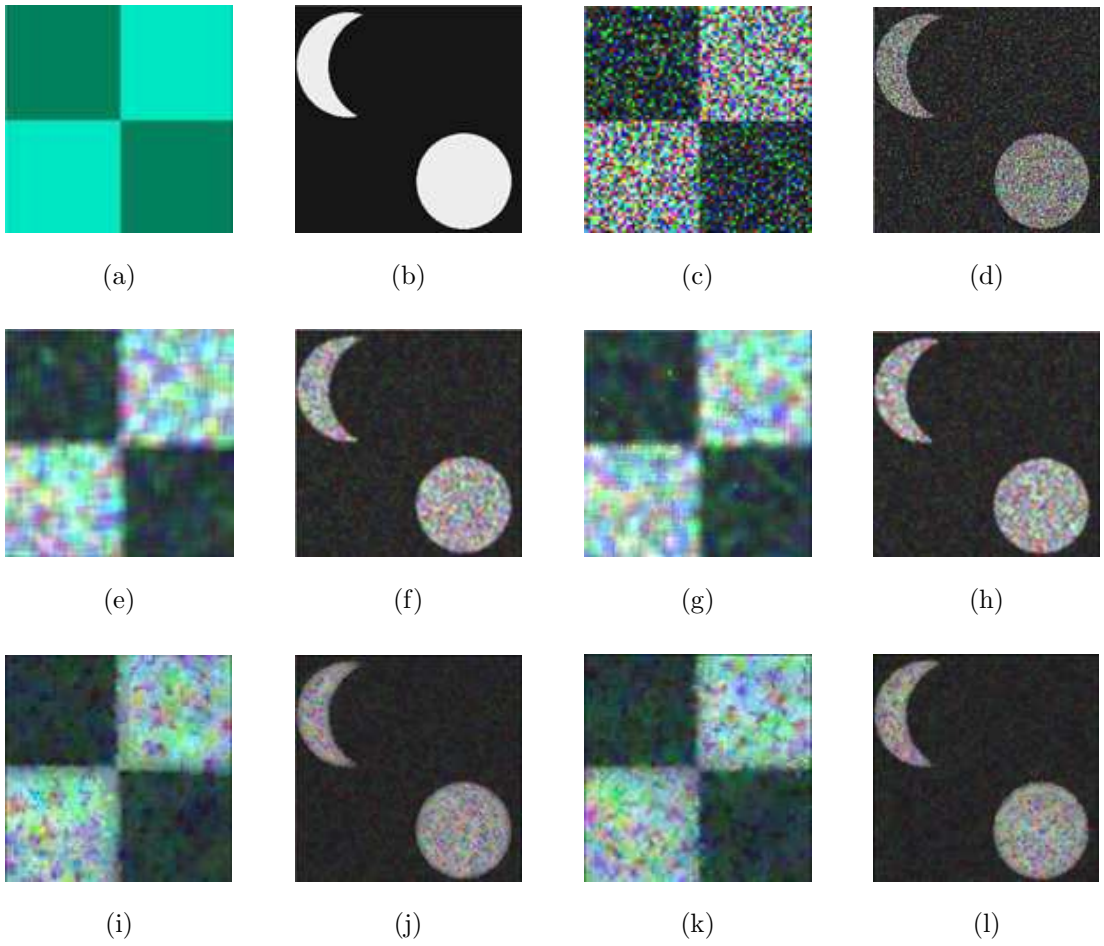

Figure 3.14: Polarimetric simulated SAR images: (a-b) The ground-truth images, (c-d) The original polarimetric images, (e-f) The 5×5 average filtered images, (g-h) Images filtered with 5×5 refined PolSAR filter, (i-j) Average filtered images with Adaptive Window Size, and (k-l) PolSAR filtered images with Adaptive Window Size.

3.6.2.2 Real PolSAR image

The proposed filtering algorithms for multi-polarized images, namely average filtering and Polarimetric filtering with Adaptive Window Size, were implemented on both full-polarimetric RADARSAT-2 images. For comparison, typical average filtering and the Lee PolSAR filter [25], as well as more advanced methods, namely Lopez [42] and Intensity Driven Adaptive Neighbourhood (IDAN) [26] filters, were applied on the image. The results for the San Francisco image are depicted in Figure 3.15. A Google Earth^{TM} snapshot for the San Francisco region was included in Figure 3.15 for a closer visual investigation. The original SAR image is represented in false color composite, having $|S_{hh}|^2$ as the red, $|S_{hv}|^2$ as the green and $|S_{vv}|^2$ as the blue channel which is clearly affected by speckle. The average filter, although reducing speckle, caused severe blurring in the image. The refined PolSAR filter shows significant improvement, but small details, for example in the urban area in the bottom right of the image, are smeared. The Lopez filter efficiently filtered the image, but some occasional brighter points are visible in the image and the urban area is slightly blurred. The IDAN filter has effectively reduced speckle while maintaining the details, which shows the value of the adaptive neighbourhood. The Average Filter with Adaptive Window Size also retained the details, suppressing speckle effectively with minimal over-filtering of some parts, although these parts cannot be easily distinguished. Finally, PolSAR filter with Adaptive Window Size performed very well, by both reducing speckle and preserving the details.

Analogous results were achieved for the St. John's full-polarimetric image, as represented in Figure 3.16. Aerial images have also been used for assistance in visual

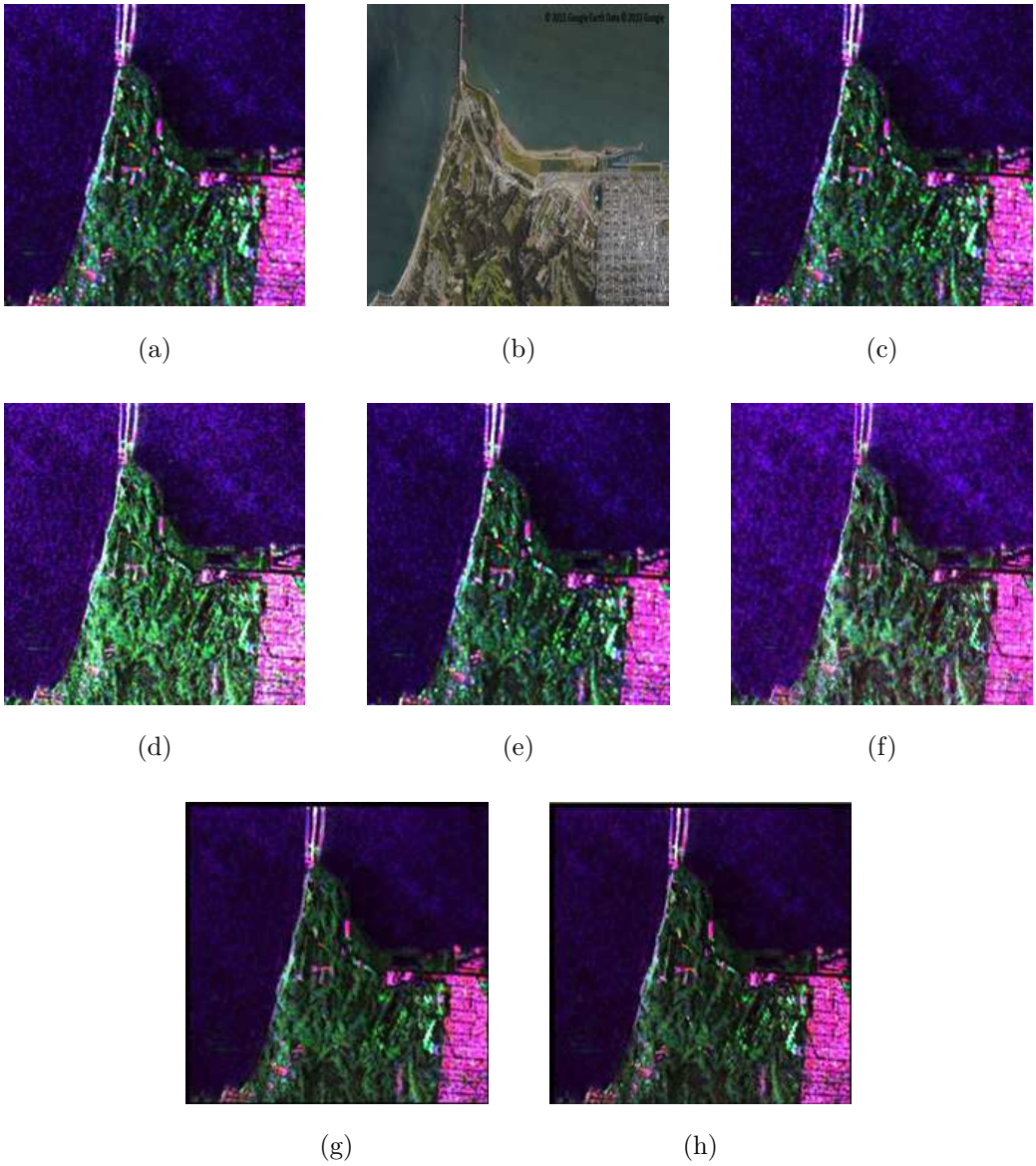

(a) (b) (c)

(d) (e) (f)

(g) (h)

Figure 3.15: San Francisco: a) Original polarimetric image, b) Snapshot of the study area from Google Earth™, c) The 5×5 average filtered image, d) Image filtered with 5×5 refined PolSAR filter, e) The 5×5 Lopez filtered image, f) IDAN filtered image with window size row of 50, g) Average filtering with Adaptive Window Size, h) PolSAR filtering with Adaptive Window Size.

inspection. The polarimetric average filter blurred the details. The refined PolSAR and Lopez filters made a considerable improvement, but the details have been slightly over-filtered, and an amount of speckle is still remaining. A non-speckled, clear image indicates that IDAN filter performed effectively. The polarimetric average filter with Adaptive Window Size offered a smooth part in terms of homogeneous regions, and maintained the details of subtle points. The PolSAR filter with Adaptive Window Size outputted almost the same image, preserving slightly more details in the urban part.

3.7 Discussion

It was observed in previous sections that the proposed adaptive window approach works well with single-band and multi-polarized SAR data. This method also can be applied to partially-polarized data, using available real and imaginary channels for estimating the best window size, and then applying the result to the intensity image.

A disadvantage of the proposed method is its computational complexity. In a typical filtering process the filtering size is manually selected which causes the filter to have a low computational complexity, but at the expense of either losing some detail, or leaving speckle in the image. The proposed method looks for the best window size for each pixel, and then applies the filter on it. For improving the computational complexity of the method, narrowing the range of window sizes for filtering each pixel based on a heterogeneity measure is suggested.

Some practical considerations are necessary when implementing the proposed algorithm. In the range of window sizes which are selected for filtering the real and

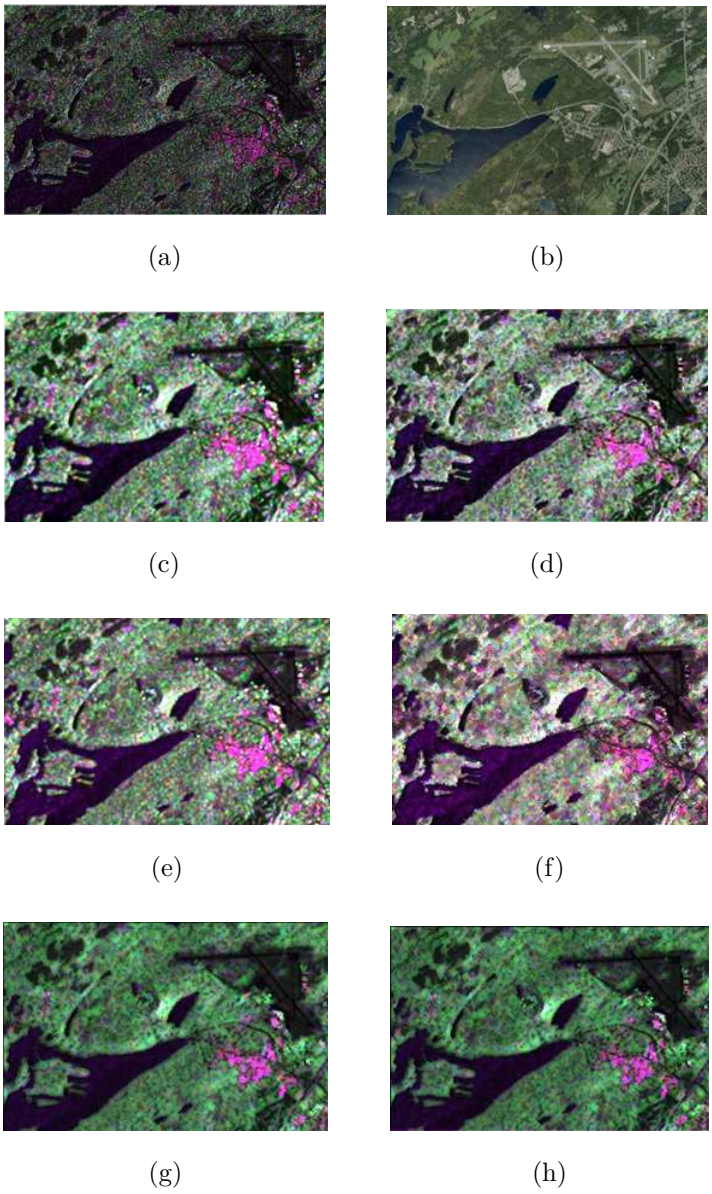

Figure 3.16: St. John's: a) Original polarimetric image, b) Snapshot of the study area from Google Earth^{TM}, c) The 5×5 average filtered image, d) Image filtered with 5×5 refined PolSAR filter, e) The 5×5 Lopez filtered image, f) IDAN filtered image with window size row of 50, g) Average filtering with Adaptive Window Size, h) PolSAR filtering with Adaptive Window Size.

imaginary images, the minimum window size is more important than the maximum one. If the minimum window size is too large, some details in the image might be blurred. Thus care must be taken in selecting the minimal window size; the most conservative choice for that is 3×3.

Computing the optimal window size using both real and imaginary images helps to estimate the best window size more accurately, but using one of them suffices. This is also true for the polarimetric filter, where all real and imaginary images are used for estimating the most appropriate filtering size. Although the three channels have different features, the definition of object is the same in all of them, although they might appear diversely in each band. Accordingly, optimal window size for each pixel must be the same for all channels.

3.8 Conclusion

Using a single fixed size rectangular window is not effective for speckle filtering of SAR images, owing to the fact that objects with different sizes need different filtering windows. To address this issue, the paper presents a novel technique for filtering with Adaptive Window Size. The method applies windows with changing sizes throughout the image based on local information (i.e. Standard Deviation) computed from neighbouring pixels. To find an optimal window size for each pixel, windows with various sizes are applied to real and imaginary SAR images separately, and the window with minimum Standard Deviation is chosen as the optimum window size for filtering. It was demonstrated that the window which yields the minimal standard deviation for each pixel over the whole range of sizes has the optimal size for filtering that pixel.

The method was applied to single-look intensity data but it can be applied to multilook and amplitude images as well. The filter has been proposed in single-band and polarimetric versions, and average and MMSE filtering methods with Adaptive Window Size have been provided in both cases. The proposed methods outperform their fixed-size counterparts both in single-band and polarimetric versions. This approach can preserve the details of the image while suppressing speckle effectively. The computational complexity of the proposed filters is greater than their fixed-size counterparts because the suggested algorithms look for the appropriate window size for each pixel, while in the typical filters the window size is fixed. The computational complexity, however, may be reduced. Finally, adjusting other filters so that they may be applied with adaptive window size is a valuable area of future study.

Acknowledgement

This project was undertaken with the financial support of the Government of Canada through the federal Department of Environment and Climate Change, and the Research & Development Corporation of Newfoundland and Labrador. The SAR imagery was provided by the Canada Center for Mapping and Earth Observation and Environment and Climate Change Canada. The authors thank these organizations for the generous financial supports and providing such valuable datasets.

Bibliography

[1] Jong-Sen Lee and Eric Pottier. *Polarimetric radar imaging: from basics to applications*. CRC press, 2009.

[2] Jong-Sen Lee. Digital image enhancement and noise filtering by use of local statistics. *IEEE transactions on pattern analysis and machine intelligence*, (2):165–168, 1980.

[3] Jong-Sen Lee. Speckle analysis and smoothing of synthetic aperture radar images. *Computer graphics and image processing*, 17(1):24–32, 1981.

[4] Jong-Sen Lee. Digital image smoothing and the sigma filter. *Computer vision, graphics, and image processing*, 24(2):255–269, 1983.

[5] Jong-Sen Lee. A simple speckle smoothing algorithm for synthetic aperture radar images. *IEEE Transactions on Systems, Man, and Cybernetics*, (1):85–89, 1983.

[6] Jong-Sen Lee, Jen-Hung Wen, Thomas L Ainsworth, Kun-Shan Chen, and Abel J Chen. Improved sigma filter for speckle filtering of SAR imagery. *IEEE Transactions on Geoscience and Remote Sensing*, 47(1):202–213, 2009.

[7] Victor S Frost, Josephine Abbott Stiles, K Sam Shanmugan, and Julian C Holtzman. A model for radar images and its application to adaptive digital filtering of multiplicative noise. *IEEE Transactions on pattern analysis and machine intelligence*, (2):157–166, 1982.

[8] VS Frost, JA Stiles, K Sam Shanmugam, JC Holtzman, and SA Smith. An adaptive filter for smoothing noisy radar images. *Proceedings of the IEEE*, 69(1):133–135, 1981.

[9] Darwin T Kuan, Alexander A Sawchuk, Timothy C Strand, and Pierre Chavel. Adaptive noise smoothing filter for images with signal-dependent noise. *IEEE transactions on pattern analysis and machine intelligence*, (2):165–177, 1985.

[10] Armand Lopes, Ridha Touzi, and E Nezry. Adaptive speckle filters and scene heterogeneity. *IEEE transactions on Geoscience and Remote Sensing*, 28(6):992–1000, 1990.

[11] Armand Lopes, E Nezry, R Touzi, and H Laur. Structure detection and statistical adaptive speckle filtering in SAR images. *International Journal of Remote Sensing*, 14(9):1735–1758, 1993.

[12] J-M Park, Woo-Jin Song, and WA Pearlman. Speckle filtering of SAR images based on adaptive windowing. *IEE Proceedings-Vision, Image and Signal Processing*, 146(4):191–197, 1999.

[13] JM Nicolas, F Tupin, and H Maitre. Smoothing speckled SAR images by using maximum homogeneous region filters: An improved approach. In *Geoscience*

and Remote Sensing Symposium, 2001. IGARSS'01. IEEE 2001 International, volume 3, pages 1503–1505. IEEE, 2001.

[14] Mihai Datcu, Klaus Seidel, and Marc Walessa. Spatial information retrieval from remote-sensing images. i. information theoretical perspective. *IEEE transactions on geoscience and remote sensing*, 36(5):1431–1445, 1998.

[15] Marc Walessa and Mihai Datcu. Model-based despeckling and information extraction from SAR images. *IEEE Transactions on Geoscience and Remote Sensing*, 38(5):2258–2269, 2000.

[16] DARWINT Kuan, ALEXANDERA Sawchuk, TIMOTHYC Strand, and Pierre Chavel. Adaptive restoration of images with speckle. *IEEE Transactions on Acoustics, Speech, and Signal Processing*, 35(3):373–383, 1987.

[17] Jean M Durand, Bernard J Gimonet, and Jacqueline R Perbos. Sar data filtering for classification. *IEEE Transactions on Geoscience and Remote Sensing*, (5):629–637, 1987.

[18] Jong-Sen Lee, L Jurkevich, P Dewaele, Pl Wambacq, and A Oosterlinck. Speckle filtering of synthetic aperture radar images: A review. *Remote Sensing Reviews*, 8(4):313–340, 1994.

[19] Ridha Touzi. A review of speckle filtering in the context of estimation theory. *IEEE Transactions on Geoscience and Remote Sensing*, 40(11):2392–2404, 2002.

[20] Leslie M Novak and Michael C Burl. Optimal speckle reduction in polarimetric SAR imagery. *IEEE Transactions on Aerospace and Electronic Systems*, 26(2):293–305, 1990.

[21] J-S Lee, Mitchell R Grunes, and Stephen A Mango. Speckle reduction in multipolarization, multifrequency SAR imagery. *IEEE Transactions on Geoscience and remote sensing*, 29(4):535–544, 1991.

[22] S Goze and A Lopes. A mmse speckle filter for full resolution SAR polarimetric data. *Journal of electromagnetic waves and applications*, 7(5):717–737, 1993.

[23] Jong-Sen Lee, Shane R Cloude, Konstantinos P Papathanassiou, Mitchell R Grunes, and Iain H Woodhouse. Speckle filtering and coherence estimation of polarimetric SAR interferometry data for forest applications. *IEEE Transactions on Geoscience and Remote Sensing*, 41(10):2254–2263, 2003.

[24] Jong-Sen Lee, Thomas L Ainsworth, Yanting Wang, and Kun-Shan Chen. Polarimetric SAR speckle filtering and the extended sigma filter. *IEEE Transactions on geoscience and remote sensing*, 53(3):1150–1160, 2015.

[25] Jong-Sen Lee, Mitchell R Grunes, and Gianfranco De Grandi. Polarimetric SAR speckle filtering and its implication for classification. *IEEE Transactions on Geoscience and remote sensing*, 37(5):2363–2373, 1999.

[26] Gabriel Vasile, Emmanuel Trouvé, Jong-Sen Lee, and Vasile Buzuloiu. Intensity-driven adaptive-neighborhood technique for polarimetric and interferometric SAR parameters estimation. *IEEE Transactions on Geoscience and Remote Sensing*, 44(6):1609–1621, 2006.

[27] Fengkai Lang, Jie Yang, and Deren Li. Adaptive-window polarimetric SAR image speckle filtering based on a homogeneity measurement. *IEEE Transactions on Geoscience and Remote Sensing*, 53(10):5435–5446, 2015.

[28] Leonardo Torres, Sidnei JS Sant'Anna, Corina da Costa Freitas, and Alejandro C Frery. Speckle reduction in polarimetric SAR imagery with stochastic distances and nonlocal means. *Pattern Recognition*, 47(1):141–157, 2014.

[29] Charles-Alban Deledalle, Florence Tupin, and Loïc Denis. A non-local approach for SAR and interferometric sar denoising. In *Geoscience and Remote Sensing Symposium (IGARSS), 2010 IEEE International*, pages 714–717. IEEE, 2010.

[30] Charles-Alban Deledalle, Loïc Denis, and Florence Tupin. Nl-insar: Nonlocal interferogram estimation. *IEEE Transactions on Geoscience and Remote Sensing*, 49(4):1441–1452, 2011.

[31] Jiong Chen, Yilun Chen, Wentao An, Yi Cui, and Jian Yang. Nonlocal filtering for polarimetric SAR data: A pretest approach. *IEEE Transactions on Geoscience and Remote Sensing*, 49(5):1744–1754, 2011.

[32] Fabrizio Argenti, Alessandro Lapini, Tiziano Bianchi, and Luciano Alparone. A tutorial on speckle reduction in synthetic aperture radar images. *IEEE Geoscience and remote sensing magazine*, 1(3):6–35, 2013.

[33] Chris Oliver and Shaun Quegan. *Understanding synthetic aperture radar images*. SciTech Publishing, 2004.

[34] Aleksandr Petrovich Korostelev and Olga Korosteleva. *Mathematical statistics: asymptotic Minimax theory*, volume 119. American Mathematical Soc., 2011.

[35] Charles Therrien and Murali Tummala. *Probability and random processes for electrical and computer engineers*. CRC press, 2011.

[36] Jong-Sen Lee. Speckle suppression and analysis for synthetic aperture radar images. *Optical engineering*, 25(5):255636, 1986.

[37] FM Henderson, AJ Lewis, and RA Reyerson. Polarimetry in radar remote sensing: Basic and applied concepts. In *Principles and Applications of Imaging Radar*, volume 2. Wiley, 1998.

[38] Jong-Sen Lee. Refined filtering of image noise using local statistics. *Computer graphics and image processing*, 15(4):380–389, 1981.

[39] Zhou Wang, Alan C Bovik, Hamid R Sheikh, and Eero P Simoncelli. Image quality assessment: from error visibility to structural similarity. *IEEE transactions on image processing*, 13(4):600–612, 2004.

[40] Charles-Alban Deledalle, Loïc Denis, and Florence Tupin. Iterative weighted maximum likelihood denoising with probabilistic patch-based weights. *IEEE Transactions on Image Processing*, 18(12):2661–2672, 2009.

[41] Stian Solbo and Torbjørn Eltoft. A stationary wavelet-domain wiener filter for correlated speckle. *IEEE Transactions on Geoscience and Remote Sensing*, 46(4):1219–1230, 2008.

[42] Carlos Lopez-Martinez and Xavier Fabregas. Model-based polarimetric SAR speckle filter. *IEEE Transactions on Geoscience and Remote Sensing*, 46(11):3894–3907, 2008.

Chapter 4

Object-based Classification of Wetlands in Newfoundland and Labrador Using Multi-Temporal PolSAR Data

4.1 Preface

In this chapter, a multi-temporal object-based classification of wetlands using PolSAR data was presented in which an alternative approach for segmentation of SAR images was introduced. The paper resulted from this chapter has been published in the *Canadian Journal of Remote Sensing*.

4.2 Abstract

Despite the fact that vast portions of Newfoundland and Labrador (NL) are covered by wetlands, to date there is no provincial inventory of wetlands in the province. In this study, we analyzed multi-temporal SAR data for wetland classification at four pilot sites across NL. Object Based Image Analysis (OBIA) using a segmentation method based on optical data (RapidEye image in this study), and well-adjusted to SAR images, was first compared to pixel-based classification. Next, multi-date object-based wetland maps using the random forest classifier were compared to single-date classification. Finally, ratio and textural features were evaluated for wetland classification. The results showed that the OBIA method demonstrated superior results, and the multi-date classification performed better than single-date classification with accuracies ranging from 75 to 95 percent. The multi-date results showed that the images acquired in August are the most appropriate for classifying wetlands, while the October images are of less value. Also, covariance matrix is a valuable feature set for wetland mapping. Besides, ratio and textural features slightly increase the overall accuracy when the initial overall accuracy is relatively low. It can be concluded that multi-date SAR classification, with the proposed segmentation method, shows great potential as a method for mapping wetlands and can be applied throughout the province.

4.3 Introduction

Wetlands have been defined as land that is saturated with water long enough to promote wetland or aquatic processes as indicated by poorly drained soils, hydrophytic vegetation and various kinds of biological activity which are adapted to a wet environment [1]. Wetlands are valuable natural resources and provide many ecosystem services such as collecting and reserving runoff water, protecting soil from erosion, purifying water and providing natural habitats for many animals and plants [2]. Currently, wetlands cover approximately 14 percent of Canada [3]. However, the development of agriculture, urbanization, industry, and recreation has resulted in alteration of wetlands to other land uses [2]. For example, only about 30% of wetlands in southern Ontario and 25% of wetlands in Manitoba remain in existence [3]. Wetland destruction results in several environmental issues. For instance, it causes the natural habitat of many animals and plants to be destroyed, reduces water supply and water storage within a wetland, and causes soil erosion [4]. Therefore, it is crucially important to monitor the existence and health of wetlands.

Newfoundland and Labrador (NL) is no exception in this regard. Wetlands in NL are important habitat for waterfowl, Canada geese, American black ducks and green-winged teal [5]. Unfortunately, however, upwards of 85 percent of wetlands in the coastal zones of Atlantic Canada have been altered or destroyed [6, 7]. Currently, NL is the only province in Atlantic that lacks a provincial wetland map [8, 9]. Also, the maps for New Brunswick and Nova Scotia are not accurate [10, 11]. Although some data has been collected through Environmental Impact Statements (EIS), they are often out of date or not publicly available and hence many researchers have noted

the need for a detailed, up-to-date provincial wetland inventory system [12].

Synthetic Aperture RADAR (SAR) images have been successfully used for wetland mapping [13–15]. SAR images have several features which make them ideal for wetland mapping. They can be acquired independent of weather conditions, and thus are not affected by cloud coverage, a particularly important feature in a place like NL, where cloud cover is frequent. Unlike optical images, SAR images can also penetrate through vegetation. This is especially useful for wetland classification as wetlands are characterized by flooded vegetation. Moreover, textural information in SAR data is an asset for classification purposes.

[13] evaluated the potential of RADARSAT-1 texture information for wetland classification. In that study, texture information improved the classification accuracy slightly. [16], after observing the high potential of RADARSAT-2 images for forest type discrimination, investigated the capability of RADARSAT-2 images for wetland mapping. They used Convair-580 full-polarimetric C-band SAR data, acquired in 1995, for this purpose. The authors noted the α parameter in Cloude and Pottier decomposition [17] was not sufficient for wetland discrimination, and thus the Touzi decomposition [18] parameters were developed instead. These parameters showed high potential for wetland mapping and even proved useful for distinguishing bogs from fens, both peatlands which, though different, share many similar ecological charcteristics [7]. In fact, the vegetation within bog and fen are very similar to each other. However, bog's only source of water is precipitation, while fen has other water sources as well. In [14], separability analysis and maximum likelihood classification were exploited for wetland classification using Convair-580 images. As expected, it was concluded that polarimetric data are more informative than dual or single po-

larization data for wetland mapping, and that polarization ratios are adequate for discrimination between flooded and non-flooded areas. A more comprehensive study was carried out by [15], who evaluated the capability of Touzi decomposition for wetland mapping. Nine RADARSAT-2 images were used from which polarimetric features were extracted and evaluated for wetland mapping. Then, a decision tree was adopted for the classification. Desirable results were obtained and the authors concluded that SAR data hold great promise for wetland mapping.

As wetlands demonstrate a high level of temporal variability, multi-date sampling is required to study them. For example, a study by [19], investigated full-polarimetric RADARSAT-2 time series to detect and locate the seasonal change of saturated areas in wetlands. The authors investigated the sensitivity of different polarimetric decomposition parameters towards the variation of the water-table in marsh-flooded areas. Shannon Entropy showed the strongest sensitivity to the changes. Then, this parameter was exploited for detection of marsh-flooded areas using a threshold method. In [20], statistical methods and a decision tree classifier were used to detect areas with a high degree of saturation using a time series of ENVISAT ASAR data. In [21], the time series of TerraSAR-X dual-polarized data was also used for classifying wetlands in Lac Bam of Africa. The authors pointed out that the accuracy of classification was significantly higher when multi-temporal data was used, especially because of the fact that the study area undergoes great fluctuations in water levels annually.

Object-based classification has proven useful for wetland mapping [22–26]. Object-Based Image Analysis (OBIA) is a classification method which is not based on individual pixels, but which considers neighbourhood information to form objects. Objects or segments are a group of homogeneous pixels whose homogeneity is based on mul-

tiple measures, e.g. spectral, texture and shape. As wetlands occur in various sizes and shapes, object-based classification is valuable for wetland mapping. [24] analyzed aerial imagery to delineate wetlands by applying OBIA and reported an overall accuracy of 89 percent. [23], analyzed RADARSAT-1 and Landsat images for mapping wetlands using different levels of segmentation. SAR and Optical images were segmented in various scales from large to fine and classified using membership function, and in each level, only a part of the image which needed a finer classification was segmented in a smaller scale. In [25], the authors used Advanced Spaceborne Thermal Emission and Reflection Radiometer (ASTER) images along with other types of datasets, including SAR images and Digital Elevation Model (DEM), to classify the wetlands of northern Brazilian Amazonia in an object-based manner. An accuracy of 88 percent was reported. Additionally, in [22] the authors combined RADAR images with medium resolution optical data to obtain wetland maps over a large area. Segmentation was applied to the images and the derived images were classified using an object oriented fuzzy method. Furthermore, the capability of RADAR texture information for improving the result of classification was examined. [26] also applied a decomposition to TerraSAR-X data. Then, the decomposition layers were segmented using the multiresolution algorithm. The authors achieved an accuracy higher than 85 percent for wetland classification.

The segmentation of imagery is the first step in object-based classification. So far, many segmentation methods have been proposed some of which are specifically applicable to SAR images. For example, [27] presented an algorithm for segmentation of SAR images based on nonlocal contour active model. Promising results were obtained for various SAR images. [28] attempted to segment SAR images in a two

phases by applying curvelet coefficient energy (KCE) and an unsupervised spectral regression (USR) method. [29] modified simple linear iterative clustering (SLIC) to segment SAR images. On the other hand, there are some segmentation methods which are most effective is applied on the optical images. The most common one is the multi-resolution algorithm which is a popular segmentation approach first proposed by [30]. In this method, pixels or existing image objects are consecutively merged until a homogeneity criterion, determined by the user as the scale parameter, is satisfied. This homogeneity criterion is a combination of spectral homogeneity and shape homogeneity, the contribution of each is determined by the user [31]. Higher values for scale parameters yield larger image objects [31]. Since SAR images are blemished with speckle, when applying segmentation methods specifically proposed for SAR imagery, sophisticated algorithm have to be applied. Also, when utilizing segmentation methods designed mainly for the optical imagery, most often results are not as accurate as desired. For that reason, in this paper, an alternative method is introduced to segment SAR images in which optical images are used for segmentation of SAR data. The details of this method are provided in the Method section.

In recent years, Random Forest (RF) [32] has supplanted conventional classifiers such as Maximum Likelihood (ML). RF classifier is an ensemble of regression trees each of which is generated using a random vector, which is sampled independently from the input vector. Each regression tree votes for a class for a given pixel/object, and finally the most popular class is assigned to that pixel/object [32]. Features from various sources with different ranges can be incorporated into RF. Moreover, the RF classifier has the least sensitivity to the size of training samples and is the least susceptible to noise [33]. Thus, RF is especially useful when insufficient training

data is available. Many researchers in recent years have applied the RF algorithm in wetland classification [33–35]. [35] applied the RF classifier to examine the potential of SAR polarimetric decompositions and LiDAR derivatives for mapping wetlands within Mer Bleue bog within southern Ontario. The authors remarked that RF is not only useful in wetland classification, but also has the potential to prioritize various features in terms of their role in classification accuracy. In [34], JERS L-band SAR imagery was used to produce a thematic map of wetlands using the RF algorithm. Different polarimetric combinations and several polarimetric decompositions were evaluated for wetland mapping. In [33], the performance of three different classifiers, namely ML, Classification and Regression Tree (CART) and RF were assessed for wetland classification in Sanjiang Plain of China. In this work, RF produced the highest accuracy.

The purpose of this study is to develop a wetland classification methodology for NL and evaluate multi-date RADARSAT-2 polarimetric C-band SAR images for object-based classification of four pilot sites using the RF classifier. This paper presents the details of the pilot sites and data sets in the next section, followed by the methodology, results and discussion sections. The paper ends with conclusions based on this study.

4.4 Study areas and Datasets

4.4.1 Study Areas

For the purpose of developing a methodology to map wetlands throughout the entire province of Newfoundland and Labrador, five pilot sites were selected (Figure

4.1). The Avalon, Grand Falls, Deer Lake, and Gros Morne pilot sites are all located on the island of Newfoundland, and Goose Bay is located in Labrador. The characteristics of the pilot sites are summarized in Table 4.1. The field data for one of the pilot sites (Grand Falls) were not available at the time of processing, and hence we performed our analyses on the other four pilot sites.

4.4.2 Field Data

The Canadian Wetland Classification System (CWCS) [7] was used for wetland classification in this research. The CWCS divides the wetlands of Canada into five main categories: Bog, Fen, Marsh, Swamp and Shallow Water. These classes are defined on the basis of floral, hydrological, pedological, and physiochemical characteristics. According to the CWCS National Wetlands Working Group (1997), the 5 classes are described as follows:

Bogs are peatlands (peat is poorly decomposed organic matter) that are ombrotrophic, meaning that a bog's only source of water is precipitation [7]. As a result, bogs are low in nutrients and are highly acidic, which influences the floral composition of these wetlands: Sphagnum Moss species and ericaceous shrubs are dominant and carnivorous plants are common [7]. *Fens*, like bogs, are peatlands. However, unlike bogs, fens receive water from multiple sources including precipitation, underground and surface water flow, which makes fens minerotrophic [7]. A fen's floral composition reflects the nutrient quality of its water sources, and thus may be considered rich (dominated by sedge, grass species and brown moss species) or poor, in which the floral composition is partly similar to bogs [36]. *Swamps* are wooded wetlands,

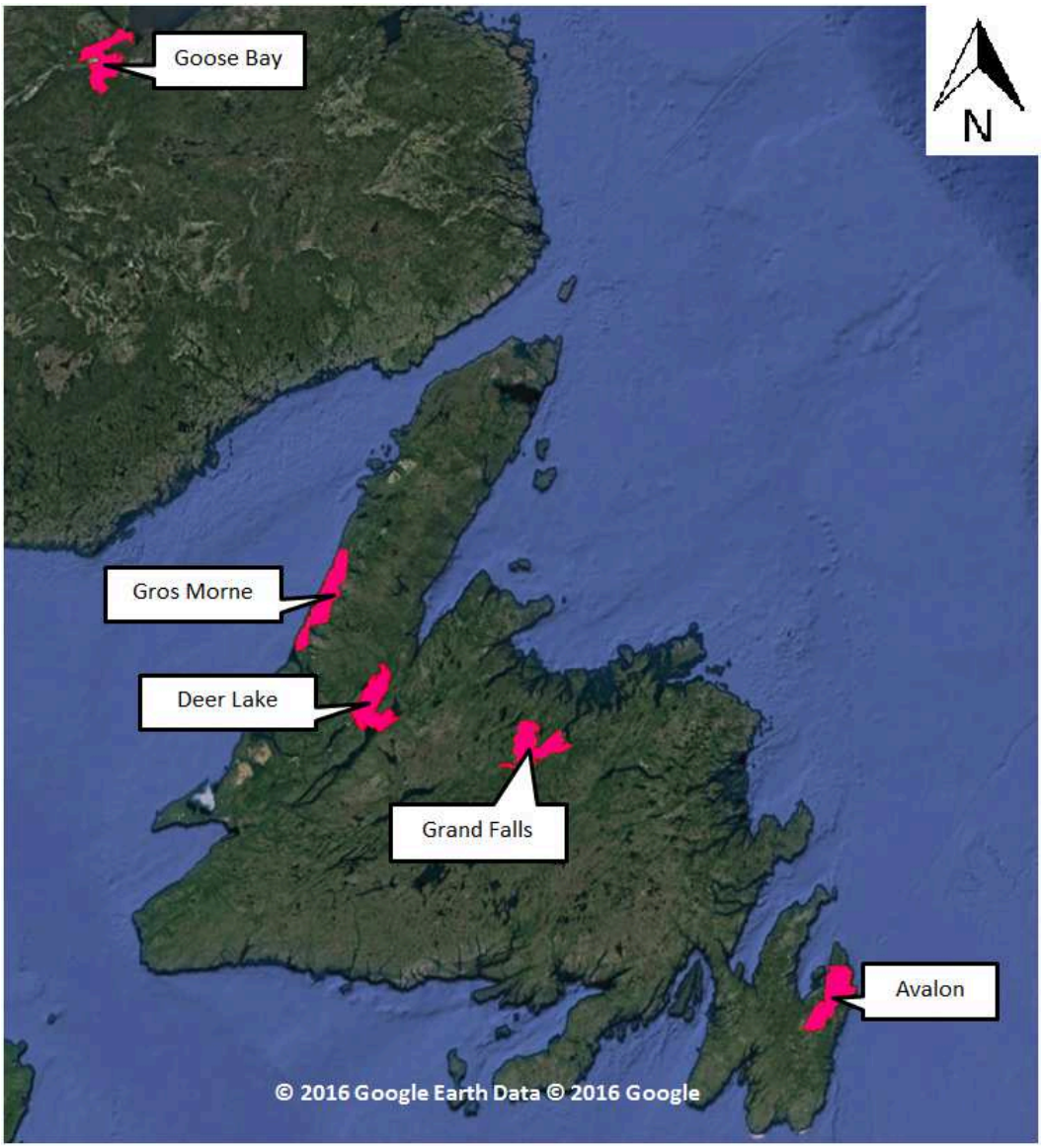

Figure 4.1: Five representative pilot sites of Newfoundland and Labrador for wetland classification of the province (adapted from Google Earth^{TM}).

Table 4.1: General characteristics of the pilot sites.

pilot site	Center's Approximate Latitude	Center's Approximate Longitude	Area (Km^2)	Climate	Ecoregion	Dominant Land Cover
Avalon	$47°27'N$	$52°52'W$	668	Oceanic	Maritime Barren Ecoregion	heathland barrens, balsam forests, urban and agricultural areas
Deer Lake	$49°16'N$	$57°15'W$	700	Continental	North Central Ecoregion of Newfoundland	extensive peatlands and balsam fir, and black spruce forests, minor urban regions
Gros Morne	$49°55'N$	$57°42'W$	700	Oceanic	Northern Pen Ecoregion of Newfoundland	low-lying peatlands, small towns, mountainous areas dominated by balsam fir and black spruce forests
Goose Bay	$53°18'N$	$60°19'W$	700	Humid-Continental	Lake Melville Ecoregion	extensive forests of balsam fir, black spruce, and white birch, peatland covers, permafrost

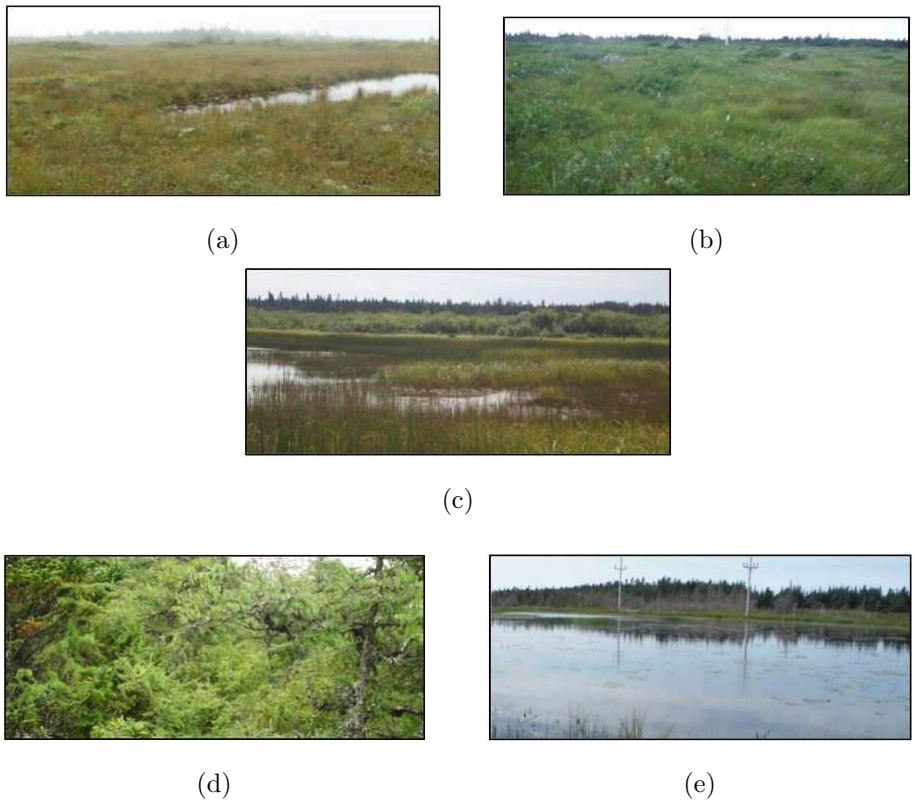

Figure 4.2: Images of wetland classes described by the Canadian Wetland Classification System across the pilot sites: a) Bog in the Avalon, b) Fen in Gros Morne, c) Marsh in Goose Bay, d) Swamp in the Avalon, e) Shallow Water in Gros Morne.

meaning that at least 30% of the wetland is dominated by woody vegetation, be that trees or tall shrubs [7]. Swamps can be located both on peat or mineral soils, and like fens are minerotrophic [7]. Swamps experience more seasonal water level fluctuations compared to that of bogs and fens [36] and may experience periods in which standing water is present. *Marshes* are located entirely on mineral soils and experience high levels of potential daily, monthly, and seasonal water fluctuations. They also can be noticeably affected by flooding, evapotranspiration and may completely dry out during drought [7]. Nutrient availability in marshes is high and can support the growth of vascular plants that are often partially submerged in water [36]. Marshes are treeless and emergent aquatic plants are a common feature of them [7]. The final class, *shallow water*, is a wetland where water is present and generally stable year round at depths of 2 meters or less. However, in times of drought, there is a possibility that the substrate of shallow water wetlands may be exposed [36]. Shallow water often occupies transitional zones between other wetlands and deep water and are dominated by submerged aquatic vegetation [7]. Photographs of different classes, acquired from the pilot sites in Newfoundland and Labrador, are illustrated in Figure 4.2. Also, these five wetland classes are superimposed on a SAR image in Figure 4.3.

For field data collection, high resolution aerial photographs were initially used for the selection of potential wetland sites. Then, a team of biologists visited candidate locations based on the convenience of accessibility, and also public or private ownership of the land. Finally, the visited sites were classified into one of the wetland classes described by the CWCS. For each wetland site, in addition to the location of the selected class, other information such as photographs, and field notes on the dominant vegetation, hydrology and adjacent landscape were provided. The classification

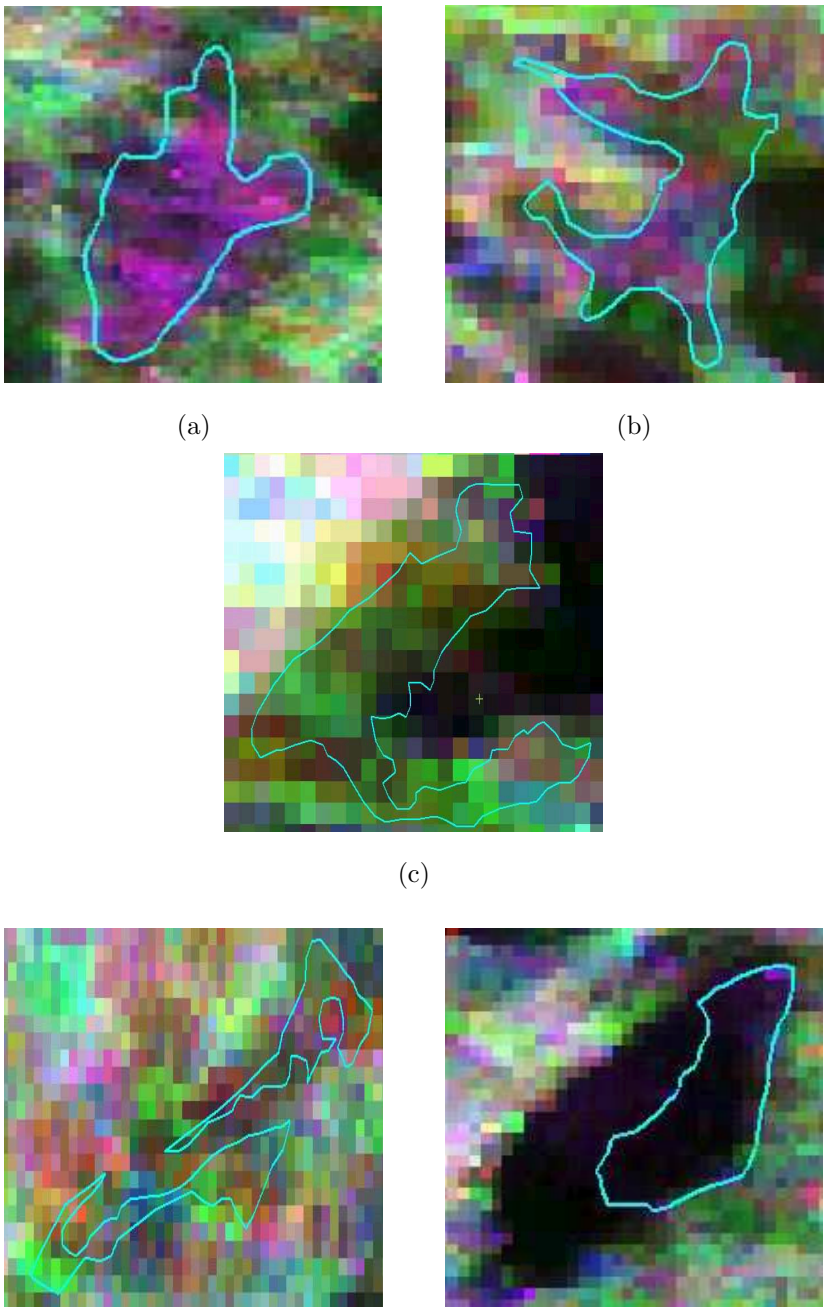

Figure 4.3: A RADARSAT-2 C-band image depicted in false color composite ($|S_{hh}|^2$ as the red, $|S_{hv}|^2$ as the green, and $|S_{vv}|^2$ as the blue channel) with a) Bog, b) Fen, c) Marsh, d) Swamp, and e) Shallow Water polygons overlaid on that.

categories, along with the ancillary information, were later processed to provide the polygons for training the classifier, as well as the accuracy assessment of the classification. 50 percent of the processed field data were used for training the classifier and the other 50 percent were used for the accuracy assessment. Table 4.2 shows the area of, and the number of training and test sites in, each pilot site. Also, Figure 4.4 shows the distribution of training and test sites in the Avalon pilot site. It is worth mentioning that at the time of writing this paper, only the first phase of in situ data collection was conducted during September and early October, 2015.

Table 4.2: The area of, and the number of training and test sites in, each pilot site.

pilot site	Total training area (ha)	Total test area (ha)	number of training sites	number of testing sites
Avalon	413.80	385.29	113	109
Deer Lake	83.95	67.89	31	32
Goose Bay	326.74	228.77	30	29
Gros Morne	537.15	411.19	54	57

4.4.3 Image Datasets

RADARSAT-2, launched in 2007, is able to acquire full-polarimetric images in C-band (5.405 GHz) with a revisit cycle of 24 days. RADARSAT-2 full-polarimetric SAR images with Fine-Resolution Quad-Polarimetric (FQ) beam modes were used in this study. Since the swath width of this type of imagery is small compared to that

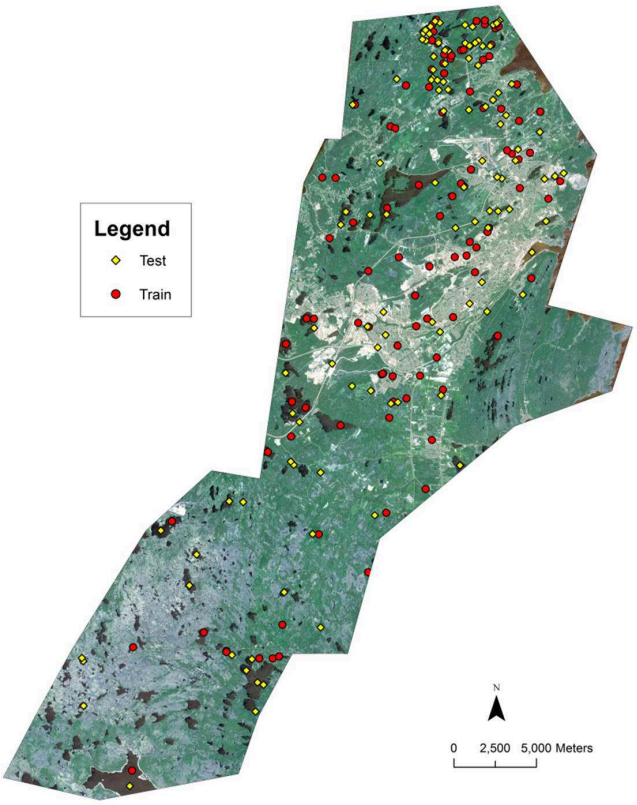

Figure 4.4: The distribution of training and test sites in the Avalon area.

of other beam modes [37], more than one image was required to cover the pilot sites for each pilot site. Moreover, as the purpose of this study is to compare the quality of classification using multi-temporal images versus single-date ones, for each pilot site at least two images from different dates were analyzed. The characteristics of the applied RADARSAT-2 images are depicted in Table 4.3. In addition to RADARSAT-2 images, optical satellite images (mainly RapidEye) were used for the purpose of initial segmentation.

Table 4.3: The characteristics of the RADARSAT-2 images used in this study

Pilot Site	Acquisition Date	Mode	Nominal Range Resolution	Incidence Angle Range	Acquisition Date of the Corresponding RapidEye Image
Avalon	2015/06/10	FQ4	13.8-12.7	22.1-24.1	2015/06/18
	2015/08/21	FQ4	13.8-12.7	22.1-24.1	
Deer Lake	2015/06/23	FQ3	14.6-13.4	20.9-22.9	2015/06/18
	2015/08/10	FQ3	14.6-13.4	20.9-22.9	
	2015/10/18	FQ16	9.0-8.6	35.4-37.0	
Gros Morne	2015/06/16	FQ2	15.4-14.1	19.7-21.7	2015/06/18
	2015/08/03	FQ2	15.4-14.1	19.7-21.7	
	2015/10/14	FQ2	15.4-14.1	19.7-21.7	
Goose Bay	2015/06/30	FQ3	14.6-13.4	20.9-22.9	2015/06/18
	2015/10/04	FQ3	14.6-13.4	20.9-22.9	

4.5 Method

A flowchart of the methods used in this study is represented in Figure 4.5 and each section is briefly explained below.

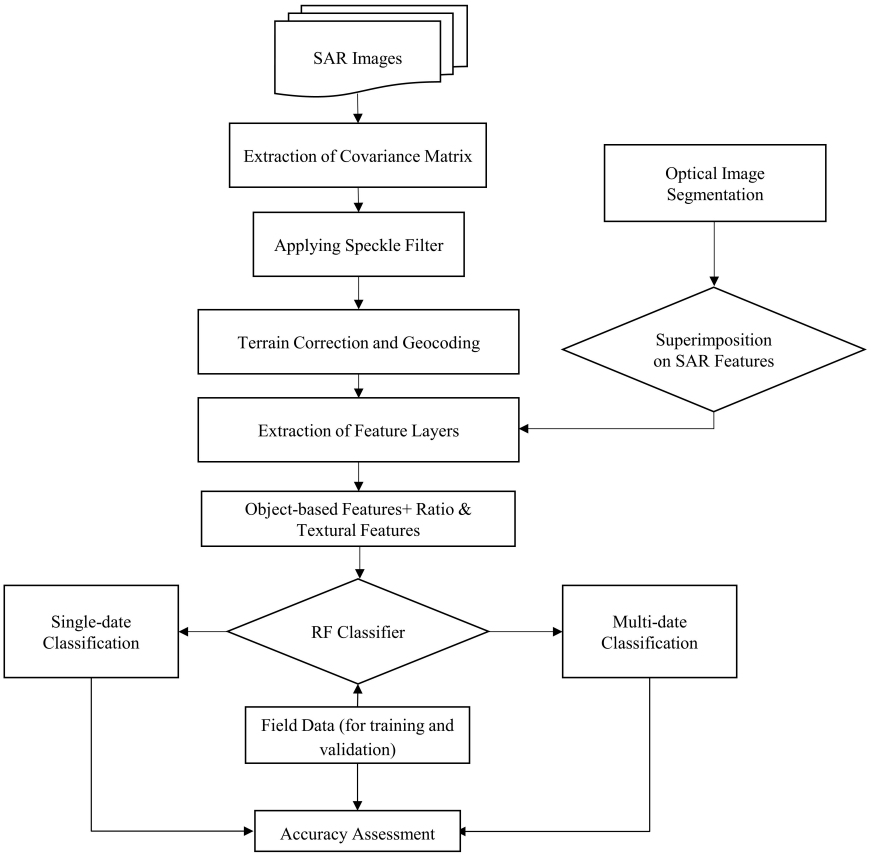

Figure 4.5: The Flowchart of the method applied in this study.

4.5.1 Extraction of Covariance Matrix

SAR images are provided in the form of a Sinclair or Scattering matrix:

$$S = \begin{bmatrix} S_{hh} & S_{hv} \\ S_{vh} & S_{vv} \end{bmatrix} \tag{4.1}$$

where S_{PQ} is the complex scattering coefficient in the transmitting polarization of P and the receiving polarization of Q [38]. The scattering matrix provides the absolute phase recorded for each polarization channel, which can be distorted during processing. Therefore, the scattering matrix should be converted to the covariance matrix, as follows [38]:

$$C = \begin{bmatrix} |S_{hh}|^2 & \sqrt{2}S_{hh}S_{hv}^* & S_{hh}S_{vv}^* \\ \sqrt{2}S_{hv}S_{hh}^* & 2|S_{hv}|^2 & \sqrt{2}S_{hv}S_{vv}^* \\ S_{vv}S_{hh}^* & \sqrt{2}S_{vv}S_{hv}^* & |S_{vv}|^2 \end{bmatrix} \tag{4.2}$$

where the superscript * implies the complex conjugate. This matrix contains the relative phase information, which is not deformed during preprocessing steps. Therefore, the covariance matrix was extracted from all available SAR images before other kinds of processing.

4.5.2 Applying Speckle Filter

SAR images are blemished with the effect of speckle. Speckle is the salt-and-pepper structure of SAR data, which occurs because of the coherent nature of SAR images. This phenomenon hinders image segmentation and classification, and thus should be reduced. For this purpose, a 7-by-7 Lee's Refined PolSAR filter [39] was applied to the images after the extraction of the covariance matrix.

4.5.3 Terrain Correction and Georeferencing

SAR imagery has a number of geometric distortions as a result of SAR side-looking geometry. The most important geometric distortions are layover, foreshortening and shadow (refer to [40] for more details) which should be removed by terrain correction. For this purpose, height information from a Digital Elevation Model (DEM) is used to remove these deformations [41]. In this work, both terrain correction and geocoding were carried out using the ASF MapReady^{TM} software and Canadian DEMs (CDEMs), produced by Natural Resources Canada (NRCan) with the vertical accuracy of 10 meters, and the horizontal resolution of 15 by 25 square meters.

4.5.4 Extraction of Different Features

4.5.4.1 Polarimetric Features

In the next step, several polarimetric features, including the covariance matrix, coherency matrix, Freeman-Durden decomposition [42] and H/A/alpha decomposition [43] were extracted from the full-polarimetric SAR images to be evaluated for classification of wetlands.

The coherency matrix is defined as below [44]:

$$T = \frac{1}{2}\begin{bmatrix} |S_{hh}|^2 + 2\Re(S_{hh}S_{vv}^*) + |S_{vv}|^2 & |S_{hh}|^2 - 2j\Im(S_{hh}S_{vv}^*) - |S_{vv}|^2 & 2S_{hh}S_{hv}^* + 2S_{vv}S_{hv}^* \\ |S_{hh}|^2 + 2j\Im(S_{hh}S_{vv}^*) - |S_{vv}|^2 & |S_{hh}|^2 - 2\Re(S_{hh}S_{vv}^*) + |S_{vv}|^2 & 2S_{hh}S_{hv}^* - 2S_{vv}S_{hv}^* \\ 2S_{hv}S_{hh}^* + 2S_{hv}S_{vv}^* & 2S_{hv}S_{hh}^* - 2S_{hv}S_{vv}^* & 4|S_{hv}|^2 \end{bmatrix} \tag{4.3}$$

The summation of diagonal elements of the covariance and the coherency matrix

is the same [44]. Also, eigenvalues of both covariance and coherency matrices are real and the same [44]. However, the interpretation of physical scattering mechanisms is performed easier using the coherency matrix [45].

Freeman-Durden decomposition divides the total power received from the sensor into three types of scattering mechanisms. Volume scattering is the type of scattering typically received from tree canopies and vegetation. Double bounce scattering represents scattering from surfaces with different dielectric properties. Finally, odd scattering shows the scattering from a moderately rough surface [42]. Some researchers have used Freeman-Durden decomposition for wetland classification, and have reported promising results (e.g. [14]).

H/A/Alpha decomposition generates parameters which can characterize the mechanism of scattering, and which therefore distinguish various targets. H (entropy), A (anisotropy) and Alpha are the parameters which are derived from the eigenvalues of coherency matrix. Each of the scattering mechanisms (surface, double bounce, and volume) has a specific range of entropy, anisotropy, and alpha. This fact helps in the determination of scattering mechanisms for a specific object, which, in turn, can determine a specific class for that object. H/A/Alpha decomposition has also been applied in several papers for wetland classification (e.g. [46]).

4.5.4.2 Ratio and Textural Features

Using other object-based features in the classification in addition to the conventional object mean can be useful [47–49]. Therefore, in this study we evaluated the effect of several ratio and texture features on the classification.

Ratio Features Although the absolute intensity values in each channel of a SAR image are valuable in classification, the relative values have also proved important, and might result in a higher distinction capability for a classifier. For this reason, the potential of ratio features was assessed in this study for wetland classification. Three types of ratio features that were applied in this study are illustrated in Equations 4.4 to 4.5.

$$\frac{|S_{hv}|^2}{|S_{hh}|^2} \tag{4.4}$$

$$\frac{|S_{hv}|^2}{|S_{vv}|^2} \tag{4.5}$$

$$\frac{|S_{hv}|^2}{|S_{hh}|^2 + 2|S_{hv}|^2 + |S_{vv}|^2} \tag{4.6}$$

The potential of the different combinations of the above features, for all available dates, was evaluated for wetland classification in all four pilot sites.

Textural Features Grey Level Co-occurrence Matrix (GLCM) is one of the most commonly used measures for evaluating texture [47]. This matrix is a tabulation of the occurrence frequency of different combinations of pixel grey levels. The evaluated combinations for the occurrence of pixel grey levels can be in various directions, including vertical, horizontal, diagonal directions, or even the summation of all directions [31, 50]. This matrix is the basis for estimation of many texture measures, such as contrast, dissimilarity, homogeneity and so on. In pixel-based GLCM, a rectangular neighbourhood is defined for each pixel based on which GLCM is constructed.

In object-based GLCM, this neighbourhood is actually the whole object in which the pixel lies which causes the estimated texture measure to be of higher reliability. As some of the texture measures proposed by [50] are strongly correlated with the others [47], two measures were selected for the assessment of the role of texture measures in wetland classification: GLCM Dissimilarity and GLCM Entropy, which have been reported popular in the literature [47]. In this paper, all GLCM criteria were computed for various combinations of multi-date intensity layers, and in all directions.

GLCM Dissimilarity is a measure of the amount of variation in an object. This measure is high if the local dissimilarity is high. Dissimilarity is computed from the GLCM matrix using the following formula [50]:

$$\sum_{i,j=0}^{N-1} P_{i,j}|i-j| \tag{4.7}$$

where i and j are row and column number, respectively, N is the total number of rows or columns and Pi,j is the normalized value in the cell i,j of the GLCM matrix.

GLCM Entropy is a measure of spatial disorder. The value of Entropy is high if a local region has a completely random distribution of grey levels. It has a low value if the corresponding image layer has a solid tone [50]. It is defined as follows [50]:

$$\sum_{i,j=0}^{N-1} P_{i,j}(-lnP_{i,j}) \tag{4.8}$$

where ln is the natural logarithm. The two previously mentioned texture measures were evaluated for wetland classification in all four pilot sites and the results are reported in the following sections.

Segmentation Our alternative method for segmentation of the SAR images was to use an optical image covering the same geographical area as the SAR image and to segment it using the multiresolution algorithm. Then, the result of the segmentation of the optical image is superimposed on the SAR feature sets. Finally, SAR feature sets are segmented using those results to generate object-based features. This method is especially useful because as a result of the presence of speckle, individual pixel values in SAR images are not meaningful even after applying filters. However, the average of a group of pixels can be an accurate representative of a class for classification.

For each SAR image, an optical image over the same area was segmented using the multiresolution algorithm by applying the eCognition Developer^{TM} 9. The co-registration accuracy for each of the four pilot sites was below half a pixel. After trial and error based on visual assessment of the obtained objects, a scale of 300 and a color weight of 0.9 (corresponding to a shape weight of 0.1) were selected for this purpose. Then, the segmentation layer was superimposed on the layers obtained from SAR features to generate object-based features. For each feature layer, the mean of the pixel values per object was assigned to the whole object. Then, based on the obtained objects, ratio and textural features were computed.

Random Forest Classification Finally, the RF classifier in eCognition Developer^{TM} 9 was used for classification. RF was selected because a study done by [51] showed RF outperforms several other classifiers such as Maximum Likelihood (ML) and Classification and Regression Tree (CART) for wetland classification. The RF classifier has various user-defined parameters. The depth of the tree is the level to which each tree is grown. The minimum number of samples per node determines the smallest number

of training samples which are used at each node to predict the label of an object. The minimum tree number is the smallest number of trees which is used to make a decision on the label of an object. The number of active variables is the number of randomly selected features in each node to be used for finding the best split. After experimenting with different values, the depth of the tree was set at 5, the minimum number of samples per node was set at 3, the maximum tree number was set at 50, and the number of active variables was set to the square root of the total number of features.

Initially, single-date classification was carried out utilizing all available single-date feature sets. Then, by analyzing the accuracy of all single-date classifications, the best multi-date combination of the feature sets was selected and assessed in terms of accuracy. Next, the results of single-date classifications were compared to that of multi-date classification. Finally, the effect of ratio and textural features was evaluated on the best classification result.

4.6 Results and Discussion

For wetland classification of each pilot site, five wetland classes (Bog, Fen, Marsh, Swamp and Shallow Water) and three non-wetland classes (Upland, Urban, and Deep Water) were initially considered for classification. However, depending on the availability of field data, the classes selected to be included in the classification differ in each pilot site. The next sections are organized as follows: first, the performance of the object-based method and the proposed segmentation method is investigated. Then, the results of classification using multi-date polarimetric features are presented.

Finally, the effect of ratio and textural features on the classification accuracy is evaluated.

4.6.1 Evaluation of the Proposed Segmentation Method

Two images, segmented with the multiresolution algorithm, along with the corresponding resulting maps are represented in Figure 4.6. In Figure 4.6 (a), the SAR image is solely segmented using SAR layers. The segments clearly do not visually match the real-world objects. That is because the segmentation algorithms developed for optical images are not appropriate for SAR images, as they do not take into account the speckle phenomenon existing in SAR images. For segmenting the image, initially an optical image covering the same geographical area as the SAR image, has been segmented (Figure 4.6 (b)) and the result of segmentation from that area has been superimposed on the SAR image. In object-based classification, the mean value of each feature is assigned to the entire image object. This causes the resulting map in Figure 4.6 (c), for which the segments do not conform to real-world objects, to be of poor quality. The reason is that with the wrong segments, the mean calculated for a given segment will be affected by several targets included in that object. However, when the segments are consistent with real-world objects, as illustrated in Figure 4.6 (d), the calculated mean belongs to one object only and hence the resulting map is of higher quality.

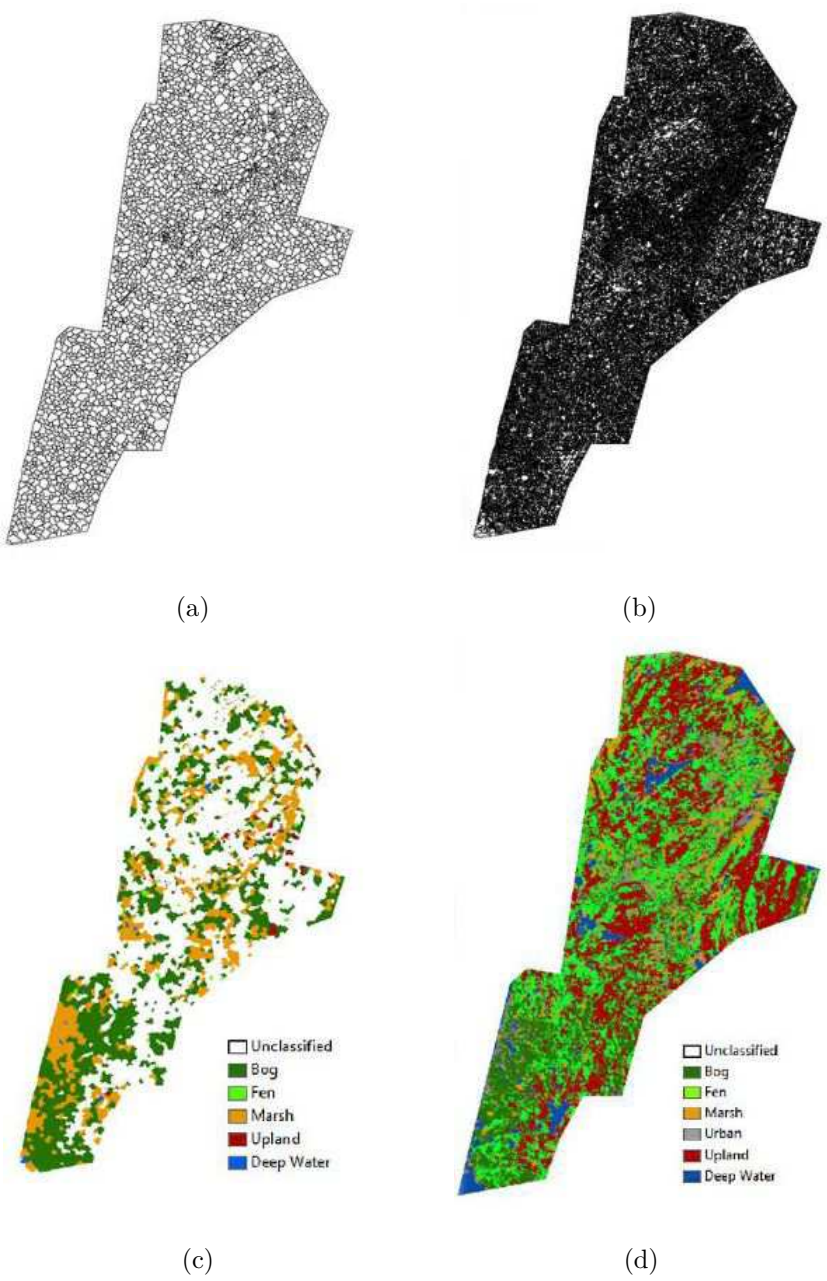

Figure 4.6: Comparison between segmentation using only SAR layers over the Avalon area versus segmentation using an optical image over the same area: a) Segmentation using only SAR layers, b) Segmentation using an optical image from the same area, c) Classification resulted from segmentation depicted in part (a), and d) Classification resulted from segmentation depicted in part (b).

4.6.2 Comparison of Object-based Classification with Pixel-based Classification

For emphasizing the advantage of object-based classification over pixel-based classification, two corresponding resulting maps for the Avalon area are illustrated in Figure 4.7. The object-based map (Figure 4.7 (b)) had greater homogeneous areas identified. Moreover, the classified image is much cleaner and the classified areas are visually more similar to real-world objects compared to pixel-based map (Figure 4.7 (a)). To compare the resulting maps quantitatively, the overall accuracy and per-class accuracies for both maps are represented in Table 4.4. Not only is the overall accuracy of the object-based map higher, but also the per-class accuracies are higher than those of the pixel-based map. The results clearly show the benefit of the object-based map over the pixel-based map.

4.6.3 Classification Results

For all pilot sites, the overall classification accuracy using various sets of parameters is reported. For the objectives of evaluating efficiency of wetland classification, overall accuracy alone is not sufficient for evaluating the quality of classification, as the accuracy of non-wetland classes also affects the value of this parameter. Therefore, the average producer and user accuracies of exclusively wetland classes are presented in addition to the overall accuracy. For the best classification result, per-class accuracy is also reported.

Based upon the above discussion, for each pilot site, the first step was to perform the classification using the available sets of features. On an individual basis, these

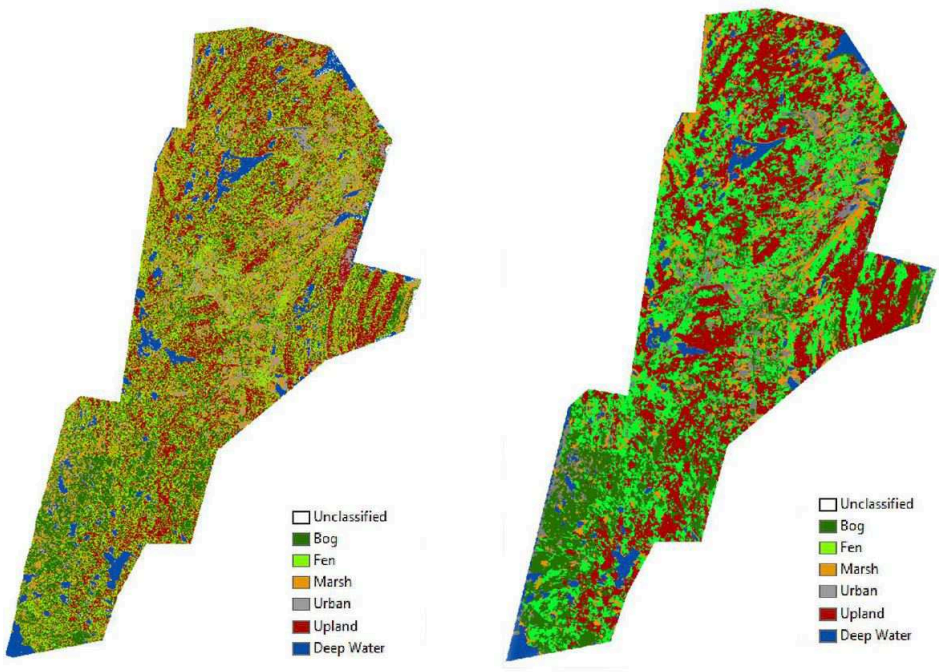

(a) (b)

Figure 4.7: Comparison between pixel-based and object-based classifications in the Avalon pilot site: a) Pixel-based classification, and b) Object-based classification.

Table 4.4: Comparison between the pixel-based and object-based classification accuracies using multi-resolution algorithm over the Avalon area.

Pixel-Based Classification			Object-Based Classification		
Class	Producer Accuracy (%)	User Accuracy (%)	Class	Producer Accuracy (%)	User Accuracy (%)
Bog	70	62	Bog	79	76
Fen	35	23	Fen	58	36
Marsh	69	26	Marsh	60	33
Urban	32	80	Urban	40	83
Upland	50	74	Upland	66	80
Deep Water	100	100	Deep Water	100	100
Pixel-Based Classification		71	Object-Based Classification		79

features include C3 and T3 matrices and Cloude-Pottier and Freeman-Durden decompositions. Then, based on the obtained results, the best multi-date combination was selected for the classification of the pilot site. As the number of training samples for the wetland classes is rather small, using all the features from multiple available dates causes the classification accuracy to decrease due to the Hughes phenomenon [52], and consequently, is not recommended.

4.6.3.1 The Avalon Area

For both single-date and multi-date classifications, the overall accuracies along with the wetlands average producer and user accuracies are depicted in Figure 4.8. The overall accuracy and the wetlands average user accuracy is higher for the multi-date classification than all single-date classifications, and the wetland's average producer accuracy is lower than only one of the single-date classifications (T31). Therefore, it can be concluded that overall, the presented multi-date classification (C31+T32) had the best performance compared to the single-date cases. The best classification map and the best classification accuracies are illustrated in Figure 4.9 and Table 4.5, respectively. Bog, Urban, and Deep Water classes had acceptable accuracies, while the producer accuracy for the Urban class and the user accuracies for the Fen and Marsh classes are low. There is a considerable amount of commission error for Fen and Marsh classes, i.e. some parts of other classes have been mistakenly classified as Fen or Marsh. Conversely, there is a high omission error for urban areas indicating that significant parts of the urban area have been mistakenly classified as either wetland or upland classes. This is also clear from Figure 4.9 because a considerable section of urban region has been classified as Marsh. The low accuracy for the urban

area can be attributed to the lack of optical data. Optical data are commonly used to accurately detect urban areas as a result of having a NIR band for distinguishing between vegetation and man-made structures. One reason for the low accuracies of wetland classes is suspected to be the small number of training samples available for them.

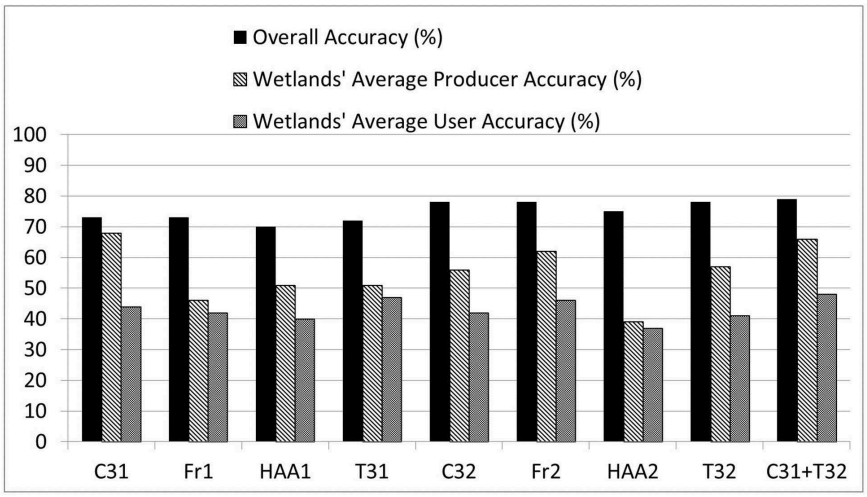

Figure 4.8: Single-date and multi-date overall and per-class accuracies for the Avalon area. C3=Covariance Matrix, T3=Coherency Matrix, Fr=Freeman-Durden Decomposition, HAA=H/A/Alpha decomposition. The rightmost number of each feature's abbreviation indicates the sequence of acquisition. Example: C31=Covariance Matrix obtained from the first acquired imagery over the pilot site.

4.6.3.2 Deer Lake

Figure 4.10 illustrates the overall accuracy using a different set of polarimetric features, as well as the average producer and user accuracies of wetland classes for both

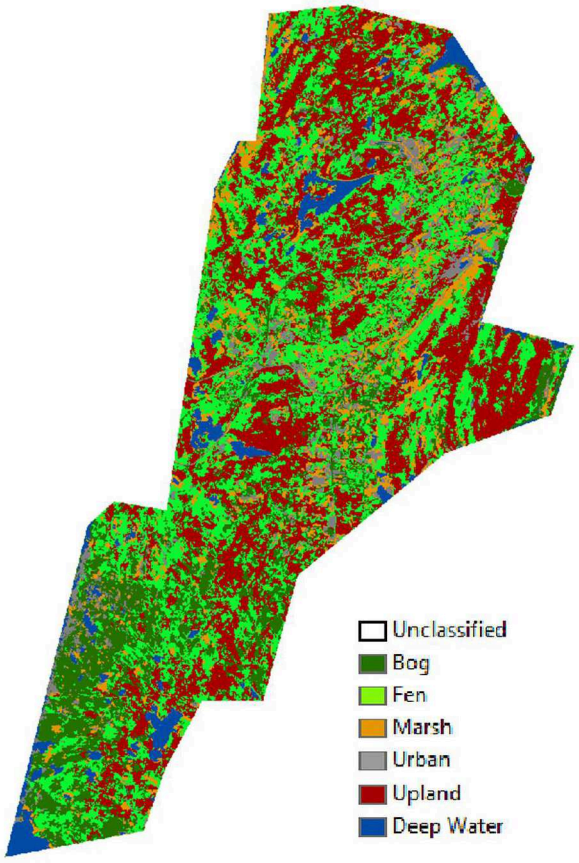

Figure 4.9: Map classified using multitemporal C31+T32 for the Avalon pilot site.

Table 4.5: Classification accuracies using multitemporal C31+T32 for the Avalon pilot site.

Class	Producer Accuracy	User Accuracy
Bog	79%	76%
Fen	58%	36%
Marsh	60%	33%
Urban	40%	83%
Upland	66%	80%
Deep Water	100%	100%
Overall Accuracy		79%

single-date and multi-date cases. The results show that when we use some single-date features, the overall accuracy is higher than that of the best multi-date combination (HAA1+HAA2+C31). However, the multi-date combination has the largest average user and producer accuracies for wetlands (87% and 68%, respectively). Figure 4.11 and Table 4.6 show the result of the best classification accuracy for Deer Lake. According to Table 4.6, with the exception of the Fen Class, which has a low user accuracy, and consequently a high amount of commission error, other classes have acceptable accuracies in spite of the low amount of training data. According to Table 4.9, which shows the confusion matrix for the best classification result of Deer Lake, a considerable part of the Upland class has been recognized as Fen.

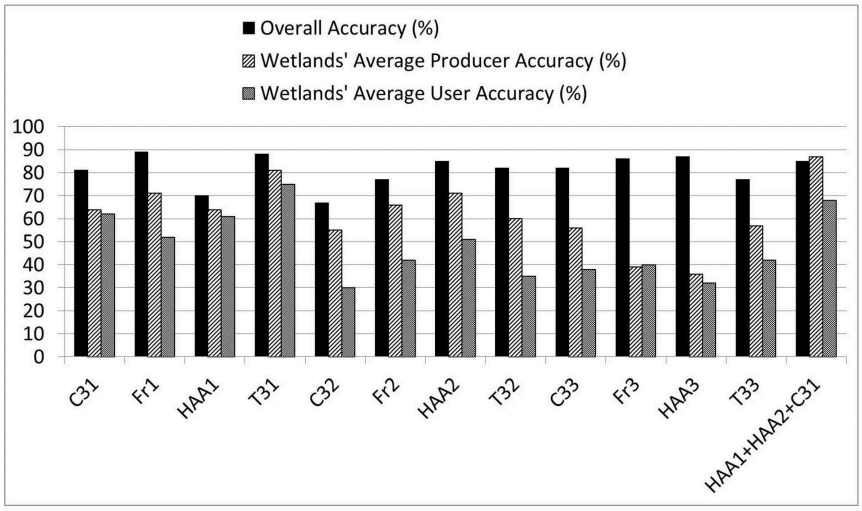

Figure 4.10: Single-date and multi-date overall and per-class accuracies for Deer Lake. C3=Covariance Matrix, T3=Coherency Matrix, Fr=Freeman-Durden Decomposition, HAA=H/A/Alpha decomposition. The rightmost number of each feature's abbreviation indicates the sequence of acquisition. Example: C31=Covariance Matrix obtained from the first acquired imagery over the pilot site.

Table 4.6: Classification accuracies using multitemporal HAA1+HAA2+C31 for the Deer Lake pilot site.

Class	Producer Accuracy	User Accuracy
Upland	74%	96%
Fen	85%	44%
Bog	97%	94%
Deep Water	100%	100%
Marsh	78%	65%
Overall Accuracy		85%

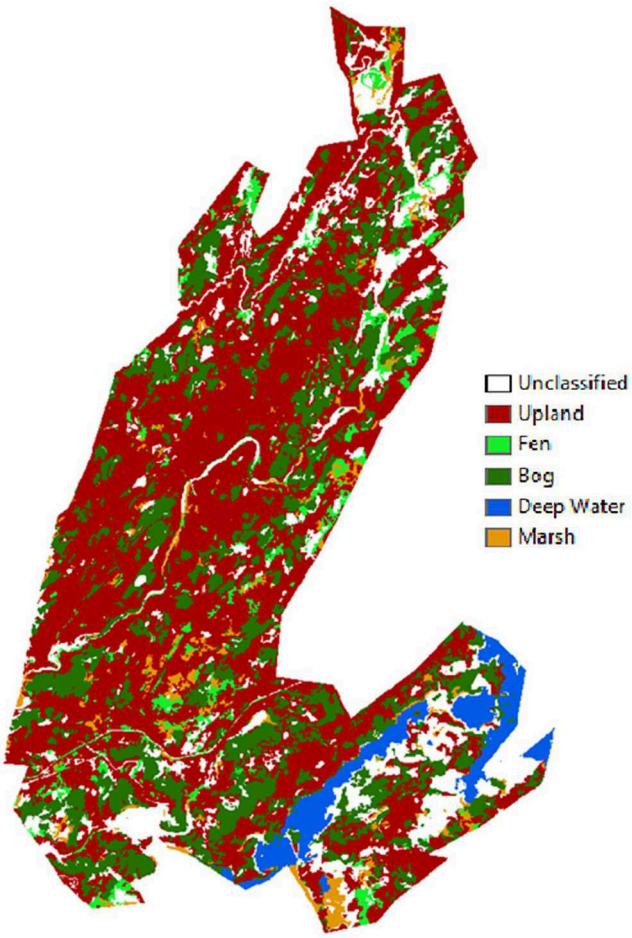

Figure 4.11: Map classified using multitemporal HAA1+HAA2+C31 for the Deer Lake pilot site.

4.6.3.3 Goose Bay

The overall accuracy along with the average wetlands producer and user accuracies using various single-date parameter sets and the selected multi-date set are demonstrated in Figure 4.12. Freeman-Durden decomposition for the first date has performed better than all other feature sets. After that, however, the multi-date combination is the only feature set for the map where all three accuracies (overall accuracy, average wetlands producer accuracy and average wetland user accuracy) are high. Moreover, in the multi-date combination average user and producer accuracies for wetlands are closer to each other compared to the first-date Freeman-Durden decomposition, which shows that the resulting map is more reliable. Figure 4.13 and Table 4.7 show the result of the best classification accuracy for Goose Bay. There are a number of low accuracies reflected in Table 4.7. The producer accuracy for the Urban class and user accuracy for the Upland class are both low which corresponds to a high omission rate for the Urban and a high commission rate the Upland class. Table 9 clearly shows the confusion between these two classes. Moreover, both user and producer accuracies are low for the Fen class. We believe the low accuracies and presence of unclassified parts of the pilot suites result from the low amount of training data.

4.6.3.4 Gros Morne

For the Gros Morne pilot site the overall classification accuracies using single-date feature sets are in the range of 80 to 85 per cent, while using the multi-date set the accuracy was 95 per cent (Figure 4.14). Although the wetlands average producer

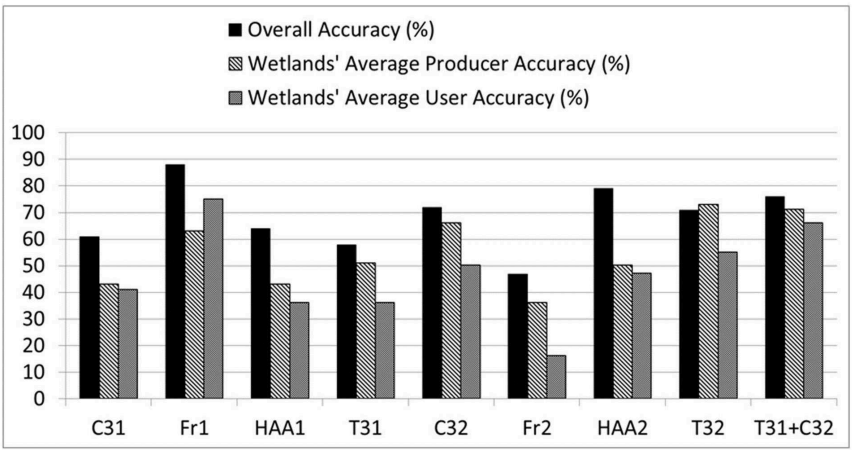

Figure 4.12: Single-date and multi-date overall and per-class accuracies for Goose Bay. C3=Covariance Matrix, T3=Coherency Matrix, Fr=Freeman-Durden Decomposition, HAA=H/A/Alpha decomposition. The rightmost number of each feature's abbreviation indicates the sequence of acquisition. Example: C31=Covariance Matrix obtained from the first acquired imagery over the pilot site.

Table 4.7: Classification accuracies using multitemporal T31+C32 for the Goose Bay pilot site.

Class	Producer Accuracy	User Accuracy
Deep Water	100%	100%
Urban	50%	85%
Bog	85%	95%
Upland	99%	44%
Fen	57%	36%
Overall Accuracy		76%

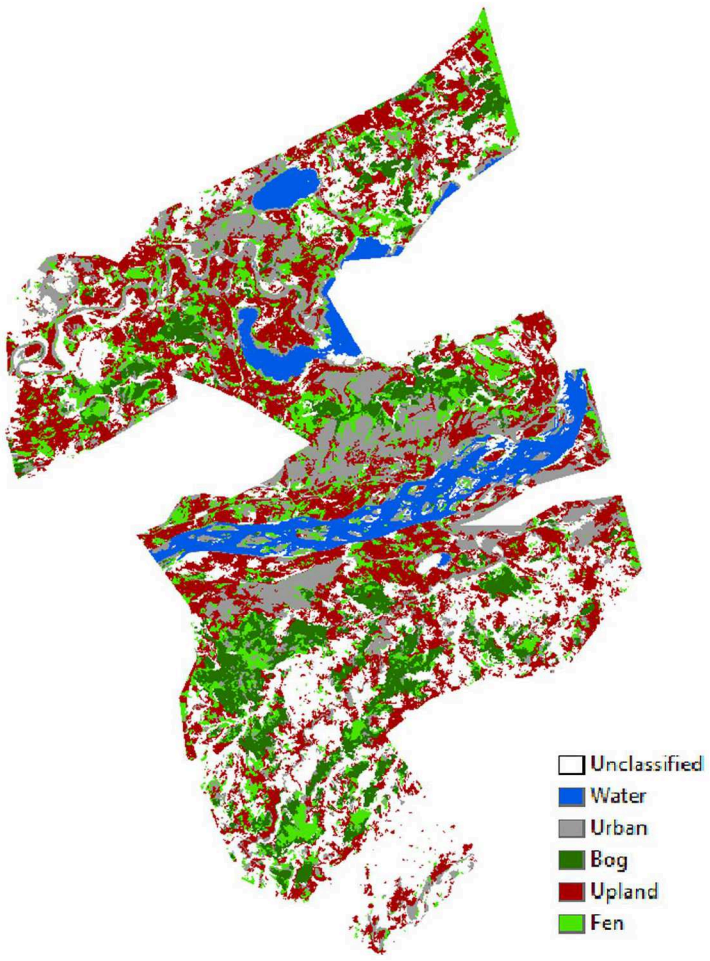

Figure 4.13: Map classified using multitemporal T31+C32 for the Goose Bay pilot site.

accuracy is sometimes higher with the single-date feature sets than the multi-date feature set, the multi-date feature set is the only situation in which both the producer and user accuracies are high and are similar in value. The best classification results for Gros Morne are reflected in Figure 4.15 and Table 4.8. All obtained accuracies are reasonable except for the Swamp class, which has a low accuracy. According to Table 9, a considerable part of the Swamp class has been recognized as Upland. This is expected, because the C-band wavelength is not long enough to penetrate through the canopy and detect the water beneath the trees, which would indicate a Swamp class.

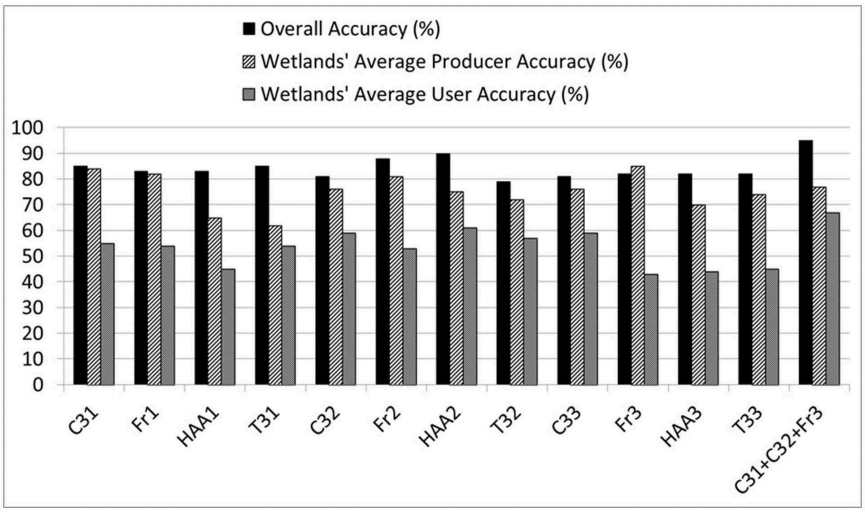

Figure 4.14: Single-date and multi-date overall and per-class accuracies for Gros Morne. C3=Covariance Matrix, T3=Coherency Matrix, Fr=Freeman-Durden Decomposition, HAA=H/A/Alpha decomposition. The rightmost number of each feature's abbreviation indicates the sequence of acquisition. Example: C31=Covariance Matrix obtained from the first acquired imagery over the pilot site.

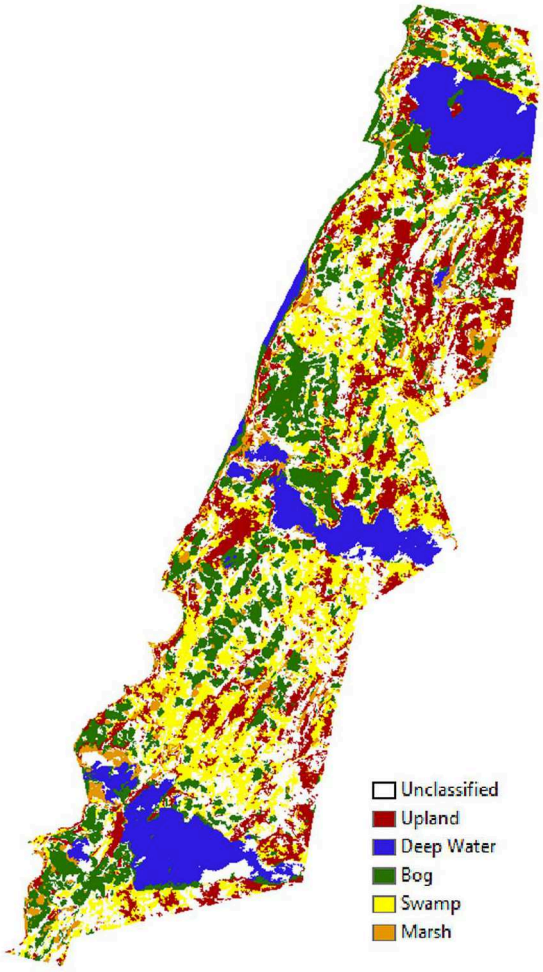

Figure 4.15: Map classified using multitemporal C31+C32+Fr3 for the Gros Morne pilot site.

Table 4.8: Classification accuracies using multitemporal C31+C32+Fr3 for the Goose Bay pilot site.

Class	Producer Accuracy	User Accuracy
Upland	84%	83%
Deep Water	100%	100%
Bog	96%	99%
Swamp	57%	39%
Marsh	77%	63%
Overall Accuracy		95%

Also, for a more detailed analysis, the confusion matrices for the best classification result of the all four pilot sites is represented in Table 4.9.

4.6.4 The Effect of Ratio and Textural Features

For each pilot site, the previously introduced texture and ratio features were added to the mean feature set, which resulted in the best classification accuracy for that pilot site. Different combinations of the ratio and texture features were evaluated for this purpose and the one that generated the best outcome is presented in Table 4.10.

For the Avalon area, amongst the different ratio features evaluated, the ratio feature of Equation 4.4, for both available dates of the Avalon area, made a 2 percent improvement in the overall accuracy. As a result of adding the mentioned features, the classification accuracy of the Fen, Urban, and Upland classes increased, which means the confusion between the Urban class and Wetland classes was reduced. Re-

Table 4.9: Confusion matrices for the best classification result in a) The Avalon area b) Deer Lake c) Goose Bay d) Gros Morne

	Bog	Fen	Marsh	Urban	Upland	Deep Water	Total
Bog	79.28	19.61	0.26	12.9	1.53	0	14.64
Fen	19.61	57.68	15.11	15.7	18.57	0	13.35
Marsh	0.57	11.16	60.03	16.74	13.44	0.1	8.11
Urban	0.15	0.06	21.78	40.37	0	0.02	5.91
Upland	0.4	11.49	2.82	14.29	66.46	0	14.5
Deep Water	0	0	0	0	0	99.88	43.49
Total	100	100	100	100	100	100	100

(a)

	Upland	Fen	Bog	Deep Water	Marsh	Total
Upland	74.34	6.43	1.85	0	13.33	35.67
Fen	23.35	84.64	0.14	0	4.44	19.6
Bog	1.83	6.43	97.15	0.23	4.44	26.66
Deep Water	0	0	0	99.77	0	16.07
Marsh	0.48	2.5	0.86	0	77.78	1.99
Total	100	100	100	100	100	100

(b)

	Deep Water	Urban	Bog	Upland	Fen	Total
Deep Water	100	0	0	0	0	20.25
Urban	0	49.59	1.43	0.75	20.36	17.12
Bog	0	0.29	85.32	0	15.35	29.5
Upland	0	30.65	0.06	98.75	7.21	17.47
Fen	0	19.47	13.19	0.5	57.08	15.66
Total	100	100	100	100	100	100

(c)

	Upland	Deep Water	Bog	Swamp	Marsh	Total
Upland	84.5	0	1.31	38	17.66	11.24
Deep Water	0	100	0	0	0	27.25
Bog	2.33	0	96.27	4.4	5.71	55.47
Swamp	11.58	0	0.56	56.8	0	2.64
Marsh	1.6	0	1.86	0.8	76.62	3.41
Total	100	100	100	100	100	100

(d)

garding textural features, using GLCM Dissimilarity of HH and VV layers for the first available date raised the overall accuracy by 1 percent. The Fen and Upland classes were better distinguished owing to the use of the discussed textural features.

The ratio features of Equation 4.6 for both available dates of Goose Bay made a 1 percent increase in the overall accuracy. Similar to the Avalon area, the accuracy of the Fen, Urban, and Upland classes was slightly improved through using the specified ratio features. Respecting textural features, GLCM Dissimilarity of the VV intensity layer for the first available date of the pilot site increased the overall accuracy by 1 percent. The Fen and Upland classes were better distinguished using the mentioned textural features.

According to Table 4.10, no improvement in classification accuracy can be obtained by using object-based features in the Deer Lake and Gros Morne pilot sites. Moreover, unlike GLCM Dissimilarity, GLCM Entropy did not have any positive effect on the classification.

4.6.5 Discussion

By investigating the single-date accuracies of all pilot sites, it can be observed that the images acquired in August yield the most accurate map for wetlands. The images taken in June resulted in suitable classification accuracies as well. The SAR images captured in October, however, do not seem to be as useful for wetland classification. Although the October imagery generated maps with an acceptable overall accuracy, they resulted in overestimation of wetland areas, as the average wetlands user accuracy associated with those images is rather low. The reason of this might

Table 4.10: The effect of ratio and textural features on classification accuracy and the percentage of change relative to the best classification accuracy.

	Ratio Feature			Texture Feature		
Pilot Site	Selected Feature	Resulting Overall Accuracy	Change (%)	Selected Feature	Resulting Overall Accuracy	Change (%)
Avalon	Ratio feature of Equation 4.4	81%	+2%	GLCM Dissimilarity of HH and VV layers for the first available date	80%	+1%
Deer Lake	No Useful Feature	85%	0%	No Useful Feature	85%	0%
Goose Bay	No Useful Ratio feature of Equation 4.6	77%	+1%	GLCM Dissimilarity for VV intensity layer for the first available date	77%	+1%
Gros Morne	No Useful Feature	95%	0%	No Useful Feature	95%	0%

lie in the fact that the growing season in Newfoundland and Labrador, generally, is during the spring and summer. During this time, plants are able to grow tall, spread their leaves, and become green. In June, the vegetation within wetlands is not at its most mature. Later, in August however, the vegetation is completely grown, and therefore the distinguishing features of wetlands are clearer. As summer ends, so does growing season. During October, plants will stop growing, and begin to die and lose their vitality. Moreover, increased precipitation may cause the presence of standing water in non-wetland areas. This can be the reason the distinctive characteristics of wetlands start to disappear and/or resemble other types of land cover.

The overall, wetlands average user, and wetlands average producer accuracies of the Deer Lake and Gros Morne pilot sites were substantially higher than those of the Avalon area and Goose Bay pilot sites. We believe higher classification accuracies resulted from images from three different dates available for Deer Lake and Goose Bay, while for the Avalon and Goose Bay, only images from two dates were used. Therefore, having images from several dates can be an asset in classification, although this higher accuracy can be accounted for by other factors.

The covariance matrix proved to be an appropriate feature for wetland classification and was used in the best feature set for every pilot site. That is probably because the covariance matrix not only contains intensity of the three main layers, but also encompasses the phase difference between channels. Phase difference between polarimetric channels is useful for flood detection and therefore, for wetland characterization [18, 53, 54].

Textural and ratio features slightly improved the classification accuracy in the Avalon area and Goose Bay while they did not have any effect on the maps of Deer

Lake and Gros Morne. However, it is important to keep in mind that these changes might have happened because of other factors, and the improvement in the accuracy might not be directly related to the aforementioned ratio and textural features.

[51] used the RF algorithm for wetland classification in the same pilot sites, but using only optical data. They reached an overall accuracy ranging from 86% to 96% and the average producer and user accuracies of 68% to 73%. This means that in our study areas, the sole use of optical data is preferred to the sole use of SAR data. Nevertheless, the fusion of the optical and SAR data is the most promising method. For example, [55] applied both SAR and optical data in our study area, and obtained the average producer and user accuracies of 71% and 72%, respectively over all pilot sites.

It is also worth mentioning that since the training data for the current classifications were collected during the first phase of the project, the data were sometimes not enough to provide the final classification results. Therefore, what is described in this paper is the preliminary classification result of the pilot sites and the completed version of classification will be presented in future work.

4.7 Conclusion

The purpose of this paper was to present preliminary wetland classification results for four pilot sites in Newfoundland and Labrador. Object-based classification was initially compared with the pixel-based classification. The results indicated that the object based method demonstrated superior performance both statistically and visually. Besides, an alternative method was introduced in this paper for segmen-

tation of SAR images. In this method, first an optical image over the same area as the SAR image is segmented, and the result of the segmentation of the optical image is then overlaid on the SAR image. This method worked well for the SAR images and improved the results. Finally, multi-date object-based classification using RADARSAT-2 data was compared with single-date classification for wetland mapping using the RF classifier. Four pilot sites within the province of Newfoundland and Labrador were selected for this purpose. It was concluded that for all the pilot sites, multi-date classification performed better than the single-date classification. Overall accuracies ranging from 75 to 95 per cent were obtained. It was observed that the images acquired in August yield the greatest accuracy for wetlands, while images captured in October were not as appropriate for wetland mapping. Moreover, it was concluded that when more acquisition dates are included in classification, the overall, as well as wetlands, accuracies become substantially higher. The covariance matrix proved useful as a wetland classification feature used in producing maps with the highest wetland classification accuracies in the four pilot sites. Ratio and textural features improved the accuracy slightly in the Avalon and Goose Bay areas. The mentioned features had the most effect on the Fen, Urban, and Upland classes. In Deer Lake and Gros Morne, however, ratio and textural features did not play a considerable role.

The presented results demonstrate that multi-date SAR classification along with the object-based method proposed in this paper, has the potential for accurate mapping wetlands throughout the province. The results in this study were obtained using a small amount of field data for training. Thus, more robust results will be provided in future work, after more field samples are collected in the next phase of the project.

Acknowledgement

This research was undertaken with financial support of the Government of Canada, National Conservation Plan, Atlantic Ecosystem Initiatives, and the Newfoundland and Labrador Research and Development Corporation. The SAR imagery was provided by the Canada Center for Mapping and Earth Observation. Field data was collected by various organizations including, Ducks Unlimited Canada, the Government of Newfoundland and Labrador Department of Environment and Conservation, and the Nature Conservancy Canada. The work was supported in part by the Natural Sciences and Engineering Research Council of Canada (NSERC) under Grants to W. Huang (NSERC 402313-2012). The authors thank these organizations for the generous financial supports and providing such valuable datasets.

Bibliography

[1] National Wetlands Working Group and others. Wetlands of canada. ecological land classification series, no. 24. *Sustainable Development Branch, Environment Canada, Ottawa, Ontario, and Polyscience Publications Inc., Montreal, Quebec*, 452, 1988.

[2] Anil Beersing. Policy for development in wetlands, 1997.

[3] Government of Canada. Water sources: wetlands, 2016.

[4] Wetlands Alberta. Wetland loss, 2016.

[5] Ducks Unlimited Canada. Newfoundland & labrador, 2016.

[6] Austin Reed. *Man and waterfowl in tidal shorelines of Eastern Canada*. Canadian Wildlife Service, 1972.

[7] G Adams, P Buteau, N Dignard, P Grondin, J Jeglum, D Keys, and S Zoltai. The canadian wetland classification system, 1997.

[8] AR Hanson and L Calkins. *Wetlands of the Maritime Provinces: revised documentation for the wetlands inventory*. Environment Canada, Canadian Wildlife Service, Atlantic Region, 1996.

[9] Ducks Unlimited Canada. High-tech mapping in Newfoundland and Labrador, 2015.

[10] A LaRocque, B Leblon, LL Bourgeau-Chavez, JL McCarty, M Mordini, NHF French, A Landon, R Woodward, TG Huntington, and P Camill. Evaluating wetland mapping techniques for new brunswick using landsat-5 tm, alos-palsar and radarsat-2 dual-polarized images. In *AGU Fall Meeting Abstracts*, 2014.

[11] Raymond Jahncke, Brigitte Leblon, Peter Bush, and Armand LaRocque. Mapping wetlands in nova scotia with multi-beam radarsat-2 polarimetric sar, optical satellite imagery, and lidar data. *International journal of applied earth observation and geoinformation*, 68:139–156, 2018.

[12] Nature Conservancy of Canada and Grenfell Campus of Memorial University of Newfoundland. Wetlands, 2014.

[13] Sepideh Arzandeh and Jinfei Wang. Texture evaluation of radarsat imagery for wetland mapping. *Canadian Journal of Remote Sensing*, 28(5):653–666, 2002.

[14] B Brisco, M Kapfer, T Hirose, B Tedford, and J Liu. Evaluation of C-band polarization diversity and polarimetry for wetland mapping. *Canadian Journal of Remote Sensing*, 37(1):82–92, 2011.

[15] Gabriel Gosselin, Ridha Touzi, and François Cavayas. Polarimetric Radarsat-2 wetland classification using the Touzi decomposition: case of the Lac Saint-Pierre Ramsar wetland. *Canadian Journal of Remote Sensing*, 39(6):491–506, 2014.

[16] Ridha Touzi, A Deschamps, and G Rother. Wetland characterization using polarimetric RADARSAT-2 capability. *Canadian Journal of Remote Sensing*, 33(sup1):S56–S67, 2007.

[17] Shane Robert Cloude. Target decomposition theorems in radar scattering. *Electronics Letters*, 21(1):22–24, 1985.

[18] Ridha Touzi. Target scattering decomposition in terms of roll-invariant target parameters. *IEEE Transactions on Geoscience and Remote Sensing*, 45(1):73–84, 2007.

[19] Cécile Marechal, Eric Pottier, Laurence Hubert-Moy, and Sebastien Rapinel. One year wetland survey investigations from quad-pol RADARSAT-2 time-series SAR images. *Canadian Journal of Remote Sensing*, 38(3):240–252, 2012.

[20] Julia Reschke, Annett Bartsch, Stefan Schlaffer, and Dmitry Schepaschenko. Capability of C-band SAR for operational wetland monitoring at high latitudes. *Remote Sensing*, 4(10):2923–2943, 2012.

[21] Linda Moser, Andreas Schmitt, Anna Wendleder, and Achim Roth. Monitoring of the Lac Bam wetland extent using dual-polarized X-Band SAR data. *Remote Sensing*, 8(4):302, 2016.

[22] L Durieux, J Kropáček, GD De Grandi, and F Achard. Object-oriented and textural image classification of the Siberia GBFM radar mosaic combined with MERIS imagery for continental scale land cover mapping. *International Journal of Remote Sensing*, 28(18):4175–4182, 2007.

[23] Marcelle Grenier, Anne-Marie Demers, Sandra Labrecque, Martine Benoit, Richard A Fournier, and Bruno Drolet. An object-based method to map wetland using RADARSAT-1 and Landsat ETM images: test case on two sites in Quebec, Canada. *Canadian Journal of Remote Sensing*, 33(S1):S28–S45, 2007.

[24] Meghan Halabisky, L Monika Moskal, and Sonia A Hall. Object-based classification of semi-arid wetlands. *Journal of Applied Remote Sensing*, 5(1):053511, 2011.

[25] Carlos Leandro de Oliveira Cordeiro and Dilce de Fátima Rossetti. Mapping vegetation in a late Quaternary landform of the Amazonian wetlands using object-based image analysis and decision tree classification. *International Journal of Remote Sensing*, 36(13):3397–3422, 2015.

[26] Sang-Hoon Hong, Hyun-Ok Kim, Shimon Wdowinski, and Emanuelle Feliciano. Evaluation of polarimetric SAR decomposition for classifying wetland vegetation types. *Remote Sensing*, 7(7):8563–8585, 2015.

[27] Gui-Song Xia, Gang Liu, Wen Yang, and Liangpei Zhang. Meaningful object segmentation from sar images via a multiscale nonlocal active contour model. *IEEE Transactions on Geoscience and Remote Sensing*, 54(3):1860–1873, 2016.

[28] Zeinab Tirandaz and Gholamreza Akbarizadeh. A two-phase algorithm based on kurtosis curvelet energy and unsupervised spectral regression for segmentation of SAR images. *IEEE Journal of Selected Topics in Applied Earth Observations and Remote Sensing*, 9(3):1244–1264, 2016.

[29] E Akyilmaz and UM Leloglu. Segmentation of SAR images using similarity ratios for generating and clustering superpixels. *Electronics Letters*, 52(8):654–656, 2016.

[30] Ursula C Benz, Peter Hofmann, Gregor Willhauck, Iris Lingenfelder, and Markus Heynen. Multi-resolution, object-oriented fuzzy analysis of remote sensing data for GIS-ready information. *ISPRS Journal of photogrammetry and remote sensing*, 58(3-4):239–258, 2004.

[31] Trimble. *eCognition Developer 9 reference book*, 2014.

[32] Leo Breiman. Random forests. *Machine learning*, 45(1):5–32, 2001.

[33] Xiaodong Na, Shuqing Zhang, Xiaofeng Li, Huan Yu, and Chunyue Liu. Improved land cover mapping using random forests combined with landsat thematic mapper imagery and ancillary geographic data. *Photogrammetric Engineering & Remote Sensing*, 76(7):833–840, 2010.

[34] Jane Whitcomb, Mahta Moghaddam, Kyle McDonald, Erika Podest, and Josef Kellndorfer. Wetlands map of Alaska using L-Band radar satellite imagery. In *Geoscience and Remote Sensing Symposium, 2007. IGARSS 2007. IEEE International*, pages 2487–2490. IEEE, 2007.

[35] Koreen Millard and Murray Richardson. Wetland mapping with LiDAR derivatives, SAR polarimetric decompositions, and LiDAR–SAR fusion using a random forest classifier. *Canadian Journal of Remote Sensing*, 39(4):290–307, 2013.

[36] SC Zoltai and DH Vitt. Canadian wetlands: environmental gradients and classification. *Vegetatio*, 118(1-2):131–137, 1995.

[37] Bob Slade. RADARSAT-2 product description. *RN-SP-52-1238*, (1/6), 2009.

[38] Jong-Sen Lee and Eric Pottier. *Polarimetric radar imaging: from basics to applications*. CRC press, 2009.

[39] Jong-Sen Lee, Mitchell R Grunes, and Gianfranco De Grandi. Polarimetric SAR speckle filtering and its implication for classification. *IEEE Transactions on Geoscience and remote sensing*, 37(5):2363–2373, 1999.

[40] John Alan Richards et al. *Remote sensing with imaging radar*, volume 1. Springer, 2009.

[41] Alaska Satellite Facility Engineering Group. Alaska Satellite Facility (ASF) MapReady User Manual, 2016.

[42] Anthony Freeman and Stephen L Durden. A three-component scattering model for polarimetric SAR data. *IEEE Transactions on Geoscience and Remote Sensing*, 36(3):963–973, 1998.

[43] Shane R Cloude and Eric Pottier. An entropy based classification scheme for land applications of polarimetric SAR. *IEEE Transactions on Geoscience and Remote Sensing*, 35(1):68–78, 1997.

[44] Canadian Center for Remote Sensing. Advanced radar polarimetry tutorial.

[45] Yasser Maghsoudi. Analysis of radarsat-2 full polarimetric data for forest mapping, 2011.

[46] Magaly Koch, Thomas Schmid, Melissa Reyes, and Jose Gumuzzio. Evaluating full polarimetric C-and L-band data for mapping wetland conditions in a semi-arid environment in Central Spain. *IEEE Journal of Selected Topics in Applied Earth Observations and Remote Sensing*, 5(3):1033–1044, 2012.

[47] Bahram Salehi, Yun Zhang, Ming Zhong, Vivik Dey, et al. A review of the effectiveness of spatial information used in urban land cover classification of VHR imagery. *International Journal of Geoinformatics*, 8(2), 2012.

[48] Bahram Salehi, Yun Zhang, and Ming Zhong. A combined object-and pixel-based image analysis framework for urban land cover classification of VHR imagery. *Photogrammetric Engineering & Remote Sensing*, 79(11):999–1014, 2013.

[49] Bahram Salehi, Yun Zhang, Ming Zhong, and Vivek Dey. Object-based classification of urban areas using VHR imagery and height points ancillary data. *Remote Sensing*, 4(8):2256–2276, 2012.

[50] Robert M Haralick, Karthikeyan Shanmugam, et al. Textural features for image classification. *IEEE Transactions on systems, man, and cybernetics*, (6):610–621, 1973.

[51] Meisam Amani, Bahram Salehi, Sahel Mahdavi, Jean Elizabeth Granger, Brian Brisco, and Alan Hanson. Wetland classification using multi-source and multi-temporal optical remote sensing data in Newfoundland and Labrador, Canada. *Canadian Journal of Remote Sensing*, 43(4):360–373, 2017.

[52] Gordon Hughes. On the mean accuracy of statistical pattern recognizers. *IEEE transactions on information theory*, 14(1):55–63, 1968.

[53] Kevin O Pope, Jose M Rey-Benayas, and Jack F Paris. Radar remote sensing of forest and wetland ecosystems in the Central American tropics. *Remote Sensing of Environment*, 48(2):205–219, 1994.

[54] Laura L Hess, John M Melack, Solange Filoso, and Yong Wang. Delineation of inundated area and vegetation along the Amazon floodplain with the SIR-C synthetic aperture radar. *IEEE Transactions on Geoscience and Remote Sensing*, 33(4):896–904, 1995.

[55] Meisam Amani, Bahram Salehi, Sahel Mahdavi, Jean Granger, and Brian Brisco. Wetland classification in Newfoundland and Labrador using multi-source SAR and optical data integration. *GIScience & Remote Sensing*, 54(6):779–796, 2017.

Chapter 5

A Novel Dynamic Classification Scheme for Mapping Spectrally Similar Classes: Application to Wetland Classification

5.1 Preface

In this chapter, an innovative dynamic classification scheme was proposed which has proved effective for classification of wetlands or other complicated land covers. The paper resulted from this chapter has been submitted and is currently *under review*.

5.2 Abstract

Land cover classification is one of the most critical, yet challenging applications of Remote Sensing (RS) technologies. Applying numerous features is common for complex land cover classification, which makes feature selection necessary. Although in the case of spectrally similar classes such as wetlands, selected feature subsets may yield high overall accuracies, several individual accuracies are often low. One of the reasons behind this phenomenon is that a single feature set used to separate one specific class from the rest might not be appropriate for delineating another class, because the nature of the classes is different from each other. An additional reason is that while the overall accuracy is applied as the measure for evaluating the potential of a feature subset, it may be influenced by a few high-accuracy classes which are spectrally distinct, and for which collecting enough training data is feasible. In this article, rather than simultaneously mapping all the classes, they were classified on an individual basis with a different feature selection associated with each. Spectral analysis was applied to determine both the order of the classes to be mapped and a merging scheme which was applied to the remaining classes to increase the accuracy of the target class. The proposed approach was applied to wetland mapping using five pilot sites throughout Newfoundland and Labrador, Canada. The dataset available for each pilot site differed in quality and quantity. However, the proposed method functioned accurately in all pilot sites, even those with limited satellite and/or field data, and outperformed the classic method by increasing the average producer and user accuracies of wetlands by up to 22% and 25%, respectively. This classification scheme can be applied for mapping any spectrally similar classes.

5.3 Introduction

Since the advent of Remote Sensing (RS), land cover classification using satellite imagery has been one of its most practical applications. Understanding land covers and their transition over time are key elements for monitoring the environment and surface energy balance, and are also principal inputs for other terrestrial processes, including biogeochemical cycles, biomass distributions, and carbon budgets [1–3]. In this regard, RS possesses numerous advantages over the classic ground-based method, which make it ideal for classification. These benefits include extensive spatial coverage, high repetitivity, the availability of images from a wide electromagnetic spectrum and various geometries, and a high potential for automation [4]. At the same time, the availability of several open source satellite images in recent years in both optical and SAR domains, such as Landsat-8, ASTER (Advanced Space borne Thermal Emission and Reflection Radiometer), and Sentinel-1 and -2, has provided the possibility of monitoring different land covers with minimal cost. This, in turn, has stimulated a growing demand on improving the existing algorithms for classification using remotely-sensed imagery.

With the advancement of the existing algorithms for image classification, and the advent of state-of-the-art techniques, such as Object Based Image Analysis (OBIA), mapping various land covers with acceptable accuracy is possible. However, distinguishing between some classes using remotely sensed imagery remains challenging, as a result of the high level of spectral resemblance between them. Urban [5, 6], crop [7, 8], sea ice [9], and wetland [10–12] classifications, for example, fall into this category.

Wetlands are highly beneficial to the environment and provide natural habitats for several species of flora and fauna. Nevertheless, these valuable natural resources have been drained and supplanted with other land uses [13, 14]. Therefore, it is pivotal to monitor the status of wetlands as well as their variation over time. However, wetland classification using remote sensing methods has always been a challenging task, because they have high intra-class and low inter-class variability, and their borders are difficult to determine [15,16]. Furthermore, wetlands are typically located in difficult to reach locales, and, therefore, collecting enough training data for them is often complicated and expensive [17]. Moreover, wetland have a high spatial and temporal variability [18].

One of the solutions sought for mapping spectrally similar classes using remote sensing methods is to apply various features from multiple sources, dates, and configurations [12, 19, 20]. However, increasing the number of features makes using an appropriate feature selection algorithm imperative. This is because the entire feature set cannot be applied in the classification due to the resulting computational complexity, and the classifier inability to sufficiently generalize the classification statistics to all feature layers due to the inadequate amount of training data.

Thus far, numerous feature selection algorithms have been proposed and have been applied in many studies [21–23]. In commonly-used feature selection methods for remote sensing applications, a single feature subset is selected for executing the whole process of classification. Usually, the measure for selecting a feature subset as the suboptimal solution for classification is the level of the overall accuracy associated with that. When the accuracies of all or most classes matter equally, the overall accuracy is one of the few measures which can be a representative of the classification

quality. However, when some of the involving classes are spectrally similar to each other, although the overall accuracy is acceptable after feature selection and classification, some individual class accuracies usually remain low. This is predictable, because:

i A single feature subset does not suffice for separating each class from the rest of the classes. The reason is that the nature of the classes and, consequently, the required features for separating each, might be different.

ii The overall accuracy is affected by the accuracy of a few classes, for which obtaining an acceptable accuracy is not difficult. This is because these classes are spectrally distinct from the rest of the classes. In addition, since these classes can be recognized using high resolution imagery without the need of visiting the field, their amount of training data is often large. On the contrary, the rest of the classes are highly similar to each other, and collecting excessive field data for them is often not feasible.

As a result, accuracy of the spectrally similar classes is unavoidably ignored in the feature selection process, as other classes considerably influence the overall accuracy.

This problem is addressed in this study by proposing a method which does not consider the feature selection and classification as two separate levels, but both steps are parts of a dynamic process. Thus, the result of each step is an active input for the other in a recursive loop, called a *Dynamic Classification Scheme*. In the described approach, all the objects are not classified simultaneously, but the objects belonging to each class are separated from the rest with a distinct feature selection and classification. Determination of the classification order, i.e. the class to be mapped

at each step (thereafter called the target class), is accomplished based on separability analysis. While the target class is being mapped, the remaining classes which are spectrally similar to each other are merged. Once the target class is mapped, it is eliminated from the rest of the process, and then, the classified area corresponding to the target class is masked.

Although the proposed method can be potentially applied to any challenging classification task, the suggested approach was applied to wetlands to evaluate its performance. In this paper, it was attempted to exploit the maximum advantage of full-polarimetric Synthetic Aperture RADAR (SAR), and also to utilize open source and recently launched satellite imagery such as Sentinel-1 and -2.

This paper is organized as follows: Section 5.4 describes the study areas and data, and Section 5.5 elaborates upon the proposed method extensively. Section 5.6 includes the results of the suggested approach, the comparison with the classic method, and some discussion regarding the applied procedure, before the paper is concluded in Section 5.7.

5.4 Study areas and Data

5.4.1 Study Areas

Five pilot sites throughout Newfoundland and Labrador, rich in wetlands, were selected in order to evaluate the proposed method for wetland classification (Figure 5.1). Figure 5.2 demonstrates the true colour composite of Landsat-8 image for Deer Lake, and RapidEye image for the other pilot sites. The acquisition dates of RapidEye

and Landsat-8 images have been mentioned in Table 5.1. Each pilot site covers an area of approximately 700 to 1000 km^2 and varies in terms of climate, location in the province, and the dominant land covers. The Avalon area and Gros Morne have oceanic climate, while the climate of Deer Lake, Grand Falls, and Goose Bay is mostly continental [24,25]. As can be seen from Figure 5.1, the four pilot sites of the Avalon, Deer Lake, Gros Morne, and Grand Falls are located on the island of Newfoundland, while Goose Bay is located in central Labrador. Other than peatlands (bogs and fens), which are the dominant wetland types in the pilot sites, the pilot sites are also covered with balsam fir, black spruce, and other land covers. For more details about these pilot sites, the interested reader can refer to [24, 25].

5.4.2 Data

5.4.2.1 Satellite Data

Table 5.1 describes the satellite data used for the classification of each study area. Thus far, research shows that amongst optical bands, the Near Infrared and Red-Edge bands are the most useful features for delineating wetlands [18]. Amongst various SAR configurations, long wavelengths and small incidence angles are appropriate for detection of woody wetlands such as Swamp, and short wavelengths and large incidence angles are useful for delineating herbaceous wetlands such as Marsh [18]. Therefore, various features from a combination of optical and SAR data can be useful for delineating wetlands. Therefore, in all five pilot sites, a combination of optical, SAR, and DEM data was applied. It was attempted to also exploit freely available satellite data, namely Landsat-8, Sentinel-2, ASTER, Sentinel-1, and ALOS PAL-

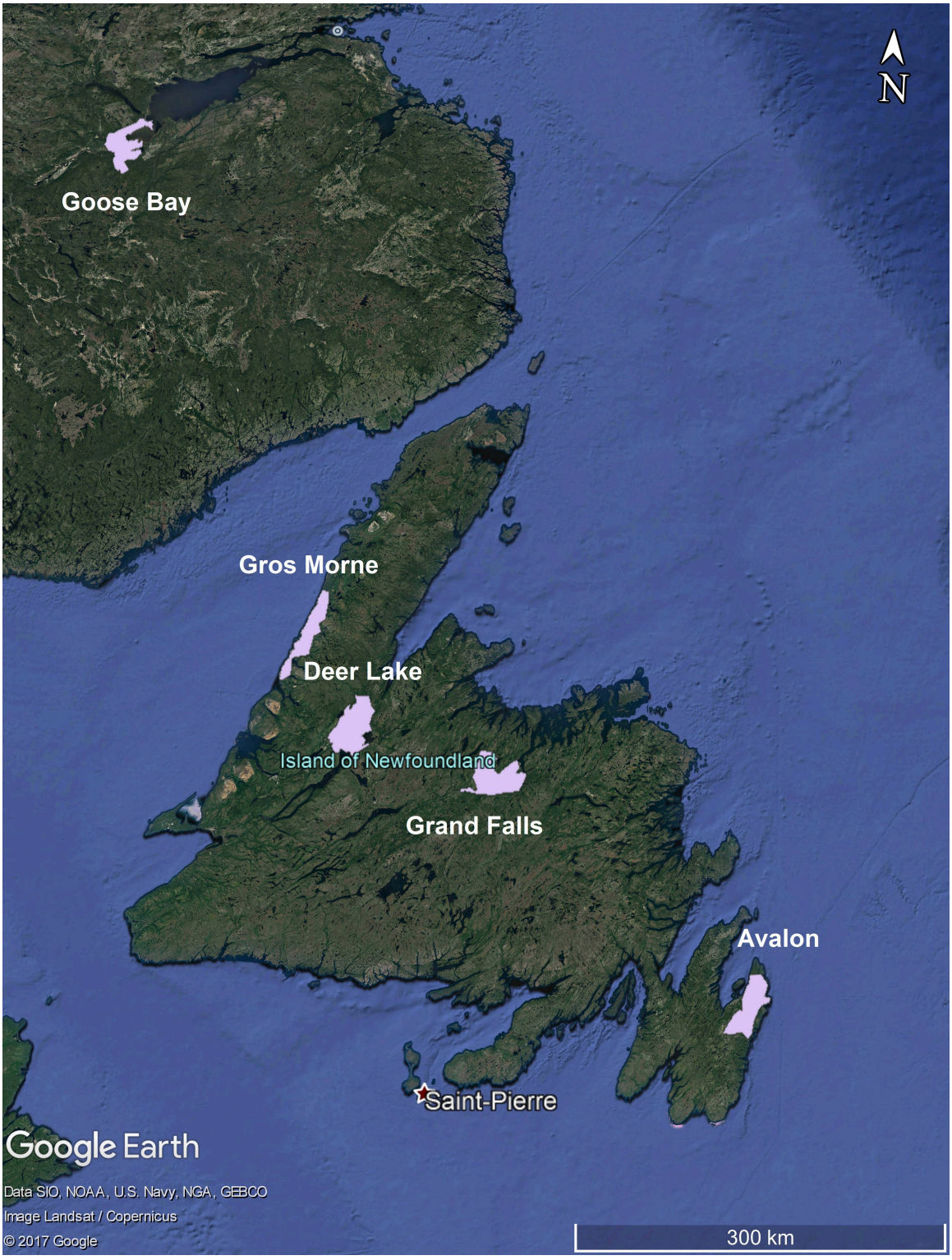

Figure 5.1: The pilot sites.

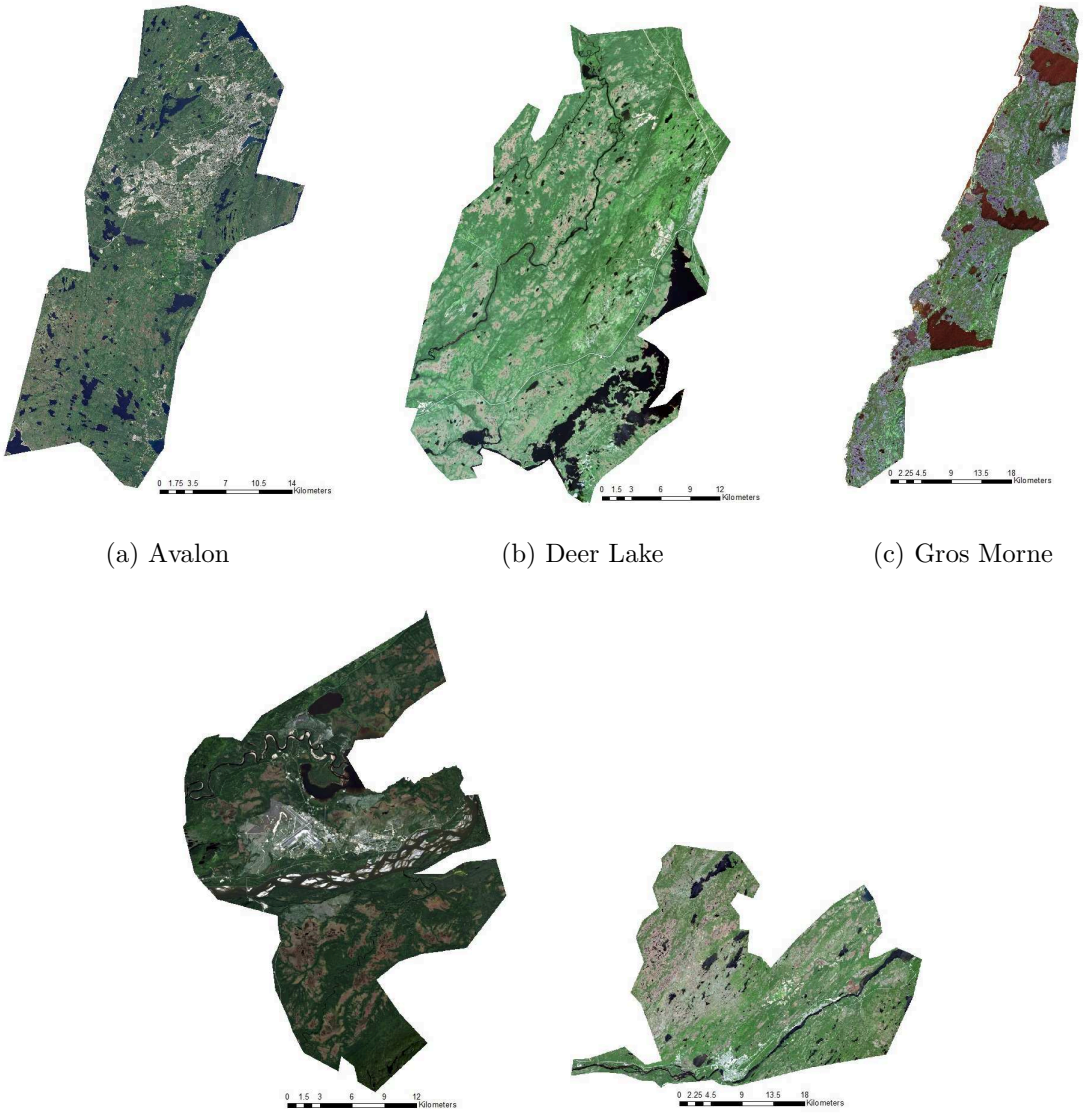

(a) Avalon (b) Deer Lake (c) Gros Morne

(d) Goose Bay (e) Grand Falls

Figure 5.2: Optical images acquired over the five pilot sites in this study.

SAR. ALOS PALSAR stopped working on May 2011 and, consequently, the images acquired by this satellite are outdated relative to the rest of the images. However, ALOS PALSAR data were included in the feature selection process, because L-band images have proved useful for the detection of woody wetlands [15]. Moreover, since wetlands show a high temporal variability, using data from multiple dates can improve the classification accuracy [10–12,26] and, thus, multi-date images were utilized as far as possible (Table 5.1). Table 5.2 demonstrates the characteristics of images used in this study.

Table 5.1: data of acquisition for the satellite images used in the study as a function of the site and the type (optical or SAR)

Sensor	Avalon	Deer Lake	Gros Morne	Goose Bay	Grand Falls
Optical Images					
RapidEye	2015/06/18	N/A	2015/06/18	2015/07/01 2015/10/04	2015/06/10
Landsat-8	2015/06/19	2016/09/30	2016/09/30	2016/09/19	2015/06/10
Sentinel-2	N/A	N/A	2016/06/25	N/A	N/A
ASTER	N/A	N/A	N/A	N/A	2015/09/23
SAR Images					
RADARSAT-2	2015/06/10 2015/08/21	2015/06/23 2015/08/10 2015/10/18	2015/06/16 2015/08/03 2015/10/14	2015/06/30 2015/10/04	N/A
Sentinel-1	2015/08/20	2015/08/15 2015/08/18	2015/08/15	2015/08/20 2015/08/23	2015/08/13
ALOS-2	2015/08/02	N/A	N/A	N/A	N/A
ALOS PALSAR	2010/08/29	2010/09/25	2010/08/10	2009/08/12	2010/08/05
Canadian Digital Surface Model (CDSM)					
Space shuttle Endeavor	2000				

Table 5.2: The characteristics of images used in this study - all available bands of sensors were used unless otherwise mentioned.

Satellite and applied bands	Mode/ Level of processing	Incidence angle range (degrees)	resolution (m) (range resolution for SAR images)
RapidEye	3A	N/A	5
Landsat-8 (Bands 2-7 & 10)	L1T	N/A	30 (Multispectral) 15 (Pan)
Sentinel-2 (Bands 2-12, excl. 10)	L1B	N/A	10 - 20
ASTER (Bands 1-3)	L1T	N/A	15
RADARSAT-2	Single Look Complex (SLC) Fine Resolution Quad Polarization	Depending on the FQ number. For more information, refer to [27]	
Sentinel-1	Interferometric Wide (IW) - level 1A	30-45	10
ALOS-1	Fine Beam Double Polarization (FBD) - level 1.5	7.9-60	20
ALOS-2	Fine Beam Double Polarization (FBD) - level 1	8-70	9.1

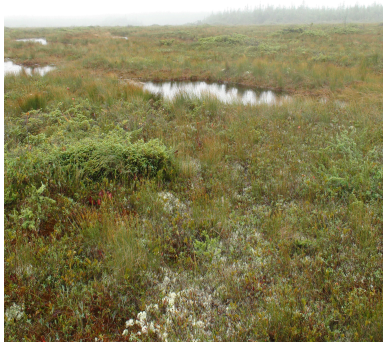

(a) Bog

(b) Fen

(c) Marsh

(d) Swamp

(e) Shallow Water

Figure 5.3: Images of the wetland classes defined by the CWCS. Images were acquired in the Avalon pilot site.

5.4.2.2 Field Data

The Canadian Wetland Classification System (CWCS), developed by Environment Canada in 1987 and updated in 1997, is a classification system specifically applicable to the Canadian Wetland Inventory (CWI) [28]. Accordingly, for the purpose of wetland classification in Newfoundland and Labrador, five wetland classes of *Bog*, *Fen*, *Marsh*, *Swamp*, and *Shallow Water*, defined by CWCS, were considered for classification. These classes are depicted in Figure 5.3, and a brief description of each, adapted from [28, 29], is provided below.

Bog is a type of peatland, the water within which comes only from precipitation. Therefore, these highly acidic and low-nutrient environments are mostly covered with *Sphagnum* moss and ericaceous shrubs. *Fen* is another type of peatland. However, its water source is not only from precipitation, but also from underground and surface flows. Sedges, brown moss, and grass species are dominant in rich fens, while poor fens are similar to bogs in terms of land covers. *Swamp* is wooded wetland, the wood within which can be from trees or shrubs. The water level fluctuation in swamps is larger than that in bogs and fens and both peat and mineral soil can form the substrate of swamps. *Marsh*, however, can only be found on mineral soil. Additionally, the water level within marshes can vary seasonally, monthly, or even daily. They can be influenced by flood and evapotranspiration, or can be parched during a dry season. Marshes are rich in nutrients, and typically appear with aquatic plants. *Shallow water* is a body of water which has a depth smaller than two meters. Occasionally, however, this depth might reduce to a level at which the substrate below is exposed. Aquatic submerged vegetation usually dominate this type of wetland.

For the purpose of field data collection, a team of biologists and wetland ecologists visited all five pilot sites in summer and fall 2015, summer 2016, and summer 2017. Initially, potential wetland sites were selected by visually analyzing aerial photos and satellite images covering the pilot sites. Afterwards, a part of the potential sites were visited based on the ease of accessibility, publicity of ownership, and the level of resemblance of the site to one of the classes defined by the CWCS. Subsequently, if the spot was in fact a wetland, several in-site GPS points along with ancillary notes and photographs would be collected. This information was later used along with several types of remote sensing data to delineate wetland training and test polygons. The minimum sampling unit was one hectare. A similar procedure was followed for collecting field data for the upland class. For other non-wetland classes such as Deep water Urban, Sand, and Lichen-Woodland an analyst selected the best spots using high-resolution aerial imagery. 50% of data was used for training, and 50% for validation in each pilot site. Table 5.3 demonstrates the quantity of training and test data in all five pilot sites in terms of the number of polygons for and the total area covered by each class.

5.5 Method

Figure 5.4 demonstrates a flowchart for the method. Various levels for implementation of the algorithm are elaborated below.

Table 5.3: The number and the area of the training and test data for each pilot site.

Pilot Site (Total Area (km^2))	Classes	# of Training Polygons	Area of Training polygons (km^2)	# of Test Polygons	Area of Test polygons (km^2)
Avalon (783)	Bog	42	1.37	41	1.3
	Fen	20	0.44	19	0.4
	Marsh	25	0.33	25	0.3
	Swamp	22	0.22	23	0.2
	Shallow Water	20	0.55	20	0.6
	Deep Water	7	1.85	8	2.3
	Urban	36	1.82	33	1.6
	Upland	29	1.99	29	2.2
	Total	201	8.6	198	8.7
Deer Lake (982)	Bog	16	1.29	15	1.07
	Fen	27	0.63	27	0.58
	Marsh	12	0.10	12	0.09
	Swamp	20	0.27	20	0.29
	Shallow Water	11	0.25	12	0.43
	Deep Water	3	0.56	3	0.52
	Upland	12	0.41	11	0.37
	Total	100	3.34	101	3.51
Gros Morne (572)	Bog	19	4.34	19	3.45
	Fen	15	0.46	16	0.52
	Marsh	16	0.37	15	0.12
	Swamp	21	0.25	21	0.23
	Shallow Water	13	0.29	14	0.23
	Deep Water	7	1.79	2	1.47
	Upland	42	1.24	43	1.34
	Total	130	7.48	134	8.74
Goose Bay (676)	Bog	14	2.07	14	1.88
	Fen	14	0.60	15	0.79
	Marsh	11	0.54	10	0.24
	Swamp	12	0.19	11	0.16
	Shallow Water	5	0.07	6	0.12
	Deep Water	4	0.73	4	0.48
	Urban	7	0.63	6	0.51
	Upland	10	0.53	11	0.60
	Sand	4	0.72	4	0.53
	Lichen-Woodland	5	0.47	5	0.69
	Total	84	6.54	86	6.01
Grand Falls (949)	Bog	15	1.53	15	2.04
	Fen	31	1.14	30	0.80
	Marsh	22	0.42	23	0.60
	Swamp	15	0.22	15	0.25
	Shallow Water	11	0.32	10	0.20
	Deep Water	219 4	1.07	3	0.60
	Urban	27	0.76	28	0.86
	Upland	9	0.90	9	0.76
	Total	134	6.37	133	6.11

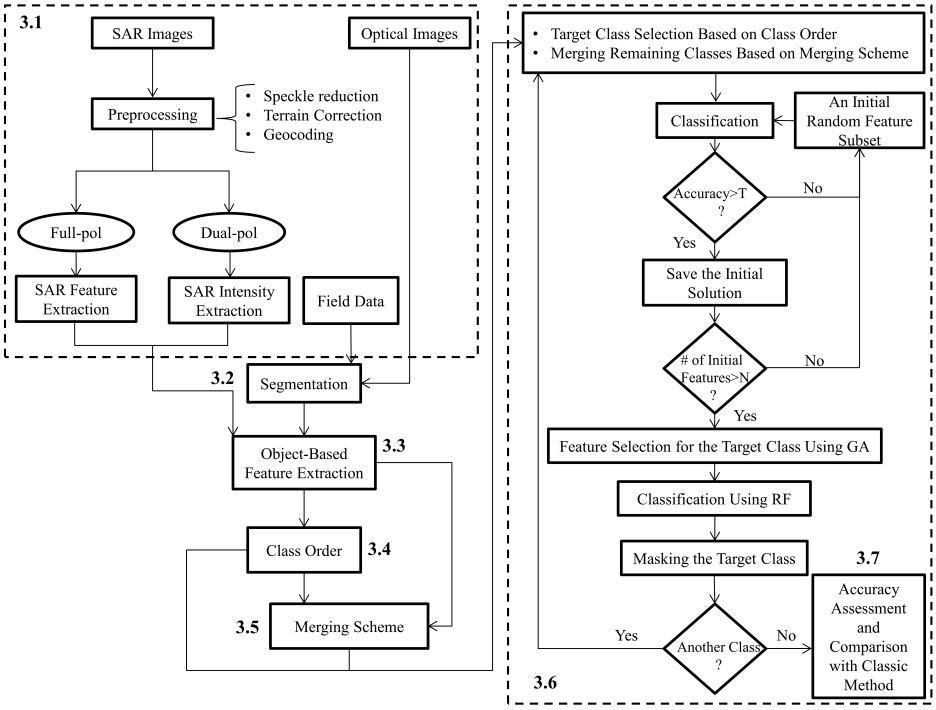

Figure 5.4: The flowchart of the dynamic classification scheme.

5.5.1 Preprocessing and Feature Extraction

Optical images used in this study were geometrically and radiometrically corrected (Table 5.2), and only clear-sky optical images were selected for this work, for which the atmospheric effect was negligible. Therefore, the pre-processing steps are predominantly described for SAR images. In the raw SAR data, the absolute phase is recorded which can be easily distorted during speckle reduction or the geo-referencing process. Consequently, data should be converted to a format in which the relative phase is recorded. Therefore, for the full polarimetric data the scattering matrix was converted to the covariance or coherency matrices, and intensity layers were extracted for other types of SAR data. In the next step, a speckle reduction filter was applied to the SAR data. Full polarimetric data were filtered

by a 7-by-7 PolSAR Lee filter [30], and other types of SAR data were filtered by a 7-by-7 Lee enhanced filter [31]. Afterwards, SAR layers were terrain corrected and georeferenced using the Mapready^{TM} toolkit, developed by Alaska Satellite Facility (ASF; https://www.asf.alaska.edu/data-tools/mapready/). Subsequently, SAR features were extracted from full polarimetric SAR data using PolSARpro^{TM} (Polarimetric SAR Data Processing and Educational Toolbox) developed by the European Space Agency (ESA). In this paper, it was attempted to utilize various polarimetric features, which could be extracted from full-polarimetric RADARSAT-2 images. Therefore, Covariance and Coherency matrices [32], Freeman-Durden [33], H-A-α [34], Krogager [35], Neumann [36], Touzi [37], VanZyl [38], and Yamaguchi [39] decompositions were extracted from all the RADARSAT-2 images using PolSARpro^{TM}. Various polarimetric decompositions divide the total SAR energy received by the sensor to different portions, each of which has a physical meaning, and is therefore useful for wetland detection and classification. As an example, Freeman-Durden decomposition divides the total energy into surface, volume, and double-bounce scatterings, the last of which has been effective for detecting flooded vegetation [15, 40]. Similarly, other polarimetric parameters have been reported useful for wetland detection [41, 42]. The effectiveness of SAR remote sensing for wetland classification have been extensively reviewed in [18].

5.5.2 Segmentation

In recent years, Object Based Image Analysis (OBIA) has proven superior to the traditional pixel-based classification method [10, 43, 44], although this might not be

always the case. In OBIA, the image is segmented into spectrally and geometrically homogeneous objects. Consequently, incorporating spectral, spatial, textural, and other features of the objects into classification is desirable. OBIA was applied in this work, for which segmentation is a prerequisite. In this level, only optical images and field data were ingested into the eCognition Developer^{TM} software to segment the pilot sites using the multi-resolution algorithm [45]. Field data polygons were required to be considered in segmentation such that the boundary of segments conforms the shape of polygons. The multi-resolution algorithm applies a *bottom-up* approach in which pixels are considered object seeds and iteratively grow by being merged with neighbouring objects in a pair-wise manner, depending on the scale, colour, and shape parameters defined by the user. The merging process continues until a user-defined threshold, based on the mentioned parameters, is satisfied [45]. As described in [10], as a result of speckle in SAR data, segmentation of SAR data is by far more difficult and less accurate than for optical imagery. Consequently, only optical images were used in segmentation. The result of segmentation was also overlaid on the SAR and DEM data.

5.5.3 Extraction of Object Based Features

Next, several object based features, including mean and standard deviation of all available bands as well as textural and ratio features of SAR intensity channels were applied. Texture of the objects was evaluated using the Grey Level Co-occurrence Matrix (GLCM), which is a common measure for this purpose [46, 47]. GLCM dissimilarity, entropy, angular second moment, standard deviation, and correlation (all

extensively described in [46]) were evaluated for the available SAR intensity bands. Moreover, various ratio features were defined based on SAR intensity bands:

$$
\begin{aligned}
R_1 &= \frac{I_{HH}}{I_{HV}} \\
R_2 &= \frac{I_{VV}}{I_{HV}} \\
R_3 &= \frac{I_{HH}}{I_{HH} + 2I_{HV} + I_{VV}} \\
R_4 &= \frac{I_{VV}}{I_{HH} + 2I_{HV} + I_{VV}}
\end{aligned}
\tag{5.1}
$$

where I_{pq} is the intensity (power) in the channel with the transmitting polarization of p and the receiving polarization of q which can be horizontal (H) or vertical (V). Note that in R_3 and R_4 the denominator represents the total power. Ratio features are useful for discriminating between the objects producing different amount of backscatter in various polarimetric channels from those having similar backscatter in all channels. These features also convert the absolute values of intensity to relative values, and therefore facilitate detection of different classes [48].

5.5.4 Determination of the Classification Order

One of the important steps in the proposed classification scheme is to decide what order to use for mapping the classes present in the study area. If the analyst is experienced and familiar with the nature of the classes, they can determine the classification order. In this case, classification can be started with the most spectrally distinguishable class (e.g. the Deep Water class in this study) and terminated with the two most spectrally similar classes (e.g. Bog and Fen in this study). However, often the analyst might not be acquainted with the spectral separability of the classes,

or an automatic approach for the entire classification scheme might be required or preferential. In that event, the separability analysis of the classes is necessary.

The Jeffries-Matusita (JM) [49] distance (Equation 6.2) was applied in this study as the separability measure.

$$J_{ij} = 2[1 - \exp(-B_{ij})] \tag{5.2}$$

in which i and j show two arbitrary classes, and B_{ij} is the Bhattacharyya distance, defined as follows:

$$B_{ij} = \frac{1}{8}(m_i - m_j)^T(\frac{\Sigma_i + \Sigma_j}{2})^{-1}(m_i - m_j) + \frac{1}{2}\frac{\ln|\frac{\Sigma_i+\Sigma_j}{2}|}{\sqrt{|\Sigma_i||\Sigma_j|}} \tag{5.3}$$

where m_i and Σ_i are the mean and the covariance matrix for the ith class, respectively, and T is the transpose of a matrix.

Since the above equation is obtained by assuming a Gaussian distribution for the data, not all the bands can be applied for computing JM distance. The optical bands of one single sensor (e.g. RapidEye or Landsat-8 layers in this study) are proper bands to be used for this purpose. However, other channels which have the Gaussian distribution, or other distance measures fitted to the distribution of available bands, can be applied for this purpose.

Using these bands, when the JM distance between all class pairs was obtained, the average separability of class i can be obtained as:

$$J_i = \frac{1}{N}\sum_{j=1}^{N} J_{ij} \tag{5.4}$$

where N is the number of classes. Then, the classification order is determined based

on the average JM distance, such that the class with the greatest average JM distance is classified first, while the class with the smallest average JM distance is classified last. It is interesting to note that determination of classification order can be redone after masking each class. However, this is not expected to change the classification order, because the class which is removed in each step is the spectrally furthest class, and has the greatest average JM distance compared to the rest of the classes.

As an example, the following classification order was considered for the Avalon pilot site:

Deep Water, Urban, Upland, Shallow Water, Marsh, Swamp, Bog, Fen

5.5.5 Determination of the Merging Scheme

When the target class is being mapped according to the classification order, among other classes, those which are spectrally similar should be merged. By merging, the remaining classes become fewer and less similar. Therefore, the classification process becomes less complicated.

Similar to the procedure of the order determination, the analyst can decide how to merge the other classes while the target class is being mapped according to their experience. However, if an automatic procedure is required, the following approach can be taken.

The merging scheme starts from the most confused class, i.e. the class with the smallest average JM distance, here referred to as A. Let the second most confused class be called B. Classes A and B are merged if

$$J_{AB} = average\{J_A, J_B\} < \tau \tag{5.5}$$

where τ is a user-defined threshold. If classes A and B are merged, then the third most confused class, let it be called C, is merged with A and B if:

$$J_{ABC} = average\{J_{AB}, J_C\} < \tau \tag{5.6}$$

This process continues until the above equation no longer holds. It should be noted that when the target class is being mapped, it should not be merged with any other classes. For instance, assuming that classes A, B, and C are merged, C should not be merged with the other two classes when the target class is C. If the analyst is aware of the nature of the classes, the threshold can be selected by investigating the obtained values of the average JM distance for individual classes, such that the classes which are spectrally similar to each other are merged. Otherwise, or if an automatic method for selecting the threshold is required, the third quartile of the average JM distance of all classes can be chosen as the threshold.

As an example, for the Avalon pilot site, four wetland classes of *Marsh*, *Swamp*, *Bog*, and *Fen* were merged during the classification process, before each of them in turn was classified.

5.5.6 Dynamic Feature Selection and Classification

Once the order of the classes as well as the merging scheme are determined, the target class is picked based on the specified order. Afterwards, the remaining classes are merged according to the merging scheme, and the process of feature selection and

classification begins.

In this article, the Genetic Algorithm (GA) [50] was used for feature selection, although any other method can be potentially applied. The principles of the GA have been fully described in many texts, such as [51], [52], and [53] to which interested readers can refer. However, a brief explanation about the GA is also provided here for the sake of completeness.

GAs lie in the group of evolutionary algorithms and can be applied in various optimization problems, one of which is feature selection. In feature selection based on GA, each feature corresponds to a gene which can either have the value of 0 (feature not included in classification) or 1 (feature included in classification). A chromosome is a binary string which is constituted by lying genes beside each other. In fact, each chromosome is a feature subset or a solution for feature selection. Note that the number of genes in a chromosome equals the total number of features. Each solution in GA is associated with a fitness measure which illustrates the solution's degree of suitability to be selected as the final answer. Normally, in feature selection the fitness measure is the overall accuracy. In this work, however, the overall accuracy is not an appropriate measure, because each class is separately classified and both the producer and user accuracies of each class are important. Consequently, the fitness measure was selected as follows:

$$f = min\{UA, PA\} \tag{5.7}$$

where UA and PA are the user and producer accuracies of the target class, respectively. The minimum of the two accuracies is selected to guarantee that both

accuracies associated with a solution are adequately high.

Feature selection using GA starts with a specific number of randomly generated initial solutions. In the proposed method, each randomly generated solution is first assessed in terms of the fitness measure (Equation 6.6), and is only allowed in the rest of the algorithm if the fitness measure of the solution exceeds a user-defined threshold. The reason for filtering the initial solutions is that sometimes, especially when the existing classes are spectrally mixed, the classification accuracy resulting from a random feature subset is too low. This can affect the accuracy associated with the final feature subset yielded by the GA. The process of filtering the initial solutions is illustrated in Figure 5.4. When enough initial solutions with a desired level of accuracy for the target class are generated, the initial solutions are ingested into the GA such that a final feature set is yielded for the target class. In the next step, classification is carried out.

In this study, Random Forest (RF) [54] is selected as the classification method, which has proved effective for wetland classification [10–12]. RF consists of an ensemble of decision trees. A decision tree consists of several nodes, which divide the input pixels/objects into mutually exclusive groups, each of which contains the most homogeneous pixels/objects. This division continues into progressively homogeneous groups until each node is representative of the one of final classes [55]. After training the classifier, the pixel/object is passed through each single tree and the final class label for the pixel/object is determined based on the majority of votes obtained by the terminal node of the trees. RF has several tuning parameters which should be determined by user. The depth of trees, minimum number of samples used per node, minimum tree number, and number of selected features in each node are the most

important user-defined parameters. These parameters can affect the classification accuracy considerably [12].

Finally, the target class is classified using the optimum feature subset obtained by the GA. When classification is terminated, the target class is masked and the described process is reiterated with the next target class until no class remains. Ultimately, all class polygons are combined into a single map and the accuracy is assessed.

5.5.7 Accuracy Assessment and Comparison with Classic Method

In this step, the accuracy of the resulting map is assessed using the test data, and the result is compared with the so-called classic method both quantitatively and qualitatively. In the classic method, the available feature set, and the training and test data are entirely identical to the features and field data available for the proposed method. The preprocessing, segmentation, and object-based feature extraction steps are the same as those described for the proposed method. In the next step, however, the initial solutions for GA are selected such that the *overall accuracy* is greater than a threshold, and GA converges to a solution which maximizes the *overall accuracy*. Next, that single feature subset is used to map all the classes simultaneously using RF. A similar scheme has been widely used in the literature for feature selection and classification [56, 57], and that is the reason the authors refer to this method as the*classic* method.

5.6 Results and Discussion

The proposed classification scheme was applied on all pilot sites. Table 5.4 demonstrates the segmentation parameters and the number of objects for all pilot sites. Moreover, Table 5.5 illustrates the accuracy thresholds for all classes used in this study. It is recommended that users select a reasonable accuracy as the threshold for each class which is achievable considering the available training data and the spectral nature of that class. It should be also mentioned that the merging threshold for each pilot site was in the range of 1.75 to 1.8. For each pilot site, the map produced from the proposed method along with the accuracies (class-based, average of wetlands, and overall) are provided. Furthermore, charts are provided to compare the proposed approach and the classic classification scheme (with a single feature selection and a single classification) in terms of all three types of accuracies. The details for each site are given below.

Table 5.4: Segmentation parameters and number of objects for all pilot sites.

Segmentation Parameters	Scale	Shape	Compactness		
	300	0.1	0.5		
Number of Objects	Avalon	Deer Lake	Gros Morne	Goose Bay	Grand Falls
	29,562	5,525	9,154	14,211	14,663

The resulting maps of five pilot sites using the proposed method are illustrated in Figure 5.5, and the classification accuracies are displayed in Table 5.6. Further, Figure 5.6 illustrates the results of the comparison between the proposed classification scheme and the classic method. In all five pilot sites, not only the proposed method has increased the overall accuracy, but also it has significantly raised the average

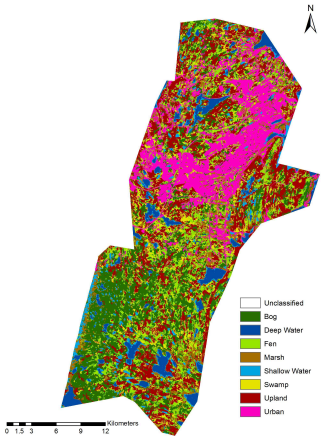

(a) Avalon

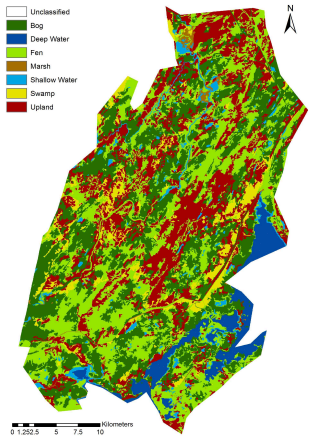

(b) Deer Lake

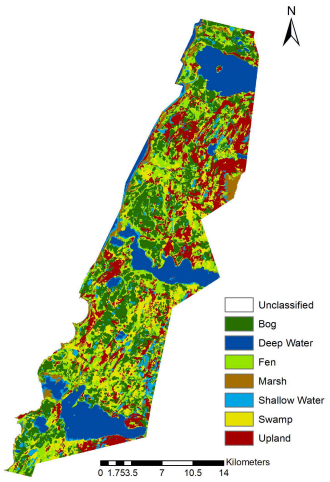

(c) Gros Morne

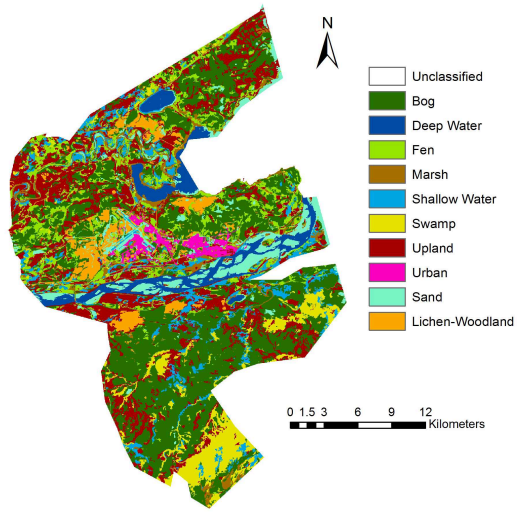

(d) Goose Bay

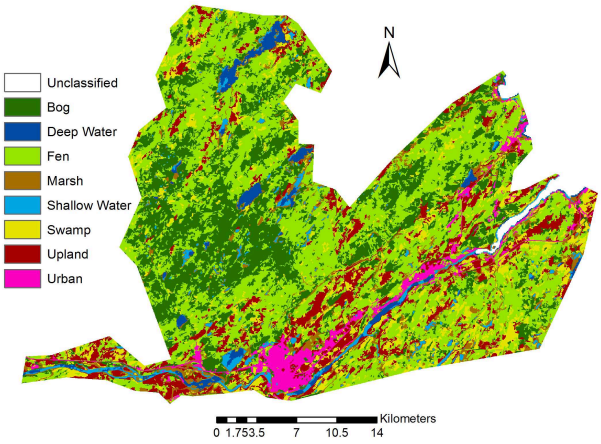

(e) Grand Falls

Figure 5.5: The classified image of five pilot sites using the proposed method.

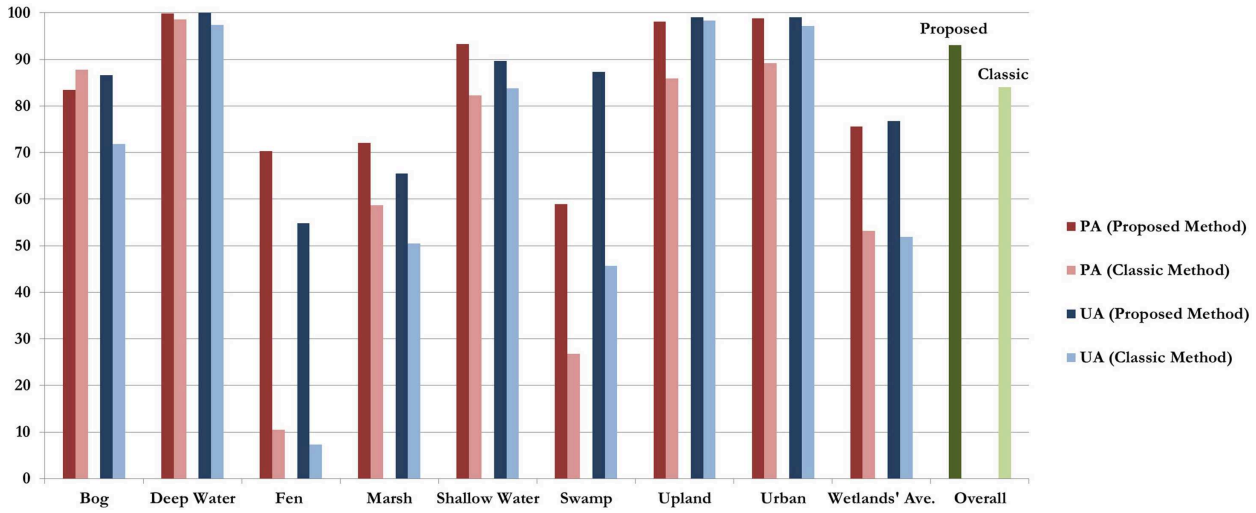

(a) Avalon

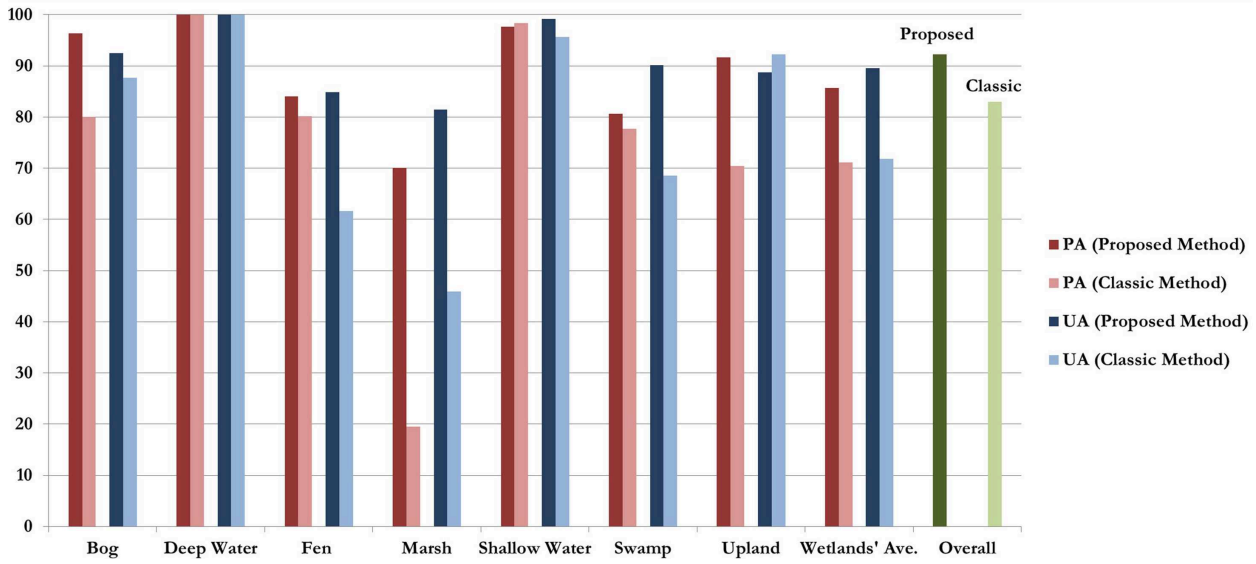

(b) Deer Lake

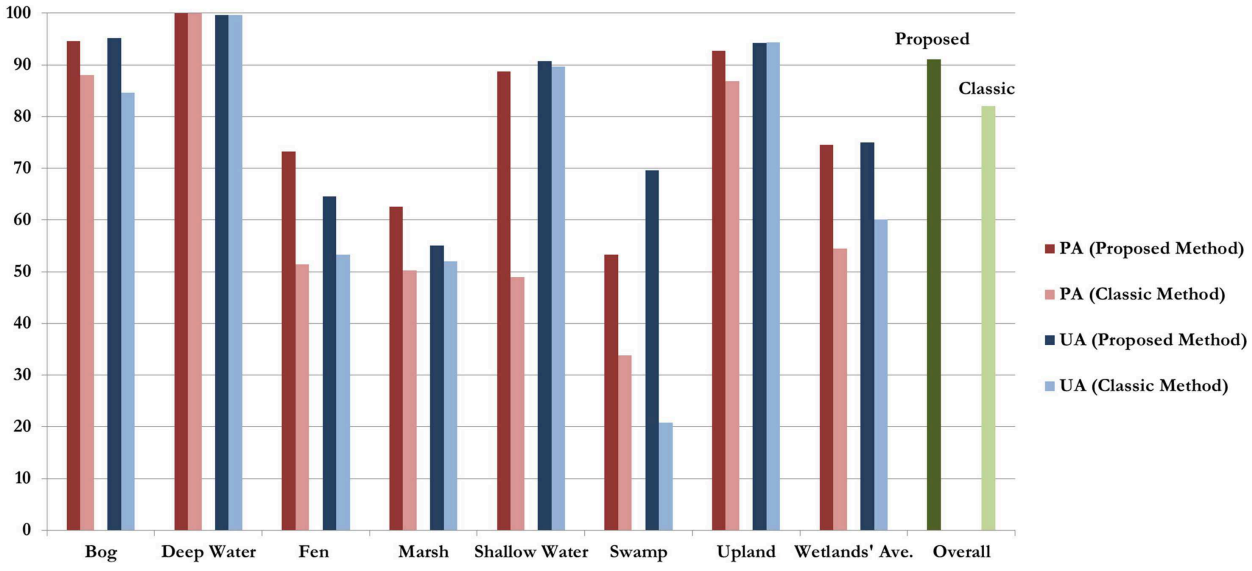

(c) Gros Morne

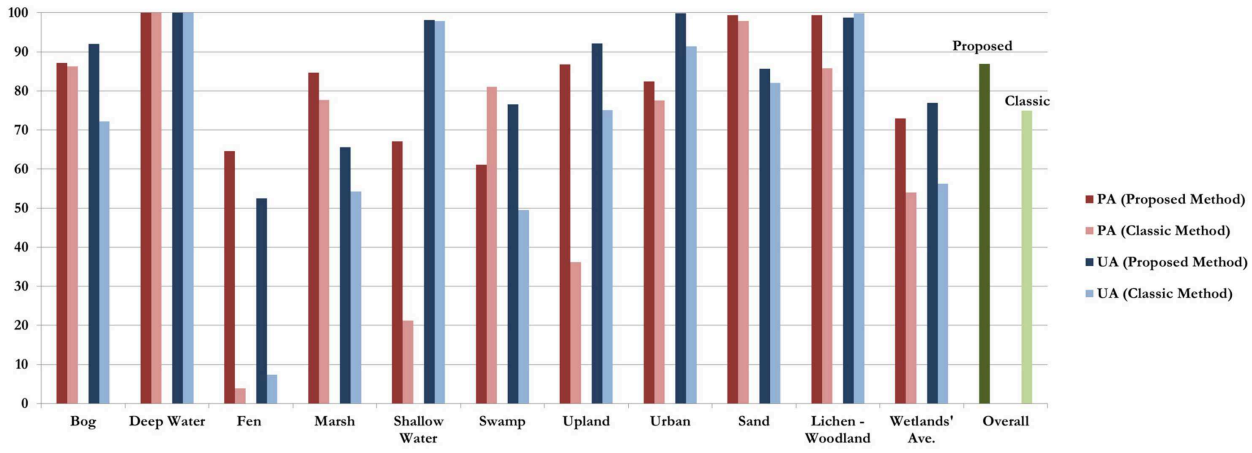

(d) Goose Bay

Table 5.5: The threshold values for the producer and user accuracies of each class in all pilot sites of this study.

	Bog	Deep Water	Fen	Marsh	Shallow Water	Swamp	Upland	Urban	Sand	Lichen-Woodland
Class producer accuracy	83	99.5	50	55	65	50	85	85	90	90
Class user accuracy	86	99.5	50	55	85	65	85	90	85	90

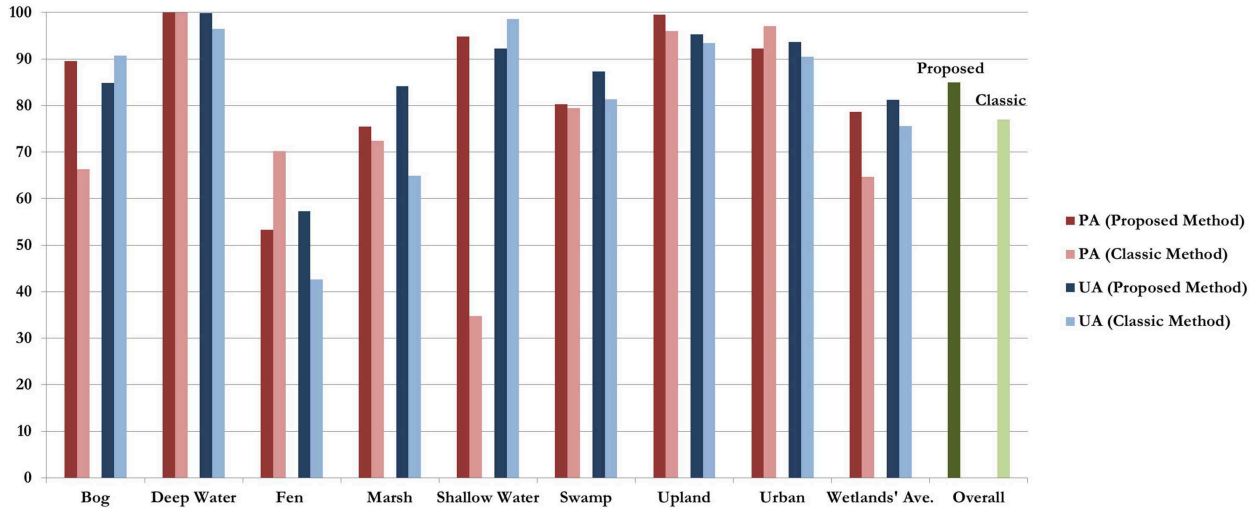

(e) Grand Falls

Figure 5.6: The comparison between the proposed method and the classic method in all five pilot sites.

Table 5.6: The individual and overall accuracies obtained for all pilot sites using the proposed method.

	Avalon		Deer Lake	
Class	Producer accuracy	User accuracy	Producer accuracy	User accuracy
Bog	83.41	86.61	96.36	92.46
Deep Water	99.85	99.97	100.00	100.00
Fen	70.36	54.78	84.03	84.88
Marsh	72.03	65.48	70.07	81.49
Shallow Water	93.32	89.67	97.65	99.15
Swamp	58.96	87.28	80.60	90.09
Upland	98.12	99.09	91.68	88.72
Urban	98.88	99.11	N/A	N/A
Overall Accuracy	93.11		92.24	
Average of Wetlands	75.62	76.76	85.74	89.61

	Gros Morne		Grand Falls	
Class	Producer accuracy	User accuracy	Producer accuracy	User accuracy
Bog	94.60	95.16	89.54	84.81
Deep Water	100.00	99.59	99.96	99.90
Fen	73.25	64.62	53.29	57.34
Marsh	62.52	55.11	75.52	84.17
Shallow Water	88.77	90.68	94.79	92.27
Swamp	53.33	69.55	80.34	87.29
Upland	92.75	94.26	99.51	95.31
Urban	N/A	N/A	92.22	93.69
Overall Accuracy	91.10		85.01	
Average of Wetlands	74.49	75.02	78.70	81.18

	Goose Bay	
Class	Producer accuracy	User accuracy
Bog	87.14	92.08
Deep Water	100.00	99.94
Fen	64.56	52.51
Marsh	84.70	65.63
Shallow Water	67.09	98.08
Swamp	61.05	76.61
Upland	86.82	92.19
Urban	82.37	99.86
Sand	99.35	85.62
Lichen-Woodland	99.36	98.73
Overall Accuracy	86.89	
Average of Wetlands	72.91	76.98

producer and user accuracies of wetlands in a range from 5% to 25%, depending on the pilot sites. Several individual class accuracies are very low in each pilot site using the classic method. By applying the proposed method, however, no individual class accuracy is below 50%, and most of them are above 70%. For the purpose of visual assessment, samples of zoomed areas from the resulting map along with the corresponding optical images over the same area are depicted in Figure 5.7. It can be observed that the resulting maps of all pilot sites are of high quality, and the classes which can be discerned from the optical imagery of the area, including the Deep Water and Urban classes, have been mapped accurately.

The selected study areas differed considerably in terms of the available datasets. For example, there was no RapidEye image in Deer Lake, and Grand Falls also lacked RADARSAT-2 full-polarimetric data. Additionally, the number of RADARSAT-2 image acquisitions per pilot site was different. Nevertheless, the results of the proposed approach in all pilot sites were satisfactory, and the obtained accuracies were all higher than those obtained using the classic method. This outcome is auspicious, because it demonstrates that the needed dataset can be minimized by adopting a proper approach, or even be restricted to freely available images. Consequently, having inexpensive and up-to-date wetland maps with minimum need of field data would be possible. Moreover, the classification of Goose Bay was more challenging compared to other pilot sites, because other than typical classes, Goose Bay also contains the Sand and Lichen-Woodland classes. Nevertheless, the proposed algorithm has successfully mapped all wetland and non-wetland classes with high accuracies. These results manifest in a way that as the classification becomes more complicated, the classic method fails to map all classes successfully. The proposed method, however,

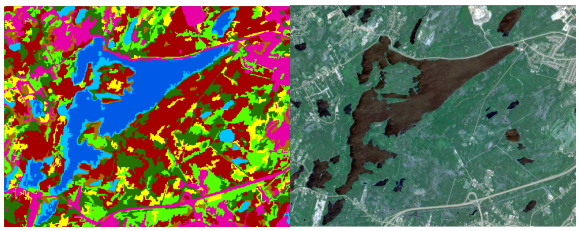

(a) Avalon (classified) (b) Avalon (optical)

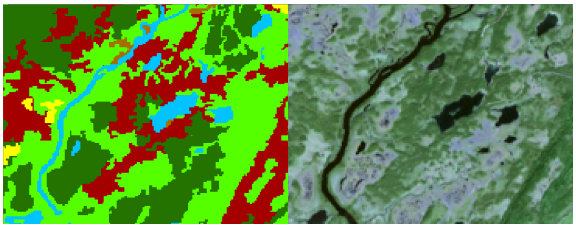

(c) Deer Lake (classified) (d) Deer Lake (optical)

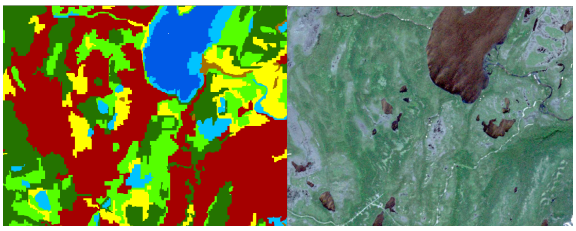

(e) Gros Morne (classified) (f) Gros Morne (optical)

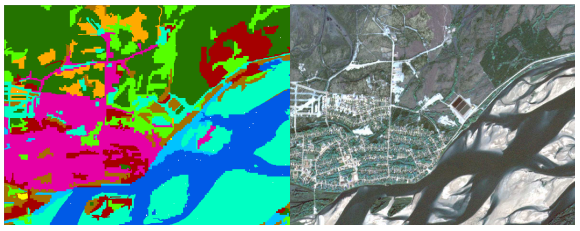

(g) Goose Bay (classified) (h) Goose Bay (optical)

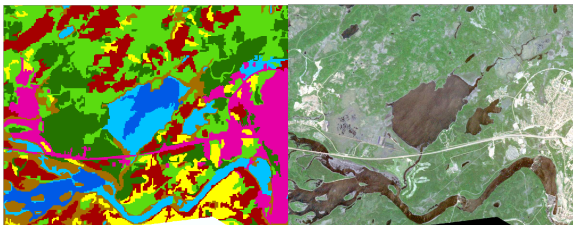

(i) Grand Falls (classified) (j) Grand Falls (optical)

Figure 5.7: Several zoomed parts of the resulting maps along with the optical images

can be regarded as a robust classification method, even when many spectrally similar classes are included in the classification process.

Figure 5.8 demonstrates the variation of producer and user accuracies of individual classes with the change in the density of training data for the Avalon pilot site. As expected, the accuracies increase with the augmentation of training data. Intriguingly, although the density of training data is low for most of wetland classes, all the accuracies are above 50% using the proposed method.

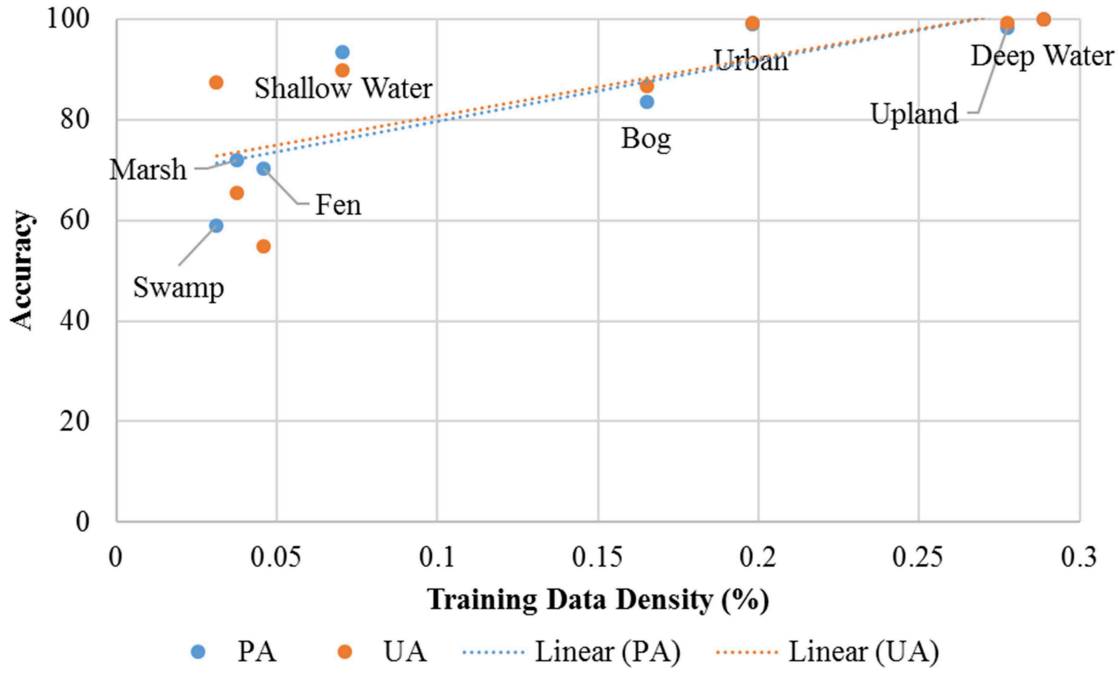

Figure 5.8: The producer and user accuracies of each class versus the density of the training data available for that class in the Avalon area. PA and UA indicate the producer and user accuracies, respectively.

The proposed algorithm is of a considerable flexibility. For instance, the fea-

ture selection algorithm and the classifier can be conveniently supplanted with other algorithms. Clearly, more advanced methods for feature selection are expected to improve the results further. Moreover, although a great number of features were used in most of the pilot sites, achieving high accuracy was possible using a fewer number of features. This fact was reflected in the classification of Grand Falls, where no full-polarimetric image was available, but the obtained accuracy remained reasonable. It is also worth mentioning that this method is especially useful when a small amount of training data is available. In this study the amount of training data for some wetland classes at most pilot sites was not massive, such that the classic method failed to map them accurately. However, the proposed method increased the accuracy of those classes considerably.

The computational complexity of the proposed classification scheme is at the most N-1 times greater than the computational complexity of the classic classification scheme, where N is the number of classes. Since wetland classification is not a real-time application, the accuracy of the final map as well as the cost of the adopted approach are more important than the computational complexity of the method.

In the proposed scheme, when a class is mapped, all objects belonging to that class are masked and are not considered in the classification process anymore. Therefore, it is important that as far as possible, no pixel from the masked class is left for the rest of the classification process. This corresponds to minimum omission or high producer accuracy for that class. Likewise, it is important that as far as possible, no pixel from the other classes exists in the masked class, which is equivalent to minimum commission or high user accuracy for that class. As a result, one of the key points in this classification scheme is to have high producer and user accuracies, especially for

initially mapped classes. If the producer and user accuracies of the initially mapped classes are high, there will be a greater probability that the accuracy for the rest of the classes will also be high. Moreover, when some classes are highly confused with each other, it is wise to map the class with a higher probability of underestimation first. In addition, it is worth noting that violating the classification order does not affect the accuracy considerably if the classes are completely separated from each other. Also, when a class tends to be underestimated, it is preferable to map that class before other classes. By doing so, there is a lower chance that pixels/objects belonging to that class are misclassified and masked in the preceding classification steps.

Another important point about the proposed classification scheme is the method for accuracy assessment. If the number of test samples for two classes is not equivalent, comparing their accuracy will not be useful. The reason is that if the number of misclassified pixels/objects is the same for two classes, the accuracy of the class with fewer test samples will be lower than that of the class with more test samples. In other words, one of the shortcomings of the current method for accuracy assessment is that the accuracies are highly dependent on the number and location of test samples, while a robust assessment should be independent from the number of test samples. Therefore, the visual assessment of the resulting map beside the quantitative assessment, is an asset. The reason is that the quantitative assessment of the output map is restricted to the test data, while the visual assessment is carried out by considering the entire map. Therefore, some defects can only be found using visual assessment.

5.7 Conclusion

In this article, a classification scheme was proposed which addresses the problem of poor individual accuracies despite having a high overall accuracy when mapping spectrally similar classes using a feature selection method. This usually happens because the features which are effective in distinguishing one class, are not necessarily appropriate for delineating another class. Furthermore, the fitness measure is usually the overall accuracy in a typical feature selection method. As a consequence, the general approach guarantees the overall accuracy to be high, while some per-class accuracies might remain low. In the proposed method, all the individual class accuracies are attempted to be made acceptable using a hierarchical scheme. In this scheme, all the objects are not mapped simultaneously, but those belonging to each class are delineated in separate steps, and each step is associated with a distinct feature selection and classification. While mapping each class according to a pre-defined order, the remaining classes, which are spectrally similar to each other are merged such that the accuracy of the target class increases.

The suggested scheme was applied for wetland classification at five pilot sites within the province of Newfoundland and Labrador, Canada. Wetland classification was selected because not only do wetland classes highly resemble each other in various remote sensing datasets, but also collecting field samples for them is arduous. This is because wetlands are mainly located in remote and inaccessible places. Moreover, aerial photo interpretation for wetland classification is not highly accurate, since some wetland classes look quite similar in aerial imagery. These issues can also contribute to low accuracies in wetland mapping, other than the inherently similar nature of

wetland classes. Nevertheless, the suggested approach resulted in acceptable per-class and overall accuracies compared to the classic method at all five pilot sites, regardless of the quality and quantity of the applied dataset, which was above the accuracies reported in similar studies. For example, [12] obtained the average producer and user accuracies of wetlands ranging from 68% to 73% by the sole use of optical data in the same study areas as the current study. Similarly, these accuracies were 71% and 72% by fusing optical and SAR data in [11] in the same study areas. Moreover, the proposed method has a high potential for performing affordable and frequent mapping when the involved classes are similar in remotely sensed data, with a computational complexity comparable to that of the classic scheme. The proposed method also has a considerable flexibility, having the capacity for a more advanced feature selection method or other classifiers. Therefore, it is expected that this method will get further attention in future studies.

Acknowledgements

This project was undertaken with the financial support of the Government of Canada through the federal Department of Environment and Climate Change, and Natural Sciences and Engineering Research Council of Canada (NSERC) under Grants to B. Salehi (NSERC RGPIN-2015- 05027). The SAR imagery was provided by the Canada Center for Mapping and Earth Observation and Environment and Climate Change Canada. Field data was collected by various organizations including, Ducks Unlimited Canada, Government of Newfoundland and Labrador Department of Environment and Conservation, and Nature Conservancy Canada. The authors thank

these organizations for the generous financial supports and providing such valuable datasets.The work of W. Huang was supported by the Natural Sciences and Engineering Research Council of Canada (NSERC) Discovery Grant RGPIN-2017-04508.

Bibliography

[1] Mark A Friedl and Carla E Brodley. Decision tree classification of land cover from remotely sensed data. *Remote sensing of environment*, 61(3):399–409, 1997.

[2] Zhe Zhu and Curtis E Woodcock. Continuous change detection and classification of land cover using all available landsat data. *Remote sensing of Environment*, 144:152–171, 2014.

[3] Suming Jin, Limin Yang, Zhe Zhu, and Collin Homer. A land cover change detection and classification protocol for updating alaska NLCD 2001 to 2011. *Remote Sensing of Environment*, 195:44–55, 2017.

[4] Norman Kerle, Lucas LF Janssen, and Gerrit C Huurneman. Principles of remote sensing. *ITC, Educational textbook series*, 2, 2004.

[5] Bahram Salehi, Yun Zhang, Ming Zhong, and Vivek Dey. Object-based classification of urban areas using VHR imagery and height points ancillary data. *Remote Sensing*, 4(8):2256–2276, 2012.

[6] Zhe Zhu, Curtis E Woodcock, John Rogan, and Josef Kellndorfer. Assessment of spectral, polarimetric, temporal, and spatial dimensions for urban and peri-

urban land cover classification using Landsat and SAR data. *Remote Sensing of Environment*, 117:72–82, 2012.

[7] Stephen South, Jiaguo Qi, and David P Lusch. Optimal classification methods for mapping agricultural tillage practices. *Remote Sensing of Environment*, 91(1):90–97, 2004.

[8] Qazi Sami Ul Haq, Linmi Tao, Fuchun Sun, and Shiqiang Yang. A fast and robust sparse approach for hyperspectral data classification using a few labeled samples. *IEEE Transactions on Geoscience and Remote Sensing*, 50(6):2287–2302, 2012.

[9] Bernd Scheuchl, Ian Cumming, and Irena Hajnsek. Classification of fully polarimetric single-and dual-frequency SAR data of sea ice using the Wishart statistics. *Canadian Journal of Remote Sensing*, 31(1):61–72, 2005.

[10] Sahel Mahdavi, Bahram Salehi, Meisam Amani, Jean Elizabeth Granger, Brian Brisco, Weimin Huang, and Alan Hanson. Object-based classification of wetlands in Newfoundland and Labrador using multi-temporal polsar data. *Canadian Journal of Remote Sensing*, 43(5):432–450, 2017.

[11] Meisam Amani, Bahram Salehi, Sahel Mahdavi, Jean Granger, and Brian Brisco. Wetland classification in Newfoundland and Labrador using multi-source sar and optical data integration. *GIScience & Remote Sensing*, 54(6):779–796, 2017.

[12] Meisam Amani, Bahram Salehi, Sahel Mahdavi, Jean Elizabeth Granger, Brian Brisco, and Alan Hanson. Wetland classification using multi-source and multi-temporal optical remote sensing data in Newfoundland and Labrador, Canada. *Canadian Journal of Remote Sensing*, 43(4):360–373, 2017.

[13] William J Mitsch and James G Gosselink. Wetlands john wiley & sons. *Inc., New York, New York*, 2000.

[14] Marcelle Grenier, Anne-Marie Demers, Sandra Labrecque, Martine Benoit, Richard A Fournier, and Bruno Drolet. An object-based method to map wetland using radarsat-1 and landsat etm images: test case on two sites in Quebec, Canada. *Canadian Journal of Remote Sensing*, 33(S1):S28–S45, 2007.

[15] Floyd M Henderson and Anthony J Lewis. Radar detection of wetland ecosystems: a review. *International Journal of Remote Sensing*, 29(20):5809–5835, 2008.

[16] Iryna Dronova. Object-based image analysis in wetland research: a review. *Remote Sensing*, 7(5):6380–6413, 2015.

[17] Alisa L Gallant, Robert W Klaver, Gary S Casper, and Michael J Lannoo. Global rates of habitat loss and implications for amphibian conservation. *Copeia*, 2007(4):967–979, 2007.

[18] Sahel Mahdavi, Bahram Salehi, Jean Granger, Meisam Amani, Brian Brisco, and Weimin Huang. Remote sensing for wetland classification: a comprehensive review. *GIScience & Remote Sensing*, (just-accepted), 2017.

[19] Cornelius Senf, Pedro J Leitão, Dirk Pflugmacher, Sebastian van der Linden, and Patrick Hostert. Mapping land cover in complex mediterranean landscapes using landsat: Improved classification accuracies from integrating multi-seasonal and synthetic imagery. *Remote Sensing of Environment*, 156:527–536, 2015.

[20] B Scheuchl, I Hajnsek, and I Cumming. Sea ice classification using multi-frequency polarimetric SAR data. In *Geoscience and Remote Sensing Symposium, IGARSS'02 proceedings*, volume 3, pages 1914–1916, 2002.

[21] Frieke MB Van Coillie, Lieven PC Verbeke, and Robert R De Wulf. Feature selection by genetic algorithms in object-based classification of IKONOS imagery for forest mapping in flanders, belgium. *Remote Sensing of Environment*, 110(4):476–487, 2007.

[22] Ben Somers and Gregory P Asner. Multi-temporal hyperspectral mixture analysis and feature selection for invasive species mapping in rainforests. *Remote Sensing of Environment*, 136:14–27, 2013.

[23] Manuel A Penaloza and Ronald M Welch. Feature selection for classification of polar regions using a fuzzy expert system. *Remote Sensing of Environment*, 58(1):81–100, 1996.

[24] Robin South. *Biogeography and Ecology of the Island of Newfoundland*, volume 48. Springer Science & Business Media, 1983.

[25] Ecological Stratification Working Group, Center for Land and Biological Resources Research, and Canada State of the Environment Directorate. *A national ecological framework for Canada*. Centre for Land and Biological Resources Research; Hull, Quebec: State of the Environment Directorate, 1996.

[26] T Lee and JA Richards. A low-cost classifier for multitemporal applications. *International Journal of Remote Sensing*, 6(8):1405–1417, 1985.

[27] Bob Slade. RADARSAT-2 product description. *RN-SP-52-1238*, (1/6), 2009.

[28] G Adams, P Buteau, N Dignard, P Grondin, J Jeglum, D Keys, and S Zoltai. The Canadian wetland classification system, 1997.

[29] SC Zoltai and DH Vitt. Canadian wetlands: environmental gradients and classification. *Vegetatio*, 118(1-2):131–137, 1995.

[30] Jong-Sen Lee, Mitchell R Grunes, and Gianfranco De Grandi. Polarimetric SAR speckle filtering and its implication for classification. *IEEE Transactions on Geoscience and remote sensing*, 37(5):2363–2373, 1999.

[31] Armand Lopes, Ridha Touzi, and E Nezry. Adaptive speckle filters and scene heterogeneity. *IEEE Transactions on Geoscience and Remote Sensing*, 28(6):992–1000, 1990.

[32] Jong-Sen Lee and Eric Pottier. *Polarimetric radar imaging: from basics to applications*. CRC press, 2009.

[33] Anthony Freeman and Stephen L Durden. A three-component scattering model for polarimetric SAR data. *IEEE Transactions on Geoscience and Remote Sensing*, 36(3):963–973, 1998.

[34] Shane R Cloude and Eric Pottier. An entropy based classification scheme for land applications of polarimetric SAR. *IEEE Transactions on Geoscience and Remote Sensing*, 35(1):68–78, 1997.

[35] E Krogager. New decomposition of the radar target scattering matrix. *Electronics Letters*, 26(18):1525–1527, 1990.

[36] Maxim Neumann, Andreas Reigber, and Laurent Ferro-Famil. Data classification based on PolInSAR coherence shapes. In *Geoscience and Remote Sensing Symposium, IGARSS'05 proceedings*, volume 7, pages 4852–4855, 2005.

[37] Ridha Touzi. Target scattering decomposition in terms of roll-invariant target parameters. *IEEE Transactions on Geoscience and Remote Sensing*, 45(1):73–84, 2007.

[38] Jakob J Van Zyl. Unsupervised classification of scattering behavior using radar polarimetry data. *IEEE Transactions on Geoscience and Remote Sensing*, 27(1):36–45, 1989.

[39] Yoshio Yamaguchi, Toshifumi Moriyama, Motoi Ishido, and Hiroyoshi Yamada. Four-component scattering model for polarimetric SAR image decomposition. *IEEE Transactions on Geoscience and Remote Sensing*, 43(8):1699–1706, 2005.

[40] Sang-Hoon Hong, Hyun-Ok Kim, Shimon Wdowinski, and Emanuelle Feliciano. Evaluation of polarimetric SAR decomposition for classifying wetland vegetation types. *Remote Sensing*, 7(7):8563–8585, 2015.

[41] B Brisco, M Kapfer, T Hirose, B Tedford, and J Liu. Evaluation of C-band polarization diversity and polarimetry for wetland mapping. *Canadian Journal of Remote Sensing*, 37(1):82–92, 2011.

[42] Cécile Marechal, Eric Pottier, Laurence Hubert-Moy, and Sebastien Rapinel. One year wetland survey investigations from quad-pol RADARSAT-2 time-series SAR images. *Canadian Journal of Remote Sensing*, 38(3):240–252, 2012.

[43] Molly Reif, Robert C Frohn, Charles R Lane, and Brad Autrey. Mapping isolated wetlands in a karst landscape: GIS and remote sensing methods. *GIScience & Remote Sensing*, 46(2):187–211, 2009.

[44] Robert Lawrence Kettig and DA Landgrebe. Classification of multispectral image data by extraction and classification of homogeneous objects. *IEEE Transactions on geoscience Electronics*, 14(1):19–26, 1976.

[45] Ursula C Benz, Peter Hofmann, Gregor Willhauck, Iris Lingenfelder, and Markus Heynen. Multi-resolution, object-oriented fuzzy analysis of remote sensing data for gis-ready information. *ISPRS Journal of photogrammetry and remote sensing*, 58(3):239–258, 2004.

[46] Robert M Haralick, Karthikeyan Shanmugam, et al. Textural features for image classification. *IEEE Transactions on systems, man, and cybernetics*, (6):610–621, 1973.

[47] ecognition developer 9 reference book, version 9.0.3, 2014.

[48] Meisam Amani, Bahram Salehi, Sahel Mahdavi, Brian Brisco, and Mohamed Shehata. A multiple classifier system to improve mapping complex land covers: a case study of wetland classification using SAR data in Newfoundland, Canada. *International Journal of Remote Sensing*, pages 1–14, 2018.

[49] Shirley M Davis, David A Landgrebe, Terry L Phillips, Philip H Swain, Roger M Hoffer, John C Lindenlaub, and Leroy F Silva. Remote sensing: the quantitative approach. *New York, McGraw-Hill International Book Co., 1978. 405 p.*, 1978.

[50] John H Holland. Adaptation in natural and artificial systems. an introductory analysis with application to biology, control, and artificial intelligence. *Ann Arbor, MI: University of Michigan Press*, 1975.

[51] David Beasley, David R Bull, and Ralph Robert Martin. An overview of genetic algorithms: Part 1, fundamentals. *University computing*, 15(2):56–69, 1993.

[52] Lawrence Davis. Handbook of genetic algorithms. 1991.

[53] Zbigniew Michalewicz. *Genetic algorithms+ data structures= evolution programs*. Springer Science & Business Media, 2013.

[54] Leo Breiman. Random forests. *Machine learning*, 45(1):5–32, 2001.

[55] Leo Breiman, Jerome Friedman, Charles J Stone, and Richard A Olshen. *Classification and regression trees*. CRC press, 1984.

[56] Liangpei Zhang, Yanfei Zhong, Bo Huang, Jianya Gong, and Pingxiang Li. Dimensionality reduction based on clonal selection for hyperspectral imagery. *IEEE Transactions on Geoscience and Remote Sensing*, 45(12):4172–4186, 2007.

[57] Hongjun Su, Qian Du, Genshe Chen, and Peijun Du. Optimized hyperspectral band selection using particle swarm optimization. *IEEE Journal of Selected Topics in Applied Earth Observations and Remote Sensing*, 7(6):2659–2670, 2014.

Chapter 6

A Polarimetric Synthetic Aperture Radar Change Detection Index Based on Neighbourhood Information

6.1 Preface

In this chapter, a polarimetric index was introduced for SAR change detection based on neighbourhood information. Since a long-term dataset of SAR images from NL was not available at the time of writing this section, the method was applied on a flooding event in Dongting lake, Hunan, China. The paper resulted from this chapter has been submitted and it is currently *under review*.

6.2 Abstract

Change detection using Remote Sensing (RS) techniques is valuable in numerous applications, including environmental management and hazard monitoring. Synthetic Aperture Radar (SAR) images have proved even more effective in this regard as a result of their all-weather, day and night acquisition capabilities. In this study, a polarimetric index based on the ratio of span (total power) values is introduced in which the neighbourhood information is considered. The role of the central pixel and its neighbourhood is adjusted using a weight parameter. The proposed index was applied to detect flooded areas in Dongting lake, Hunan, China, and was then compared with the Wishart Maximum Likelihood Ratio (MLR) test. Results demonstrated that although the proposed index and the Wishart MLR test provided similar accuracies (accuracy of 94% and 93%, and Kappa Coefficient of 0.82 and 0.86, respectively), inclusion of neighbourhood information in the proposed measure makes the objects within the yielded map more connected and less noisy.

6.3 Introduction

Change detection in Remote Sensing (RS) is estimating the amount of change between two images acquired on different dates over the same geographical area. RS Change detection has been widely used for assessing the effect of natural hazards, tracking environmental contaminations, monitoring water resources, monitoring crops and vegetation, and other applications [1–4]. Change detection using SAR images is advantageous as a result of their all-weather, day and night acquisition capability.

Furthermore, with the growth in the number of active SAR satellites, the use of multi-temporal images is facilitated. However, SAR change detection demands specific techniques as a result of the presence of speckle in SAR images.

In general, SAR change detection algorithms can be divided into pre-classification and post-classification methods. While post-classification methods are limited to comparing the accuracy of two classified maps [5], in recent years a variety of pre-classification approaches have emerged.

Among the pre-classification methods, quite a few are applicable to single-channel SAR images. The most basic methods for single-channel SAR change detection include algebraic operations, such as computing the difference and ratio of images [6]. Ratio and log-ratio operations are popular for SAR images because of the reduction of speckle and changing the image distribution to Gaussian, respectively. For example, [7] fused the complementary information in the mean-ratio and log-ratio images to generate a difference image in which the changed areas are effectively highlighted. Moreover, [8] automatized thresholding the log-ratio image by analyzing a cost function.

Other approaches which are also suitable for single- or dual-channel SAR images include Principal Component Analysis (PCA) and Change Vector Analysis (CVA). In [9], for example, PCA was used to reduce the dimension of a neighbourhood feature vector proposed by the authors in the context of change detection. Similarly, in [10], PCA was applied on non-overlapping blocks of difference image before they were projected on eigenvector space. Furthermore, [11] combined CVA with post-classification comparison to detect changes using RADARSAT-2 images.

At the same time, several change detection indices, derived from the covariance

matrix, are utilized for polarimetric change detection. For instance, in [12], two indices of Contrast Ratio and Ellipticity were compared with five other measures for a change detection study. For deriving these two indices, eigen values of a matrix generated from the covariance matrices of the two dates needed to be extracted. Another successful method for polarimetric change detection is the Wishart Maximum Likelihood Ratio (MLR) test proposed by [13] which has proved effective in this regard. In this method, a test was performed for equality of two matrices with a complex Wishart distribution, from which an index was proposed. The index image was then thresholded to highlight the changed areas.

Moreover, there are several distance measures which can be used in change detection studies based on the covariance or coherency matrix. As an example, Wishart-Chernoff distance was utilized in [11] for investigating the potential of compact polarimetric SAR data with the aim of monitoring wetlands. Moreover, [14] introduced a new distance measure entitled Generalized Likelihood Ratio Test (GLRT) distance for detecting changes in urban areas.

Most of the above mentioned methods have proved accurate in change detection studies using SAR images. In order to make correct managerial decisions, however, it is crucial to provide maps which are harmonious with real-world objects, and do not suffer from the salt-and-pepper structure. This goal is facilitated by taking neighbourhood information into account in the case of SAR images which are blemished with the effect of speckle. Although there are a few studies which have considered neighbourhood information in SAR change detection [15–17], most of them ignore this valuable information.

In this paper, a single channel change detection index based on neighbourhood

information is extended to polarimetric SAR data. This index uses span (total power) values, and considers the ratio of the minimum to the maximum intensity values between two dates, such that the effect of backscatter variation among different classes, noise, and errors are minimized. In this index, the role of the central pixel and its neighbourhood is adjusted using a weight parameter. This index is then compared with the Wishart MLR index, both quantitatively and qualitatively.

The paper is organized as follows. In Section 2, the dataset and study area are explained. The methodology is outlined in Section 3, and Results are discussed in Section 4, before the concluding remarks are provided in Section 5.

6.4 Study Areas and Dataset

Dongting lake in the Hunan province of China, located approximately at $29°19'N$ and $112°57'E$, was selected as the study area in this research. This area is prone to flooding from July to September each year which makes it ideal for change detection studies. Figure 6.1 shows two true color composite Landsat 5 images over the study area before and after a flooding event. As can be observed, cloud cover is a common problem of optical images which hinders change detection studies using these images.

Full-polarimetric SAR images used in this study are shown in Table 6.1 and their corresponding colour composite is depicted in Figure 6.2. The reference image, obtained by visual analysis of the SAR images, is also illustrated in Figure 6.2(c).

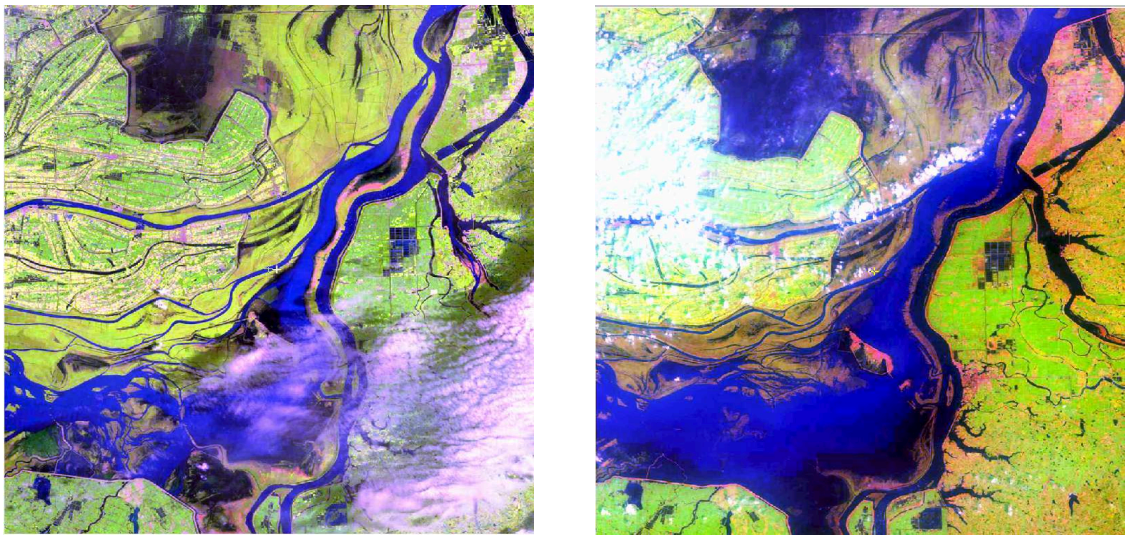

(a) (b)

Figure 6.1: Two optical images over the study area, before and after a flood event.

Table 6.1: The characteristics of images used in this study.

Acquisition date	Mode	Polarization Type	Incidence angle range (degrees)	Nominal range resolution (m)
2008/06/06 2008/08/17	FQ16	Quad-pol	35.4-37	8.6-9

(a)

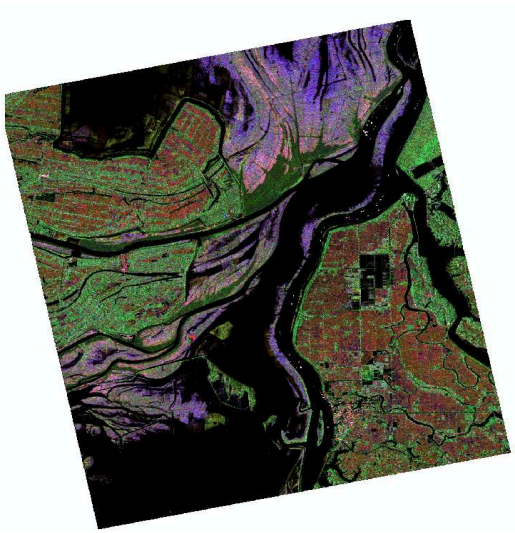

(b)

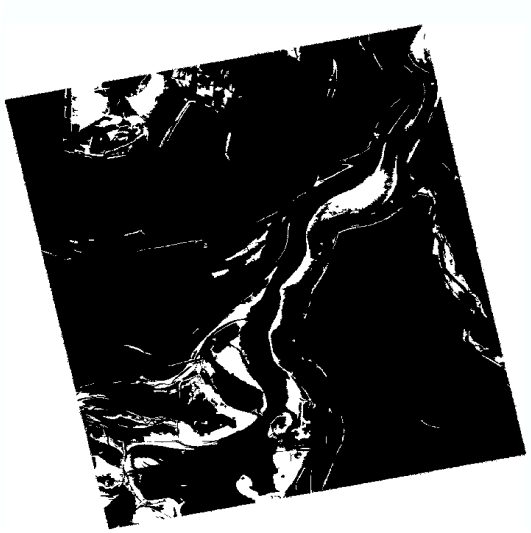

(c)

Figure 6.2: The color composite of the SAR images a) before, and (b) after the flooding event. Red, green, and blue channels correspond to the HH, HV, and VV intensity images, respectively. (c) The reference image.

6.5 Methodology

In the first step, the scattering matrix of each full polarimetric SAR image is converted to the covariance matrix to avoid distorting the absolute phase information during processing. Covariance matrices are subsequently filtered by a 7-by-7 PolSAR Lee filter [18] and are terrain-corrected and geocoded using the Mapready^{TM} toolkit, developed by the Alaska Satellite Facility (ASF). Afterwards, the span image corresponding to each date is calculated as follows:

$$S_i = |S_{HH}|_i^2 + 2|S_{HV}|_i^2 + |S_{VV}|_i^2 \qquad i = \{1, 2\} \tag{6.1}$$

where S_{PQ} is the element of the scattering matrix recorded for the transmitting polarization of P and receiving polarization of Q.

In the next step, a neighbourhood is considered for each pixel in the SAR image. In this work, a 7-by-7 window is considered for this purpose, but this can change depending on the level of noise in the image. Then, the difference image proposed in [15] can be heuristically extended to the Polarimetric Difference Image (PDI) as follows:

$$PDI(x) = \delta_s \times \frac{min\{S_1(x), S_2(x)\}}{max\{S_1(x), S_2(x)\}} + (1 - \delta_s) \times \frac{\sum\limits_{i \in \Omega_x \wedge i \neq x} min\{S_1(i), S_2(i)\}}{\sum\limits_{i \in \Omega_x \wedge i \neq x} max\{S_1(i), S_2(i)\}} \tag{6.2}$$

$$\delta_s = \frac{\sigma_s(x)}{\mu_s(x)}$$

where $S_i(x)$ is the span image for the pixel x in the ith image, Ω_x is the neighbourhood of the pixel, and $\sigma_s(x)$ and $\mu_s(x)$ are the standard deviation and the average of the span image neighbourhood, respectively. δ_s is a weight measure which determines the

effect of the pixel and its neighbourhood in the measure. When δ_s is large, the area is heterogeneous and the role of central pixel is more important than its neighbourhood. When δ_s is small, however, the area is homogeneous and the neighbourhood effect is more significant [15]. Moreover, since there is the ratio of the minimum to maximum intensity in both parts of Equation 6.2, the effect of the variation of intensity among different classes, the level of noise, and the presence of errors on the change detection map is minimized. After computing the PDI measure, an image is obtained in which the magnitude of each pixel demonstrates the level of similarity between two images. If the change of a specific class is of interest, the image can be thresholded to highlight those changes. The aim of this work is the detection of flooded areas and therefore the histogram of the PDI image is thresholded by Otsu's method [19]. In Otsu's method, the threshold(s) of the histogram are determined by maximizing between class variance or minimizing within class variance [19].

For comparing the proposed measure with another polarimetric index, the Wishart MLR test is selected [13]:

$$Q = \frac{(n+m)^{p(n+m)}}{n^{pm} m^{pm}} \frac{|X|^n |Y|^m}{|X+Y|^{n+m}} \tag{6.3}$$

where X and Y are the first and second covariance matrices, respectively, and n and m demonstrate the number of looks in the first and second image, respectively, $|.|$ denotes the determinant of a matrix, and P is the size of the matrix which is 3 in this study.

When $m = n$, which is the case in our work, lnQ can be defined as follows:

$$lnQ = n\,(2p\,ln2 + ln|X| + ln|Y| - 2\,ln|X+Y|) \tag{6.4}$$

Similar to the map produced by PDI, the lnQ image can be finally thresholded by Otsu's method to emphasize the areas of interest. Then, the measures are compared both quantitatively and qualitatively. For quantitative comparison, the number of False Negatives (FNs), False Positives (FPs), True Negatives (TNs), and True Positives (TPs) is computed. Then, the Overall Error (OE) and the Percentage Correct Classification (PCC) are obtained by:

$$OE = FN + FP \tag{6.5}$$

$$PCC = (TN + TP)/(TN + TP + FN + FP) \tag{6.6}$$

Moreover, if we consider a confusion matrix with two classes of *change* and *no change*, Kappa coefficient can be calculated as follows [20]:

$$\kappa = \frac{P\sum_{k} x_{kk} - \sum_{k} x_{k+}x_{+k}}{P^2 - \sum_{k} x_{k+}x_{+k}} \tag{6.7}$$

where P is the total number of elements in the confusion matrix, x_{ij} is the element in the ith row and jth column, x_{i+} is the summation of the elements in the ith row, and x_{+j} is the summation of the elements in the jth column. Kappa is another measure of the accuracy assessment which can take values in the range of [0, 1]. A value of 0 for Kappa means there is no agreement between the produced map and the reference data, while a value of 1 for Kappa demonstrates the complete agreement between the generated map and the reference data.

6.6 Results and Discussion

Figure 6.3 demonstrates the yielded PDI and lnQ maps. It can be observed that both measures have delineated the flooded areas effectively, and could be used to locate and estimate the flooded regions accurately. However, it is clear that the quantization of the changes in the PDI image is more detailed than lnQ image. For example, the left part of the lnQ image near the top provides a rather homogeneous area with small changes being missed. However, if we consider the same area in the PDI image, we can see how different amounts of change have been effectively quantized. A more important feature of the PDI map is that it provides objects which are less speckled as a result of considering neighbourhood information. On the contrary, some of the objects within the lnQ maps have a salt-and-pepper structure.

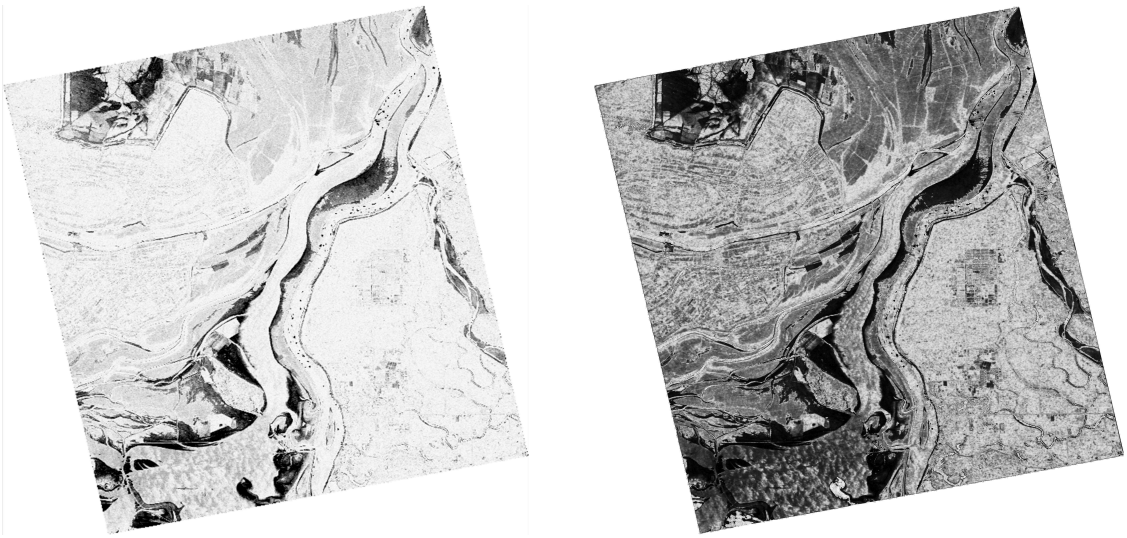

(a) lnQ map (b) PDI map

Figure 6.3: Change detection maps obtained by lnQ and PDI measures.

The histogram of the lnQ and PDI maps have been demonstrated in Figure 6.4

(a-b). The fact that there are more quantizations in the PDI image than the lnQ image is clear from their histograms as well. In the next step, the histogram of the PDI and lnQ maps was thresholded using Otsu's method to detect the flooded areas. The range of data for the lnQ and PDI images was (-1461 , 0] and [0, 1], respectively. The thresholds selected for binarizing the images were -160 for the lnQ image, and 0.118 for the PDI image.

Figure 6.4 (c-d) demonstrates the binarized lnQ and PDI images. At first, both images look similar to each other. However, the objects produced by the lnQ map appear more speckled and disconnected compared to PDI map. When examining the maps more closely, several subsets of the images were selected and the zoomed areas of the lnQ and PDI images, along with their corresponding binary maps, are depicted in Figure 6.5. It is clear that while the zoomed regions in the lnQ map (Figure 6.5, i-l) are slightly speckled, disparate, and unconnected, the regions in the PDI map (Figure 6.5, m-p) are more homogeneous and linked. This fact has caused the thresholded lnQ map to contain more discrete and noisy objects (Figure 6.5, q-t), while the binary PDI map provides clean and connected regions (Figure 6.5, u-x).

For a quantitative assessment of both maps, the binarized maps were compared with the reference image. Table 6.2 shows the comparison results. It is viewed that both methods have generated a highly accurate map with the PCC of 93% and 94%, and the Kappa coefficient of 0.82 and 0.86, respectively. However, the accuracies of the PDI map are slightly greater as a result of including neighbourhood information. Interestingly, the number of FNs is high in the lnQ map, while the number of FPs is high in the PDI image. This shows that the lnQ index overestimates, while the PDI index underestimates the amount of change.

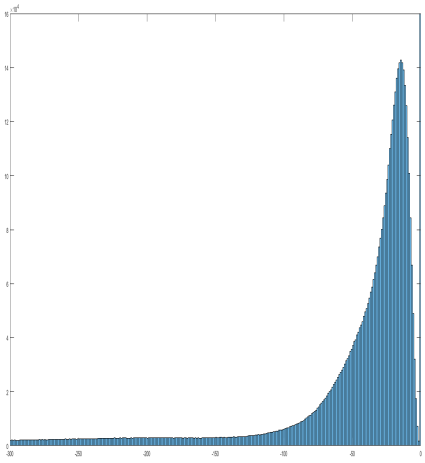

(a) Histogram of the lnQ image

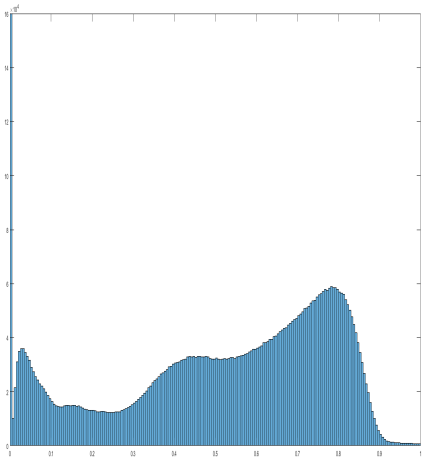

(b) Histogram of the PDI image

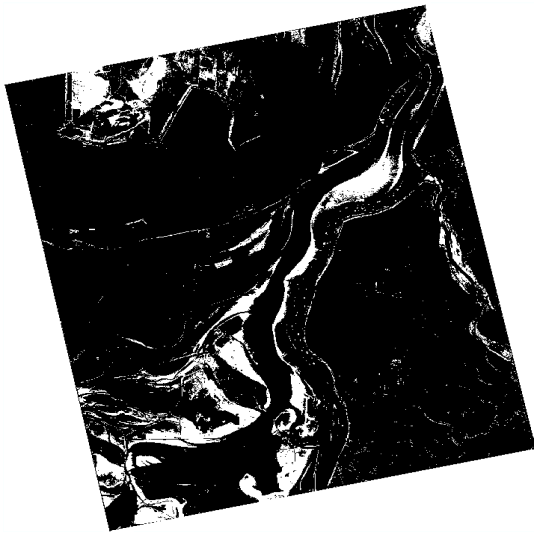

(c) Thresholded lnQ map

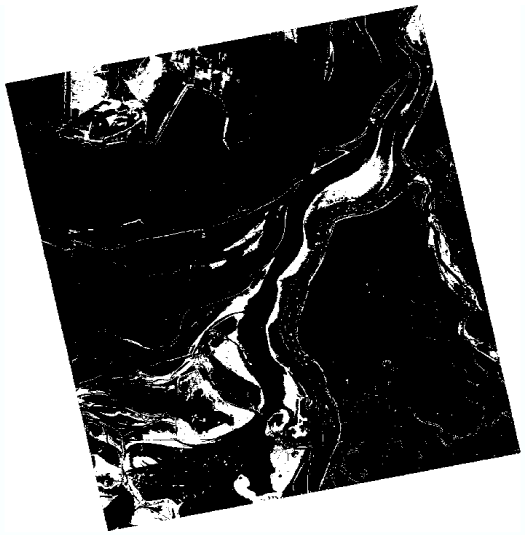

(d) Thresholded PDI map

Figure 6.4: Binary change detection maps obtained by lnQ and PDI measures.

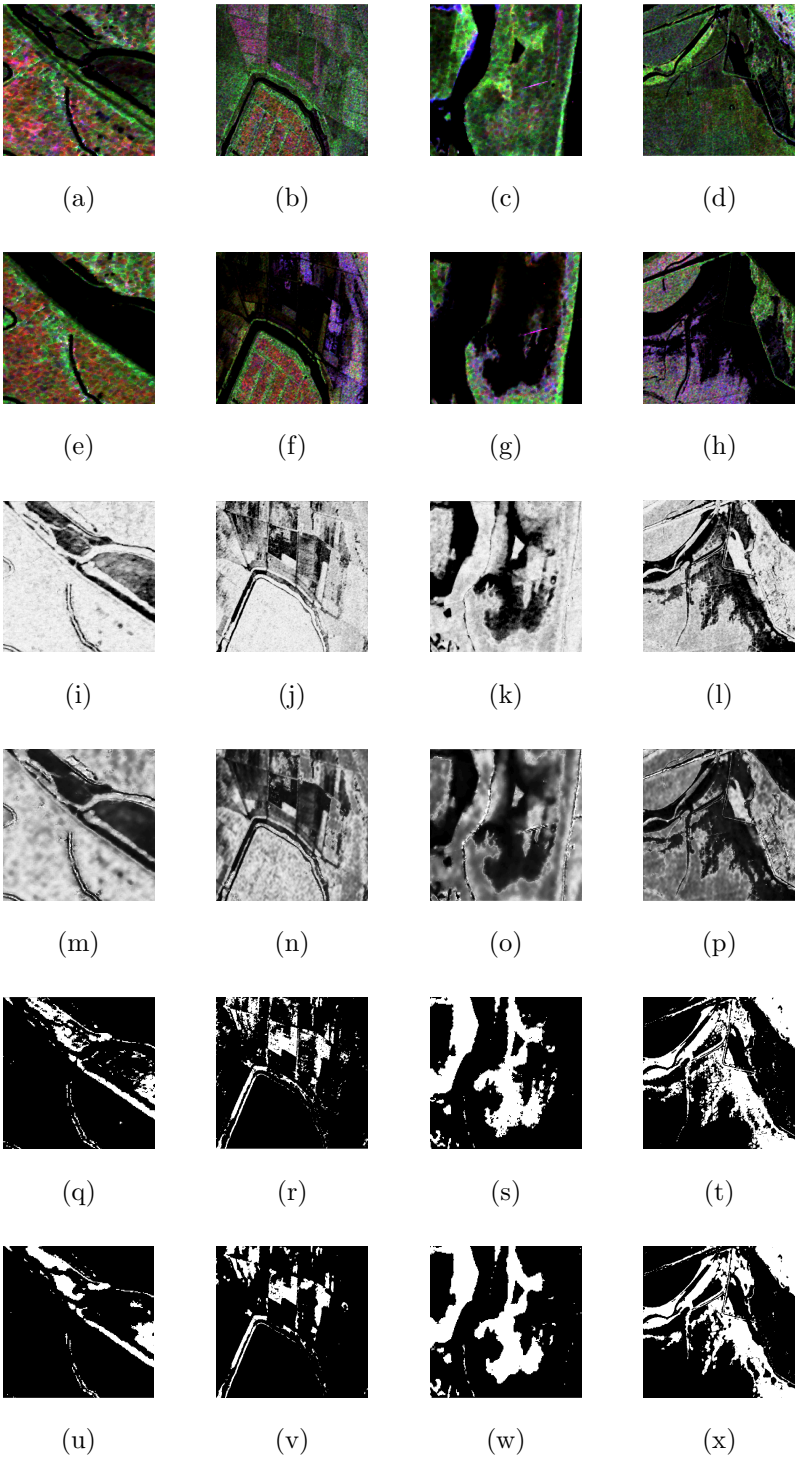

Figure 6.5: Selected samples of image pairs and their corresponding change detection maps: the colour composite of the image (a-d) before, and (e-h) after the flooding event, (i-l) The lnQ map, (m-p) The PDI map, (q-t) The thresholded lnQ map; and (u-x) The thresholded PDI map.

Table 6.2: Accuracy assessment of the change detection maps obtained by both methods

Measures	lnQ	PDI
FN	556122	11057
FP	13325	464162
TN	5364371	4913534
TP	1822370	2367435
OE	569447	475219
PCC	0.927	0.938
Kappa	0.816	0.863

6.7 Conclusion

In this study, a polarimetric index for change detection was introduced based on the ratio of span (total power) which exploits neighbourhood information. The index was applied on a flooding event in Dongting lake, Hunan, China, and then was compared with the Wishart MLR test, another measure for polarimetric change detection. The results demonstrated that although both measures provide an accurate change detecton map with comparable accuracies, the objects produced by the proposed change detection measure are more homogeneous and less noisy. Also, the lnQ map overestimates the amount of change, while underestimation occurs in the PDI map. The result of this research shows the importance of including neighbourhood information in change detection analyses.

Acknowledgement

This project was undertaken with the financial support of the Government of Canada through the federal Department of Environment and Climate Change, and Natural Sciences and Engineering Research Council of Canada (NSERC) under Grants to B. Salehi (NSERC RGPIN-2015- 05027). The work of W. Huang was supported by the Natural Sciences and Engineering Research Council of Canada (NSERC) Discovery Grant RGPIN-2017-04508. Brian Brisco was supported by the RSS program at CCMEO.

Bibliography

[1] Shiqi Huang, Xinhua Cai, Shunxiang Chen, and Daizhi Liu. Change detection method based on fractal model and wavelet transform for multitemporal SAR images. *International Journal of Applied Earth Observation and Geoinformation*, 13(6):863–872, 2011.

[2] Laura Giustarini, Renaud Hostache, Patrick Matgen, Guy J-P Schumann, Paul D Bates, and David C Mason. A change detection approach to flood mapping in urban areas using TerraSAR-X. *IEEE transactions on Geoscience and Remote Sensing*, 51(4):2417–2430, 2013.

[3] Jan Verbesselt, Rob Hyndman, Achim Zeileis, and Darius Culvenor. Phenological change detection while accounting for abrupt and gradual trends in satellite image time series. *Remote Sensing of Environment*, 114(12):2970–2980, 2010.

[4] Komeil Rokni, Anuar Ahmad, Karim Solaimani, and Sharifeh Hazini. A new approach for surface water change detection: Integration of pixel level image fusion and image classification techniques. *International Journal of Applied Earth Observation and Geoinformation*, 34:226–234, 2015.

[5] Masroor Hussain, Dongmei Chen, Angela Cheng, Hui Wei, and David Stanley. Change detection from remotely sensed images: From pixel-based to object-based approaches. *ISPRS Journal of Photogrammetry and Remote Sensing*, 80:91–106, 2013.

[6] Eric JM Rignot and Jakob J Van Zyl. Change detection techniques for ERS-1 sar data. *IEEE Transactions on Geoscience and Remote sensing*, 31(4):896–906, 1993.

[7] Jingjing Ma, Maoguo Gong, and Zhiqiang Zhou. Wavelet fusion on ratio images for change detection in SAR images. *IEEE Geoscience and Remote Sensing Letters*, 9(6):1122–1126, 2012.

[8] Yakoub Bazi, Lorenzo Bruzzone, and Farid Melgani. Automatic identification of the number and values of decision thresholds in the log-ratio image for change detection in SAR images. *IEEE Geoscience and Remote Sensing Letters*, 3(3):349–353, 2006.

[9] Osama Yousif and Yifang Ban. Improving urban change detection from multitemporal SAR images using pca-nlm. *IEEE Transactions on Geoscience and Remote Sensing*, 51(4):2032–2041, 2013.

[10] Yong-Qiang Cheng, Heng-Chao Li, Turgay Celik, and Fan Zhang. FRFT-based improved algorithm of unsupervised change detection in SAR images via PCA and K-means clustering. In *Geoscience and Remote Sensing Symposium (IGARSS), 2013 IEEE International*, pages 1952–1955. IEEE, 2013.

[11] Mohammed Dabboor, Lori White, Brian Brisco, and François Charbonneau. Change detection with compact polarimetric SAR for monitoring wetlands. *Canadian Journal of Remote Sensing*, 41(5):408–417, 2015.

[12] Matthieu Molinier and Yrjo Rauste. Comparison and evaluation of polarimetric change detection techniques in aerial SAR data. In *Geoscience and Remote Sensing Symposium, 2007. IGARSS 2007. IEEE International*, pages 2386–2389. IEEE, 2007.

[13] Knut Conradsen, Allan Aasbjerg Nielsen, Jesper Schou, and Henning Skriver. A test statistic in the complex wishart distribution and its application to change detection in polarimetric SAR data. *IEEE Transactions on Geoscience and Remote Sensing*, 41(1):4–19, 2003.

[14] Meng Liu, Hong Zhang, Chao Wang, and Zili Shan. Urban change detection for high-resolution fully polarimetric SAR using a modified heterogeneous clutter model. In *Synthetic Aperture Radar, 2012. EUSAR. 9th European Conference on*, pages 87–90. VDE, 2012.

[15] Maoguo Gong, Yu Cao, and Qiaodi Wu. A neighborhood-based ratio approach for change detection in SAR images. *IEEE Geoscience and Remote Sensing Letters*, 9(2):307–311, 2012.

[16] Lu Jia, Ming Li, Yan Wu, Peng Zhang, Hongmeng Chen, and Lin An. Semisupervised SAR image change detection using a cluster-neighborhood kernel. *IEEE Geoscience and Remote Sensing Letters*, 11(8):1443–1447, 2014.

[17] Lu Jia, Ming Li, Peng Zhang, Yan Wu, and Huahui Zhu. SAR image change detection based on multiple kernel K-means clustering with local-neighborhood information. *IEEE Geoscience and Remote Sensing Letters*, 13(6):856–860, 2016.

[18] Jong-Sen Lee, Mitchell R Grunes, and Gianfranco De Grandi. Polarimetric SAR speckle filtering and its implication for classification. *IEEE Transactions on Geoscience and remote sensing*, 37(5):2363–2373, 1999.

[19] Nobuyuki Otsu. A threshold selection method from gray-level histograms. *IEEE transactions on systems, man, and cybernetics*, 9(1):62–66, 1979.

[20] Jacob Cohen. A coefficient of agreement for nominal scales. *Educational and psychological measurement*, 20(1):37–46, 1960.

Chapter 7

Summary and Conclusion

7.1 Research Summary

This thesis proposed algorithms and solutions for wetland classification using Remote Sensing (RS), and suggested pre-processing or post-processing techniques for facilitating this procedure. This aim was divided into several research segments described in this thesis in separate chapters. The first step for reaching the thesis goals was to conduct a thorough literature review to gain a deeper understanding of wetland characteristics, RS advances in the case of wetlands, and areas that could be improved. To this end, Chapter 2 was devoted to a literature review on various aspects of wetland studies and different approaches for wetland classification. The comparison between pixel-based and object-based approaches and the role of several classifiers in wetland classification was also provided. In Chapter 3, a novel method for pre-processing SAR images, namely speckle reduction, was proposed, which plays an important role in wetland mapping using SAR imagery. In this method, rather

than adjusting the filtering window shape based on the pixel neighborhood characteristics, the window size was also adapted to the object size in which the pixel was placed. For selecting the best window size, the minimum standard deviation over a range of window sizes in in-phase and quadrature components of a SAR image was considered. Then, the pixel was filtered with its own optimal window size in the intensity image. In Chapter 4, multi-temporal RADARSAT-2 data within four pilot sites in Newfoundland and Labrador (NL) were classified in an object-based manner using the proposed segmentation method. The study determined the optimal feature and time for conducting wetland studies using SAR images, and proved the effectiveness of using multi-temporal data for wetland mapping. In Chapter 5, a novel dynamic classification scheme, well-fitted to the nature of wetlands and other complicated land covers, was proposed. In this method, the objects are not all assigned a label simultaneously; rather, the classes were mapped on an individual basis with a separate feature selection and classification associated with each. This method was applied to classify wetlands in five pilot sites of the province of NL, and increased the wetland classification accuracy considerably compared to the classic method. Finally, in Chapter 6, a full-polarimetric SAR change detection measure was introduced based on neighborhood information as a postprocessing technique for monitoring land covers. Although data from a flood event in NL were unavailable, this measure produced accurate, noiseless, and connected changed objects for a flood event in Dongting Lake, Hunan, China, and can be applied for monitoring other types of land covers, including wetlands.

7.2 Research Achievements

In each of research segments conducted in this thesis several conclusions were identified. A summary of the chapter-wise achievements of the dissertation follows.

In Chapter 2, by reviewing the literature, it is concluded that red edge and near infrared bands are the most appropriate optical bands for wetland delineation. In terms of SAR imagery, different configurations should be selected depending on whether the aim is to classify herbaceous or woody wetlands. For classification of herbaceous wetlands, short wavelengths and shallow incidence angles are more appropriate, while long wavelengths and steep incidence angles are preferred for detecting shrubby or forested wetlands. Full-polarimetric SAR data are favoured for wetland classification, but HH is the most useful polarization for this purpose. Among the available classifiers, RF is the best algorithm for delineating wetlands.

The adaptive window size speckle filters introduced in Chapter 3 outperformed their fixed-size counterparts in both simulated and real images and in single-channel and polarimetric cases. This shows the concept of adaptive window size is more fitted to SAR images, and can in turn improve the performance of algorithms subsequent to filtering.

In Chapter 4, by analyzing the results of classification using SAR data, it is concluded that August is the best time for wetland classification. Features of wetlands are most distinguishable in August, since the vegetation within wetlands is mature. Although vegetation is not mature yet, June is also an appropriate time for classification, because the leaves are fairly fresh. The images obtained in fall or spring, however, are not appropriate for wetland mapping in Canada, because during this

time the vegetation within wetlands is dormant and cannot be applied for discriminating wetlands from each other, or non-wetlands. It should be also mentioned that using images from several dates can increase the accuracy of wetland classification considerably, as the significant dynamicity of wetlands can be used as a distinguishing feature for their classification. One of the most optimal features for wetland classification is the covariance matrix. In addition to intensity layers, covariance matrix also includes phase differences between channels, which are useful for wetland characterization [1–3].

The dynamic classification scheme proposed in Chapter 5 resolved the problem of poor individual accuracies after feature selection despite having a high overall accuracy. By applying the proposed method in wetland classification, the average producer and user accuracies of wetlands increased by up to 22% and 25%, respectively, compared to the classic method. This demonstrates that the proposed method is appropriate for classifying wetlands and other complicated land covers.

The change detection measure proposed in Chapter 6 performs similar to another commonly-used change detection index in terms of accuracy. In terms of visual assessment, the proposed measure generates less noisy and more connected objects that can facilitate making correct managerial decisions.

To recapitulate, in this thesis several innovative methods and solutions are proposed to facilitate the study of wetlands and other complicated land covers, the most important of which follow:

- A thorough literature review was provided on wetlands, which considers all aspects of wetland studies;

- A pre-processing method for the classification of land covers, namely a speckle reduction method, was proposed which adjusts the filtering size based on the area of the object. This is useful for study of wetlands as they can vary considerably in size;

- A multi-temporal study was conducted in which the most appropriate time and features for wetland classification were determined and an alternative method for segmentation of SAR data was applied;

- A novel classification scheme was introduced that was well fitted to the nature of wetlands and, therefore, increased wetland accuracy considerably; and

- A new change detection scheme was presented that delineated the changed areas with a high accuracy and without noise, which can be applied for monitoring various land covers.

7.3 Recommendation for Future Work

Based on the results achieved by this thesis, the following items are recommended for future work:

- **Developing up-to-date Canada-wide and Global wetland inventories.** Currently, there is no up-to-date and precise estimation of Canada-wide or global coverages of wetlands. However, it is important to develop an operational global wetland mapping and monitoring scheme by which estimation of global wetland coverage and frequent update of wetland conditions is possible. For reaching this goal, wetland-related organizations all over the world need to

collaborate in terms of field data collection and developing classification methods. Moreover, satellite data and RS algorithms should be provided such that the cost and computational complexity of producing and updating maps is minimized. In fact, freely available satellite imagery should be utilized as much as possible. Moreover, there should be an overall agreement on a unique classification scheme that can be implemented globally or in most parts of the world. An example of such a classification scheme is the Ducks Unlimited Enhanced Wetland Classification System [4].

- **Adjusting the common speckle filters to be applied with adaptive window size.** Currently, there are several common filters, such as the Lee's improved Sigma [5], Frost [6], and Kuan [7] filters, that use a fixed window size for filtering SAR imagery. These algorithms, which have already proved effective, can be adjusted to be applied with adaptive window size. This is expected to further improve the performance of these algorithms.

- **Utilizing the proposed alternative SAR segmentation scheme in other applications.** SAR images are speckled and this causes the segmentation of SAR images to be less accurate than that of optical images. Therefore, in Chapter 4 an alternative segmentation method was proposed in which the result of the segmentation of an optical image was superimposed on the SAR image of the same area. As a result of doing this, speckle is considerably reduced or eliminated in SAR data, while their valuable characteristics remain preserved. It is recommended that this method is applied in applications involving SAR imagery other than wetland classification which is included in this thesis. Thus,

researchers could benefit from the advantages of object-based classification over the traditional pixel-based classification when SAR images are used in their studies.

- **Operational implementation of the proposed dynamic classification scheme.** As mentioned earlier, there is a need for robust classification algorithms which can be used to map wetlands globally. The algorithm proposed in Chapter 5, which has proved effective in NL, can be applied in different parts of the world to examine its effectiveness. Moreover, as the proposed scheme has a high flexibility, different parts of the algorithm can be replaced with more advanced or less computationally complex methods to adjust its performance. For example, the proposed feature selection method (i.e., GA) can be replaced with a more advanced method like Particle Swarm Optimization (PSO) [8].

- **Applying the proposed change detection scheme for wetland studies.** Although wetland classes are highly dynamic, changing permanently from one wetland type to another takes several years. Unfortunately, a long-term dataset (e.g. 10-year period) of SAR images from NL required for applying the proposed change detection method was not available at the time of writing this thesis. However, it is suggested that upon the availability of the required dataset, this method is applied in wetland studies. For example, a pilot study in China revealed this technique was useful in monitoring a dynamic short-term flood event. Thus, the suggested method might facilitate monitoring of wetlands using remote sensing data.

Bibliography

[1] Kevin O Pope, Jose M Rey-Benayas, and Jack F Paris. Radar remote sensing of forest and wetland ecosystems in the Central American tropics. *Remote Sensing of Environment*, 48(2):205–219, 1994.

[2] Laura L Hess, John M Melack, Solange Filoso, and Yong Wang. Delineation of inundated area and vegetation along the Amazon floodplain with the SIR-C synthetic aperture radar. *IEEE Transactions on Geoscience and Remote Sensing*, 33(4):896–904, 1995.

[3] Ridha Touzi. Target scattering decomposition in terms of roll-invariant target parameters. *IEEE Transactions on Geoscience and Remote Sensing*, 45(1):73–84, 2007.

[4] KB Smith, CE Smith, SF Forest, and AJ Richard. A field guide to the wetlands of the boreal plains ecozone of Canada. *Ducks Unlimited Canada, Western Boreal Office: Edmonton, Alberta*, 2007.

[5] Jong-Sen Lee, Jen-Hung Wen, Thomas L Ainsworth, Kun-Shan Chen, and Abel J Chen. Improved sigma filter for speckle filtering of SAR imagery. *IEEE Transactions on Geoscience and Remote Sensing*, 47(1):202–213, 2009.

[6] Victor S Frost, Josephine Abbott Stiles, K Sam Shanmugan, and Julian C Holtzman. A model for radar images and its application to adaptive digital filtering of multiplicative noise. *IEEE Transactions on pattern analysis and machine intelligence*, (2):157–166, 1982.

[7] Darwin T Kuan, Alexander A Sawchuk, Timothy C Strand, and Pierre Chavel. Adaptive noise smoothing filter for images with signal-dependent noise. *IEEE transactions on pattern analysis and machine intelligence*, (2):165–177, 1985.

[8] James Kennedy. Particle swarm optimization. In *Encyclopedia of machine learning*, pages 760–766. Springer, 2011.